



**Calhoun: The NPS Institutional Archive**  
**DSpace Repository**

---

Theses and Dissertations

1. Thesis and Dissertation Collection, all items

---

1994-12

A ground support electronic interface for the  
Ionospheric Spectroscopy and Atmospheric  
Chemistry (ISAAC) ultraviolet spectrograph

MacQuarrie, Jeffrey Alan

Monterey, California. Naval Postgraduate School

---

<http://hdl.handle.net/10945/42835>

*Downloaded from NPS Archive: Calhoun*

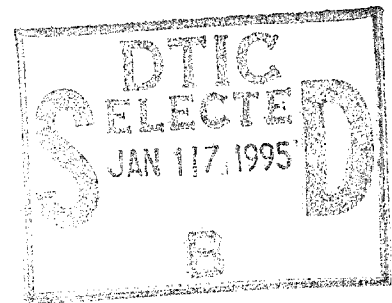


Calhoun is a project of the Dudley Knox Library at NPS, furthering the precepts and goals of open government and government transparency. All information contained herein has been approved for release by the NPS Public Affairs Officer.

**Dudley Knox Library / Naval Postgraduate School**  
**411 Dyer Road / 1 University Circle**  
**Monterey, California USA 93943**

<http://www.nps.edu/library>

**NAVAL POSTGRADUATE SCHOOL**  
**Monterey, California**



**THESIS**

**A GROUND SUPPORT ELECTRONIC  
INTERFACE FOR THE IONOSPHERIC  
SPECTROSCOPY AND ATMOSPHERIC  
CHEMISTRY (ISAAC) ULTRAVIOLET  
SPECTROGRAPH**

by

Jeffrey A. MacQuarrie

December, 1994

Thesis Advisor:  
Co-Advisor:

David D. Cleary  
Oscar Biblarz

**Approved for public release; distribution is unlimited.**

19950113 002

# REPORT DOCUMENTATION PAGE

*Form Approved OMB No. 0704-0188*

Public reporting burden for this collection of information is estimated to average 1 hour per response, including the time for reviewing instruction, searching existing data sources, gathering and maintaining the data needed, and completing and reviewing the collection of information. Send comments regarding this burden estimate or any other aspect of this collection of information, including suggestions for reducing this burden, to Washington Headquarters Services, Directorate for Information Operations and Reports, 1215 Jefferson Davis Highway, Suite 1204, Arlington, VA 22202-4302, and to the Office of Management and Budget, Paperwork Reduction Project (0704-0188) Washington DC 20503.

<b>1. AGENCY USE ONLY</b> <i>(Leave blank)</i>		<b>2. REPORT DATE</b> December, 1994	<b>3. REPORT TYPE AND DATES COVERED</b> Master's Thesis	
<b>4. TITLE AND SUBTITLE</b> A GROUND SUPPORT ELECTRONIC INTERFACE FOR THE IONOSPHERIC SPECTROSCOPY AND ATMOSPHERIC CHEMISTRY (ISAAC) ULTRAVIOLET SPECTROGRAPH			<b>5. FUNDING NUMBERS</b>	
<b>6. AUTHOR(S)</b> MacQuarrie, Jeffrey A.				
<b>7. PERFORMING ORGANIZATION NAME(S) AND ADDRESS(ES)</b>  Naval Postgraduate School Monterey CA 93943-5000			<b>8. PERFORMING ORGANIZATION REPORT NUMBER</b>	
<b>9. SPONSORING/MONITORING AGENCY NAME(S) AND ADDRESS(ES)</b>			<b>10. SPONSORING / MONITORING AGENCY REPORT NUMBER</b>	
<b>11. SUPPLEMENTARY NOTES</b> The views expressed in this thesis are those of the author and do not reflect the official policy or position of the Department of Defense or the U.S. Government.				
<b>12a. DISTRIBUTION / AVAILABILITY STATEMENT</b> Approved for public release; distribution is unlimited.			<b>12b. DISTRIBUTION CODE</b>	
<b>13. ABSTRACT</b> <i>(Maximum 200 words)</i> This thesis details the design and development of an electronic Ground Support Equipment (GSE) interface for the Naval Postgraduate School's (NPS) Ionospheric Spectroscopy and Atmospheric Chemistry (ISAAC) spectrograph. The ISAAC spectrograph, which was designed at NPS and built by Research Support Instruments, Inc., is intended to observe atmospheric airglow and auroral emissions in the ultraviolet (1800Å to 3300Å) wavelength region. It is to be included as one of several sensors flown onboard the Advanced Research and Global Observation Satellite (ARGOS), which is scheduled for an early 1996 launch. The GSE was developed in order to allow ground testing and calibration of the instrument prior to and during integration with the satellite bus. The GSE includes hardware to provide the connections between various components of the spectrograph and a Macintosh computer with an installed I/O card. The GSE also includes a user-friendly software interface written with LabVIEW 2.2 that provides the ability to view spectra obtained from the instrument and to remotely control mechanical functions of the spectrograph. An initial wavelength calibration of the spectrograph has been performed using the completed GSE.				
<b>14. SUBJECT TERMS</b> Ionosphere, Electron Density, Ultraviolet Spectroscopy, Ebert-Fastie Spectrograph, ISAAC, ARGOS Satellite, Ground Support Equipment, Electronic Interface			<b>15. NUMBER OF PAGES</b> 222	
			<b>16. PRICE CODE</b>	
<b>17. SECURITY CLASSIFICATION OF REPORT</b> Unclassified	<b>18. SECURITY CLASSIFICATION OF THIS PAGE</b> Unclassified	<b>19. SECURITY CLASSIFICATION OF ABSTRACT</b> Unclassified	<b>20. LIMITATION OF ABSTRACT</b> UL	



Approved for public release; distribution is unlimited.

**A GROUND SUPPORT ELECTRONIC INTERFACE FOR THE IONOSPHERIC  
SPECTROSCOPY AND ATMOSPHERIC CHEMISTRY (ISAAC) ULTRAVIOLET  
SPECTROGRAPH**

Jeffrey Alan MacQuarrie  
Lieutenant, United States Navy  
B.A., University of Maryland, 1986  
M.B.A., New Hampshire College, 1989

Submitted in partial fulfillment of the  
requirements for the degrees of

**MASTER OF SCIENCE IN ASTRONAUTICAL ENGINEERING**

and

**MASTER OF SCIENCE IN APPLIED PHYSICS**

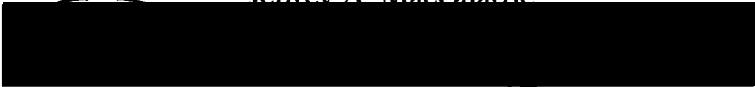
from the

**NAVAL POSTGRADUATE SCHOOL  
December, 1994**


Author:

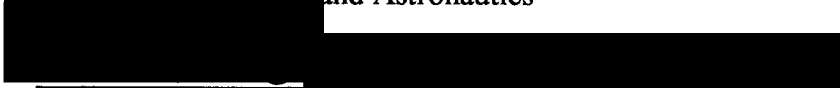
  
Jeffrey A. MacQuarrie

Approved by:

  
David D. Cleary, Thesis Advisor

  
Oscar Biblarz, Co-Advisor

  
Daniel J. Collins, Chairman, Department of Aeronautics  
and Astronautics

  
William B. Colson, Chairman, Department of Physics



## ABSTRACT

This thesis details the design and development of an electronic Ground Support Equipment (GSE) interface for the Naval Postgraduate School's (NPS) Ionospheric Spectroscopy and Atmospheric Chemistry (ISAAC) spectrograph. The ISAAC spectrograph, which was designed at NPS and built by Research Support Instruments, Inc., is intended to observe atmospheric airglow and auroral emissions in the ultraviolet (1800Å to 3300Å) wavelength region. It is to be included as one of several sensors flown onboard the Advanced Research and Global Observation Satellite (ARGOS), which is scheduled for an early 1996 launch. The GSE was developed in order to allow ground testing and calibration of the instrument prior to and during integration with the satellite bus. The GSE includes hardware to provide the connections between various components of the spectrograph and a Macintosh computer with an installed I/O card. The GSE also includes a user-friendly software interface written with LabVIEW 2.2 that provides the ability to view spectra obtained from the instrument and to remotely control mechanical functions of the spectrograph. An initial wavelength calibration of the spectrograph has been performed using the completed GSE.

Accession For	
NTIS GRA&I	<input checked="" type="checkbox"/>
DTIC TAB	<input type="checkbox"/>
Unannounced	<input type="checkbox"/>
Justification	
By _____	
Distribution/_____	
Availability Codes	
Dist	Avail and/or Special
A-1	





## TABLE OF CONTENTS

I. INTRODUCTION .....	1
A. THESIS OBJECTIVES .....	2
B. THESIS OUTLINE .....	3
II. BACKGROUND .....	5
A. THE ATMOSPHERE .....	5
1. Temperature Classification .....	5
2. Chemical Composition Classification .....	6
3. Chemical Process Classification .....	9
a. The Chemosphere .....	9
b. The Ionosphere .....	9
(1) The <i>D</i> -Layer .....	10
(2) The <i>E</i> -Layer .....	11
(3) The <i>F</i> -Layer .....	12
B. ATOMIC SPECTROSCOPY .....	13
1. The Bohr Atom .....	13
2. Quantum Mechanical Interpretation of the Atom .....	14
a. Stationary States .....	15
b. Quantized Energy of an Atom .....	16
c. Shells, Subshells and Orbitals .....	17
d. The Pauli Exclusion Principle and Hund's Rule .....	17
e. Orbital Angular Momentum .....	18
f. Spin Angular Momentum .....	20
g. Total Angular Momentum - LS Coupling .....	21
h. Spectroscopic Notation .....	22
i. Selection Rules .....	23
C. DIATOMIC MOLECULAR SPECTROSCOPY .....	24
1. Rotational Spectra - The Rigid Rotator .....	25
2. Vibrational Spectra .....	27

3.	The Anharmonic Oscillator, Nonrigid Rotator and the Vibrating Rotator . . . . .	29
a.	The Anharmonic Oscillator . . . . .	29
b.	The Nonrigid Rotator . . . . .	30
c.	The Vibrating Rotator . . . . .	31
4.	Spectroscopic Notation . . . . .	31
a.	Orbital Angular Momentum . . . . .	32
b.	Spin . . . . .	32
c.	Total Angular Momenta . . . . .	33
d.	Rotational, Vibrational Transitions . . . . .	34
e.	Electronic States . . . . .	34
D.	ATMOSPHERIC AIRGLOW AND AURORAL EMISSIONS . . . . .	37
1.	Airglow . . . . .	37
a.	Photoexcitation . . . . .	37
b.	Electron-Impact Excitation . . . . .	37
c.	Pre-dissociation . . . . .	38
d.	Photochemical Reactions . . . . .	38
2.	Aurora . . . . .	39
3.	Airglow and Auroral Emission Features . . . . .	40
a.	Atomic Nitrogen . . . . .	44
b.	Molecular Nitrogen . . . . .	45
c.	Atomic Oxygen . . . . .	47
d.	Molecular Oxygen . . . . .	49
e.	Nitric Oxide . . . . .	51
E.	TEMPERATURE AND ELECTRON DENSITY PROFILES . . . . .	53
III.	ARGOS SATELLITE AND PAYLOAD . . . . .	57
A.	ELECTRIC PROPULSION SPACE EXPERIMENT (ESEX) . . . . .	60
B.	CRITICAL IONIZATION VELOCITY (CIV) . . . . .	60
C.	GLOBAL IMAGING MONITOR OF THE IONOSPHERE (GIMI) . . . . .	60

D. UNCONVENTIONAL STELLAR ASPECT (USA) .....	61
E. EXTREME ULTRAVIOLET IMAGING PHOTOMETER (EUVIP) .....	61
F. SPACE DUST EXPERIMENT (SPADUS) .....	61
G. HIGH TEMPERATURE SUPERCONDUCTIVITY SPACE EXPERIMENT (HTSSE II) .....	62
H. HIGH RESOLUTION AIRGLOW AND AURORAL SPECTROSCOPY (HIRAAS) .....	62
IV. ISAAC SPECTROGRAPH .....	65
A. EBERT-FASTIE SPECTROGRAPH .....	67
B. ITT IMAGE INTENSIFIER .....	69
C. HAMAMATSU CCD IMAGE SENSOR .....	69
1. Photodiodes .....	70
2. Shift Register .....	70
3. C4350 Driver/Amplifier Circuit .....	70
D. ISAAC STEPPER MOTOR AND DUST COVER .....	71
1. Stepper Motor .....	71
2. Dust Cover Door .....	72
E. STEPPER MOTOR CONTROLLER .....	74
1. J1 Interface .....	75
a. Motor Step .....	75
b. Fiducial Signal .....	75
c. Dust Cover Door Micro Switches .....	77
2. J2 Interface .....	77
3. J3 Interface .....	77
V. GSE HARDWARE DESIGN .....	79
A. NATIONAL INSTRUMENTS NB-MIO-16 I/O BOARD .....	79
1. Clocks .....	83
a. Counter 1 .....	83
b. Counter 2 .....	83

c. Counter 5 .....	83
2. Video Data and Clock Timing .....	84
3. A/D Conversions .....	84
4. Digital I/O .....	86
a. Digital I/O Ports and Technical Specifications .....	86
b. Configuration of Digital I/O Ports for ISAAC GSE .....	86
c. Method to Increase Available Output Ports .....	87
B. ISAAC ELECTRONICS INTERFACE BOX .....	89
1. Power Supply .....	89
2. Front Panel Output Connections .....	92
3. I/O Connectors and Internal Wiring .....	92
VI. GSE SOFTWARE DESIGN .....	99
A. ISAAC GSE SOFTWARE USER INTERFACE .....	99
B. THE ISAAC GSE PROGRAM .....	101
1. ISAAC Initialization Sub-VI .....	105
2. Acquire Data .....	119
3. Save to Disk .....	125
4. Select Grating Position .....	126
VII. WAVELENGTH CALIBRATION .....	133
VIII. CONCLUSIONS .....	151
A. SUMMARY OF ISAAC DEVELOPMENT .....	151
B. POTENTIAL FOLLOW-ON WORK .....	151
APPENDIX A. ITT IMAGE INTENSIFIER TECHNICAL DATA .....	153
APPENDIX B. GBS HIGH-VOLTAGE MICRO POWER SUPPLY TECHNICAL DATA .....	157
APPENDIX C. HAMAMATSU S3904 MOS LINEAR IMAGE SENSOR TECHNICAL DATA .....	163
APPENDIX D. HAMAMATSU C4070/C4350 DRIVER/AMPLIFIER CIRCUIT TECHNICAL DATA .....	171

APPENDIX E. HAMAMATSU C4070/C4350 DRIVER/AMPLIFIER	
OPERATION INSTRUCTION .....	173
APPENDIX F. RSI MODEL 480-229 STEPPER MOTOR DRIVER	
TECHNICAL DATA AND TEST REPORT .....	179
APPENDIX G. ISAAC GSE USER'S MANUAL .....	187
LIST OF REFERENCES .....	195
INITIAL DISTRIBUTION LIST .....	199



## LIST OF TABLES

2-1. Mass of the Atmosphere and its Constituents . . . . .	8
2-2. Quantum Numbers for the Hydrogen Atom and Allowed States . . . . .	16
2-3. Atomic Shell and Subshell Notations . . . . .	17
4-1. Detector Interface Pinout . . . . .	71
4-2. J1 Interface Pinout . . . . .	76
4-3. Motor Steps to Select Grating Positions . . . . .	77
4-4. J2 Motor & Fiducial Interface Pinout . . . . .	78
4-5. J3 Dust Cover Interface Pinout . . . . .	78
5-1. NB-MIO-16 I/O Connector . . . . .	82
5-2. Selections of BDIO0 through BDIO2 to Create Eight Output Lines as shown in Figure 5-4 . . . . .	89
5-3. Pin Functions and Internal Connections for GSE-1 I/O Connector . . . . .	93
5-4. Pin Functions and Internal Connections for GSE-2 I/O Connector . . . . .	94
5-5. Pin Functions and Internal Connections for GSE-3 I/O Connector . . . . .	95-96
5-6. Pin Functions and Internal Connections for GSE-4 I/O Connector . . . . .	97
5-7. Cable A 37-pin Female to 25-pin Female Interconnections . . . . .	98
7-1. Spectral Emissions Used for Wavelength Calibration . . . . .	135
7-2. Identified Spectral Emissions, Actual and Calculated Linear and Polynomial Wavelengths and Corresponding Errors in Fit for Grating Position ONE . . . . .	146
7-3. Identified Spectral Emissions, Actual and Calculated Linear and Polynomial Wavelengths and Corresponding Errors in Fit for Grating Position TWO . . . . .	147
7-4. Identified Spectral Emissions, Actual and Calculated Linear and Polynomial Wavelengths and Corresponding Errors in Fit for Grating Position THREE . . . . .	148
7-5. Identified Spectral Emissions, Actual and Calculated Linear and Polynomial Wavelengths and Corresponding Errors in Fit for Grating Position FOUR . . . . .	149





## LIST OF FIGURES

2-1. Temperature Layers of the Atmosphere . . . . .	7
2-2. Chapman Profile . . . . .	10
2-3. Distribution of Positive Ions for a Daytime Ionosphere at Solar Minimum . . . . .	11
2-4. Bohr Model of the Hydrogen Atom with Spectral Emissions . . . . .	14
2-5. The Balmer Series of Spectral Lines for Hydrogen . . . . .	15
2-6. (a) Allowed Projections of the Orbital Angular Momentum for the Case $\ell = 2$ . (b) Orbital Angular Momentum Vector . . . . .	19
2-7. Space Quantization of Spin Angular Momentum . . . . .	21
2-8. Some Allowed Electron Transitions for Hydrogen . . . . .	24
2-9. (a) A Diatomic Molecule Oriented Along the x-axis Modeled as a Rigid Rotator. (b) Allowed Rotational Energies of a Diatomic Molecule . . . . .	26
2-10. (a) Diatomic Molecule Modeled as a Spring System. (b) Potential Energy versus Atomic Separation. (c) Allowed Vibrational Energies of a Diatomic Molecule . . . . .	28
2-11. Molecular Energy versus Internuclear Separation for two Electronic States . . . . .	33
2-12. Vibrational-Rotational Energy Level Diagram Showing both P and R Branches . . . . .	35
2-13. Potential Energy Diagram for the Principal States of the Oxygen Molecule . . . . .	39
2-14. Spectrum of the Earth's UV Dayglow . . . . .	41
2-15. Ultraviolet Nightglow Spectra . . . . .	42
2-16. Auroral Spectrum . . . . .	43
2-17. Energy Level Diagram for $N^+$ Showing Transitions Observed in the Airglow or Aurora . . . . .	44
2-18. Potential Energy Curves for $N_2^-$ (unstable), $N_2$ , and $N_2^+$ . . . . .	46
2-19. Energy Level Diagram for Atomic Oxygen Showing the Transitions Observed in the Airglow and Aurora . . . . .	47
2-20. Energy Level Diagram for Singly Ionized Atomic Oxygen . . . . .	48
2-21. Potential Energy Diagram for Molecular Oxygen . . . . .	50
2-22. Potential Energy Diagram for Nitric Oxygen States . . . . .	52

2-23. Synthetic Spectra for the (1,1) Gamma Band at a Temperature of 280 K and at 710 K .....	54
2-24. Schematic Representation of the Production of Odd Nitrogen in the Thermosphere .....	56
3-1. ARGOS Space Vehicle and Payload Configuration .....	57
3-2. 7920-10 Delta II Launch Vehicle .....	58
3-3. ARGOS P91-1 Launch Ascent Profile .....	59
3-4. HIRAAS Assembly .....	62
3-5. HIRAAS Limb Imaging Concept .....	63
4-1. The ISAAC Spectrograph .....	65
4-2. Mechanical Drawing of the ISAAC Spectrograph .....	66
4-3. Mechanical Drawing of the ISAAC Spectrograph Showing Path of Incident Light .....	67
4-4. Reflecting Diffraction Grating Depicting Several Diffraction Orders .....	68
4-5. Stepper Motor Cam Track .....	73
4-6. Stepper Motor Controller Mechanical Drawing .....	74
5-1. The ISAAC Spectrograph Connected to the GSE .....	80
5-2. ISAAC GSE Hardware Interface .....	81
5-3. Timing Diagram for Master Clock, Master Start Clock, A/D Trigger, and Video Data .....	85
5-4. Demultiplexer that could be Implemented to Create Additional Output Lines ...	88
5-5. ISAAC GSE Electronics Interface Box .....	90
5-6. AC/DC Converter and Voltage Regulators Schematic for GSE Power Supply ..	91
6-1. <i>ISAAC GSE</i> Front Panel with Sample Pt-Lamp Spectrum .....	100
6-2. <i>ISAAC GSE</i> Sub-VI Hierarchy .....	102
6-3. <i>ISAAC GSE</i> VI Block Diagram and Additional Cases of Case Structures .....	103
6-4. <i>ISAAC GSE</i> VI Block Diagram (continued) .....	104
6-5. ISAAC GSE <i>ISAAC INIT</i> sub-VI Front Panel .....	106
6-6. ISAAC GSE <i>ISAAC INIT</i> sub-VI Block Diagram .....	108

6-7.	ISAAC GSE <i>ISAAC INIT</i> sub-VI Block Diagram (continued) . . . . .	109
6-8.	ISAAC GSE <i>ISAAC INIT</i> sub-VI Block Diagram (continued) . . . . .	110
6-9.	ISAAC GSE <i>ISAAC INIT</i> sub-VI Block Diagram (continued) . . . . .	111
6-10.	ISAAC GSE <i>ISAAC INIT</i> sub-VI Block Diagram (continued) . . . . .	112
6-11.	ISAAC GSE <i>ISAAC INIT</i> sub-VI Block Diagram (continued) . . . . .	113
6-12.	ISAAC GSE <i>INIT ISAAC MIO</i> sub-VI Block Diagram . . . . .	114
6-13.	ISAAC GSE <i>INIT ISAAC MIO</i> sub-VI Block Diagram (continued) . . . . .	115
6-14.	ISAAC GSE <i>INIT ISAAC MIO</i> sub-VI Block Diagram (continued) . . . . .	116
6-15.	ISAAC GSE <i>GO TO FIDUC</i> sub-VI Block Diagram . . . . .	117
6-16.	ISAAC GSE <i>GO TO FIDUC</i> sub-VI Block Diagram (continued) . . . . .	118
6-17.	ISAAC GSE <i>AVG N SPEC</i> sub-VI Block Diagram . . . . .	121
6-18.	ISAAC GSE <i>AVG N SPEC</i> sub-VI Block Diagram (continued) . . . . .	122
6-19.	ISAAC GSE <i>WAVELENGTH CONVERTER</i> sub-VI Block Diagram . . . . .	123
6-20.	ISAAC GSE <i>WAVELENGTH CONVERTER</i> sub-VI Block Diagram (cont.) . .	124
6-21.	ISAAC GSE <i>SAVE-To-DISK</i> sub-VI Block Diagram . . . . .	125
6-22.	ISAAC GSE <i>STEPPER DRIVER</i> sub-VI Front Panel . . . . .	127
6-23.	ISAAC GSE <i>STEPPER DRIVER</i> sub-VI Block Diagram . . . . .	128
6-24.	ISAAC GSE <i>STEPPER DRIVER</i> sub-VI Block Diagram (continued) . . . . .	129
6-25.	ISAAC GSE <i>SET POSIT</i> sub-VI Block Diagram . . . . .	130
6-26.	ISAAC GSE <i>SET POSIT</i> sub-VI Block Diagram (continued) . . . . .	131
7-1.	Platinum Spectrum at ISAAC Grating Position ONE . . . . .	136
7-2.	Mercury Spectrum at ISAAC Grating Position ONE . . . . .	136
7-3.	Platinum Spectrum at ISAAC Grating Position TWO . . . . .	137
7-4.	Mercury Spectrum at ISAAC Grating Position TWO . . . . .	137
7-5.	Platinum Spectrum at ISAAC Grating Position THREE . . . . .	138
7-6.	Mercury Spectrum at ISAAC Grating Position THREE . . . . .	138
7-7.	Platinum Spectrum at ISAAC Grating Position FOUR . . . . .	139
7-8.	Mercury Spectrum at ISAAC Grating Position FOUR . . . . .	139

7-9. Difference Between Linear Fit and Actual Wavelengths at Grating	
Position ONE .....	140
7-10. Difference Between Linear Fit and Actual Wavelengths at Grating	
Position TWO .....	140
7-11. Difference Between Linear Fit and Actual Wavelengths at Grating	
Position THREE .....	141
7-12. Difference Between Linear Fit and Actual Wavelengths at Grating	
Position FOUR .....	141
7-13. Quadratic Fit to Identified Platinum Spectral Lines at Grating Position ONE ..	142
7-14. Quadratic Fit to Identified Platinum and Mercury Spectral Lines at Grating	
Position TWO .....	142
7-15. Quadratic Fit to Identified Platinum and Mercury Spectral Lines at Grating	
Position TWO .....	143
7-16. Quadratic Fit to Identified Platinum and Mercury Spectral Lines at Grating	
Position TWO .....	143
7-17. Difference Between Quadratic Fit and Actual Wavelengths at Grating	
Position ONE .....	144
7-18. Difference Between Quadratic Fit and Actual Wavelengths at Grating	
Position TWO .....	144
7-19. Difference Between Quadratic Fit and Actual Wavelengths at Grating	
Position THREE .....	145
7-20. Difference Between Quadratic Fit and Actual Wavelengths at Grating	
Position FOUR .....	145

## LIST OF ABBREVIATIONS, ACRONYMS AND SYMBOLS

Å	Angstrom, unit of wavelength measure equal to $10^{-10}$ meters.
AC	Alternating Current
A/D	Analog to Digital
ARGOS	Advanced Research and Global Observation Satellite
CCD	Charge Coupled Device
CIV	Critical Ionization Velocity - ARGOS experiment
D/A	Digital to Analog
DC	Direct Current
DMSP	Defense Meteorological Satellite Program
DoD	Department of Defense
EUV	Extreme Ultraviolet
EUVIP	Extreme Ultraviolet Imaging Photometer - ARGOS experiment
ESEX	Electric Propulsion Space Experiment - ARGOS experiment
FUV	Far Ultraviolet
GIMI	Global Imaging Monitor of the Ionosphere - ARGOS experiment
GSE	Ground Support Equipment
I/O	Input/Output
IDL	Interactive Data Language - published by Research Systems, Inc.
ISAAC	Ionospheric Spectroscopy and Atmospheric Chemistry
HIRAAS	High Resolution Airglow and Auroral Spectroscopy - ARGOS experiment
HITS	High Resolution Ionospheric/Thermospheric Spectrograph - HIRAAS sub-experiment
HTSSE II	High Temperature Superconductivity Space Experiment - ARGOS experiment
JCS	Joint Chiefs of Staff
LBH	Lyman-Birge-Hopfield - nitrogen emissions
LORAAS	Low Resolution Airglow/Aurora Spectrograph - HIRAAS sub-experiment
MOS	Metal Oxide Semiconductor

MUSTANG	Middle Ultraviolet Spectral Analysis of Nitrogen Gases Spectrograph; predecessor to ISAAC
MUV	Middle Ultraviolet
NRL	Naval Research Laboratory
NPS	Naval Postgraduate School
RSI	Research Support Instruments, Inc. - fabricated ISAAC
SPADUS	Space Dust Experiment - ARGOS experiment
SSULI	Special Sensor for UV Limb Imaging - DMSP satellite sensor
STP	Space Test Program
TTL	Transistor-transistor logic
USA	Unconventional Stellar Aspect - ARGOS experiment
UV	ultraviolet, band of the electromagnetic spectrum between 600Å and 3800Å
VI	Virtual Instrument - program in LabVIEW software.
V-K	Vegard-Kaplan - nitrogen emissions

## ACKNOWLEDGMENT

It has been a tremendous privilege and great learning opportunity to work with the ISAAC experiment and ARGOS satellite project. I am highly indebted to the researchers involved with this project at both the Naval Postgraduate School and the Naval Research Laboratory without whom I would not have been able to complete this project.

First, I thank the United States Navy and the Naval Security Group for providing the opportunity for exceptional graduate education. The Navy has truly provided me with limitless opportunities.

I am especially thankful to have been allowed to work with *Professor Dave Cleary*, who provided many hours of his time schooling me in a wide range of topics with clarity and patience. His interest in the education of his students is greatly appreciated. Through his efforts, I was given the opportunity to witness and participate in the integration and testing of the MUSTANG spectrograph with its sounding rocket at Wallops Island, VA and later to participate in the third launch of the MUSTANG experiment from Poker Flat, Alaska in March, 1994. I was also able to participate in the Preliminary Design Review of the ARGOS Satellite in 1993. I believe that these experiences have provided an outstanding education in Space Systems Engineering thanks to the efforts of this professor and Navy funding.

*Dr. Oscar Biblarz*, my co-advisor, provided much-appreciated advice in refining the text of this thesis.

*Dr. Larry Scoggin*, ARGOS Project Manager, *Dr. Robert McCoy*, HIRAAS Principal Investigator, *Dr. Ken Dymond*, Project Scientist, and *Mr. Joe Mathews* and *Mr. Pat Dement*, HIRAAS Control Electronics Engineers were all extremely helpful in providing me with data and in accommodating an experience tour to NRL in March, 1994.

*Dale Galarowicz* provided the necessary education in electronics to assemble the GSE power supply and *George Jaksha* instructed me in working with metal shop machinery and provided many tips for completion of the GSE hardware.

Finally, I must thank my family, *Carolyn*, *Heather*, and *Richard* for their patience and understanding during many months of thesis work and the preparation of this document.

## I. INTRODUCTION

Witness, you ever-burning lights above,  
you elements that clip us round about . . . .

from *Othello* by William Shakespeare

The Ionospheric Spectroscopy and Atmospheric Chemistry (ISAAC) spectrograph was designed and developed at the Naval Postgraduate School (NPS) in order to provide a spaceborne method of examining the auroral and dayglow ultraviolet (UV) spectral emissions of the upper atmosphere. In addition to allowing a greater scientific understanding of the chemistry of the upper atmosphere, these observations will provide a passive method of determining electron-density and temperature profiles of the ionosphere. The ISAAC spectrograph will directly measure the intensities of the ultraviolet spectral emissions of several atomic and molecular atmospheric constituents. Electron density and temperature profiles of the upper atmosphere can then be inferred from these measurements.

ISAAC is to be launched along with eight other experiments aboard the Advanced Research and Global Observation Satellite (ARGOS) in early 1996. The payload of this satellite will both provide for greater scientific understanding of the physics and chemistry of the upper atmosphere and satisfy Department of Defense needs.

Study of the atmosphere is important as the conditions that permit life on Earth are fragile extremely dependent on the atmospheric content. The atmosphere provides a warm thermal blanket about the Earth. It is mostly transparent to the incoming 6000-K solar blackbody radiation, although ozone, carbon dioxide and water vapor have strong absorption bands that trap infrared radiation re-emitted by the Earth. The temperature of the Earth's surface without an atmosphere would have warmed to an average temperature of only about 200 K, though the absorptive features of the atmosphere warm the surface temperature of the Earth to about 300 K in the temperate regions.

The atmosphere also screens life on Earth from lethal ultraviolet radiation. Atomic oxygen absorbs all solar radiation shorter than 1850 Å. An ozone layer forms in a region about 30 km above the Earth's surface where upward-diffusing molecular oxygen and downward-diffusing atomic oxygen



react. Ozone strongly absorbs all radiation below about 3150 Å and therefore this ozone layer screens out lethal solar UV radiation.

The physical properties of the atmosphere also affect the transmission of electromagnetic waves through this medium. An understanding of these properties is therefore necessary for effective use of the atmospheric medium for radio and other electromagnetic communications and targeting.

The Joint Chiefs of Staff (JCS) prioritized the military requirements for defense environmental satellites in a 1986 memorandum (The Joint Chiefs of Staff, 1986). The ISAAC spectrograph will be able to provide global observation of several of these prioritized items. Among 43 sensing requirements, the collection of vertical temperature profiles was the second highest priority, the profiling of electron densities was the fifth highest, and observation of auroral emissions and airglow was the eighteenth priority.

Vertical temperature profiles are used to determine radiative transfer properties of the atmosphere such as atmospheric transmission, refractivity and optical turbulence. These data are needed for the employment of electro-optical weapons systems, high-frequency and microwave communications and many other military applications. Electron density profiles are needed to analyze and forecast the ionosphere for frequency management of long-haul high-frequency communications and long-range radars. These profiles are also used to determine the refractive properties of the ionosphere to allow for accurate geolocation of ground targets and for forecasting potential satellite communications and navigation system problems. Auroral emissions and airglow observations are required by the Department of Defense in order to distinguish targets from ionospheric backgrounds at ultraviolet frequencies.

## **A. THESIS OBJECTIVES**

The objectives of this thesis were to design and develop the ISAAC Ground Support Equipment (GSE) needed for pre-launch calibration and testing of the spectrograph. The GSE includes a Macintosh Quadra 650 computer, a data acquisition board, an electronic interface to the spectrograph and software that allows for testing spectrograph mechanical functions and obtaining test spectra for calibration. The electronic interface and controlling software were developed as part

of this thesis project. An initial wavelength calibration of the ISAAC spectrograph is also accomplished using the completed GSE.

## **B. THESIS OUTLINE**

This thesis is divided into eight chapters and seven appendices. Chapter II provides a background description of ionospheric chemistry and physics and includes a discussion of the methods that will be used by ISAAC to produce useful data. Chapters III and IV contain further background material describing the existing systems and equipment to which the GSE will interface. Chapter III includes a description of the ARGOS satellite and the mission of each of its payload experiments. This chapter also outlines the satellite's proposed orbital parameters. Chapter IV presents a detailed description of the ISAAC spectrograph. Chapter V discusses the design of the GSE hardware and also serves as a reference for hardware test operations. Chapter VI documents the development and operation of the ISAAC GSE software. This chapter serves as a reference for operation of the GSE software and provides the necessary details to allow for future modification as needed. Chapter VII details the initial wavelength calibration performed on the ISAAC instrument using the GSE hardware and software. Chapter VIII presents conclusions and recommendations for future modifications and thesis projects associated with the ISAAC spectrograph. Appendices A through F provide technical data of the ISAAC image intensifier, detector sensor, detector driver/amplifier circuit and the stepper motor driver. Appendix G is a short user's manual for operation of the ISAAC GSE.



## II. BACKGROUND

To allow an understanding of the objectives of the ISAAC instrument, this chapter provides a background of some of the fundamentals necessary to the study of *aeronomy*. Aeronomy is “the study of the physical and chemical processes in the upper atmosphere of the Earth, or of other planets” according to the *Penguin Dictionary of Astronomy* (1993). The Earth’s atmosphere is described in this chapter to facilitate an understanding of the environment in which ISAAC will function. The fundamentals of atomic and diatomic molecular structure are explored to allow an understanding of the source of the spectra that ISAAC will directly measure and to develop the spectroscopic notation. An identification and description of the atmospheric airglow and auroral emissions that ISAAC will measure is then provided and the chapter concludes with a survey of the methods that will be used to gain useful information from the ISAAC measurements.

### A. THE ATMOSPHERE

The atmosphere is the gaseous shell that surrounds Earth. It is vertically differentiated by temperature, chemical composition and the dominant chemical processes. These differentiations lead to classifications of layers within the atmosphere. Each of these classification regimes is useful for understanding the physics and chemistry of the atmosphere.

#### 1. Temperature Classification

The most pronounced feature of the atmosphere is variation of temperature with altitude. The *troposphere* is the lower region of the atmosphere, where most weather phenomena occur. Its upper boundary varies from 16 km at the equator to 8 km at the poles. This region is characterized by a negative temperature gradient in which temperature normally decreases with increasing altitude. This is due to efficient heat transport between layers which is in turn due to absorption and emission of infrared radiation by molecules such as water vapor, carbon dioxide and ozone. The *lapse rate* is defined as  $-dq/dz$ , the rate of decrease with altitude  $z$  of any atmospheric variable  $q$ . The standard lapse rate in the troposphere is about -6.5 K/km. Atop this region is an isothermal layer called the *tropopause*. The *stratosphere* lies above the tropopause and extends to an altitude of approximately 45 km. In this region of the atmosphere there is an *inversion* in which the temperature increases with

increasing altitude. This inversion is a result of ozone absorption of UV radiation which shields the Earth from otherwise lethal radiation and in turn heats this portion of the atmosphere. Above the stratosphere is the *stratopause*.

Another layer in which temperature decreases with increasing altitude, called the *mesosphere*, extends from the stratopause to the mesopause at approximately 80-85 km altitude. Heat in this region is removed by radiation due to vibrational relaxation of carbon dioxide molecules. The *mesopause* is the coldest region of the entire atmosphere, with a temperature of approximately 180 K. Above the mesopause is the *thermosphere* in which temperature increases with increasing altitude as a result of UV absorption. The thermopause is at the top of this layer and at this altitude the atmosphere becomes isothermal. Temperatures within the thermosphere vary with solar activity and can be as high as 1800 K under conditions of high solar activity. At these altitudes, density is low and the temperatures referred to are kinetic temperatures, not sensible temperatures. The above temperature classifications are indicated in Figure 2-1.

## 2. Chemical Composition Classification

In this classification scheme, the atmosphere is divided into three regions based on chemical composition: the *homosphere*, *heterosphere* and *exosphere*. The lower 100 km is known as the homosphere (older texts refer to the *turbosphere*) and includes the troposphere, stratosphere and mesosphere. This region is so named as vertical mixing or eddy diffusion of the atmosphere keeps the relative concentration of gases nearly constant. The homosphere is approximately composed of 78% molecular nitrogen ( $N_2$ ), 21% molecular oxygen ( $O_2$ ), and 1% argon. Trace amounts of water vapor, carbon dioxide ( $CO_2$ ), nitric oxide (NO), ozone ( $O_3$ ) and other gases and molecules are also present. Table 2-1 provides the masses of the primary atmospheric constituents. Although these atoms and molecules represent a very small part of the homosphere, they can often play a vital role as evidenced by the important function of ozone. The homosphere is bounded above by the *turbopause* at approximately 105 km altitude, where eddy and molecular diffusion are equally present.

Above the homopause is the heterosphere in which diffusive separation of atmospheric constituents is dominant (molecular diffusion). This region extends to approximately 500 km altitude. The heterosphere is composed primarily of molecular nitrogen ( $N_2$ ), molecular oxygen ( $O_2$ ), atomic

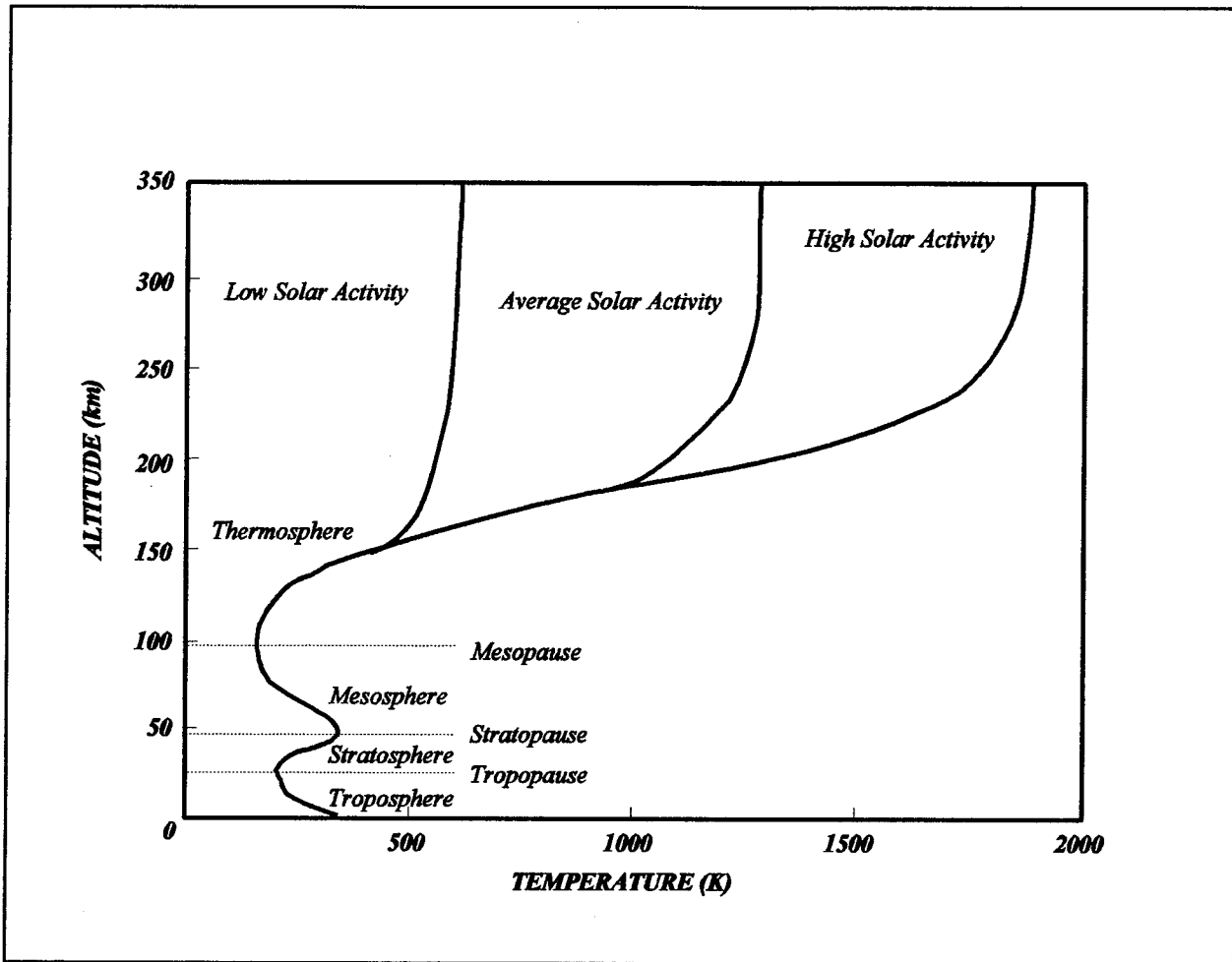


Figure 2-1 Temperature layers of the atmosphere. (After Tascione, 1988).

oxygen (O), argon (Ar), helium (He), and atomic hydrogen (H). The lighter gases dominate at the upper levels of this region, while the heavier gases (Ar, O<sub>2</sub>, N<sub>2</sub>, O) are more predominant at the lower altitudes.

Beyond the heterosphere is a region known as the exosphere. The exosphere is characterized by extremely low molecular densities and continual loss of atmospheric particles due to long mean free paths and high kinetic energies (temperatures). The *exobase* separates the heterosphere and exosphere and is that part of the atmosphere where the mean free paths are equal to the average *scale height* of the atmosphere. Scale height refers to the altitude increase that corresponds to a density decrease of 1/e.

<b>Substance</b>	<b>Volume percentage of dry air</b>	<b>Molecular weight</b>	<b>Total mass (kg x 10<sup>11</sup>)</b>
Total atmosphere	-	-	51 300 000
Dry air	100.00	28.97	51 170 000
Nitrogen	78.09	28.02	38 648 000
Oxygen	20.95	32.00	11 841 000
Argon	0.93	39.88	655 100
Water vapor	-	18.02	130 000
Carbon dioxide	0.03	44.00	23 320
Neon	0.0018	20.0	636
Krypton	0.00010	82.9	146
Helium	0.00053	4.00	37
Ozone	-	48.00	30
Xenon	0.000008	130.2	18
Hydrogen	0.00005	2.02	2

**Table 2-1** Mass of the atmosphere and its constituents. (Encyclopedia of Physics, 1991, p. 65).

### 3. Chemical Process Classification

A third classification scheme differentiates the atmosphere according to the dominant chemical processes within a given layer. Under this differentiation scheme, the atmosphere is separated into two overlapping layers: the chemosphere and the ionosphere.

#### a. *The Chemosphere*

The *chemosphere* extends from approximately 20 km to 100 km and is dominated by neutral photochemical reactions. Variations with altitude in the relative abundance of trace species such as ozone is common in this region.

#### b. *The Ionosphere*

The *ionosphere* is the region of the upper atmosphere above approximately 50-70 km where free electrons exist in numbers sufficient to affect the propagation of radio waves. In this region, ion chemistry is important. Free electrons result from photoionization of the atmosphere due to solar radiation. The recombination of ions and electrons proceeds slowly due to low gas densities and therefore high concentrations of free electrons exist, and even persist through the night. The ionosphere has no well-defined upper boundary, though 2000 km is arbitrarily set as the upper limit. The ionosphere also varies significantly with geomagnetic latitude. The high-latitude ionosphere is directly coupled to the magnetospheric tail by stretched magnetic field lines. The low-latitude ionosphere varies with plasma instabilities and changes in the magnetospheric ring current. The classical ionospheric model that follows most closely resembles the mid-latitude ionosphere.

The rate of photoionization  $Q_{\lambda}(z)$  is proportional to the photon flux intensity  $I_{\lambda}(z)$ , the density of molecules exposed to the solar flux  $n(z)$ , and the efficiency with which the photons cause ionization. The efficiency is termed the ionization cross-section  $\sigma_i(\lambda)$ . Hence

$$Q_{\lambda}(z) = n(z) I_{\lambda}(z) \sigma_i(\lambda) \quad (2-1)$$

Since the concentration of molecules (density) decreases with increasing altitude and the solar flux intensity increases with increasing altitude, the photoionization rate has a distinct maximum. A curve



that depicts the variation of the ionization rate with altitude is called a *Chapman ionization profile* (Figure 2-2).

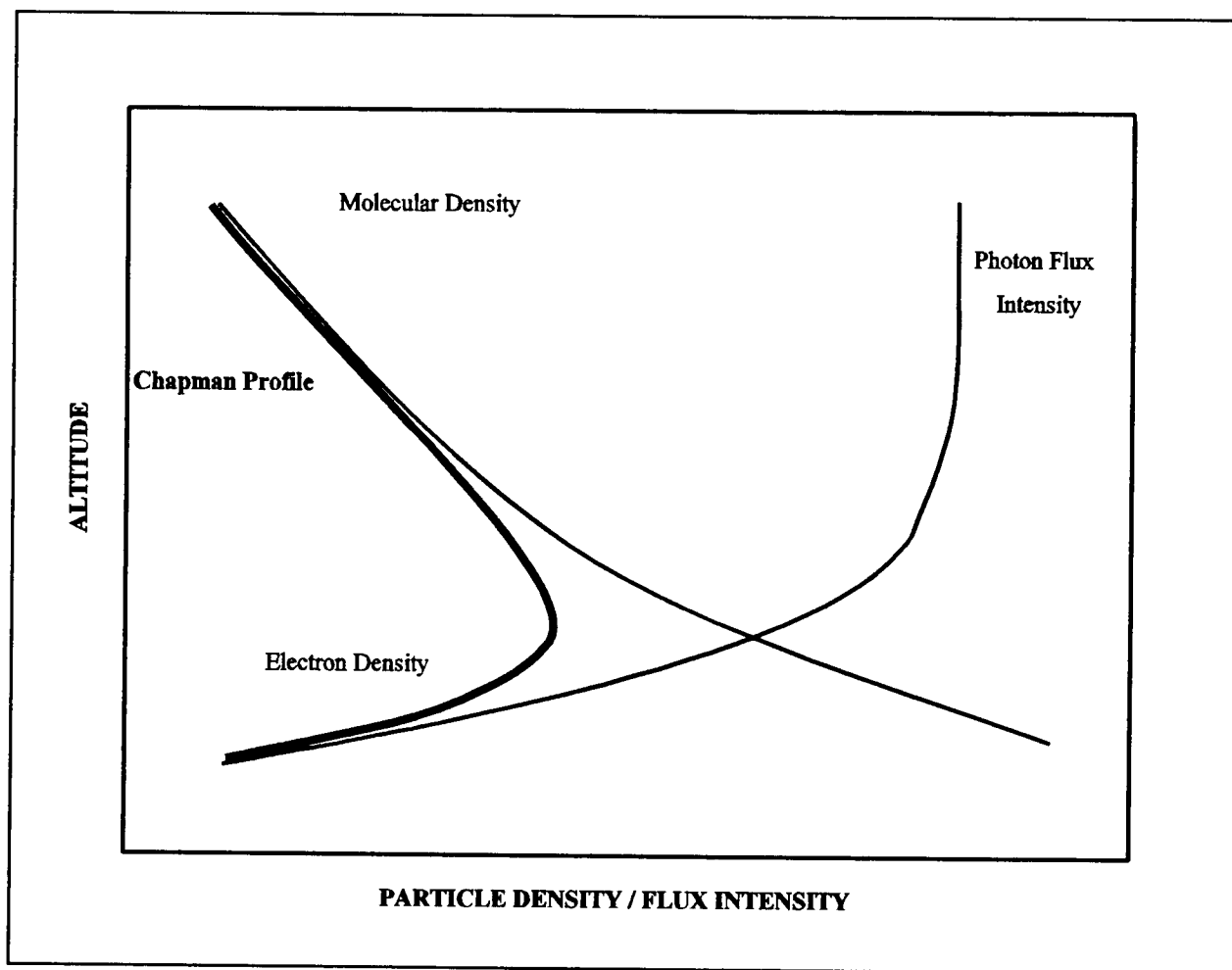


**Figure 2-2** Chapman profile.

The ionosphere is further subdivided into four layers characterized by the electron densities of the regions. These layers are designated as *D*, *E*, *F*<sub>1</sub> and *F*<sub>2</sub> in ascending order. An electron-density profile for the ionosphere with contributions from positive ions is shown in Figure 2-3. These distinct ionospheric regions arise due to differing physical processes (see Tascione, 1988).

(1) The *D*-layer. The lowest subdivision is the *D*-layer, which extends from about 50 km to 90 km altitude. In this layer, ionization is due primarily to absorption of solar Lyman- $\alpha$  radiation (1216 Å) by NO. This process is shown in Equation (2-2).

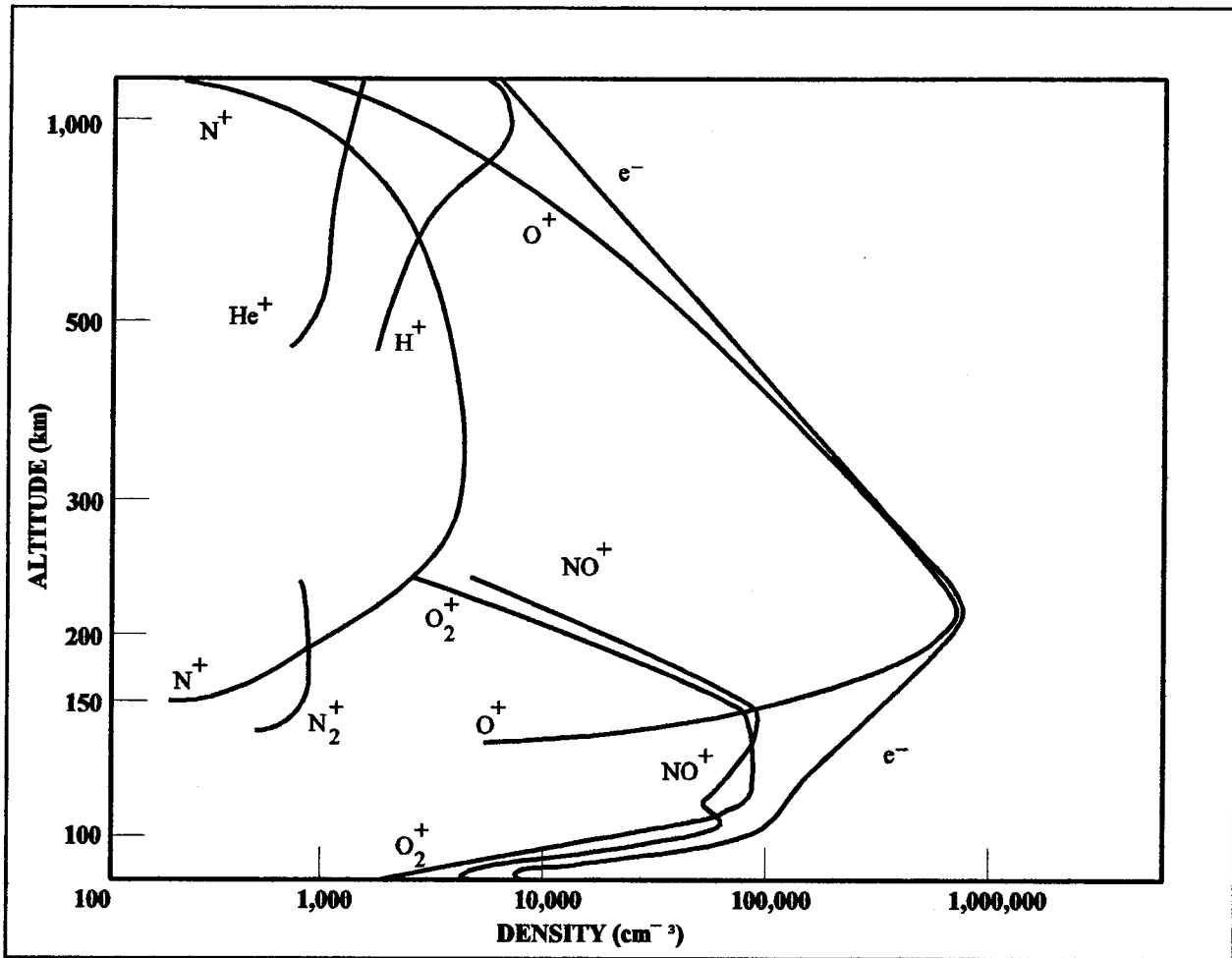
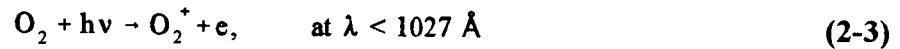


Figure 2-3 Distribution of positive ions for a daytime ionosphere at solar minimum. (Johnson, 1966).

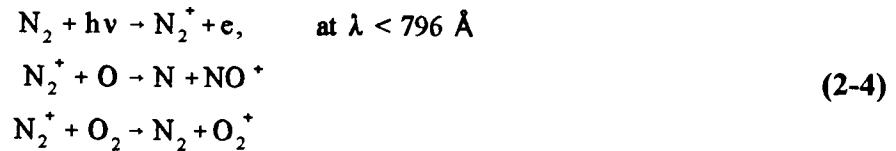


Enhanced ionization in this region can also occur following solar flares due to absorption of x-rays by  $\text{N}_2$  and  $\text{O}_2$ . The distinguishing feature of this region is the predominance of negative ions. This layer usually disappears at night due to recombination of ions and electrons.

(2) The *E*-layer. The *E*-layer is located between 90 km and 140 km. In this region, ionization is primarily due to  $\text{O}_2$  absorption of extreme ultraviolet (EUV)



and coronal soft x-rays by  $\text{N}_2$

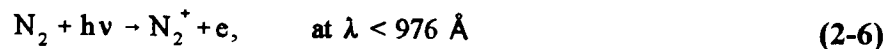


A nighttime  $E$  and sporadic  $E$  (thin patches of enhanced ionization) can also result from electron and meteor bombardment. Figure 2-3 shows that  $\text{NO}^+$  and  $\text{O}_2^+$  dominate the  $E$ -layer, though  $\text{O}^+$  rapidly increases in this region and it is this ion that dominates the  $F$ -layer.

(3) The  $F$ -layer. The  $F_1$ -layer extends from approximately 140 km to 200 km, while the  $F_2$ -layer extends to approximately 400 km. These two layers are produced by ionization due to absorption of EUV by  $\text{O}$ . Equation (2-5) represents this process.



This ionization is probably accompanied by  $\text{N}_2$  ionization in the  $F_1$  layer, which rapidly disappears at night, while the  $F_2$  layer persists. Ionization of  $\text{N}_2$  is represented by the chemical process given in Equation (2-6).



The *topside ionosphere* is a region above the  $F_2$  layer. In this region, the dominant ion becomes  $\text{He}^+$  and eventually  $\text{H}^+$  dominates in a region called the *plasmasphere*.

## B. ATOMIC SPECTROSCOPY

The ISAAC spectrograph will directly measure spectral emissions of the atmospheric gases and the auroral spectral emissions. These measurements can yield valuable information about the physical content of the atmosphere and several physical properties and processes in the emitting region when the physics of the emissions are understood. This section provides a brief description of atomic spectra, while the following section will review diatomic molecular spectra. A thorough discussion of these topics is presented in Eisberg and Resnick (1985) and also in Herzberg (1944).

### 1. The Bohr Atom

Neils Bohr first postulated the classical model of the atom as a positively charged nucleus surrounded by electrons in concentric orbits or shells. In this model, the orbital level of the electrons determine the energy state of the atom and only specific, discrete energy states (or stationary states) are allowed. The energy states are thus said to be quantized. Electromagnetic radiation is emitted from the atom if an electron moves to an orbital shell of lower energy as indicated in Figure 2-4.

A measurement with a spectroscope will reveal discrete emission lines associated with these electron energy changes (Figure 2-5). The radiation emitted by the atom when the electron moves from a more energetic state to a lower state is a photon with frequency given by the Planck-Einstein formula

$$f = \frac{E_i - E_f}{h} \quad (2-7)$$

where  $E_i$  is the energy of the initial state,  $E_f$  is the energy of the final state, and  $h$  is Planck's constant. The set of wavelengths observed for a specific species is called an *emission spectrum*. Atoms can also absorb electromagnetic radiation at specific wavelengths which causes an *absorption spectrum*. Although the classical Bohr model is convenient for describing the hydrogen atom, it is unable to accurately describe the emissions of other atoms.

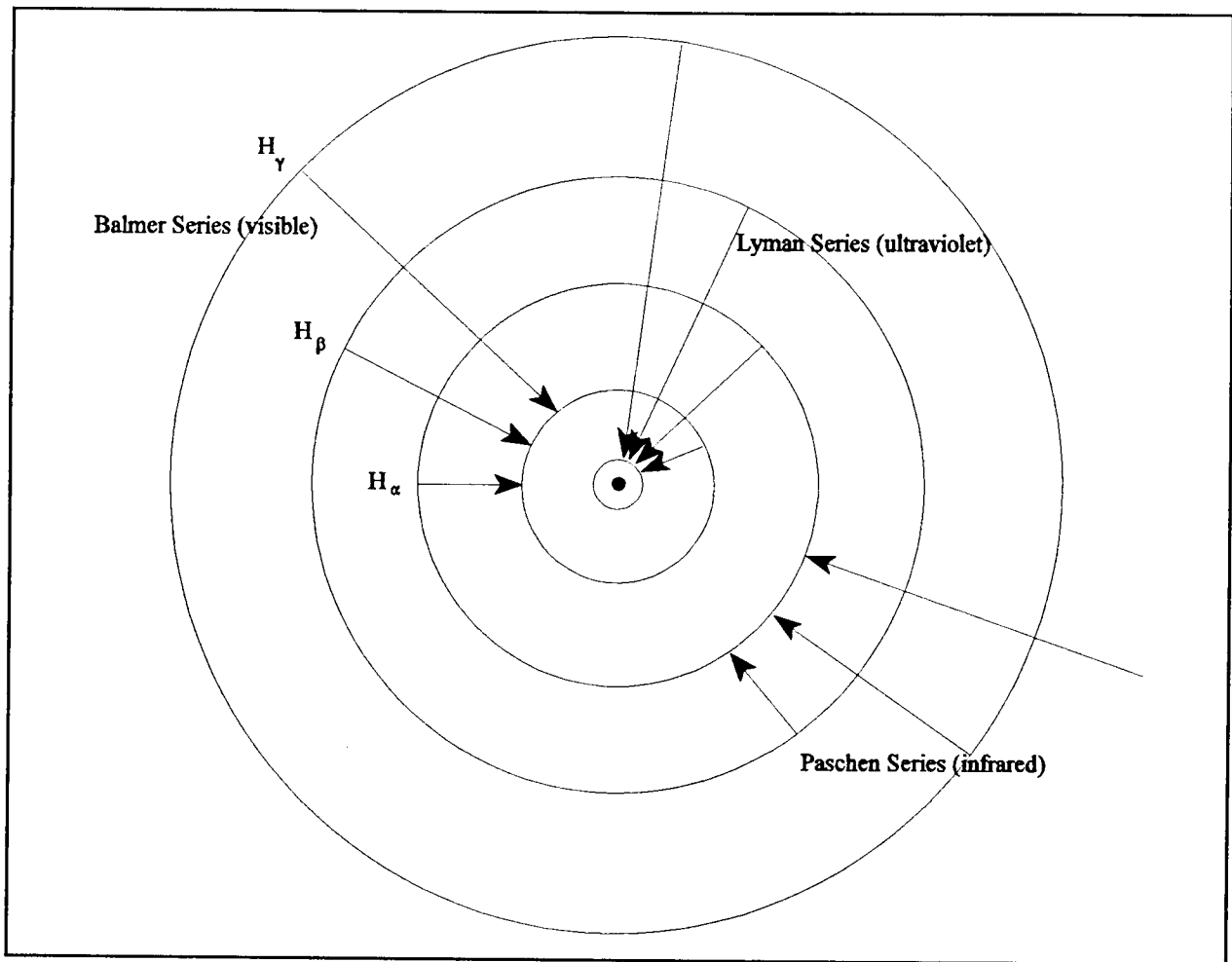


**Figure 2-4** Bohr model of the Hydrogen atom with spectral emissions.

## 2. Quantum Mechanical Interpretation of the Atom

Quantum mechanics provides a more accurate description of the atom. Matter is described as having a wave nature as well as particle nature. In this model, the atom is described as a nucleus surrounded by a series of stationary waves. These stationary waves represent orbits in the classical Bohr model. The absolute square of the wave at any point is the probability that an electron will be found at that point at any time.

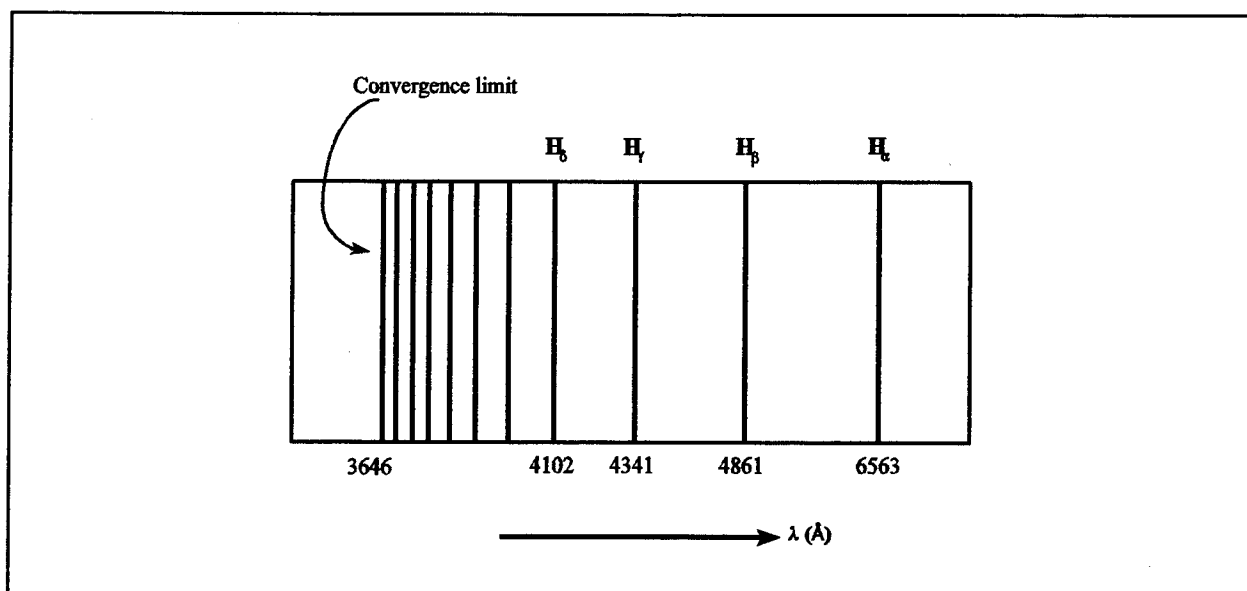


Figure 2-5 The Balmer series of spectral lines for hydrogen.

*a. Stationary States*

The specification of the stationary states of an atom is given by the solutions of the time-independent Schrödinger equation

$$-\frac{\hbar^2}{2\mu}\nabla^2\psi + V\psi = E\psi \quad (2-8)$$

where  $\psi$  = wave function,  $\hbar = h/2\pi$  ( $h$  = Planck's constant),  $\mu$  = reduced mass,  $V$  = potential energy function, and  $E$  is the energy. The finite solutions,  $\psi$ , to this equation are called eigenfunctions and associated with these solutions are specific energy values,  $E$ , known as eigenvalues. These solutions take the form

$$\psi_{n\ell m_\ell}(r, \theta, \phi) = R_{n\ell}(r) \Theta_{\ell m_\ell}(\theta) \Phi_{m_\ell}(\phi) \quad (2-9)$$

where the subscripts,  $n$ ,  $\ell$  and  $m_\ell$  represent quantum numbers. In the three-dimensional problem of the hydrogen atom, these three quantum numbers are needed for each stationary state, corresponding to the three independent degrees of freedom for the electron. The quantum number  $n$  is called the

principal quantum number,  $\ell$  is called the *orbital quantum number*, and  $m_\ell$  is the *orbital magnetic quantum number*. An additional quantum number, the *spin magnetic quantum number*,  $m_s$ , was later discovered to be required to more accurately describe observed spectra. Dirac solved the relativistic wave equation for the electron in a potential well using the relativistic form of the total energy and confirmed the nature of the electron spin. The solutions to Equation (2-8) impose restrictions on these quantum numbers which are summarized in Table 2-2.

Quantum Number	Name	Allowed Values	Number of Allowed States
$n$	Principal quantum number	1, 2, 3, ...	Any number
$\ell$	Orbital quantum number	0, 1, 2, ..., $n-1$	$n$
$m_\ell$	Orbital magnetic quantum number	$-\ell, -\ell+1, \dots, 0, \dots, \ell-1, \ell$	$2\ell+1$
$m_s$	Spin magnetic quantum number	$-1/2, +1/2$	2

**Table 2-2** Quantum numbers for the hydrogen atom and allowed values.

***b. Quantized Energy of an Atom***

The energy,  $E$ , is an eigenvalue of Equation (2-8) and is given by

$$E = -\frac{\mu Z^2 e^4}{(4\pi\epsilon_0)^2 \hbar^2 n^2} \quad (2-10)$$

where  $\mu$  = reduced mass,  $Z$  = atomic number,  $e$  = electron charge,  $\epsilon_0$  = permittivity of free space,  $\hbar = h / 2\pi$  (Planck's constant), and  $n$  = principal quantum number.

### c. Shells, Subshells and Orbitals

All states with the same principal quantum number are said to form a *shell*. These shells are identified by the letters K, L, M, . . . , which designate states  $n = 1, 2, 3, \dots$ . States with the same values for  $n$  and  $\ell$  form a *subshell*. Letters  $s, p, d, f, g, h, \dots$  are used to designate the states for which  $\ell = 0, 1, 2, 3, \dots$ . (The letters  $s, p, d, f$  represent designations for spectral series: *sharp, principal, diffuse, and fundamental*, so named for their appearance before their origins were fully understood). States with the same values for  $n, \ell$ , and  $m_\ell$  form an *orbital*. These notations are summarized in Table 2-3.

$n$	Shell Symbol	$\ell$	Subshell Symbol
1	K	0	$s$
2	L	1	$p$
3	M	2	$d$
4	N	3	$f$
5	O	4	$g$
6	P	5	$h$
...	...	...	...

**Table 2-3** Atomic shell and subshell notations.

A closed subshell occurs when all  $m_\ell$  and  $m_s$  states are occupied for a given  $n$  and  $\ell$ .

A closed shell occurs when all  $\ell, m_\ell$ , and  $m_s$  states are filled for a given  $n$ .

### d. The Pauli Exclusion Principle and Hund's Rule

The *Pauli Exclusion Principle* states that no two electrons in an atom can ever be in the same quantum state; that is, no two electrons in the same atom can have the same set of quantum numbers  $n, \ell, m_\ell$ , and  $m_s$ . The Pauli Exclusion Principle limits two electrons to any orbital, one electron with spin quantum number,  $m_s = +1/2$ , and the other with  $m_s = -1/2$ . Therefore, the electrons



in a multi-electron atom fill successive levels of increased energy. The outermost electrons, generally responsible for the chemical properties of an element, are called *optically active* or *valence electrons*.

*Hund's rule* states that for an atom with orbitals of equal energy, electrons will fill the orbitals such that a maximum number of electrons will have unpaired spins. An electronic state must obey both the Pauli exclusion rule and Hund's rule.

### *e. Orbital Angular Momentum*

The orbital angular momentum  $L$  of an atom is also quantized and is related to the orbital quantum number. For the hydrogen atom this relationship is

$$L = \sqrt{\ell(\ell + 1)} \hbar \quad (2-11)$$

where  $\ell = 0, 1, 2, \dots, n - 1$ . The allowed angles with respect to any axis are also quantized. The projections of  $L$  along the  $z$  axis are given by

$$L_z = m_\ell \hbar \quad (2-12)$$

These restrictions on the direction of the angular momentum vector with respect to an external magnetic field are called *space quantization*.

The allowed values for  $L_z$  for the case  $\ell = 2$  are shown in Figure 2-6(a). In the presence of an external magnetic field along the  $z$  axis, the angular momentum vector precesses about this axis as represented in Figure 2-6(b).

The total orbital angular momentum for a multi-electron atom is found by taking the vector sum of the orbital angular momenta of the electrons. It has magnitude

$$L' = \sqrt{L(L + 1)} \hbar \quad (2-13)$$

where  $L$  has maximum value  $L = \sum \ell_i$ .

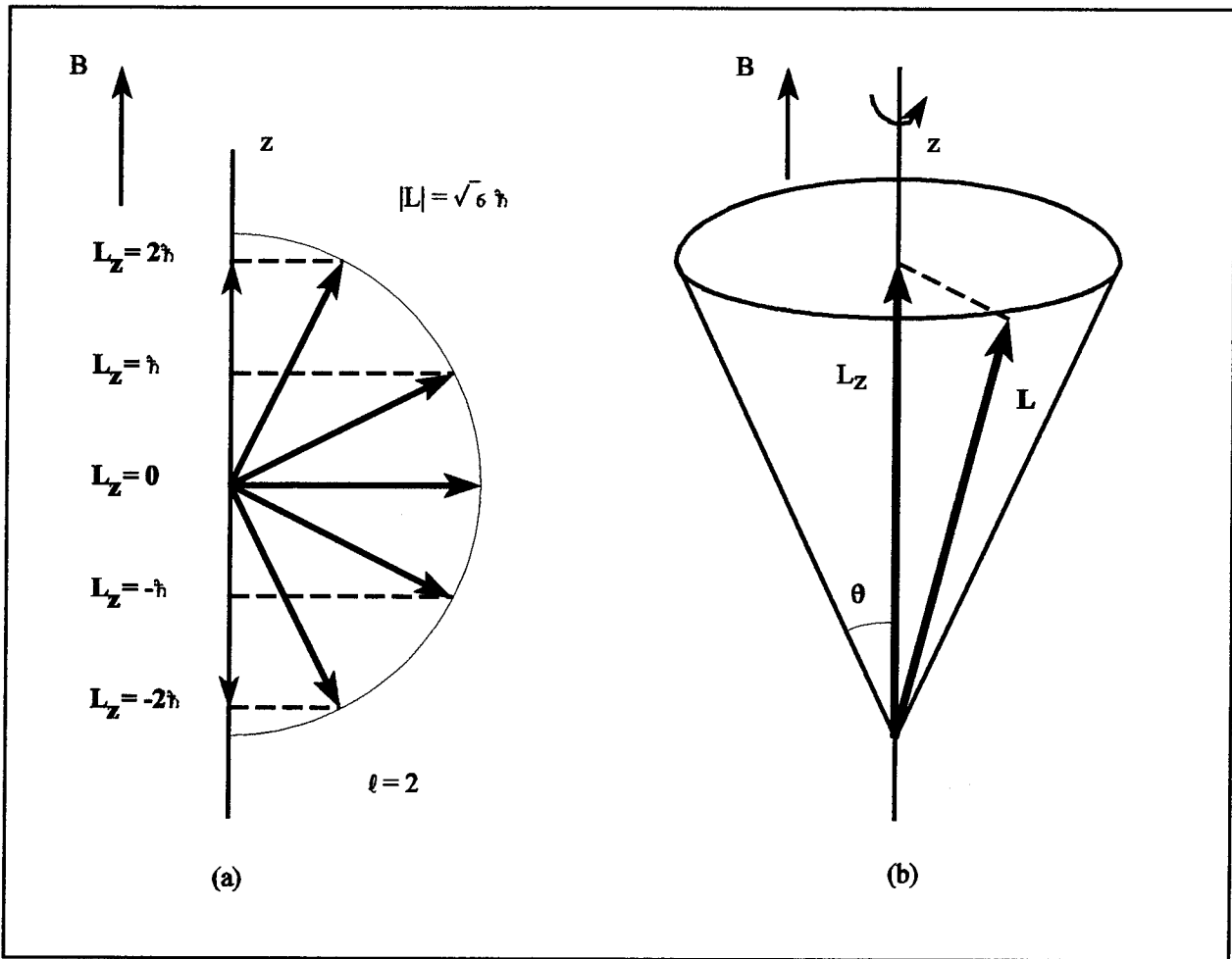


**Figure 2-6** (a) Allowed projections of the orbital angular momentum for the case  $\ell = 2$ . (b) Orbital angular momentum vector lies on the surface of a cone and precesses about the  $z$  axis when a magnetic field  $B$  is applied in this direction.

### *f. Spin Angular Momentum*

Electrons also have an intrinsic *spin angular momentum*, which is also space quantized. The electron spin was found to be described by a single quantum number,  $s$ , that has the value  $\frac{1}{2}$ . The magnitude of the spin angular momentum  $S$  for the electron is given by

$$S = \sqrt{s(s+1)} \hbar = \frac{\sqrt{3}}{2} \hbar \quad (2-14)$$

The  $z$  projection of the spin angular momentum is restricted to two values

$$S_z = m_s \hbar = \pm \frac{\hbar}{2} \quad (2-15)$$

as depicted in Figure 2-7.

The total spin angular momentum for a multi-electron atom is found by taking the vector sum of the spin angular momenta of the electrons. It has magnitude

$$S' = \sqrt{S(S+1)} \hbar \quad (2-16)$$

where  $S$  is an integer with maximum value  $S = \sum m_s$ .

It is only necessary to consider the optically active electrons in finding the  $L$  or  $S$  values, since in closed subshells there are as many electrons quantized in one direction as there are in the opposite direction. This results in a net orbital and spin momenta of zero for closed subshells.

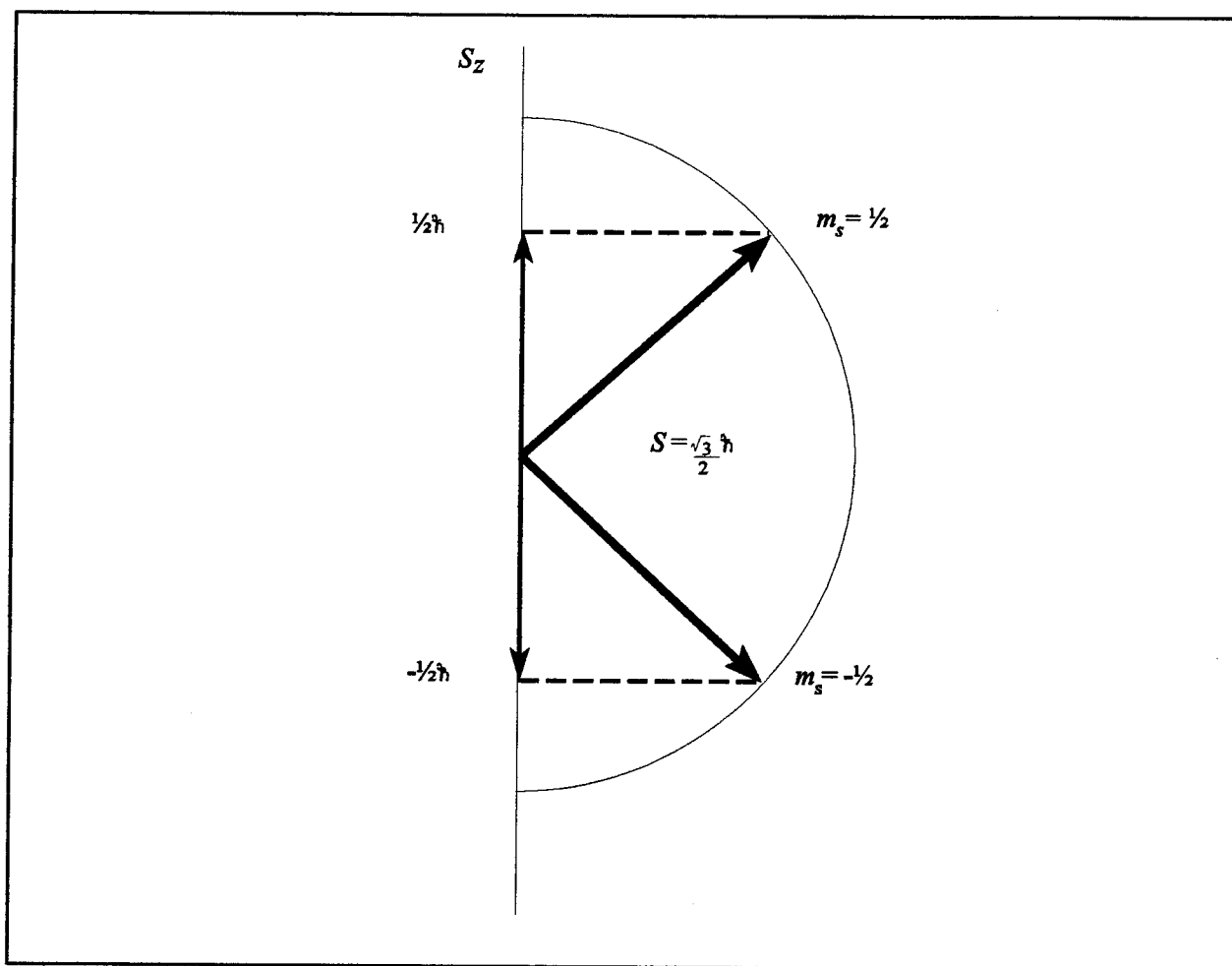


**Figure 2-7** Space quantization of spin angular momentum. Two orientations of the spin vector  $S$  are allowed for an electron.

***g. Total Angular Momentum - LS Coupling***

The interaction of an electron's intrinsic magnetic moment with its motion-induced magnetic field modifies its energy to depend on  $n$  and another quantum number,  $j$ , the *total angular momentum quantum number*. The orbital angular momenta and the spin angular momenta of electrons couple vectorially to form the *total angular momentum*

$$\mathbf{J} = \mathbf{L} + \mathbf{S} \quad (2-17)$$

This coupling is referred to as *LS coupling* or *Russell-Saunders coupling* in honor of the two astronomers who first used it in studying stellar atomic spectra. As energy and angular momenta can assume discrete values only, the total angular momentum quantum number  $j$  is also space quantized. This quantum number can assume only positive values between  $(\ell + s)$  and  $(\ell - s)$  in integer steps. As  $s$  is  $\frac{1}{2}$  for the single electron in a hydrogen-like atom,  $j$  is  $\frac{1}{2}$  for  $\ell = 0$ ; while  $j = 1/2$ , or  $3/2$  for  $\ell = 1$ , etc.

The total orbital angular momentum for a multi-electron atom is found by taking the vector sum of the orbital angular momenta of the electrons. It has magnitude

$$J' = \sqrt{J(J + 1)} \hbar \quad (2-18)$$

where  $J$  can assume any value between  $|L + S|$  and  $|L - S|$  in integer steps. For example, if  $L = 1$  and  $S = 3/2$ ,  $J$  can be  $5/2$ ,  $3/2$ , or  $1/2$ .

A *term* is the set of all states with a given configuration  $L, S, J$ .

#### ***h. Spectroscopic Notation***

A *spectroscopic notation* is used to describe the quantum state of an atom. The one electron in a hydrogen atom in its ground state is designated as  $1s^1$ . The notation  $1s$  indicates a state in which  $n = 1$  and  $\ell = 0$ , while the superscript indicates that one electron is present at this level. For a multi-electron atom, groups of electrons are listed in order of successively higher energy levels. For example, boron has an electron configuration of  $1s^2 2s^2 2p^1$ .

To completely specify an atomic state, the coupling of the angular momenta for all unfilled subshells must also be specified. The notation follows the form  $^{2S+1}L_J$ , where  $S = \sum |m_s|$ ,  $L = \sum \ell$ , and  $J$  specifies the possible *LS* coupling which can take values from  $|L+S|$  to  $|L-S|$ . The atomic level is specified using capital letters following the scheme in Table 2-3 for  $\ell$ . For example, a nitrogen atom with three optically active electrons in the  $2p$  subshell all spin “up” and having a value for  $J = 3/2$  would have a complete notation  $1s^2 2s^2 2p^3 \ ^3P_{3/2}$ . The last term of the notation is read “triplet P three-half.” The  $2S+1$  term is called the *multiplicity*, which refers to the number of possible

discrete  $J$  energy levels that an electron can assume within an orbital. When the multiplicity is greater than one, a transition is made up of a *multiplet* of discrete spectral lines.

*i. Selection Rules*

Electron transitions between energy levels in an atom must obey certain *selection rules*. Transitions that do not obey these rules are called *forbidden*. Such transitions can occur by other processes, although are much less probable than the *allowed* transitions. These selection rules are

$$\Delta \ell = \pm 1$$

$$\Delta S = 0 \quad (\text{no spin change})$$

$$\Delta L = 0, \pm 1$$

$$\Delta J = 0, \pm 1 \quad (0-0 \text{ forbidden})$$

The change in the principal quantum number,  $\Delta n$  is not restricted. An energy level diagram for hydrogen is shown in Figure 2-8. This diagram shows some of the allowed electronic transitions.

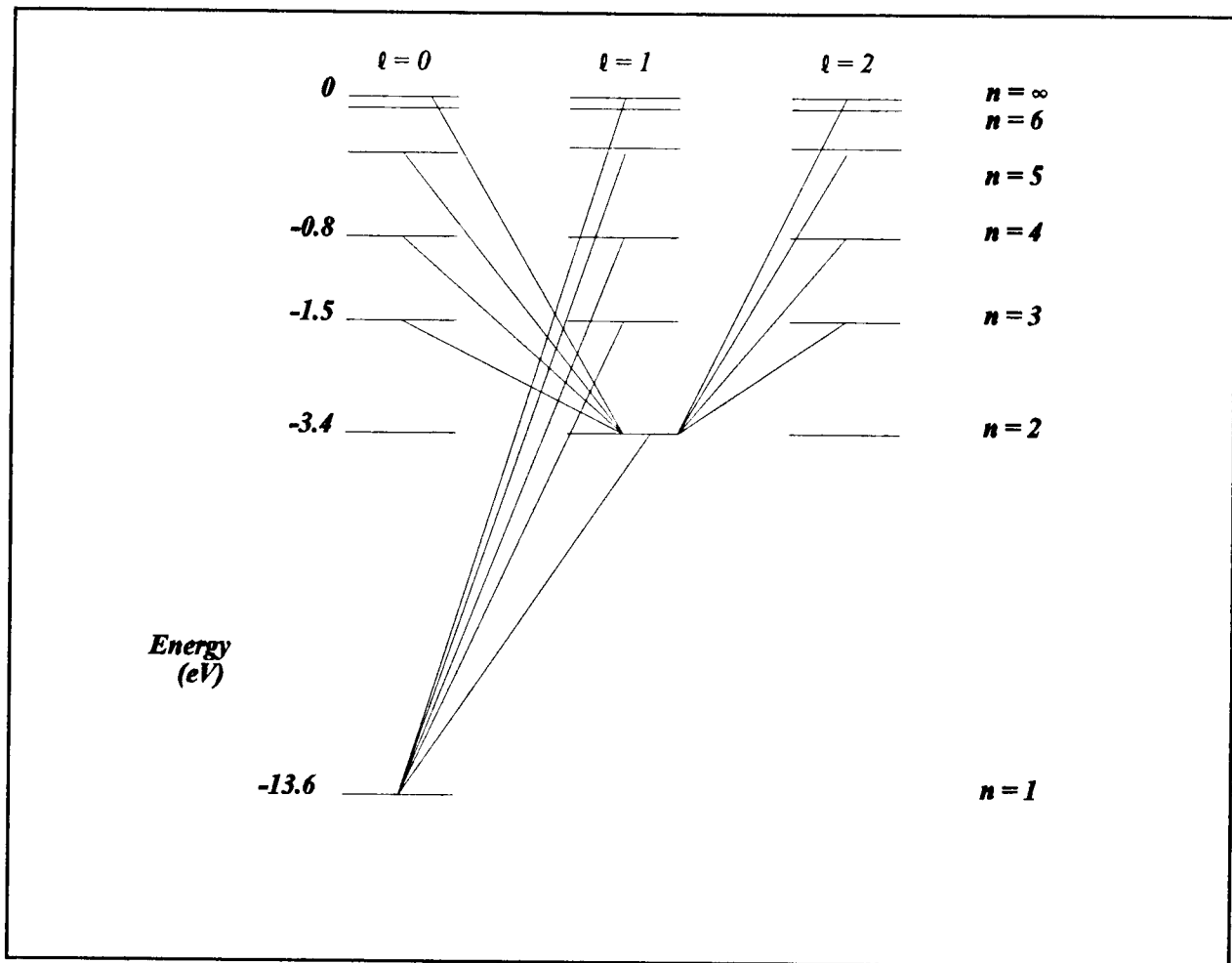


Figure 2-8 Some allowed electron transitions for hydrogen.

### C. DIATOMIC MOLECULAR SPECTROSCOPY

Diatomic molecules are important constituents of the ionosphere. However, their spectra are significantly different from atomic spectra for several reasons. The diatomic molecule can be modeled as two spheres of mass  $m_1$  and mass  $m_2$  separated by a distance  $r$  and bound by an electrostatic attraction. Diatomic molecular states cannot be classified according to their electronic orbital angular momenta as the force on an electron is no longer a central force and therefore the magnitude of the orbital angular momentum  $L$  is not conserved. However, the total charge distribution is symmetric about an axis connecting the nuclei and so the component angular momentum about this axis is conserved (normally chosen as  $z$  axis -  $L_z$ ). Also, the nuclei in a

molecule can move relative to one another. Diatomic molecules can vibrate about their equilibrium center and can also rotate about their center of mass and the energy released in each of these motions is also quantized. Diatomic molecular spectra contain many more lines than atomic spectra due to the many different possible energy levels. For a thorough treatment of molecular spectroscopy, see Herzberg (1950).

Solution of the Schrödinger equation (Equation 2-8) is more difficult for molecules, though empirical discoveries in molecular spectroscopy have revealed that the energy of the molecule can be assumed to be composed of three parts: electronic, vibrational and rotational and so the Schrödinger equation can be solved for each of these three motions separately.

### 1. Rotational Spectra - The Rigid Rotator

The rotational motion of a diatomic molecule can be modeled as the rotation of a rigid body about its center of mass which lies on an axis connecting the two nuclei as in Figure 2-9. The rotational kinetic energy about an axis is given by

$$E_{rot} = \frac{1}{2} I \omega^2 \quad (2-19)$$

while the rotational inertia about the axis due to the nuclei is

$$I = \mu r^2 \quad (2-20)$$

where  $\mu$  is the reduced mass of the system. The rotational angular momentum is quantized and is given by

$$I\omega = \sqrt{J(J+1)} \hbar \quad (2-21)$$



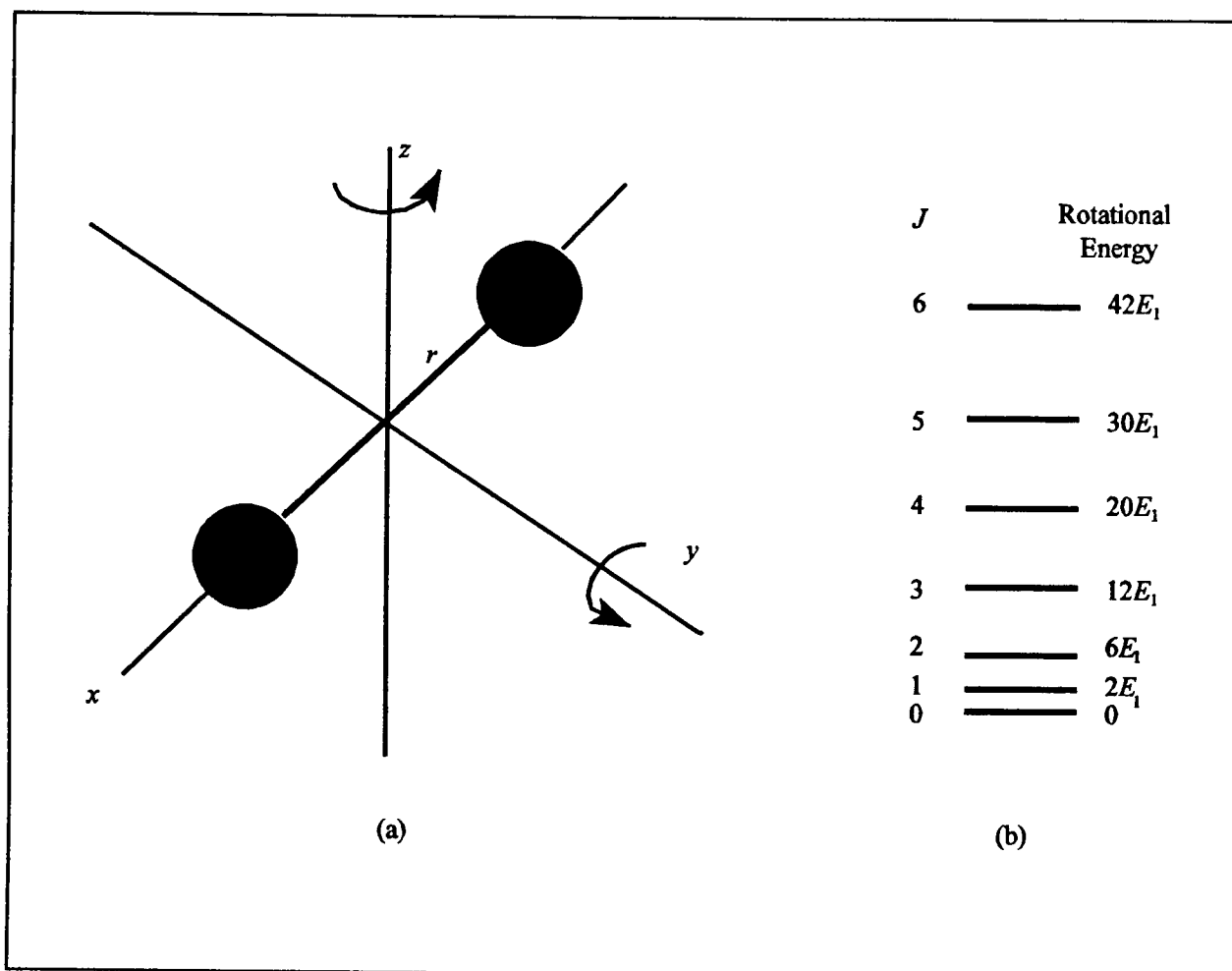


**Figure 2-9** (a) A diatomic molecule oriented along the  $x$ -axis modeled as a rigid rotator separated by internucleus distance  $r$ . (b) Allowed rotational energies of a diatomic molecule as calculated using Equation (2-22). (After Serway, 1990).

where  $J$  is an integer called the *rotational quantum number* (not the same as the total angular momentum quantum number). Substitution of Equations (2-20) and (2-21) into Equation (2-19) yields the discrete energy levels for rotational motion

$$E_{rot}(J) = \frac{\hbar^2}{2\mu r^2} J(J+1) \quad (2-22)$$

Molecular spectroscopists use the *rotational term value*, which is the energy divided by  $hc$  and is given by

$$F(J) = \frac{E_{rot}}{hc} = BJ(J + 1) \quad (2-23)$$

where  $B$  is the *rotational constant*, a constant of molecule given by

$$B = \frac{h}{8 \pi^2 c I} \quad (2-24)$$

## 2. Vibrational Spectra

A model of the vibrational motion of the diatomic molecule assumes that the two nuclei move toward or away from each other in simple harmonic motion as if separated by a spring as in Figure (2-10). This motion can be reduced to the harmonic vibration of a single mass point about an equilibrium position. In classical mechanics, the harmonic oscillator is defined as a mass point acted on by a force  $F$  proportional to the distance  $x$  from the equilibrium position and directed toward the equilibrium position.

$$F = -kx = m \frac{d^2x}{dt^2} \quad (2-25)$$

The frequency of vibration of such a system is

$$f = \frac{1}{2\pi} \sqrt{\frac{k}{\mu}} \quad (2-26)$$

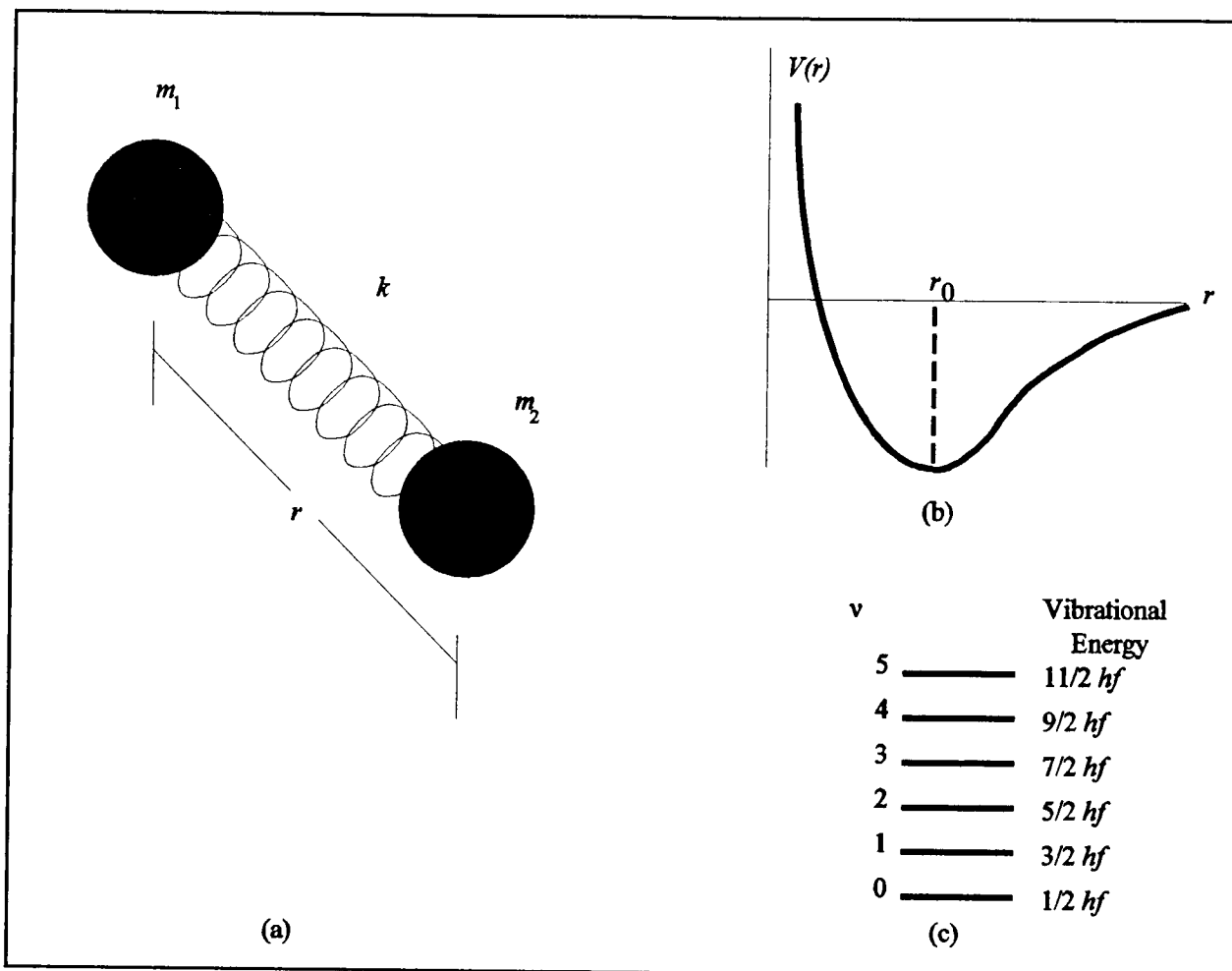


**Figure 2-10** (a) Diatomic molecule modeled as a spring system with two nuclei of masses  $m_1$  and  $m_2$  separated by distance  $r$  and with a spring constant  $k$ . (b) Potential energy versus atomic separation for such a molecule, where  $r_0$  is the equilibrium atomic separation. (c) Allowed vibrational energies of a diatomic molecule, where  $f$  is the fundamental frequency of vibration, given by Equation (2-26). Note that the spacing between adjacent vibrational levels are equal as determined by Equation (2-28). (After Serway, 1990).

Since force is the negative derivative of the potential energy  $V$ , the potential energy for a harmonic oscillator is given by

$$V = \frac{1}{2} kx^2 \quad (2-27)$$

The solution to Schrödinger's equation for this potential energy function shows that the vibrational energy is also quantized and yields the following expression for this energy

$$E(v) = \hbar \sqrt{\frac{k}{\mu}} \left( v + \frac{1}{2} \right) = hf \left( v + \frac{1}{2} \right) \quad (2-28)$$

where  $v$  is an integer called the *vibrational quantum number* and  $f$  is the vibrational frequency of the harmonic oscillator. Inspection of Equation (2-28) shows that the energy difference between any two successive vibrational levels is equal.

The *term value* for vibrational energy is also given by dividing Equation (2-28) by  $hc$

$$G(v) = \frac{E(v)}{hc} = \omega \left( v + \frac{1}{2} \right) \quad (2-29)$$

where  $\omega = f/c$  is the vibrational frequency measured in  $\text{cm}^{-1}$  and is a constant of the molecule.

### 3. The Anharmonic Oscillator, Nonrigid Rotator and the Vibrating Rotator

The previous first-approximation models require some improvements as the molecule does not behave exactly as a harmonic oscillator. Nor can the molecule both act as a harmonic oscillator and simultaneously as a rigid rotator. Finally, both types of motion must be considered together. The following models provide some improvements and account for observed spectral characteristics of the molecule.

#### a. The Anharmonic Oscillator

The harmonic oscillator is characterized by a potential energy curve that is parabolic (Equation (2-27)). However, in a true harmonic oscillator the restoring force increases indefinitely with increasing distance from the equilibrium position. The atoms in a molecule do not have this relationship; at great distance the attractive force between the atoms is zero and therefore the potential energy curve of the molecule has the form shown in Figure 2-10(b). Near the equilibrium position, the characteristics of this true potential energy curve do closely resemble a parabola.

A better approximation of the actual potential energy function of the molecule includes an extra cubic term. When this improved potential function is used, a better approximation for the energy of the *anharmonic oscillator* is given by

$$G(v) = \omega_e \left( v + \frac{1}{2} \right) - \omega_e x_e \left( v + \frac{1}{2} \right)^2 + \omega_e y_e \left( v + \frac{1}{2} \right)^3 + \dots \quad (2-30)$$

where  $\omega_e$ ,  $\omega_e x_e$ , and  $\omega_e y_e$  are constants of the molecule. Note that the energy levels of the anharmonic oscillator are not equidistant as those of the harmonic oscillator.

### ***b. The Nonrigid Rotator***

The above expressions for the rotational and vibrational energies are approximations since they assumed differing models of the molecule. The molecule cannot both be a rigid rotator and also possess harmonic (or anharmonic) oscillation; therefore, a more accurate model would be a *nonrigid rotator*. The nonrigid rotator is system consisting of two point masses connected by a massless spring rather than a rigid rod. In this system, the action of centrifugal force, the internuclear distance and the moment of inertia increases with increasing rotation. This improved model results in a better approximation for the rotational energy

$$F(J) = BJ(J + 1) - DJ^2(J + 1)^2 \quad (2-31)$$

where  $D$  is a *rotational constant* given by

$$D = \frac{4B^3}{\omega^2} \quad (2-32)$$

### c. The Vibrating Rotator

The above equations for the energy of the molecule have modeled one type of motion (vibration or rotation) independent of the other. However, it should be assumed that these motions do occur simultaneously and observed molecular spectra indicate such combined motion. A model called the *vibrating rotator* (or the *rotating oscillator*) accounts for this simultaneous vibration and rotation. The resultant rotational term value in a given vibrational level is given by

$$F_v(J) = B_v J(J+1) - D_v J^2(J+1)^2 + \dots \quad (2-33)$$

where  $B_v$  and  $D_v$  are given by

$$B_v = \frac{h}{8\pi^2 c \mu r_o^2} - \alpha_e \left( v + \frac{1}{2} \right) = B_e - \alpha_e \left( v + \frac{1}{2} \right) \quad (2-34)$$

$$D_v = \frac{4B_e^3}{\omega_e^2} + \beta_e \left( v + \frac{1}{2} \right) + \dots = D_e + \beta_e \left( v + \frac{1}{2} \right) + \dots \quad (2-35)$$

and  $B_e$ ,  $\alpha_e$ ,  $\beta_e$ , and  $D_e$  are constants of a given molecule available in Huber and Herzberg (1979).

Additional complexities may be added to these models to account for angular momenta coupling. In the case of NO molecules, Hund's case (a) and Hund's case (b) are used.

#### 4. Spectroscopic Notation

A spectroscopic notation is used to label the different spectral emissions observed from molecules. Molecular spectral emissions can occur as a result of electronic, vibrational and/or rotational transitions. Within a given electronic energy state there are many vibrational energy levels and within each vibrational level there are many rotational levels as represented in Figure (2-11). Transitions between the rotational and vibrational levels within a given electronic state of a molecule may take place according to the following selection rules

$$\Delta v = \pm 1$$

$$\Delta J = \pm 1$$

### a. *Orbital Angular Momentum*

The motion of electrons in an atom are subject to a spherically symmetric field of force. For this reason, the electronic orbital angular momentum  $L$  of an atom is a constant of the motion. Diatomic molecules do not have this spherical symmetry, though do have a symmetry about the internuclear axis. Therefore, for diatomic molecules only the component of the orbital angular momentum about this internuclear axis is a constant of the motion. A precession of  $L$  about this axis occurs with constant component  $\hbar M_L$ , where  $M_L$  is restricted to  $M_L = L, L - 1, L - 2, \dots, -L$ .

In an electric field, reversing the directions of electron motion does not change the energy of the system. Therefore, states differing only in the sign of  $M_L$  are degenerate (same energy). States with different  $|M_L|$  have different energies and for this reason, electronic states of diatomic molecules are classified according to the value of  $|M_L|$  vice  $L$ . Therefore, the quantum number  $\Lambda = |M_L|$  is used to denote the molecular state, where  $\Lambda$  can take the values  $\Lambda = 0, 1, 2, \dots, L$ . The molecular state is designated by the Greek letters  $\Sigma, \Pi, \Delta, \Phi, \dots$  for  $\Lambda = 0, 1, 2, 3, \dots$  just as the letters  $s, p, d, f, \dots$  are used for atoms.

### b. *Spin*

As with atoms, the spin of the electrons in the molecule causes a *multiplet structure*. The spins of the individual electrons form a resultant spin  $S$  with a corresponding quantum number  $S$  that is integral for the case of an even number of electrons in the molecule and half-integral for the case of an odd number of electrons. For  $\Lambda \neq 0$ , there is an internal magnetic field created by the electron motion in the direction of the internuclear axis. This field causes  $S$  to precess about this axis with a constant component  $\hbar M_s$ . This magnetic spin quantum number is denoted by  $\Sigma$  and is restricted to the values

$$\Sigma = S, S - 1, S - 2, \dots, -S \quad (2-36)$$

There are  $2S+1$  possible values for  $\Sigma$  and it is not defined for  $\Lambda = 0$  ( $\Sigma$  states).

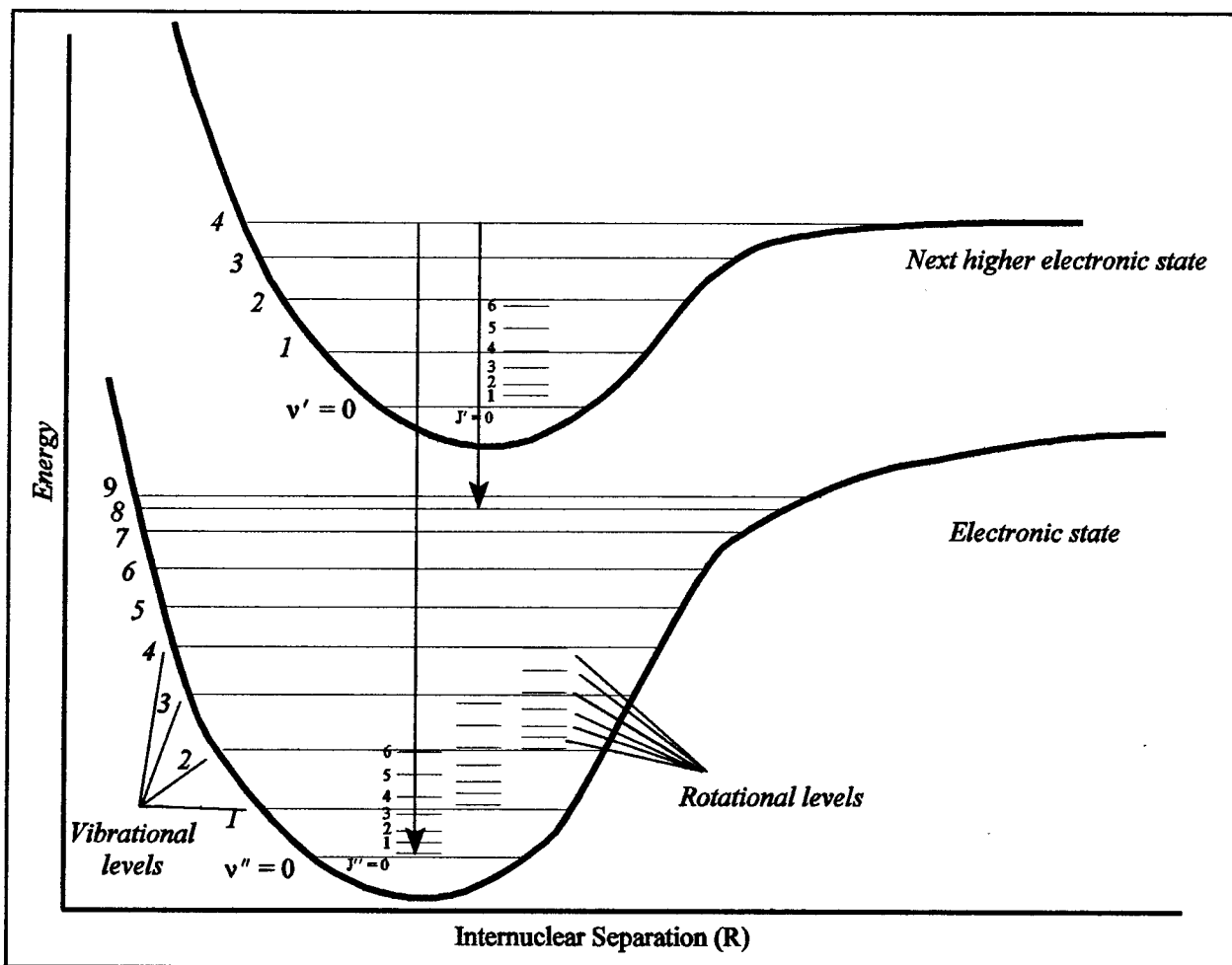


Figure 2-11 Molecular energy versus internuclear separation for two electronic states. Each electronic state has its own set of vibrational levels and each vibrational level has its own set of rotational levels. (After Eisberg and Resnick, 1985).

### c. Total Angular Momenta

The total electronic angular momentum about the internuclear axis is denoted by  $\Omega = \Lambda + \Sigma$ . Since both vectors lie along the same axis, the quantum number  $\Omega = |\Lambda + \Sigma|$  corresponds to the particular multiplet of  $2S + 1$  possible different energies. These multiplets are caused by the interaction of the spin with the magnetic field produced by the orbital angular momentum. For  $\Lambda = 0$ , there is no interaction and thus no multiplets; however, in all cases  $2S + 1$  is called the *multiplicity* of a state. This multiplicity term is added as a left superscript to the molecular notation and  $\Omega$  as a subscript (similar to  $J$  for atoms). For example,  ${}^3\Delta_2$  is a “triplet Delta two” representing  $S=1$ ,  $\Lambda = 3$ , and  $\Sigma = -1$ .



#### *d. Rotational, Vibrational Transitions*

Transitions between the rotational levels of two different vibrational levels produce *vibration-rotation* spectra. Transitions between the rotational levels within vibrational levels of a given electronic state are governed by  $\Delta J = \pm 1$ . In molecular spectroscopy, a single prime is used to denote the upper state of a transition, while a double prime is used to denote the lower state. Therefore, a molecule in the  $J' = 5$  state can make a transition to the  $J'' = 4$  or  $J'' = 6$  state. Transitions involving  $\Delta J = +1$  are termed *R-branch transitions*, while  $\Delta J = -1$  transitions are termed *P-branch transitions* (see Figure 2-12). Transitions between rotational levels are designated as  $(v', v'')$ ; for example the left-most transition shown in Figure 2-11 would be labeled (4,0).

#### *e. Electronic States*

To fully specify a given molecular energy transition, the electronic states are also given letter designations. The ground state of a molecule is designated X and the higher energy states with same multiplicity are labeled A, B, C, . . . . For the case where the multiplicity between states differ, lower case letters are used instead (a, b, c, . . .).

In addition, symmetry properties of the electronic eigenfunctions are often labeled. In a diatomic molecule, any plane through the internuclear axis is a plane of symmetry. The electronic eigenfunction of a non-degenerate state ( $\Sigma$  state) remains unchanged or may change sign when reflected at any plane passing through both nuclei. The former case is called a  $\Sigma^+$  state, and the latter is called a  $\Sigma^-$  state.

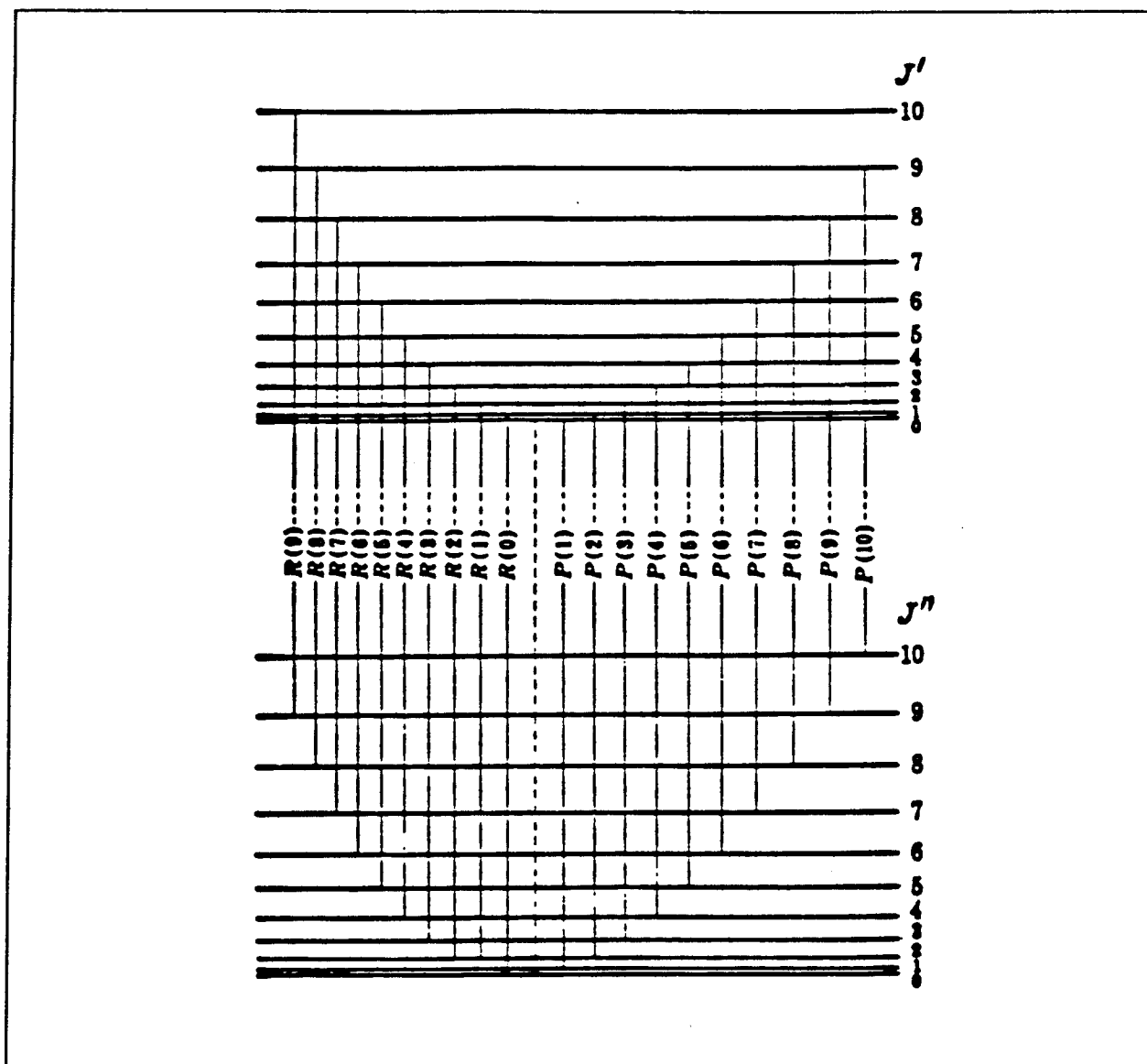


**Figure 2-12** Vibrational-rotational energy level diagram showing both P and R branches. (After Herzberg, 1950).

Also, if the two nuclei in the molecule have the same charge, the field in which the electrons move has a *center of symmetry* in addition to the symmetry axis. This means that the field remains unchanged by a reflection of the nuclei at this center of symmetry located at the midpoint along the internuclear axis. This symmetry results in the electronic eigenfunctions either changing sign or remaining unchanged when reflected at the center. The state that the eigenfunction

corresponds to is called an *odd state* or *even state*, respectively. This symmetry property is indicated by a subscript *u* (*ungerade*) for an odd state and subscript *g* (*gerade*) for an even state (for example  $\Sigma_g$  or  $\Sigma_u$ ). The selection rules impose that *g* - *u* transitions are allowed, while *u* - *u* and *g* - *g* are forbidden.

The selection rules for electronic transitions are different than those given above for vibrational-rotational transitions within a given electronic state. These transitions involve electric dipole radiation (Herzberg, 1950).

$$\begin{aligned}\Delta S &= 0 \\ \Delta \Lambda &= 0, \pm 1 \\ \Delta J &= 0, \pm 1 \\ + &\leftrightarrow - \\ g &\leftrightarrow u \\ s &\leftrightarrow s, a \leftrightarrow a\end{aligned}$$

The  $\Delta J$  rule gives rise to three branches; the nomenclature remains the same for  $\Delta J = \pm 1$  (*R-branch* for +1, *P-branch* for -1), while  $\Delta J = 0$  is termed the *Q-branch*. The  $s \leftrightarrow s, a \leftrightarrow a$  rule refers to symmetric and antisymmetric terms; symmetric to symmetric and antisymmetric to antisymmetric transitions are allowed.

There are exceptions to the above rules for transitions commonly observed in the atmosphere. Other types of radiation are also involved including magnetic dipole and electric quadrupole radiation. The selection rules for these types of radiation allow

$$\begin{aligned}+ &\leftrightarrow +, - \leftrightarrow - \\ g &\leftrightarrow g, u \leftrightarrow u\end{aligned}$$

## D. ATMOSPHERIC AIRGLOW AND AURORAL EMISSIONS

### 1. Airglow

The ISAAC spectrograph will record ultraviolet emission and absorption spectra generated in the upper atmosphere. Optical photon emissions from within the upper atmosphere are termed the *airglow*, which includes the *dayglow*, *twilight glow*, and *nightglow*. Dayglow is that light emitted by a layer of the atmosphere that is illuminated from above by the sun, while twilight glow is the radiation emitted by a layer when illuminated from below by the Sun. The airglow is continuously emitted by the atmosphere in the wavelength range of the far ultraviolet to the near infrared. The more predominant processes that lead to airglow are:

#### a. Photoexcitation

*Photoexcitation* is the process whereby the electrons in an atom or molecule are excited to a higher energy state by the absorption of a photon. This process will normally follow the selection rules of quantum mechanics discussed earlier in this chapter. The normal lifetime of a particle in an "allowed" excited state is on the order of  $10^{-8}$  seconds (Eisberg and Resnick, 1985). The excited atom or molecule will then emit at least one photon as it seeks the ground state in a process known as *fluorescence*.

#### b. Electron-Impact Excitation

The electrons in an atom or molecule may be excited to a higher-energy state by collision with other particles. This process is not subject to the selection rules described above. Photons are emitted as the electrons return to their ground state and in some cases this will involve *forbidden* transitions. An excited state that has only forbidden transitions available to it is said to be a *metastable state*. Such states may have lifetimes up to several seconds. Metastable states are more likely to transfer energy through collision with other particles in a process called *quenching* rather than through emission.

### *c. Pre-dissociation*

Molecules in an excited state may pre-dissociate if they are excited to a state above the pre-dissociation limit. Figure 2-13 is a partial potential curve diagram showing the principal states of the oxygen molecule. In this figure it can be seen, for example, that excitation to a vibrational level of the  $A^3\Sigma^+u$  state above the pre-dissociation limit can lead to pre-dissociation to two  $O(^3P)$  atoms. Also, excitation can lead to dissociation through curve crossing onto a pre-dissociating state. This is also represented in Figure 2-13, where an excitation to the  $B^3\Sigma^-u$  may result in crossing onto the  $^3\Pi_u$  repulsive state (Brasseur and Solomon, 1984).

### *d. Photochemical Reactions*

Photochemical reactions are a relatively minor source of dayglow emissions, though they are a more important factor in nightglow emissions in the absence of solar photons. In this process, a photon may be absorbed placing a molecule into an excited state from which secondary chemical reactions may occur that were otherwise not available from the ground state. The new species created in the process may then emit photons; this process is called *chemiluminescence*.

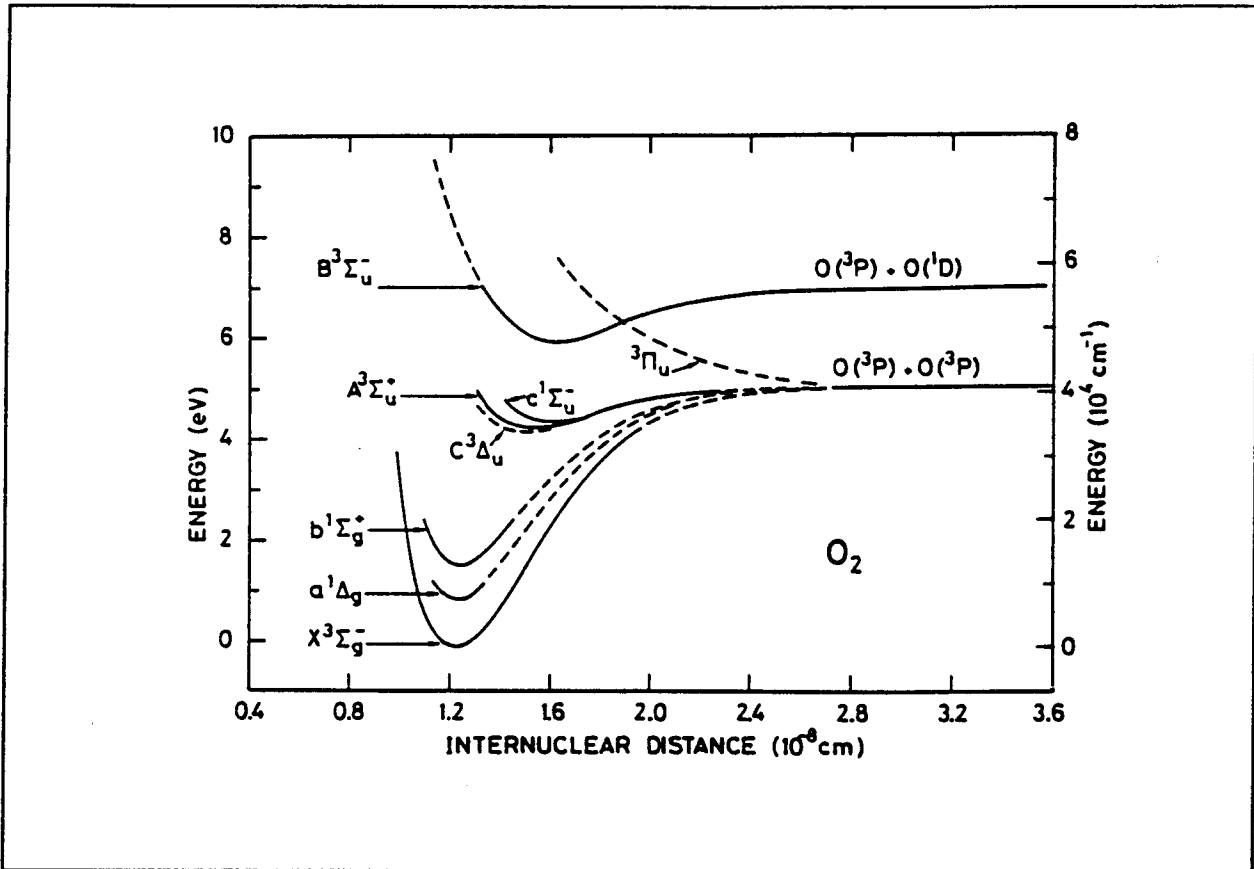


**Figure 2-13** Potential energy diagram for the principal states of the oxygen molecule. (Brasseur and Solomon, 1984).

## 2. Aurora

*Aurora*, like the airglow, is an optical emission from the upper atmosphere, though it is distinguished by its source of excitation, its geographic confinement and its sporadic occurrence. Auroral emissions are primarily the result of oxygen and nitrogen bombardment by electrons that travel along the Earth's magnetic field lines. The aurora is observed only rarely outside the polar and subpolar geographic regions as the Earth's magnetic field lines converge at the poles. Auroral studies remain important both for greater scientific understanding of the processes involved and to investigate observed radio wave distortions during high auroral activity.

### 3. Airglow and Auroral Emission Features

The emissions that may be observed by the ISAAC instrument in the 1800-3325Å range have been identified by previous rocket launches and satellite observations. Danczyk (1989) compiled identifications of emissions in this wavelength band and also ISAAC's predecessor, the Middle Ultraviolet Spectrograph (MUSTANG) has successfully flown three times on sounding rockets (twice from White Sands, New Mexico and once most recently from Poker Flat, Alaska) confirming the ability to view the dayglow, nightglow and auroral emissions.

Sample ultraviolet airglow and auroral spectra representative of those that ISAAC will be able to record are shown in Figures (2-14) through (2-16); though, ISAAC will provide higher resolutions than those illustrated in these figures. Figure (2-14) shows three ultraviolet dayglow spectra between 1900 and 3400-Å obtained from the MUSTANG spectrograph on board a sounding rocket at altitudes 305 km, 165 km, and 115 km above White Sands, New Mexico. Figure (2-15) shows a sample nightglow spectrum obtained by a spectrograph on board the S3-4 satellite over the equatorial region. An auroral spectrum in the ultraviolet wavelengths obtained from a spectrograph on board the OGO-4 satellite is shown in Figure (2-16).

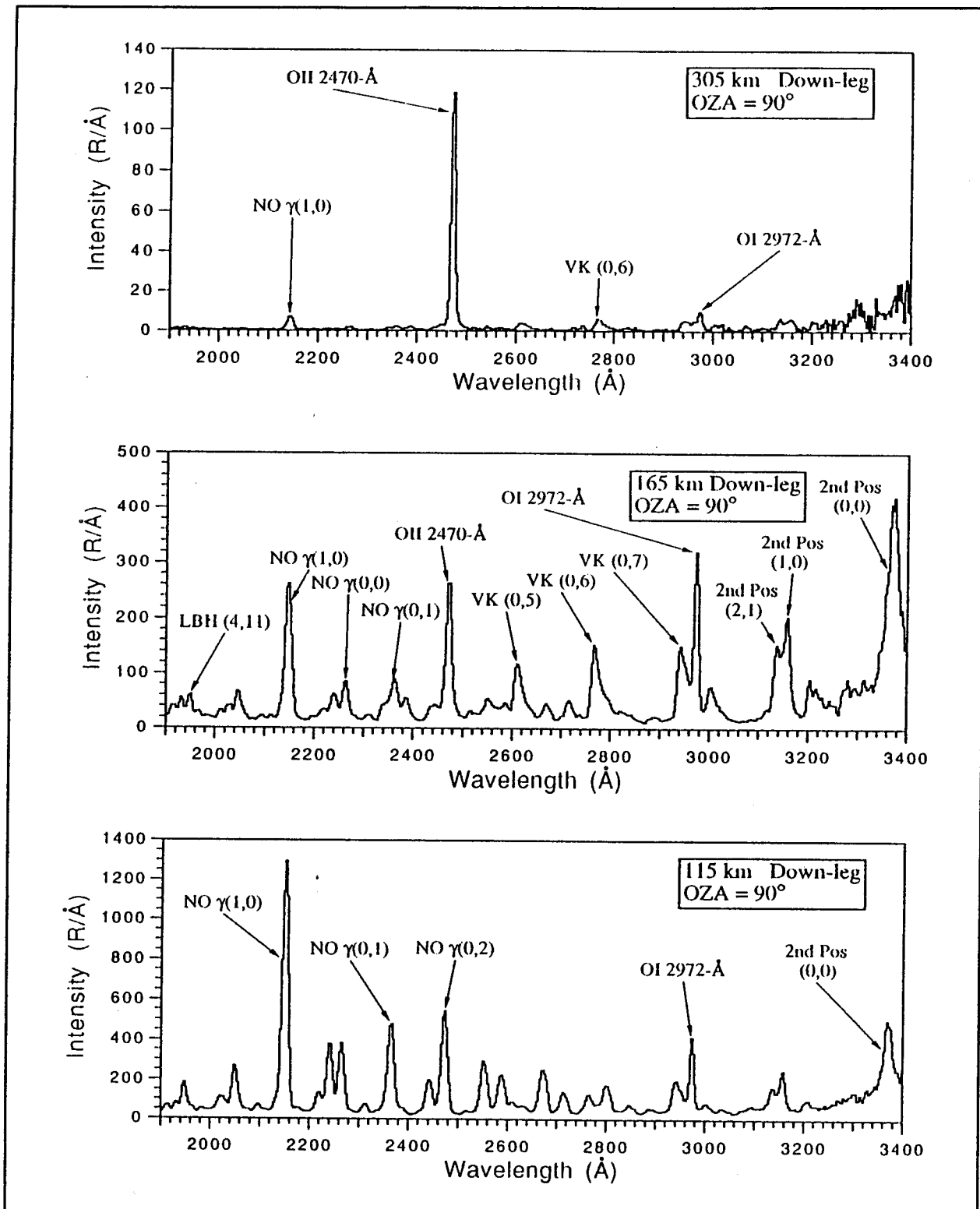


**Figure 2-14** Spectrum of the Earth's UV dayglow between 1900 and 3400 Å at a resolution of 10Å, obtained from altitude of 305 km, 165 km, and 115 km above White Sands, New Mexico. (Cleary, et al, 1994).



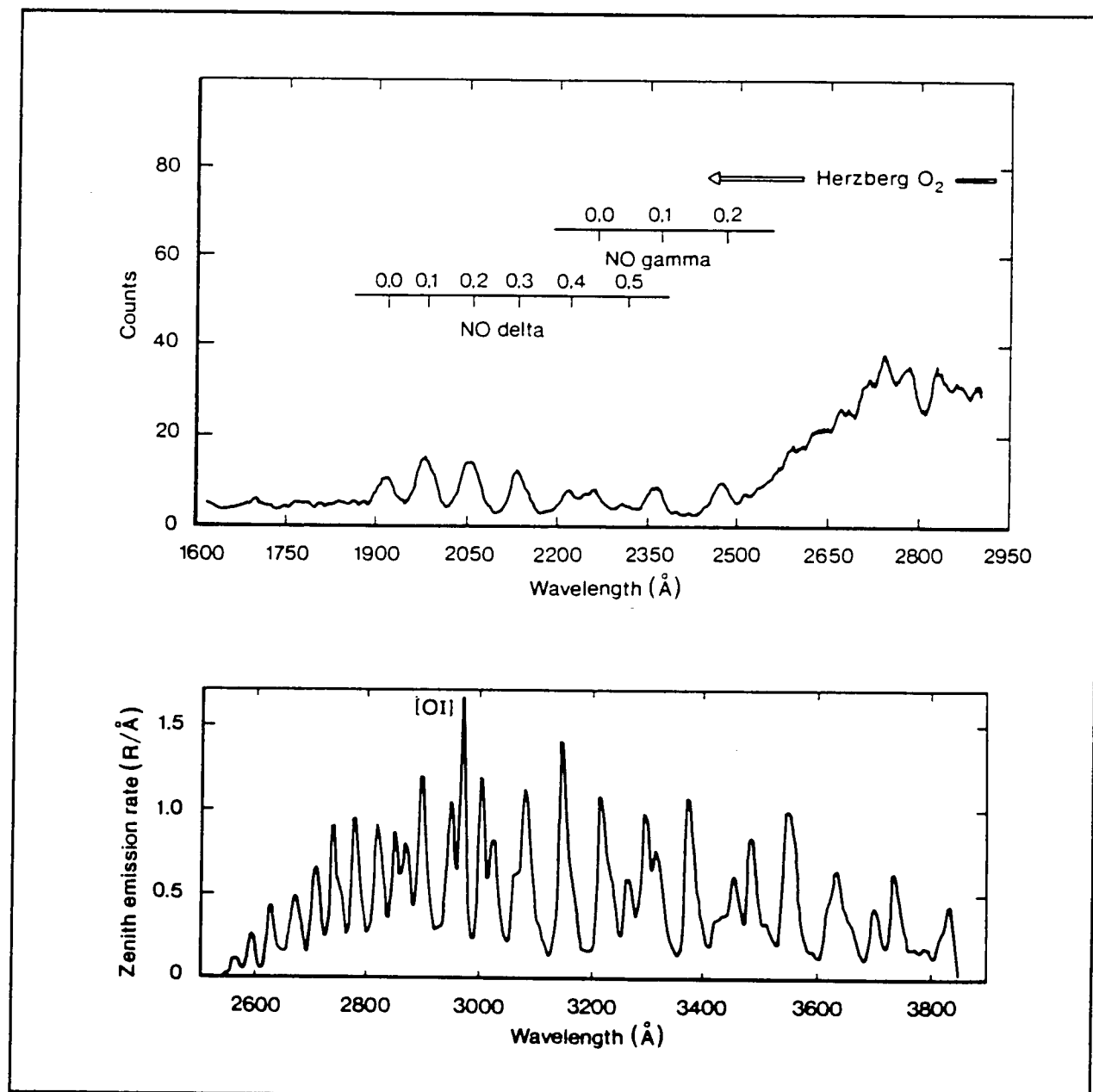


**Figure 2-15** (top) Ultraviolet nightglow spectrum (1600-2950 Å) obtained from the S3-4 satellite in the equatorial region. Spectrograph resolution was approximately 25 Å. (bottom) Nightglow spectrum (2500-3900 Å) acquired by a spectrograph with 12 Å resolution carried on board a rocket launched from White Sands, New Mexico. (Rees, 1989).

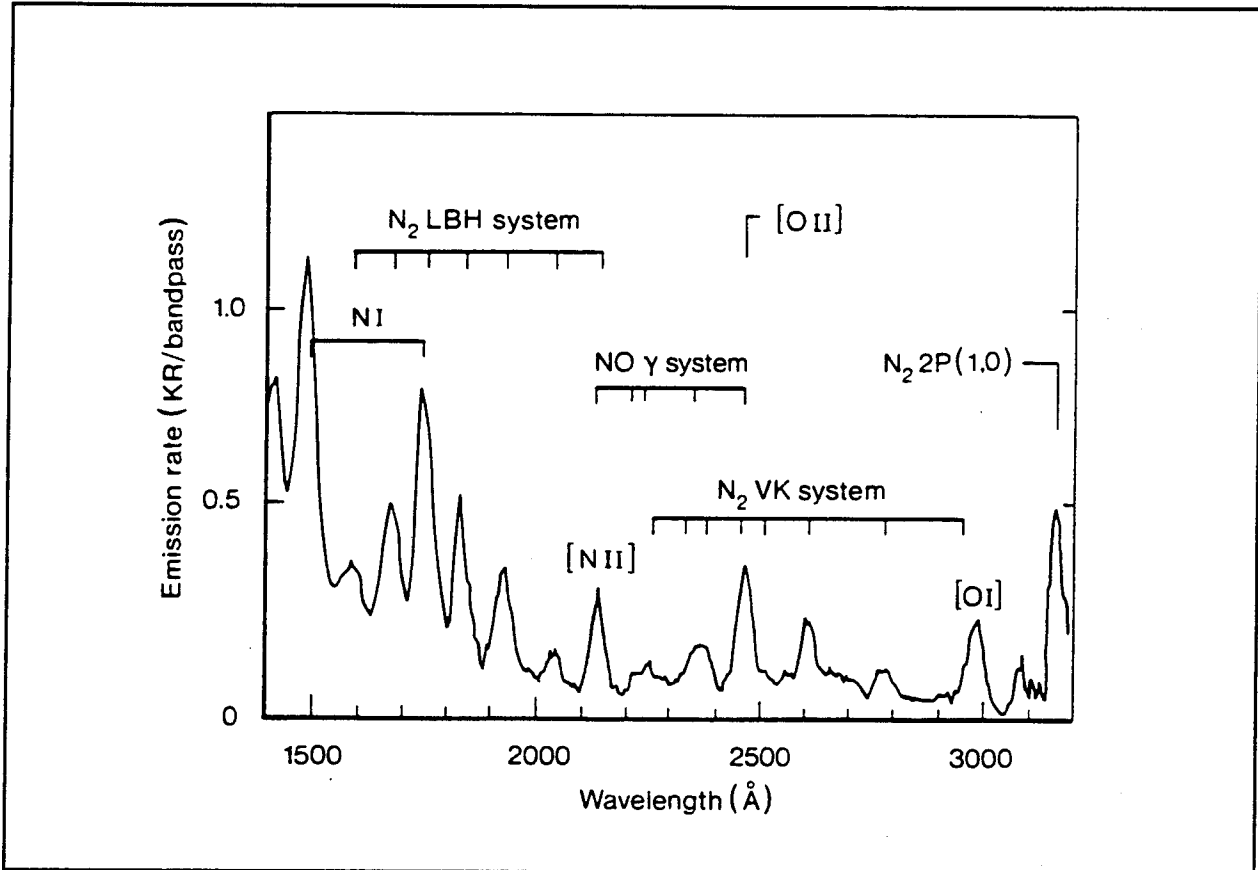


**Figure 2-16** Auroral spectrum acquired by a nadir viewing spectrograph on board the OGO-4 satellite. (Rees, 1989).

Some of the important spectral emission features grouped according to their source atmospheric constituents are presented below.

*a. Atomic Nitrogen*

Figure 2-17 displays an energy level diagram for  $N^+$  showing transitions that have been identified in the airglow or aurora. ISAAC will observe the 2143Å atomic nitrogen emission shown in this diagram.

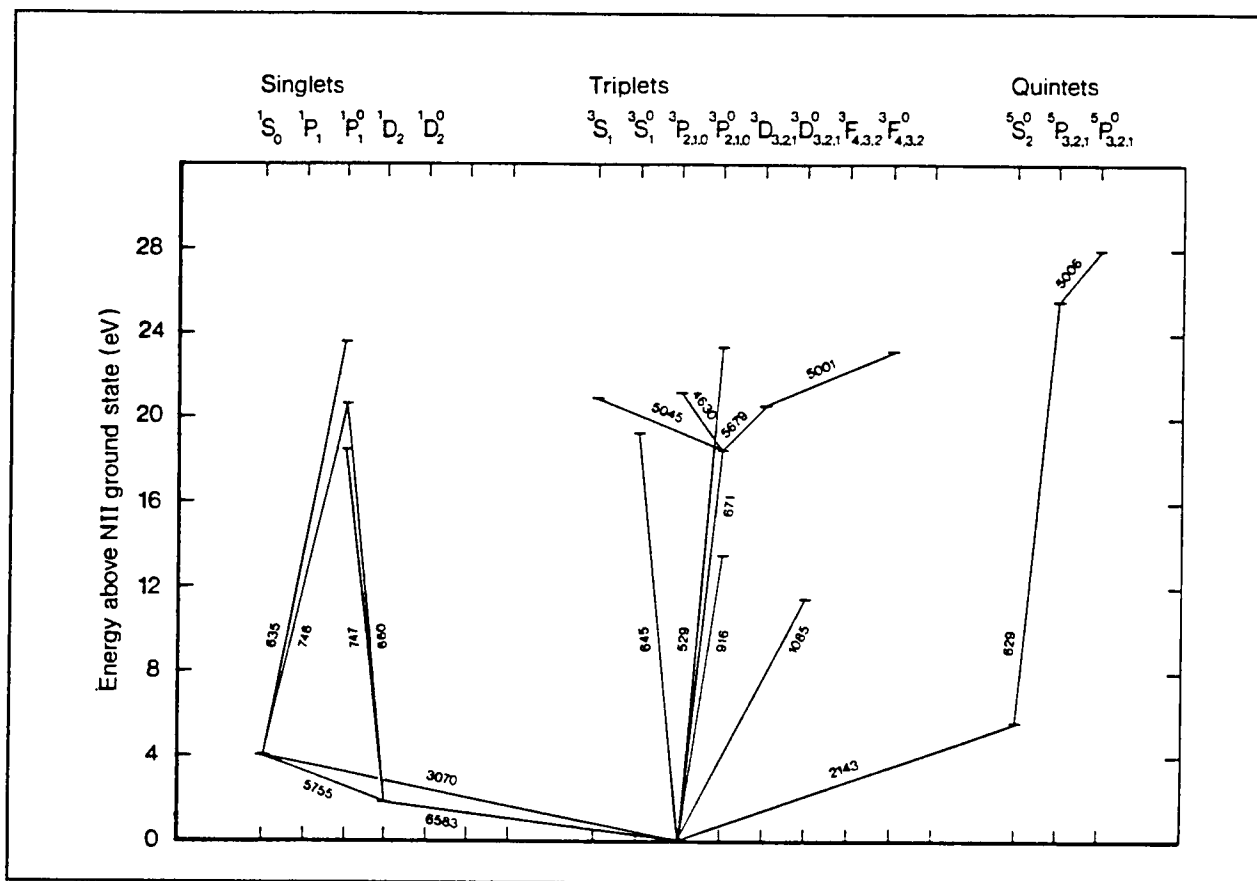


**Figure 2-17** Energy level diagram for  $N^+$  showing transitions observed in the airglow or aurora. (Rees, 1989).

### ***b. Molecular Nitrogen***

A potential energy curve for  $N_2$ ,  $N_2$  and  $N_2^+$  is shown in Figure 2-18. Three transition bands that are observable within the wavelength range of the ISAAC instrument and are observed in the airglow and aurora are the *Vegard-Kaplan*, *Lyman-Birge-Hopfield*, and the *Second Positive* bands. The Vegard-Kaplan (V-K) system is the name given to the band of  $A^3\Sigma_u^+ \rightarrow X^1\Sigma_g^+$  transitions. The Lyman-Birge-Hopfield (LBH) system is the name applied to  $a^1\Pi_g \rightarrow X^1\Sigma_g^+$  transitions of molecular nitrogen. The  $N_2$  Second Positive is the system of transitions  $C^3\Pi_u \rightarrow B^3\Pi_g$ .

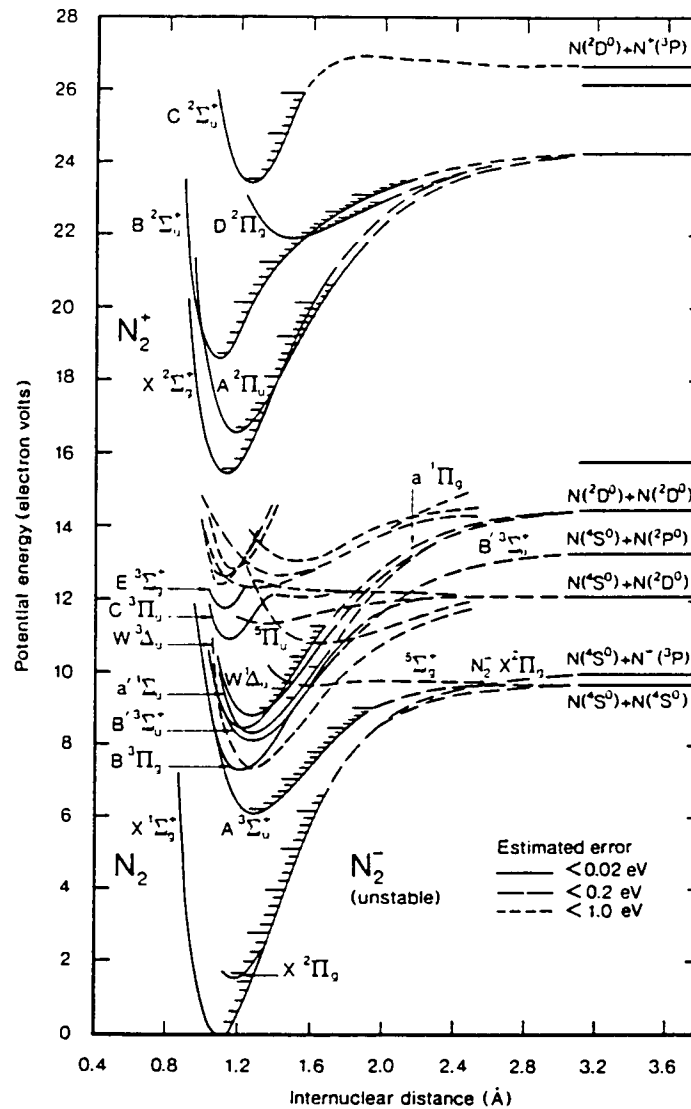
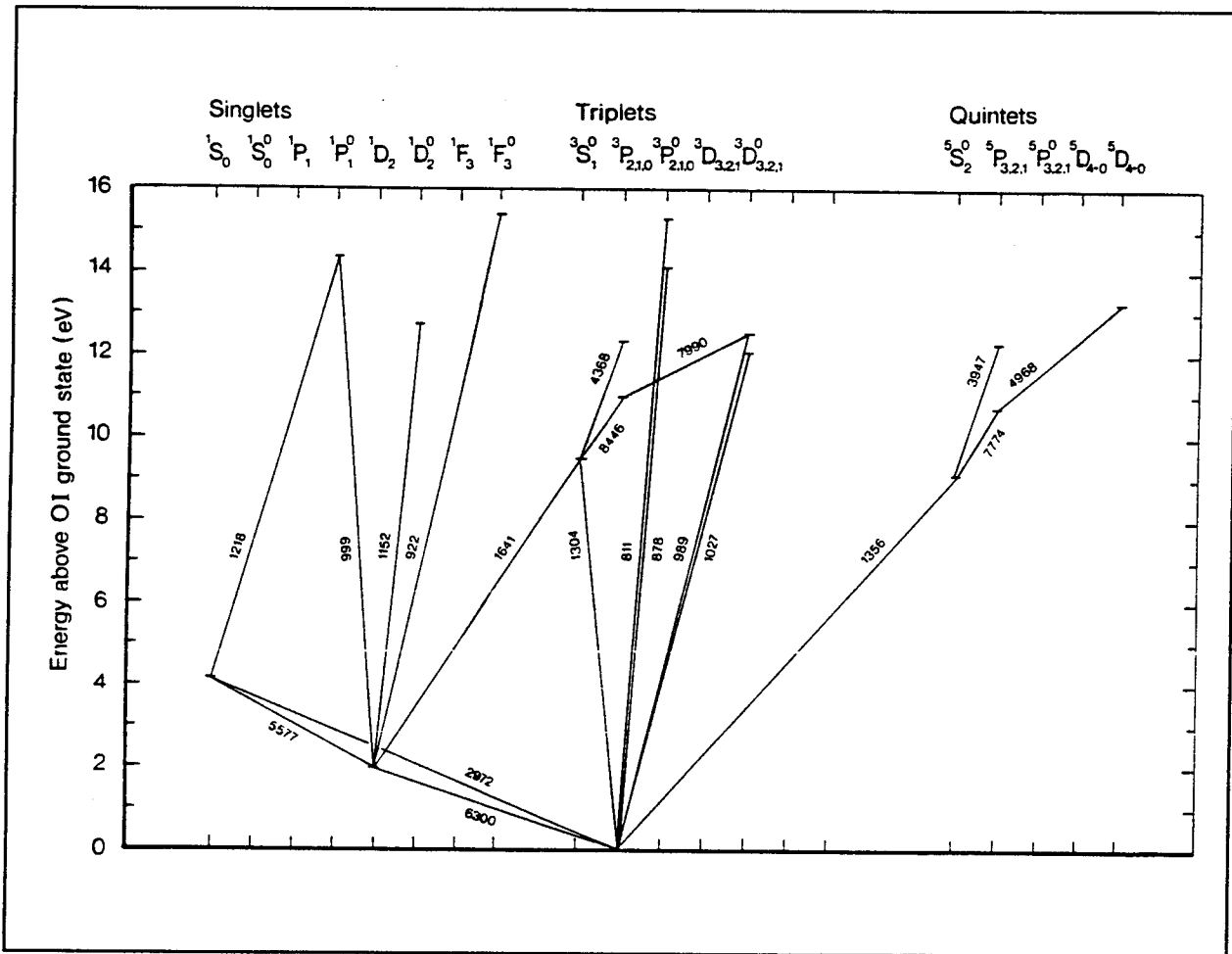


Fig. A3.5 Potential energy curves for  $N_2^-$  (unstable),  $N_2$ , and  $N_2^+$ .

Figure 2-18 Potential energy curves for  $N_2^-$  (unstable),  $N_2$ , and  $N_2^+$ . (Rees, 1989).

*c. Atomic Oxygen*

Figure 2-19 shows an energy level diagram for atomic oxygen, while Figure 2-20 shows a similar diagram for singly ionized atomic oxygen; both figures show the transitions that have been observed in the airglow or aurora. ISAAC will observe the 2972Å and 2470Å oxygen emissions shown in these two figures.



**Figure 2-19** Energy level diagram for atomic oxygen showing the transitions observed in the airglow and aurora. (Rees, 1989).

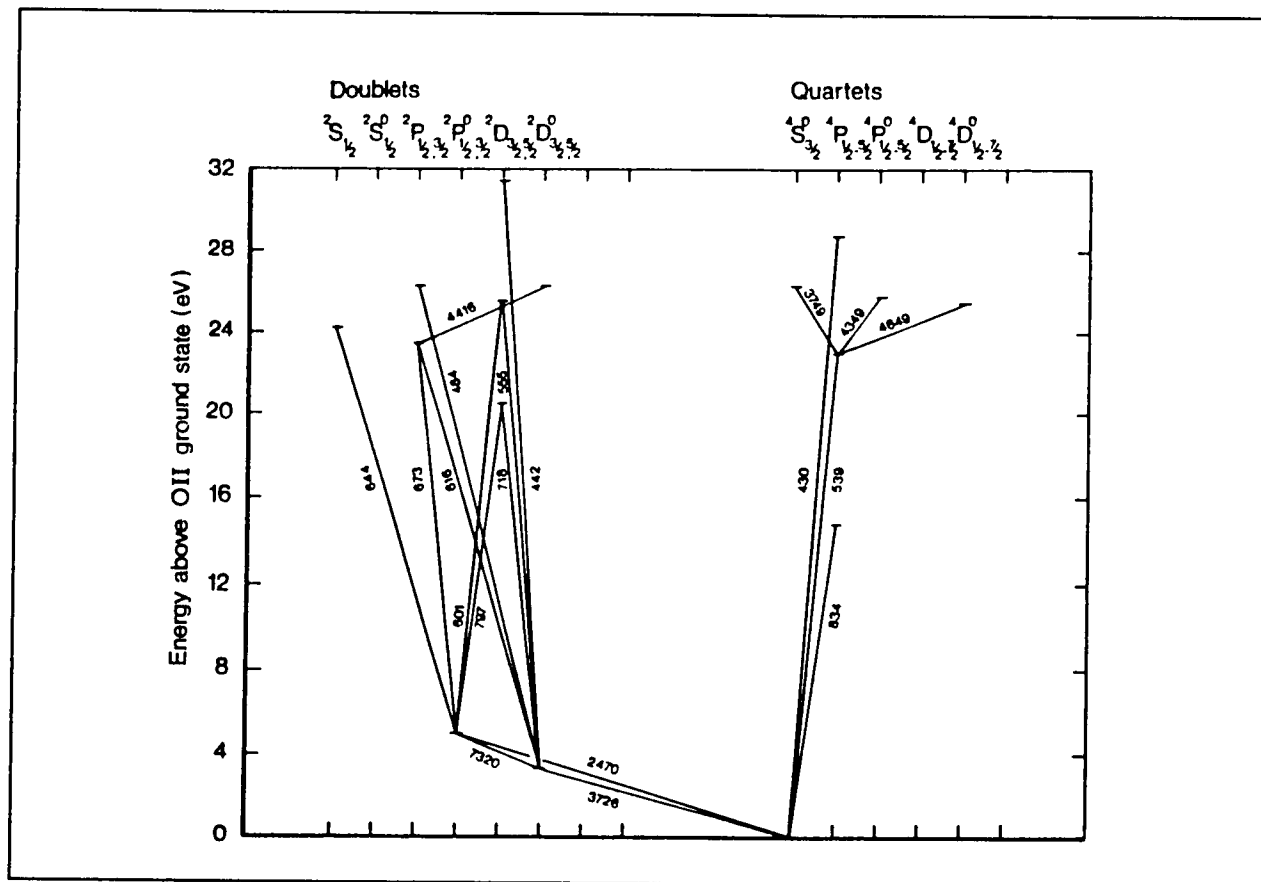


Figure 2-20 Energy level diagram for singly ionized atomic oxygen. (Rees, 1989).

#### *d. Molecular Oxygen*

A potential energy diagram for  $O_2^-$ ,  $O_2$ , and  $O_2^+$  is shown in Figure 2-21. The *Schumann-Runge* (SR) system results from  $B^3\Sigma_u^- \rightarrow X^3\Sigma_g^-$  transitions in the 1750-5350 Å wavelength range. This band has not yet been observed in the thermosphere, though could theoretically exist.

Another feature involving molecular oxygen is the Herzberg transition ( $A^3\Sigma_u^+ - X^3\Sigma_g^-$ ) which emits in the 2590-4880 Å range. This is a prominent system that has been observed in the nightglow as indicated in Figure 2-15. The excitation source for this system is *preassociation* (or *inverse pre-dissociation*), where oxygen atoms approach along a preassociation potential curve to the  $A^3\Sigma_u^+$  state.



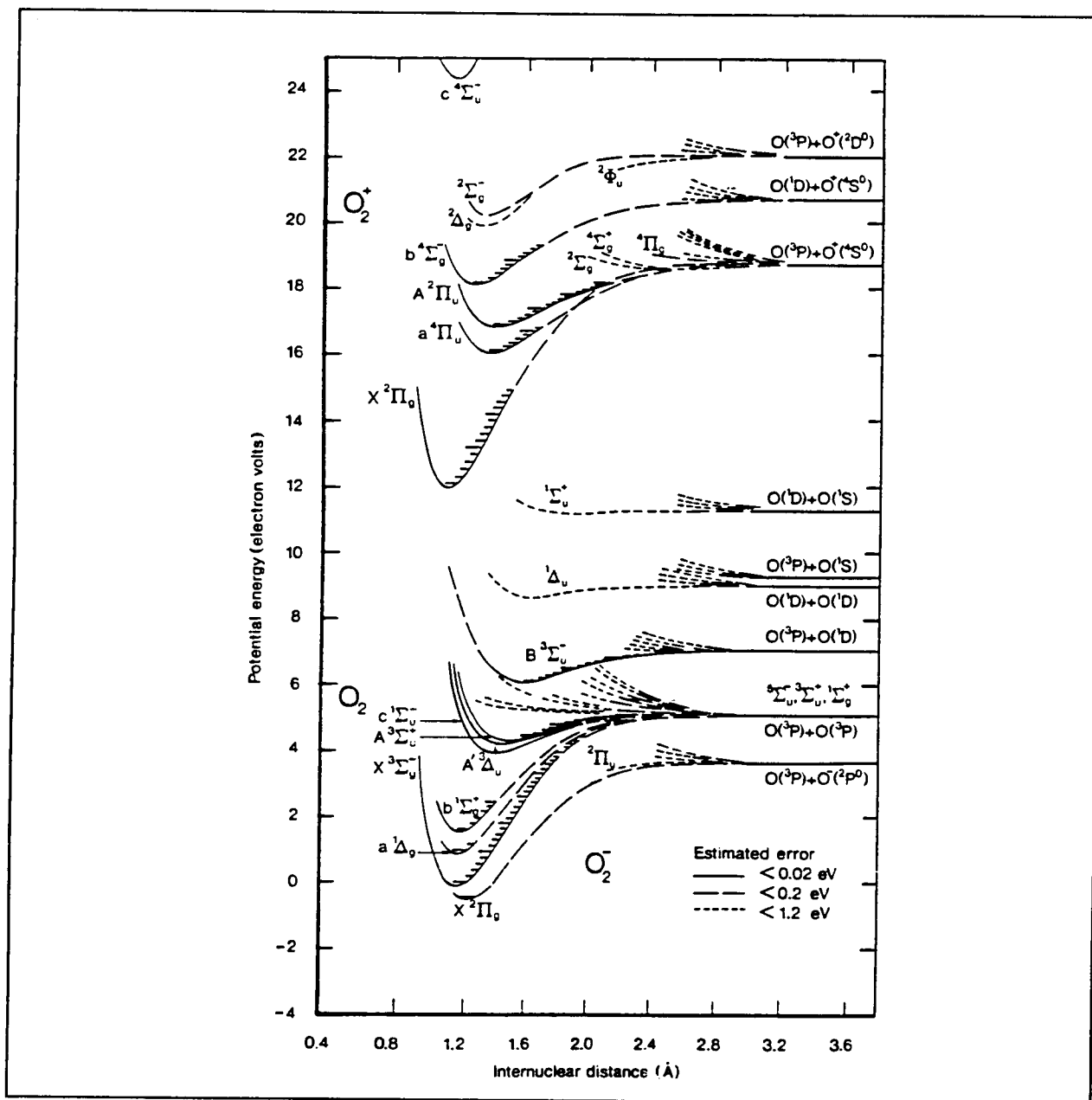


Figure 2-21 Potential energy diagram for molecular oxygen. (Rees, 1989).

*e. Nitric Oxide*

Figure 2-22 presents a potential energy diagram for  $\text{NO}^-$ ,  $\text{NO}$ , and  $\text{NO}^+$ . There are three bands of interest in the wavelength range of the instrument: the  $\gamma$ ,  $\delta$ , and  $\epsilon$  bands. The *Gamma* bands of nitric oxide arise from  $\text{A}^2\Sigma^+ \rightarrow \text{X}^2\Pi$  transitions. These bands emit in the range 1873-6126 Å. The *Delta* bands arise from the  $\text{C}^2\Pi \rightarrow \text{X}^2\Pi$  transitions and are in the wavelength range 1621-4288 Å. The *Epsilon* bands arise from  $\text{D}^2\Sigma^+ \rightarrow \text{X}^2\Pi$ . Emissions are in the wavelength range 1800-2385 Å. These three bands have been observed in airglow and auroral spaceborne spectroscopy (refer to Figures 2-14 to 2-16).

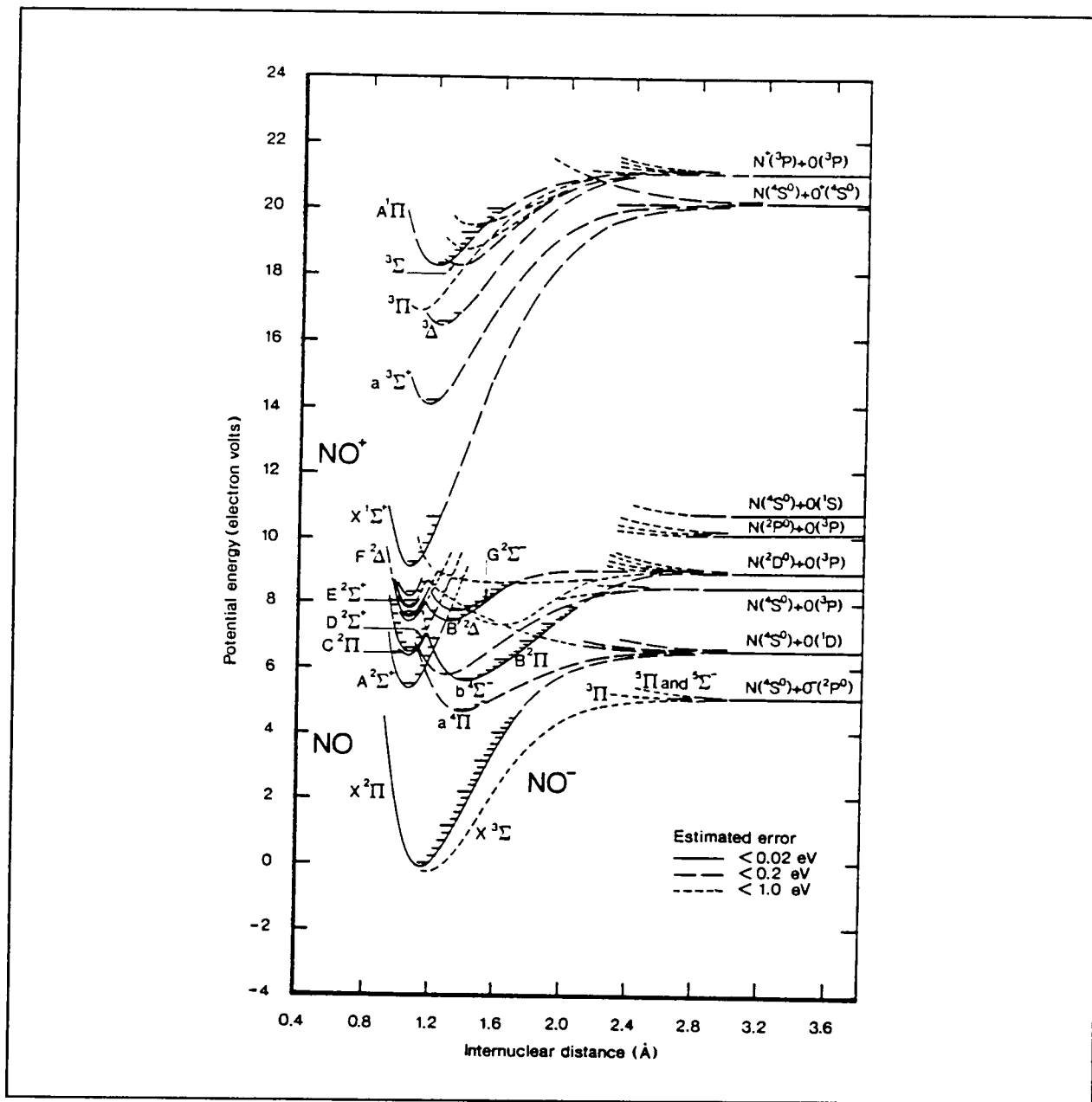


Figure 2-22 Potential energy diagram for nitric oxygen states. (Rees, 1989).

## E. TEMPERATURE AND ELECTRON DENSITY PROFILES

Thermospheric temperatures and electron densities are desired products of the ISAAC spectra as discussed in the introduction. This section will describe how these data from the spectrograph may be used to provide useful information and satisfy the requirements delineated in The Joint Chiefs of Staff Memorandum (1986).

The number-two priority collection requirement according to the JCS memorandum is the collection of thermospheric temperatures. The temperature model of the thermosphere in current use is the MSIS-86 (Hedin, 1987) which is based on data from satellites, numerous rocket probes and five incoherent scatter stations. Barth and Eparvier (1993) have shown that upper atmospheric temperatures, accurate to within  $\pm 20^\circ$ , may be determined in the 110-140 km altitude range by analysis of the rotational structure of nitric oxide. The technique involves comparison of synthetic spectra with observed spectra. Synthetic spectra are developed through knowledge of the processes involved in production of the rotational emissions. The details of the rotational structure depend on the processes that create the excited states, the populations of the rotational levels of the ground state molecule observed, and the line strengths of the rotational transitions in absorption and emission. Figure 2-23 shows a comparison of synthetic spectra for the NO (1,1) Gamma Band at two temperatures. ISAAC will allow the ability to perform such measurements from a spaceborne platform, thereby permitting measurements over extensive spatial and temporal ranges.

The fifth highest priority collection requirement according to the JCS memorandum is the detection of electron densities in the upper atmosphere. The current primary means of measuring electron densities are *ionosonde* measurements and *incoherent scatter* radar measurements. Currently more than one hundred ionosonde stations throughout the world make measurements every hour (Crowley, 1994). Ionosondes transmit frequency modulated pulses of electromagnetic energy toward the ionosphere. The critical frequency at which the energy is refracted back toward the transmitter is a function of the electron density and is given by

$$v_c = \frac{9 \times 10^{-3}}{\cos \alpha} \sqrt{N_e} \quad (2-37)$$

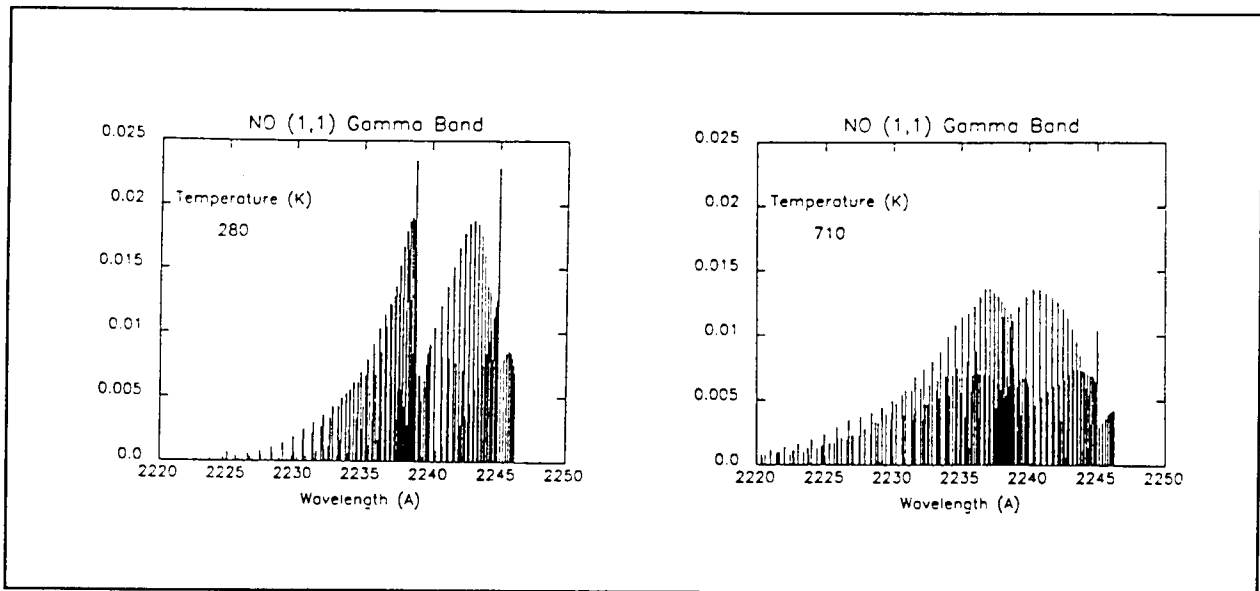


**Figure 2-23** Synthetic spectra for the (1,1) Gamma band at a temperature of 280 K and at 710 K. (Barth and Eparvier, 1993).

where  $\nu_c$  is the critical frequency,  $\alpha$  is the angle of incidence and  $N_e$  is the electron density. A limitation is that ground-based sounders are incapable of reaching above the peak of the  $F_2$ -layer of the ionosphere. This problem is overcome with the use of orbiting spaceborne sounders, called *topside sounders*, though they are infrequently used due to size and weight limitations.

Incoherent scatter stations measure the returned power of high-powered radars. A weak echo is observed that arises from the incoherent scattering from individual electrons in the ionosphere. The echoed signal is proportional to the electron density at the height at which the scatter occurred. This technique has the advantage of allowing observation of electron densities above the  $F_2$  peak, not accessible to ground-based ionosonde measurements.

New techniques to passively measure electron densities and layer heights in the ionosphere through remote sensing of neutral ionospheric constituents are being tested and ISAAC will allow further analysis of this developing technique. As revealed in Figure 2-3 earlier in this chapter, the positive ions  $\text{NO}^+$  and  $\text{O}_2^+$  contribute the most to electron density in the region of the  $E$ -layer of the ionosphere (90-140 km), while the  $\text{O}^+$  ion contributes almost exclusively to the electron density in the  $F$ -layer at altitudes above 140 km. Therefore, measurements or inferences of the densities of

these ions would allow inference of the corresponding electron densities assuming a neutral atmosphere.

Measurements of atomic oxygen radiative recombination emissions have been shown to permit inference of electron density profiles in the  $F$ -region (Chandra *et al.*, 1975; Tinsley and Bittencourt, 1975). The technique involves derivation of a relationship between the height of the  $F_2$  peak and column emission rates of atomic oxygen emission lines. The atomic oxygen 2972-Å emission (within the ISAAC wavelength range) may be useful to this technique. However, daytime solar-induced emissions prohibit observation of these weak emissions.

Analysis of the  $O^+$  834-Å dayglow emission has been used to profile the electron densities in the  $F_2$  region (Feldman, *et al.*, 1981; McCoy, *et al.*, 1985; Cleary, *et al.*, 1989; Meier, 1991). These 834-Å photons are created in the lower thermosphere by the ionization-excitation of atomic oxygen through solar photoionization and photoelectron impact excitation. Some of these photons are radiated into the upper atmosphere and can be resonantly scattered by  $O^+$  ions in the  $F_2$  region. Through multiple scattering, the 834-Å airglow assumes the  $O^+$  ionospheric signature. While outside of the wavelength range of the ISAAC spectrograph, a companion spectrograph on the ARGOS satellite, the High Resolution Ionospheric/Thermospheric Spectrograph (HITS) will be able to image this important emission.

ISAAC will also be used to directly measure the concentrations of *odd nitrogen* in the  $E$ -region of the ionosphere.  $N_2$  is an extremely stable molecule although various thermospheric processes lead to its dissociation. These processes provide the source for what is known as the odd nitrogen family. Odd nitrogen refers to all photochemically active species that contain nitrogen. This includes: ground state atomic nitrogen  $N(^4S)$  and its first and second excited states  $N(^2D)$  and  $N(^2P)$  and the molecules  $NO_2$  and  $NO$ . Measurements of these odd nitrogen constituents will be used to attempt to infer the  $E$ -layer electron densities through use of a photochemical model of this region, developed by Cleary (1986), which relates these neutral constituents to the  $NO^+$  and  $O_2^+$  ion densities. A schematic representation of the production of odd nitrogen in the thermosphere is shown as Figure 2-24.

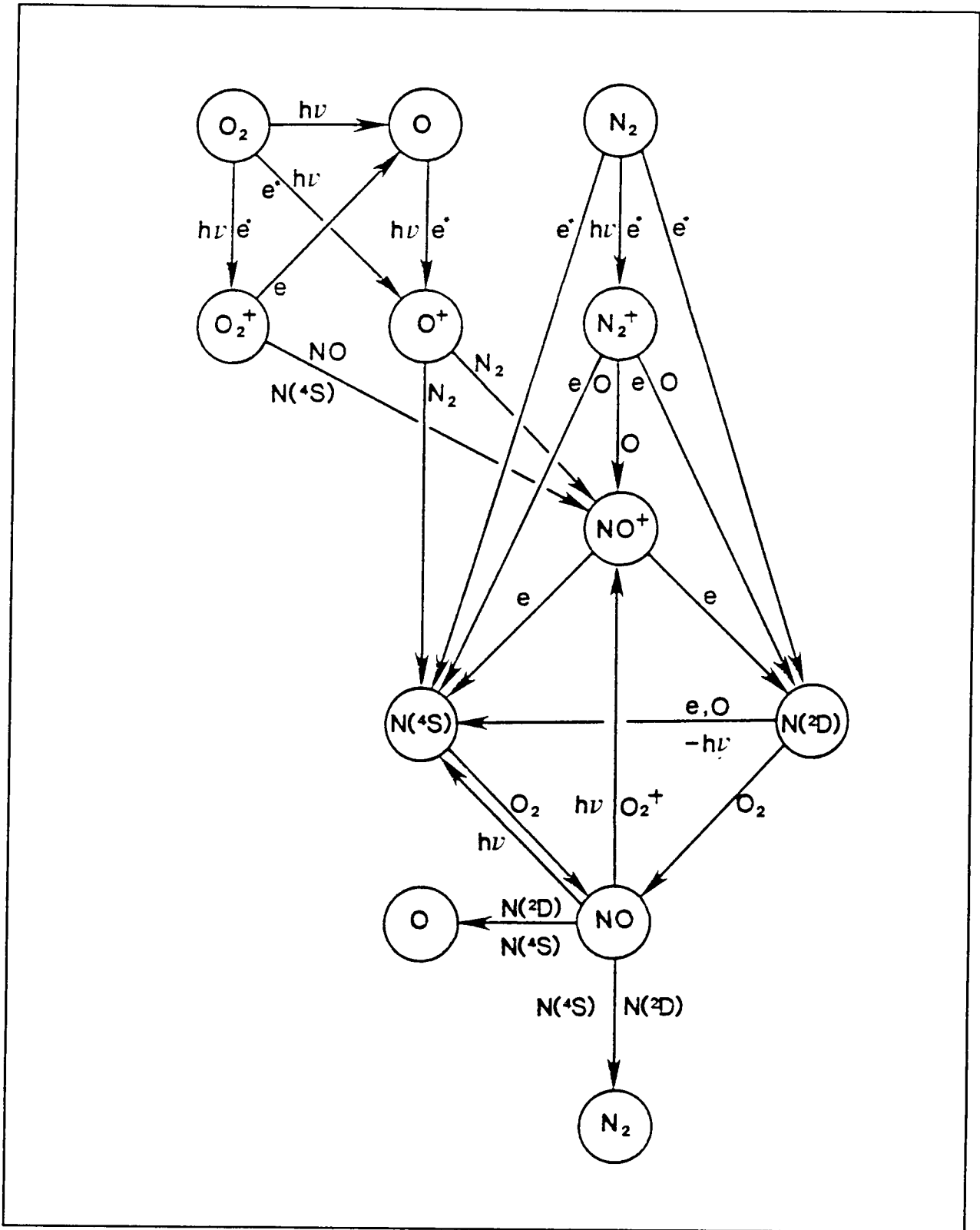


**Figure 2-24** Schematic representation of the production of odd nitrogen in the thermosphere. (Cleary, 1985).

### III. ARGOS SATELLITE AND PAYLOAD

ISAAC will be carried aloft, along with 30 other sensors, on board the P91-1 Advanced Research and Global Observation Satellite (ARGOS) through the Air Force Space Test Program (STP) in early 1996. This chapter presents a brief survey of the satellite and its payload complement.

The satellite is a 6000 lb spacecraft with a 44 ft span across the solar arrays. The satellite will carry eight experiments that include 31 sensors and sub-experiments. Figure 3-1 is a representation of the integrated space vehicle and payload complement. Launch vehicle and satellite bus specifications are available in Turner and Agardy (1994).

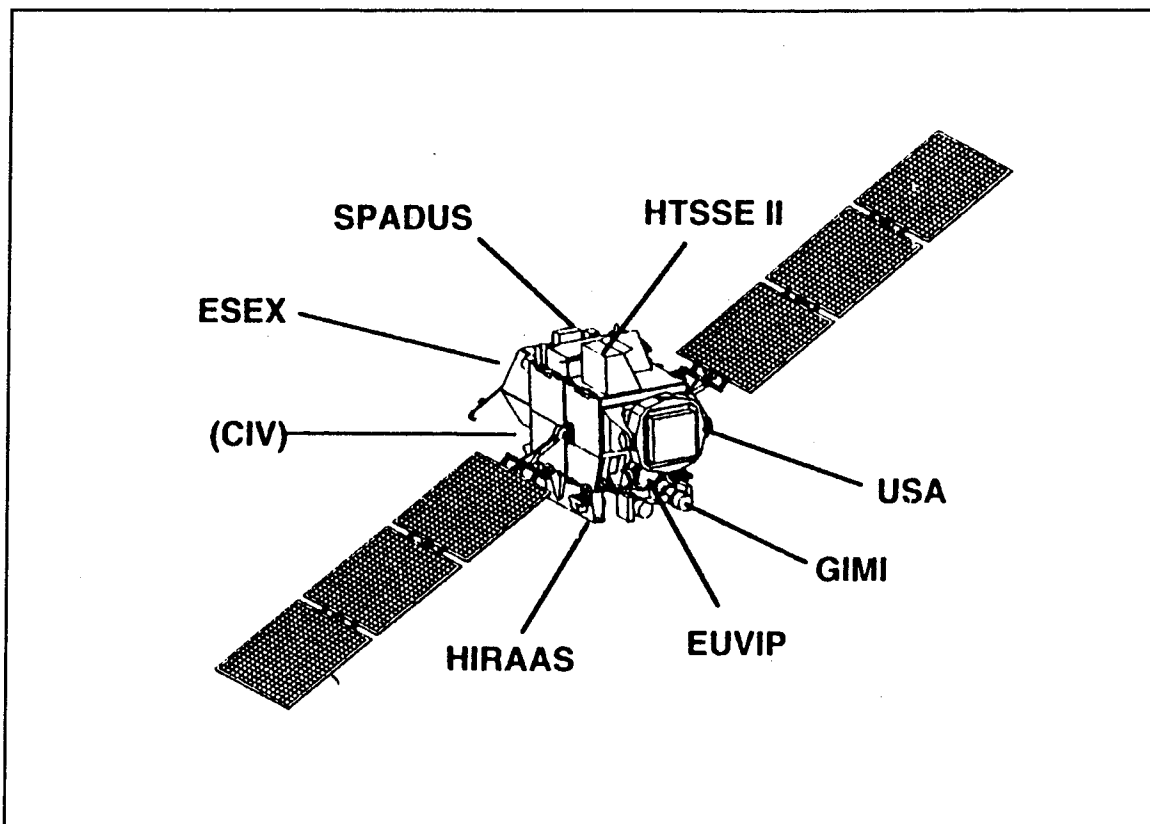


**Figure 3-1** ARGOS space vehicle and payload configuration. (ARGOS CDR, 1993).

ARGOS will be placed in a low-earth-orbit (450 nmi) sun-synchronous (98.7° inclination) orbit by a Delta II 7920-10 launch vehicle. The launch vehicle is depicted in Figure 3-2 and the launch profile is represented in Figure 3-3.



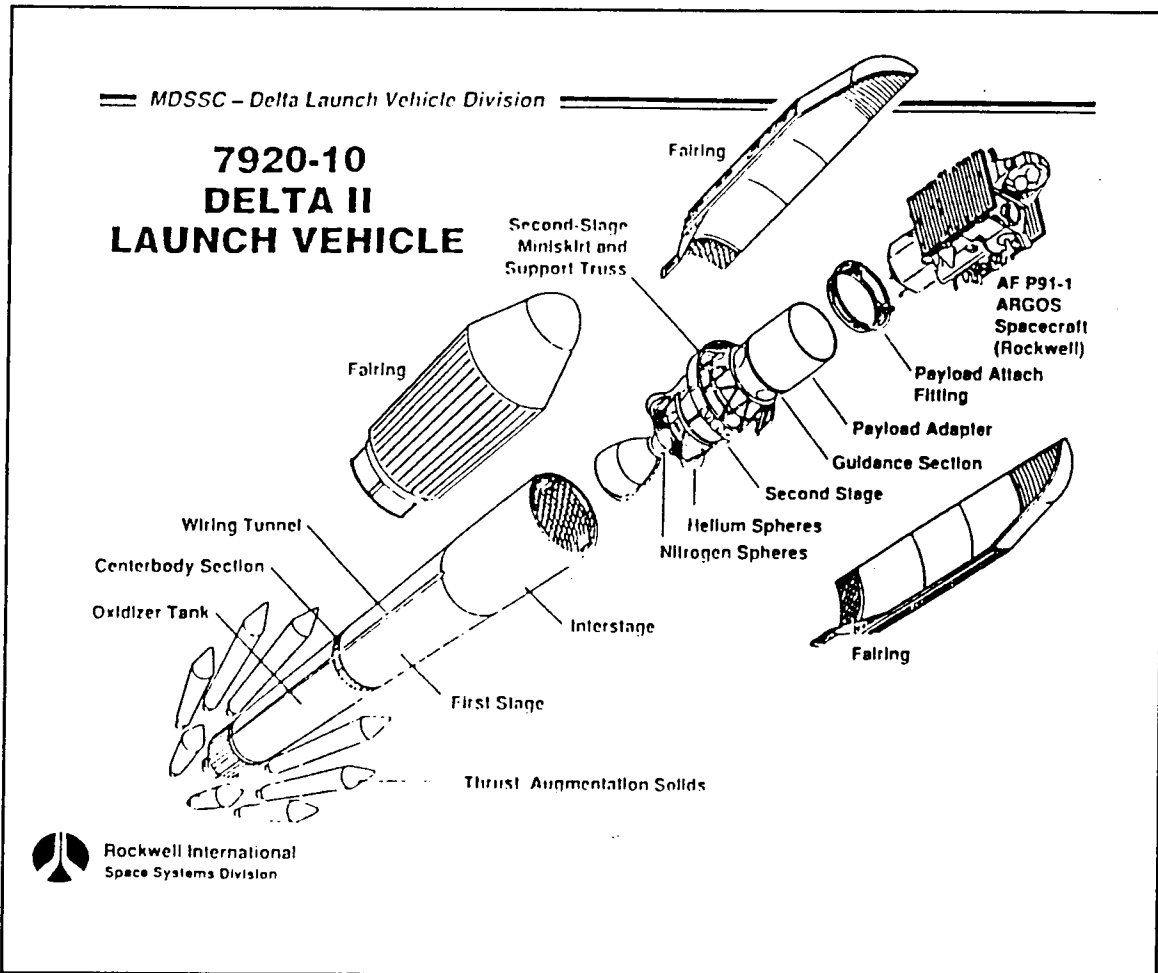


Figure 3-2 7920-10 Delta II launch vehicle. (ARGOS CDR, 1993).

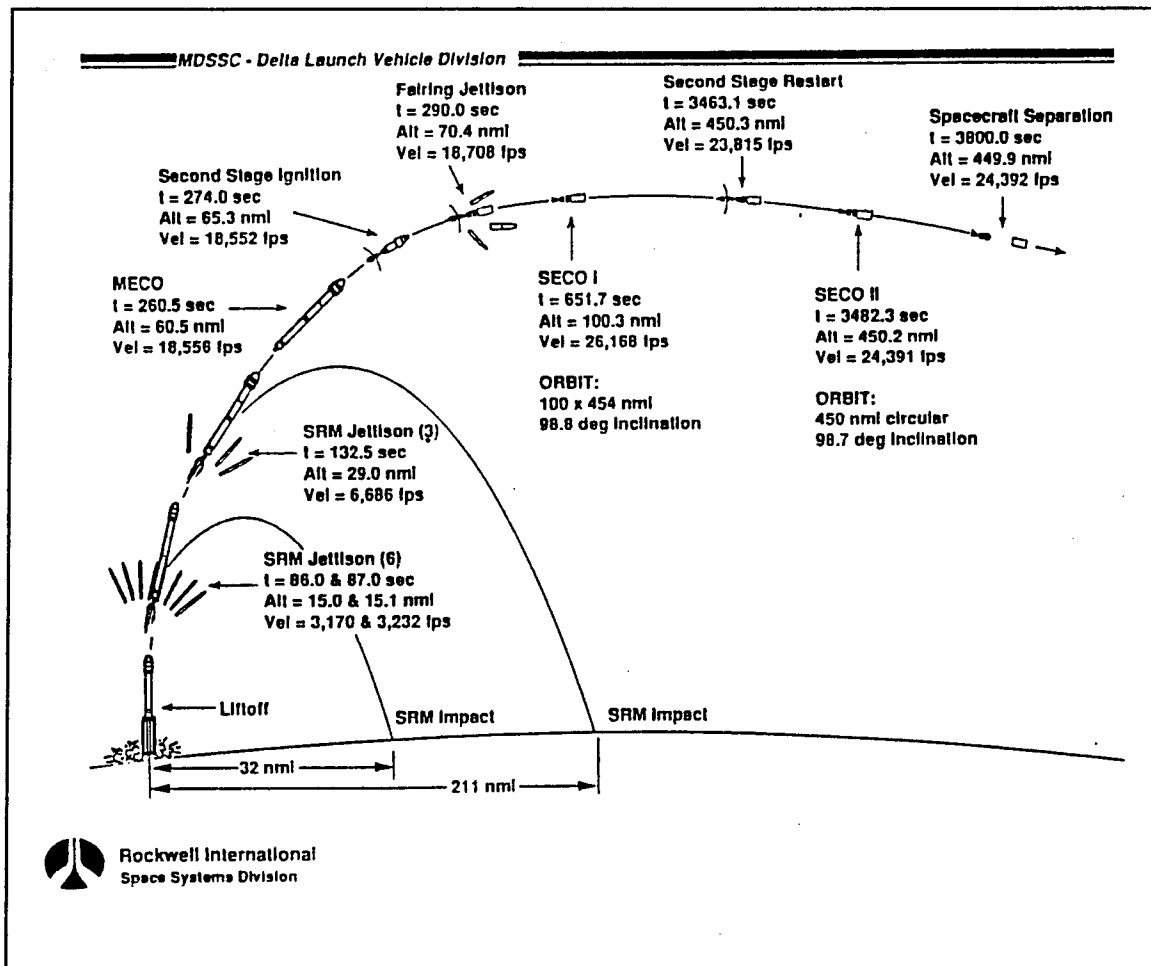


Figure 3-3 ARGOS P91-1 launch ascent profile. (ARGOS CDR, 1993).

The suite of sensors on ARGOS will provide the capability to simultaneously sense ionospheric phenomena in UV and x-ray wavelengths. The eight experiments carried onboard the ARGOS satellite are the ESEX, CIV, GIMI, USA, EUVIP, SPADUS, HTSSE II, and HIRAAS, each of which are briefly described below (see Agardy and Cleave, 1993; ARGOS Comprehensive Design Review, 1993).

#### **A. ELECTRIC PROPULSION SPACE EXPERIMENT (ESEX)**

ESEX will demonstrate electric propulsion technology required for cost-effective access to space. It is a 26-kW class ammonia arcjet that will operate for ten 15-minute firings while collecting performance data. This arcjet provides a specific impulse of 800 seconds (vacuum) at a thrust level of 2 N.

#### **B. CRITICAL IONIZATION VELOCITY (CIV)**

This experiment will release xenon and carbon dioxide to study ionization processes caused by molecular collisions in the upper atmosphere. This experiment is a follow-on to a previous CIV experiment onboard STS 39 and will provide data needed to improve the ability to sense rocket and spacecraft plumes. It will observe Xe ion formation, the optical signature, and spatial distribution. Carbon dioxide will be released to quantify CO<sub>2</sub> collisional reactions with the atmosphere.

#### **C. GLOBAL IMAGING MONITOR OF THE IONOSPHERE (GIMI)**

This experiment is designed to obtain ultraviolet images to map and monitor the ionospheric O<sup>+</sup> and electron density in the upper atmosphere (Carruthers and Seeley, 1992). It will provide wide-field imaging of ultraviolet emissions in the 750-1050-Å and 1310-1600-Å spectral ranges, specifically allowing observation of the important 834-Å O<sup>+</sup> dayglow emission and the 1356-Å O nightglow emission. The sensors are mounted on a two-axis gimbal which will allow observation of celestial targets and Earth atmospheric emissions. The experiment objectives include: the measurement and monitoring of atomic nitrogen in the middle atmosphere through observations of NO nightglow, demonstration of remote sensing of neutral atmosphere (O<sub>2</sub>, N<sub>2</sub>) at night by observations of the occultations of

UV-bright stars by the atmosphere, and wide-field imaging of celestial sources (stars, nebulae, and diffuse background) in the 920-1100-Å and 1310-1600-Å wavelength ranges. This instrument will provide simultaneous observations of the airglow and aurora in conjunction with HIRAAS and ISAAC.

#### **D. UNCONVENTIONAL STELLAR ASPECT (USA)**

The USA experiment consists of two counter detectors to measure X-rays in the 1-15 keV range. Astronomical X-ray sources will be investigated to determine potential use for position, attitude and timekeeping for autonomous military space systems. Additionally, the experiment will conduct the first X-ray tomographic survey of the Earth's atmosphere.

#### **E. EXTREME ULTRAVIOLET IMAGING PHOTOMETER (EUVIP)**

This EUV imaging photometer will measure stellar and atmospheric spectra at the 100-Å, 304-Å, and 834-Å wavelengths. The experiment will image the *F*-region ionosphere, EUV celestial sources and the auroral oval. This instrument is hard mounted within the space vehicle with a 5° circular field of view.

#### **F. SPACE DUST EXPERIMENT (SPADUS)**

This experiment is designed to measure the mass, flux, charge, velocity, and trajectory of incoming dust particles measuring 2-200 μm in size and to measure the local radiation environment in the 0.2-20 MeV range. This debris data will provide measurements of the orbital debris at 450 nmi altitude and allow spatial mapping of the present dust distribution. This information is needed to predict debris "showers" that could affect future DoD spacecraft. The collection device consists of two parallel grids of 32 polyvinylidene fluoride sensors oriented in the velocity vector direction. The radiation measurements are needed to design future shielding and electronics that are resistant to the environment in this orbit.

## G. HIGH TEMPERATURE SUPERCONDUCTIVITY SPACE EXPERIMENT (HTSSE II)

This important experiment will space qualify High Temperature Superconductivity (HTS) technology. This HTS digital technology provides more than 10 times higher speed than silicon or gallium arsenide technology, and weight and power reduction.

## H. HIGH RESOLUTION AIRGLOW AND AURORAL SPECTROSCOPY (HIRAAS)

This experiment includes three UV spectrographs including the ISAAC instrument. Figure 3-4 shows the HIRAAS system and identifies the subcomponents: the High Resolution Ionospheric/Thermospheric Spectrograph (HITS), the Low Resolution Airglow/Aurora Spectrograph (LORAAS) and the ISAAC spectrograph.

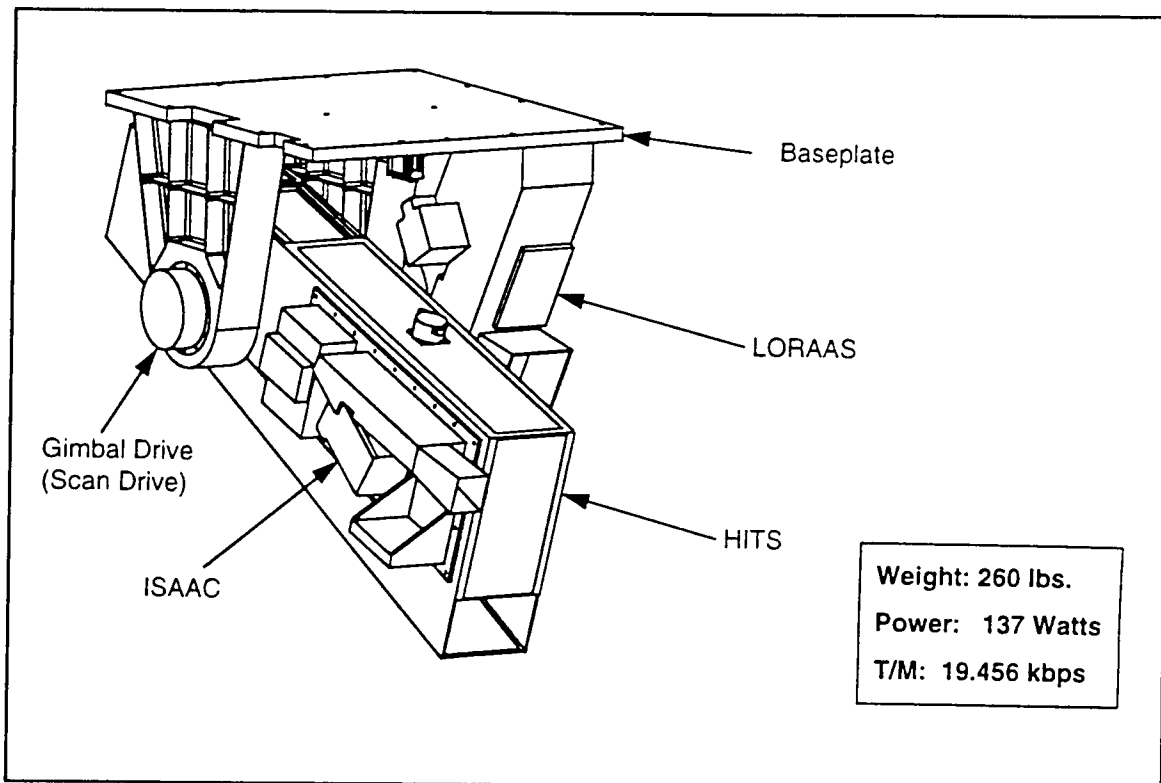


Figure 3-4 HIRAAS assembly. (McCoy, 1993).

LORAAS is an optical copy of the DMSP Special Sensor for UV Limb Imaging (SSULI) that will provide a calibration/validation opportunity prior to the first SSULI flight. It has a fixed passband from 800-1700-Å with a 12-Å resolution. HITS provides an 80-Å selectable passband within the 500-1500-Å range with a resolution of less than 0.5-Å. ISAAC will provide approximately 2.5-Å resolution in the 1800-3300-Å range.

HITS and ISAAC are stationed on a mechanical scanning platform that will allow scanning of the Earth's limb. The scan platform will perform a slow downward scan lasting approximately 90 seconds providing observation of tangent altitudes between 0-750 km as depicted in Figure 3-5. A scan mirror on LORAAS will be synchronized to scan along with HITS and ISAAC.

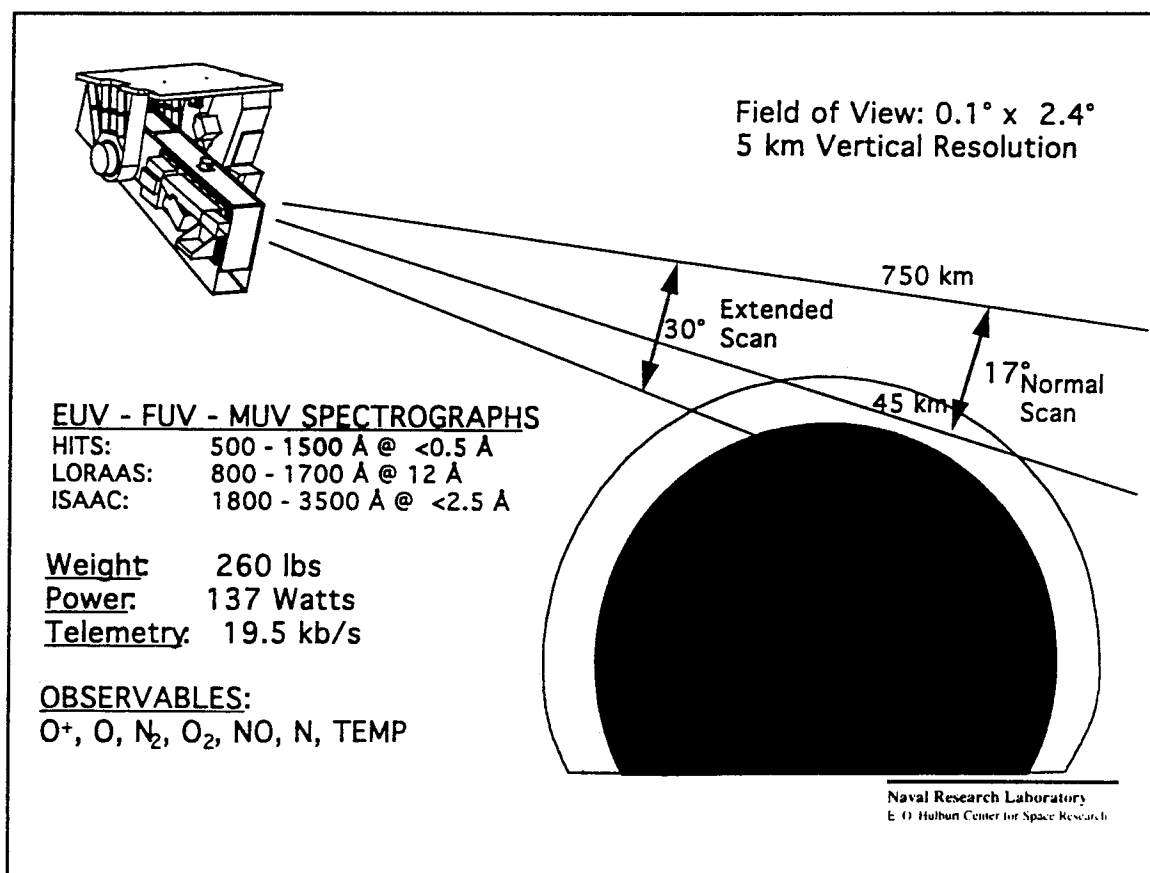


Figure 3-5 HIRAAS limb imaging concept. (McCoy, 1993).

Stated objectives of the HIRAAS array of spectrographs include (ARGOS CDR, 1993):

- Perform a high spectral resolution study of thermospheric and Ionospheric EUV/FUV/MUV airglow
- Measure vertical profiles of the major and minor atmospheric constituents to study photochemistry, thermodynamics, and couplings between regions
- Develop and test a new technique for 3-D ionospheric remote sensing
- Use high resolution spectroscopy to study radiation transfer in optically thick lines in the Earth's atmosphere
- Measure the distribution of odd nitrogen in the lower thermosphere to help determine densities in the  $E$  and  $F_1$  regions of the ionosphere
- Use high spectral resolution to determine Doppler widths and shifts of precipitating ions in proton auroras
- Study the effects of the buildup of greenhouse gases on the composition and thermal structure of the upper atmosphere

The following chapter will discuss the ISAAC instrument in greater detail.

#### IV. ISAAC SPECTROGRAPH

The ISAAC instrument consists of a 1/8-m off-axis telescope, a 1/8-m Ebert-Fastie spectrograph, with a movable reflecting diffraction grating, and an image intensifier coupled to a linear CCD photodetector. The diffraction grating can be rotated to one of four positions through operation of a stepper-driver motor. A remote-controlled mechanical dust cover door is located at the entrance to the telescope. The instrument is depicted in Figure 4-1 and a mechanical drawing of the instrument is shown in Figure 4-2. Figure 4-3 is a simplified drawing of the instrument showing the path of incident photons. The optical equipment was designed at the Naval Postgraduate School and the instrument was fabricated by Research Support Instruments, Inc. This background chapter is included to allow an understanding of the instrument functions that the GSE is designed to control and to document all spectrograph technical specifications and I/O connections.

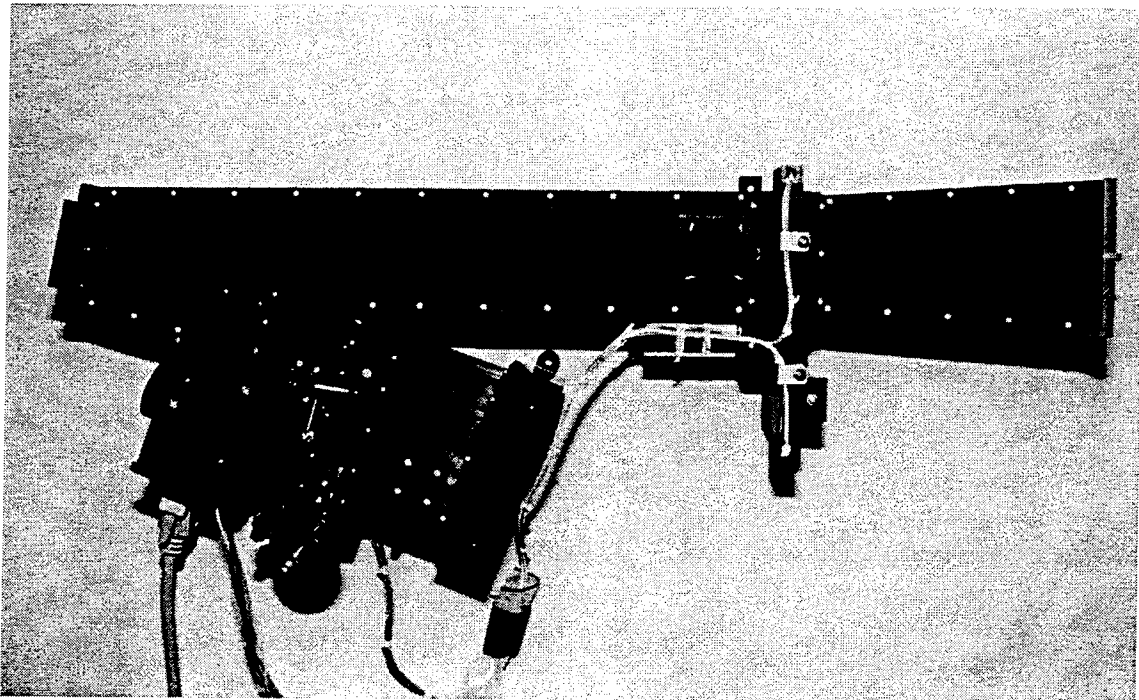


**Figure 4-1** The ISAAC spectrograph.



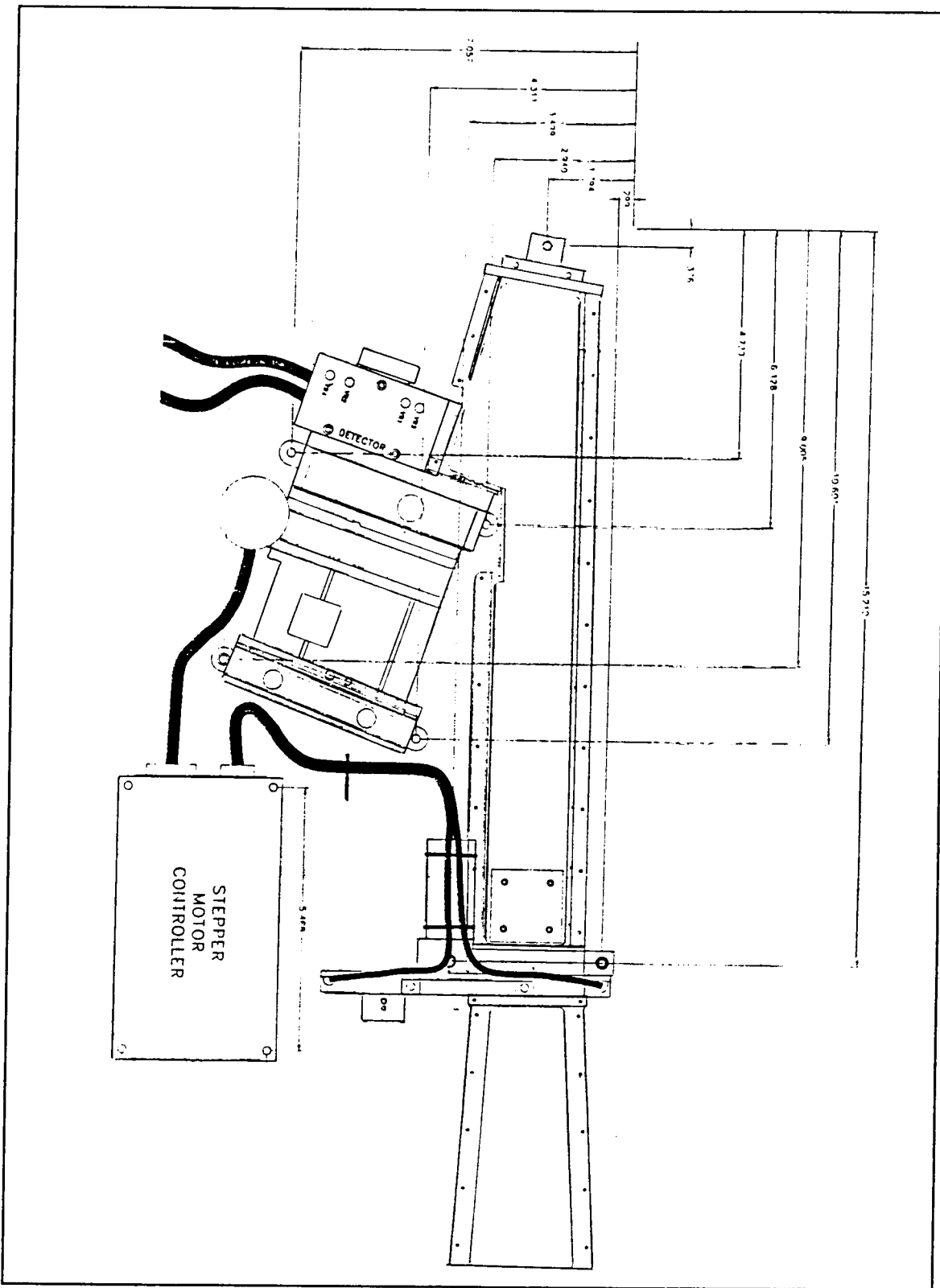


**Figure 4-2** Mechanical drawing of the ISAAC spectrograph. (Reduced from a RSI blueprint).

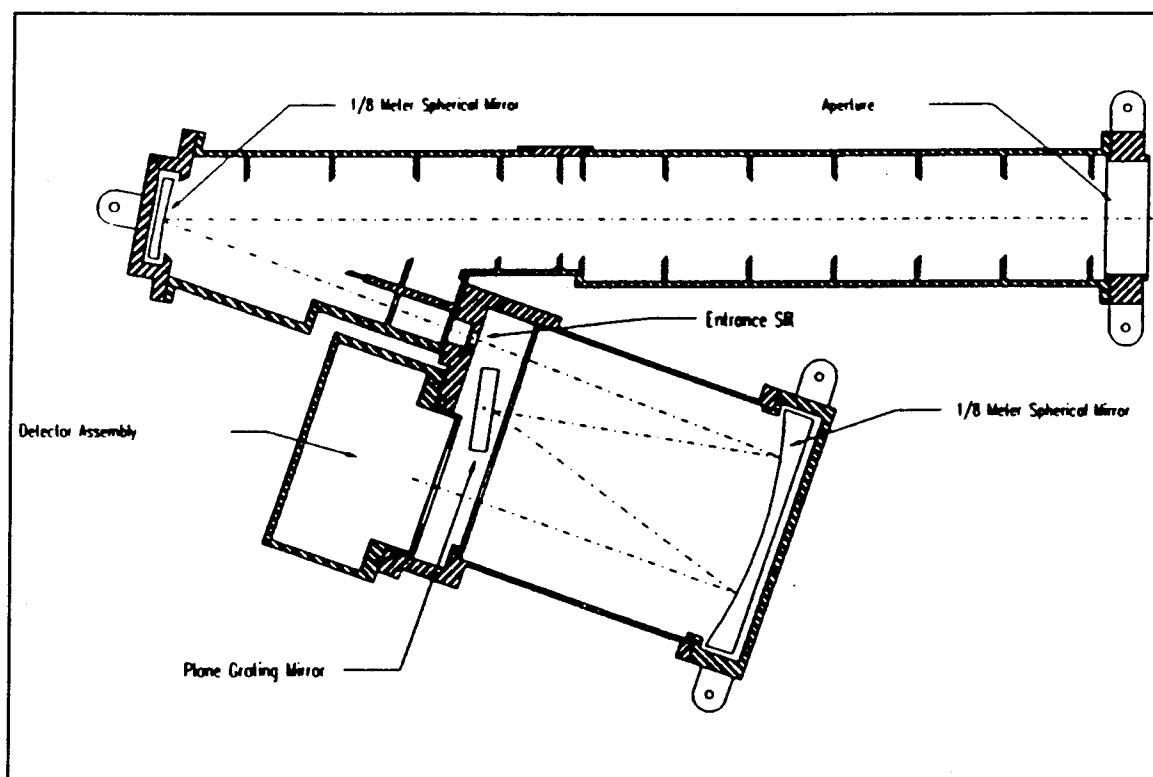


**Figure 4-3** Mechanical drawing of the ISAAC spectrograph showing path of incident light.

### A. EBERT-FASTIE SPECTROGRAPH

The optical components of the ISAAC spectrograph consist of a 1/8-m telescope mirror, a 1/8-m Ebert mirror, and a movable reflecting diffraction grating. As shown in Figure 4-3, light entering the telescope is reflected from the telescope mirror and is focused at an entrance slit. Baffling along the telescope tube prevents stray light from reaching the mirror. Light then passes through the 75  $\mu\text{m}$ -wide-by-2.52 mm-long entrance slit and reaches the 1/8-m Ebert mirror which collimates the light onto the reflecting plane-diffraction grating. This diffraction grating, which has 3600 grooves/mm, disperses incoming electromagnetic radiation according to the grating equation

$$m \lambda = d (\sin \theta_m - \sin \theta_i) \quad (4-1)$$

where  $m$  is the diffraction order,  $\lambda$  is the wavelength,  $d$  is the distance between grooves or slits,  $\theta_i$  is the incident angle and  $\theta_m$  is the diffracted angle for the  $m$ th order. Figure 4-4 shows a diagram representing a reflecting diffraction grating. In the spectrograph, light is dispersed from the grating according to Equation (4-1) back to the Ebert mirror where it is focused onto the image intensifier. The rated efficiency of this grating is 69% for light at 2500-Å, 70% at 2600-Å, and 67% at 2700-Å. The efficiency measures the fraction of light that is directed into the first order diffraction.

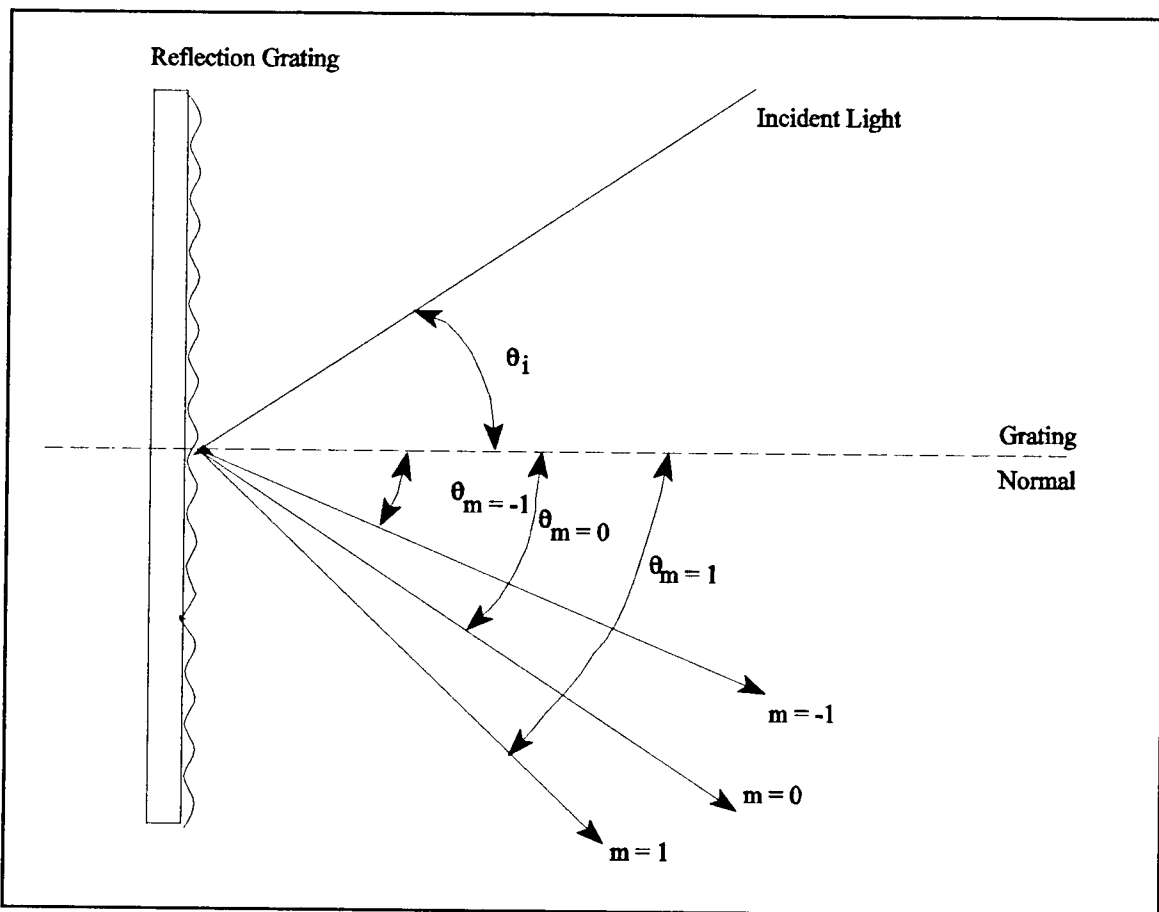


**Figure 4-4** Reflecting diffraction grating depicting several diffraction orders.

## **B. ITT IMAGE INTENSIFIER**

The image intensifier is used to amplify and convert incoming ultraviolet photons to visible photons at a wavelength near the peak in the sensitivity curve of the Hamamatsu detector (described in the following section). The intensifier used in ISAAC is an ITT F4145 Proximity Focused Channel Intensifier Tube with Dual Microchannel Plates. Technical data for this device is included in Appendix A. The intensifier consists of a quartz input window, a cesium telluride (CsTe) photocathode, two microchannel plates, a phosphor-coated aluminum screen, and a fiber optic output window.

UV photons at the exit focal plane of the spectrograph strike the CsTe photocathode which causes photoelectrons to be produced. The electrons are then accelerated to the first microchannel plate due to a 175 V applied voltage between the photocathode and the first microchannel plate. Electrons that enter the microchannel plate are accelerated through an electric field induced through a variable 400-2000 V applied voltage. This voltage produces an avalanche of electrons at the output of the plate. For each electron that enters the plate, approximately 300 exit. These electrons then enter the next microchannel plate and again, the electrons are multiplied. On the order of  $10^5$  electrons exit the second plate for each electron that enters the first plate. These electrons are accelerated into a phosphor-coated aluminum screen through an electric field induced by an approximately 6000 V applied voltage between the microchannel plate and the aluminum screen. As electrons strike the phosphor-coated screen, visible photons are produced.

The ITT high-voltage power supply (model 200057) provides the high voltages across the intensifier with an input voltage of +5 V. An additional 0-10 V variable voltage input varies the voltage across the microchannel plates, thereby allowing adjustment of the gain of the ISAAC output. Technical data for this high-voltage power supply is included as Appendix B.

## **C. HAMAMATSU CCD IMAGE SENSOR**

The Hamamatsu S3904 MOS Linear Image Sensor is a linear array of 1024 photodiodes that offers a low dark current, low power consumption (less than 1 mW) and

high sensitivity. Technical data for this sensor is included as Appendix C. The spectral response of the sensor is shown in Figure 3 of Appendix C, which indicates that the photodiodes are sensitive to light in the wavelength range 2000-11000-Å. However, the greatest response is at approximately 6000-Å and for this reason the image intensifier includes a phosphor screen to convert ultraviolet to visible light.

### **1. Photodiodes**

The S3904 sensor consists of 1024 p-n junction photodiodes arranged in a linear array with spacing as depicted in Figure 2 of Appendix C. The photodiodes are 2.5 mm in height with a pitch of 25  $\mu\text{m}$ . They convert the optical energy of incident photons into electrical energy which is then stored in a capacitor as a charge. The photodiodes have a high sensitivity to visible photons and offer a low dark current. Dark current is the charge accumulated in the photodiodes in the absence of incident light and is a function of temperature.

### **2. Shift Register**

A shift register is used to successively send out the charge stored on each photodiode. Three clock pulses are used to operate this shift register:  $\phi_1$ ,  $\phi_2$ , and  $\phi_{st}$ .  $\phi_{st}$  is the input clock pulse to start operation of the shift register and the time interval between start pulses is equal to the signal accumulation time.  $\phi_1$  and  $\phi_2$  are the pulses used to operate the shift register. A photodiode signal is obtained at the rise of every  $\phi_2$  and so this clock pulse frequency determines the video data rate. A timing diagram for these clocks is included in Figure 5 of Appendix C. The C4350 Driver/Amplifier Circuit is used to provide these timing clocks.

### **3. C4350 Driver/Amplifier Circuit**

The Hamamatsu C4350 Driver/Amplifier Circuit provides the start pulse and two phase clock pulses used to drive the MOS linear image sensor and also provides a charge amplifier used to read out the video signal. The required inputs to the C4350 are a Master Start pulse, a Master Clock pulse, +5 V and  $\pm 15$  V. The start pulse initializes the circuit and the MOS shift register, while the clock pulse synchronizes the circuit and the MOS shift

register. The outputs from this board are Video Data, Sample-and-Hold, and End-of-Scan. The Video Data is the integrated, low-noise video signal of the MOS image sensor. Sample-and-Hold is a trigger that can be used for A/D conversion. End-of-Scan signals the end of the signal from the MOS shift register. A 15-pin male connector located on the side of the detector housing of ISAAC provides the interface to these signals. The pin functions for this connector are listed in Table 4-1. The C4350 Driver/Amplifier is a compact, circularly-shaped version of the C4070 Driver/Amplifier, though both circuits are functionally identical. Technical data for the C4070 Driver/Amplifier is provided as Appendix D and operating instructions are included as Appendix E. (Note that this circuit will be replaced by an equivalent circuit built at NRL prior to launch as the Hamamatsu circuit does not meet spaceflight qualifications).

PIN	INTERFACE FUNCTION	PIN	INTERFACE FUNCTION
1	N/C	9	AI Ground
2	N/C	10	Video Data
3	+15 V input	11	Digital Ground
4	-15 V input	12	N/C
5	+5 V input	13	Digital Ground
6	Master Start Clock	14	N/C
7	Master Clock (Bit Clock)	15	Sample and Hold (Trigger)
8	End of Scan		

**Table 4-1** Detector interface pinout.

#### **D. ISAAC STEPPER MOTOR AND DUST COVER**

##### **1. Stepper Motor**

A stepper motor is located on the outside of the ISAAC housing that encases the grating and optics. This motor drives a cam which has four circularly curved sections as

shown in Figure 4-5. A shaft between the grating and the track inside this cam rotates the grating. As the radius of the inner track of the cam increases, the movable grating rotates clockwise as viewed from above. The motor allows grating selection of one of four overlapping wavelength bands as follows:

grating position 1	1817-2290Å
grating position 2	2203-2656Å
grating position 3	2609-3026Å
grating position 4	2898-3290Å

The cam also has a small pinhole that allows detection of the initial position of the grating through use of a photodiode. This *fiducial* output signals the initial grating position. A cable ending in a 15-pin female I/O connector extends from the motor providing an interface between the motor and a stepper motor controller.

## **2. Dust Cover Door**

A mechanical dust cover door is located inside the entrance to the telescope. This door provides protection of the instrument's optics during launch, outgassing and also during ARGOS mission phases that will include experimental release of gases. This door is controlled with a solenoid. When power is applied to the solenoid, a pin disengages from the door allowing it to pull open by action of an attached spring mechanism. Upon cessation of the applied power, the solenoid then reinserts the pin into the door, locking it in the open position. The door can be mechanically reclosed, though not remotely.

The position of this dust cover door can also be remotely monitored through use of two micro switches located inside the telescope housing. Micro "X" provides continuity between the Normally Closed (NC) position and Common when the dust cover door is open, while Micro "Y" provides continuity between the Normally Open (NO) position and its Common. Similarly, when the dust cover door is closed, Micro "X" provides continuity between NO and Common while Micro "Y" provides continuity between NC and Common. Interface with these functions is possible through a 9-pin I/O connector at the end of a cable extending from the front of the telescope housing.

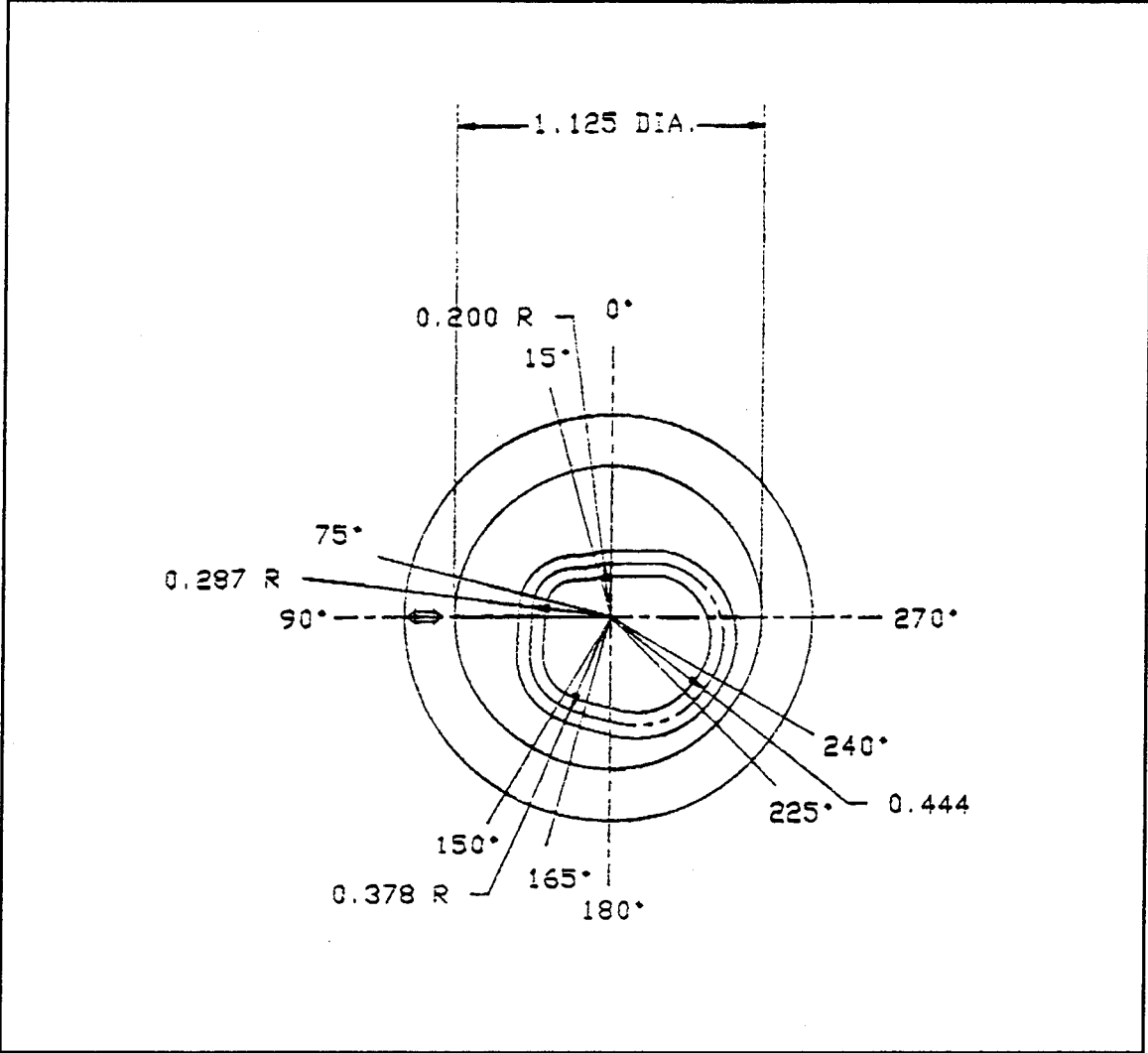


Figure 4-5 Stepper motor cam track.



### E. STEPPER MOTOR DRIVER

The RSI Model 480-229 Stepper Motor Driver provides an interface between the spacecraft bus and the ISAAC stepper motor and dust cover door. It provides a means to control the grating stepper motor and telescope dust cover door. The stepper driver has three connector interfaces labeled J1, J2, and J3 as drawn in Figure 4-6. Additional technical data and an RSI test report for this controller is provided as Appendix F.

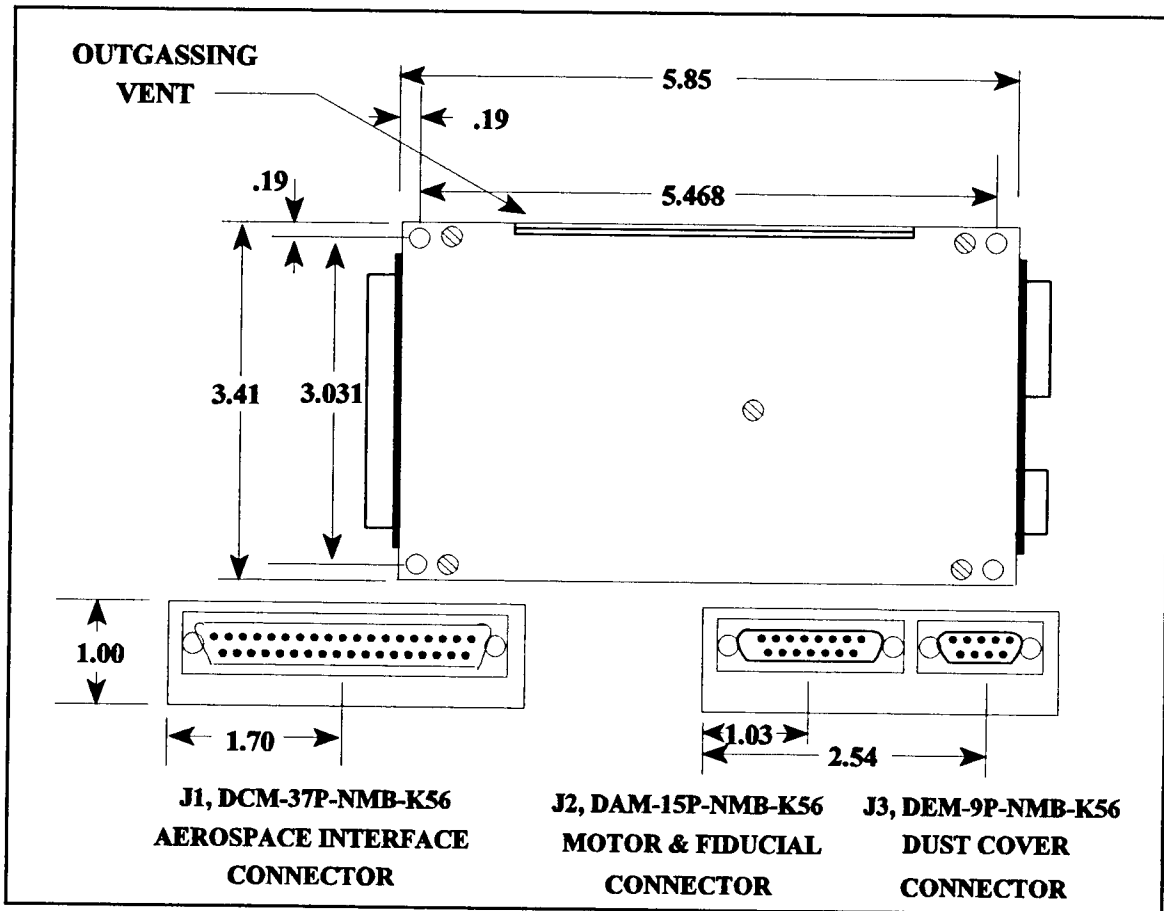


Figure 4-6 Stepper Motor Driver mechanical drawing.

## **1. J1 Interface**

J1 is a male 37-pin connector that supplies input and output connections to the spacecraft bus for external control and monitoring of the door position and stepper motor. It also allows selection of several power sources within the stepper motor driver: Primary Motor Power or Secondary Motor Power and Normal Motor Power or 3X Motor Power. One of these power sources is selected through an on-off application of 28 V to the appropriate J1 pin (29-32). Similarly, pins 33 and 34 provide the ability to select Run Motor Power or Hold Motor Power. Table 4-2 provides pinout functions for this connector.

### ***a. Motor Step***

The trailing edge of a TTL pulse applied to the Motor Step function (pin 6 of the J1 interface) causes the stepper driver to move the cam one discrete step. A complete turn of the cam is 1,998 steps. The circularly-curved sections of the cam provide a range of motor steps that correspond to a given grating position. Testing of the motor step function revealed the parameters for the lowest and highest step number for each of the four grating positions. These parameters are listed in Table 4-3 along with the median step number for each grating position. Step numbers are measured from the first fiducial signal as described in the next subsection. The stepper driver Motor Step function may be driven at frequencies up to 200 Hz (Berends, 1994).

### ***b. Fiducial Signal***

The Fiducial Signal (pin 8 of the J1 interface) provides a digital signal that indicates the position of the cam. A digital high-to-low on this line indicates that the cam has reached the initial or 'zero' position. This signal remains low for 30 steps of the cam and then remains high for the remaining 1,968 steps. The first digital low received will be referred to as the initial position.

PIN	J1 INTERFACE FUNCTION	PIN	J1 INTERFACE FUNCTION
1	+5 V	20	5 V Return
2	+5 V	21	5 V Return
3	+5 V	22	5 V Return
4	+5 V	23	5 V Return
5	Motor Step Repeat	24	Chassis Common
6	Motor Step	25	+28 V Motor
7	Current Monitor	26	28 V Motor Return
8	Fiducial Signal	27	Not Used
9	Not Used	28	Not Used
10	Not Used	29	Primary Motor Power
11	+28 V Solenoid Return	30	Secondary Motor Power
12	Micro "Y" NC (Cover Closed)	31	Normal Motor Power
13	+28 V Solenoid	32	3X Motor Power
14	Micro "Y" NO (Cover Closed)	33	Run Motor Power
15	Micro "Y" Common (Closed)	34	Hold Motor Power
16	Micro "X" NO (Cover Open)	35	N/C
17	Micro "X" Common (Open)	36	N/C
18	Micro "X" NC (Cover Open)	37	N/C
19	Fiducial Out(redundant w/pin 8)		

**Table 4-2** J1 interface pinout.

Grating Position	Start Step	End Step	Median
1	0	110	55
2	410	530	470
3	840	960	900
4	1240	1410	1345

**Table 4-3** Motor steps to select grating positions.

*c. Dust Cover Door Micro Switches*

The dust cover door micro switches are monitored through the stepper motor driver. Table 4-2 shows the pin functions that provide the ability to monitor the states of the Micro “X” and Micro “Y” switches discussed earlier in this chapter.

**2. J2 Interface**

J2 is a male 15-pin Motor and Fiducial connector that provides a link to the 15-pin output from the stepper motor on the ISAAC spectrograph. This connector provides stepper motor control timing signals and receives ISAAC stepper motor fiducial signals. Table 4-4 lists the J2 pinouts.

**3. J3 Interface**

J3 is male 9-pin connector that provides the link to the ISAAC dust cover door. The Micro “X” and Micro “Y” pins are used to read the position of the door. Application of 28V to pin 13 of J1 and thus pin 3 of J3 causes the dust cover door to open and lock in place. Table 4-5 lists the J3 pinouts.

PIN	J2 INTERFACE FUNCTION	PIN	J2 INTERFACE FUNCTION
1	Motor $\phi 1$	9	Motor CT
2	Motor $\phi 2$	10	Motor $\phi 3$
3	Motor $\phi 4$	11	Chassis Common
4	+5 V Fiducial LED Return	12	+5 V Fiducial Phototran. Ret.
5	+5 V Fiducial Power	13	N/C
6	Fiducial Signal	14	N/C
7	N/C	15	N/C
8	N/C		

**Table 4-4** J2 Motor & Fiducial interface pinout.

PIN	J3 INTERFACE FUNCTION	PIN	J3 INTERFACE FUNCTION
1	N/C	6	Micro "X" Common
2	Solenoid Return	7	Micro "Y" NO
3	+28 V Solenoid	8	Micro "Y" NC
4	Micro "X" NO	9	Micro "Y" Common
5	Micro "X" NC		

**Table 4-5** J3 Dust Cover interface pinout.

## V. GSE HARDWARE DESIGN

The ISAAC Ground Support Equipment (GSE) provides a means to test the operation of the spectrograph independent of the spacecraft bus at any time. It will also allow calibration of the instrument prior to integration with the HIRAAS and ultimately the ARGOS satellite. This chapter describes the design and development work performed as part of this thesis.

The GSE consists of a Macintosh Quadra 650 computer running National Instruments LabVIEW 2.2.1 software, with an installed National Instruments NB-MIO-16 I/O board and also an electronics interface box. The ISAAC GSE Electronics Interface Box, designed and built as part of this thesis, provides all necessary interfaces between the computer, high-voltage power supply, stepper-motor driver, and the ISAAC spectrograph. This interface box also contains the power supplies to provide all required voltages for operation of the detector, image intensifier and stepper motor. The advantage of this interface box is that it provides a portable means of testing the spectrograph at any time during the integration process. The GSE hardware and the ISAAC spectrograph are depicted in Figure 5-1. The overall GSE is represented in Figure 5-2, which shows how all components are connected. The following sections will discuss the NB-MIO-16 I/O board and the electronic interface box, while the software portion of the GSE will be discussed in the next chapter.

### A. NATIONAL INSTRUMENTS NB-MIO-16 I/O BOARD

The National Instruments NB-MIO-16 I/O board provides a means of generating timing clocks, receiving input data and performing analog-to-digital (A/D) conversions. The board's functions can be controlled and monitored by LabVIEW software. Components of the board include: sixteen 12-bit A/D converters, two 12-bit digital-to-analog (D/A) converters, eight lines of TTL-compatible digital I/O, and three 16-bit counter/timer channels for timing I/O. The pinouts for this device are listed in Table 5-1. The parts of the board that are used are discussed in the following sections, while software control of these elements is addressed in the next chapter.

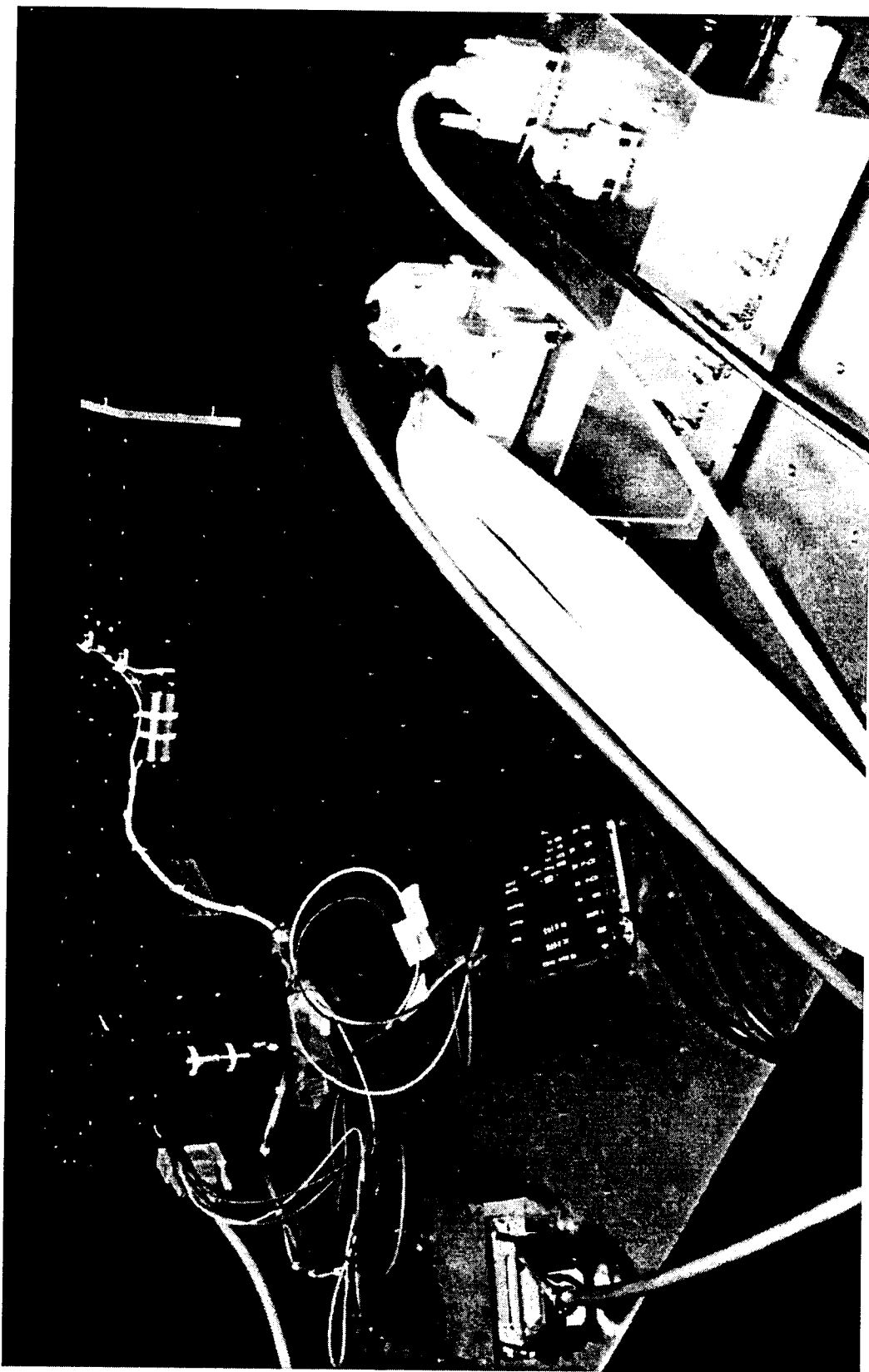


**Figure 5-1** The ISAAC Spectrograph connected to the GSE

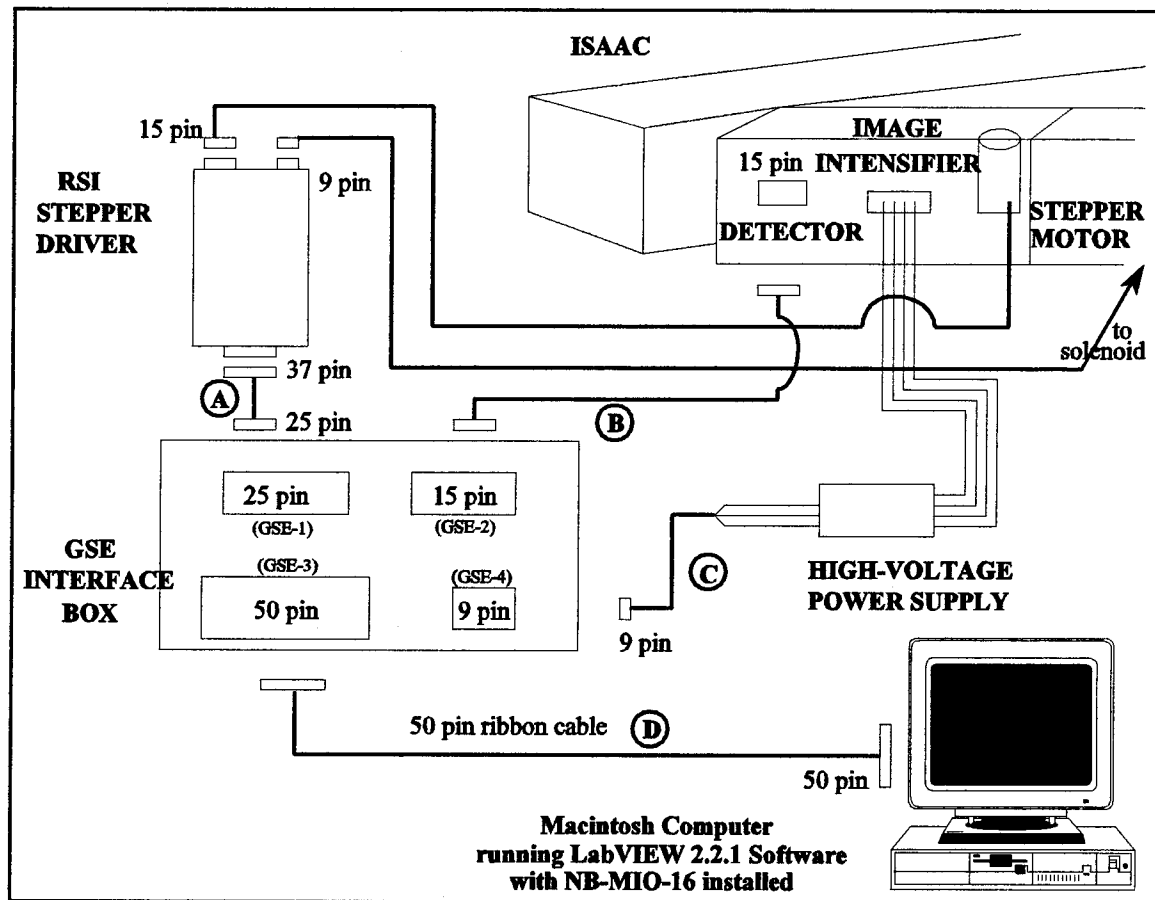


**Figure 5-2** ISAAC GSE hardware interface.



PIN	FUNCTION	PIN	FUNCTION
1	AI GND	26	BDIO0
2	AI GND	27	ADIO1
3	ACH0 (READ VIDEO)	28	BDIO1 (STEP MOTOR)
4	ACH8	29	ADIO2
5	ACH1	30	BDIO2
6	ACH9	31	ADIO3
7	ACH2	32	BDIO3 (TRIGGER)
8	ACH10	33	DIG GND
9	ACH3	34	+5 Volts
10	ACH11	35	+5 Volts
11	ACH4	36	SCANCLK
12	ACH12	37	EXTSTROBE*
13	ACH5	38	EXTTRIG*
14	ACH13	39	EXTGATE
15	ACH6	40	EXTCONV*
16	ACH14	41	SOURCE1
17	ACH7	42	GATE1
18	ACH15	43	OUT1 (START CLOCK)
19	AI SENSE	44	SOURCE2
20	DAC0 OUT	45	GATE2
21	DAC1 OUT	46	OUT2 (A/D TRIGGER)
22	EXTREF	47	SOURCE 5
23	AI GND	48	GATE5
24	DIG GND	49	OUT5 (BIT CLOCK)
25	ADIO0 (READ FIDUCIAL)	50	FOUT

**Table 5-1** NB-MIO-16 I/O Connector. (After NB-MIO-16 User Manual, 1989).

## 1. Clocks

General-purpose timing signals (or clocks) can be generated by the NB-MIO-16 I/O board through an AM9513 Counter/Timer chip. (Note: this chip was factory soldered onto the board, though was later replaced due to chip failure. It now has a holder soldered onto the board into which the chip is inserted to allow easy future replacement). This chip provides three gated counters: Counters 1, 2, and 5, and also the FOUT timer. The FOUT timer cannot be gated and so was not used. The frequencies of each of these clocks and the periods of the "on" pulses are selectable through the LabVIEW software.

### *a. Counter 1*

Counter 1 is used to generate the Master Start Pulse (or Start Clock) required by the Hamamatsu C4350 Driver/Amplifier to initialize the driver/amplifier circuit and the MOS shift register. The circuit and shift register are initialized on the trailing edge of a digital high pulse. The output of Counter 1 is at pin 43 of the NB-MIO-16 I/O connector and the gate used to initialize the counter is at pin 42.

### *b. Counter 2*

Counter 2 is used to provide an A/D trigger and is wired directly back to the NB-MIO-16 board's EXTTRIG\*. This function will be discussed further below in the section describing the A/D conversions. The output of this counter is at pin 46 and the gate is at pin 45.

### *c. Counter 5*

Counter 5 is used to generate the Master Clock (or Bit Clock) used by the Hamamatsu C4350 Driver/Amplifier circuit to synchronize the circuit and MOS shift register. The frequency of this clock determines the video data rate. This frequency is selectable using the ISAAC GSE software, though it is currently set at 100 kHz. The output for this counter is at pin 49 and the gate is at pin 48.

## 2. Video Data and Clock Timing

Pins 1 through 19 of the NB-MIO-16 board are dedicated to analog input. The only analog input used for the ISAAC GSE is the video signal input from pin 10 of the detector interface. This analog signal consists of a sequence of voltages that correspond to the intensity received at each of the 1024 pixels of the linear image sensor. A video *Word* is the term used to refer to an analog pulse of the video signal. The C4350 shift register begins sending video Words for each of the 1024 photodiodes in sequential order on the trailing edge of a TTL pulse to the Master Start Clock. The period between successive video Words is equal to the period of six oscillations of the Master Clock (six Bits per Word). The pulse width of one video Word is equal to the period of two Master Clock periods.

The Master Start Clock should have a period equal to the period of 1024 words and should have a pulse width equal to one period of the Master Clock. Therefore, there will be 1024 Words per Start and 6144 Bits per Start. These timing signals are shown in Figure 5-2.

## 3. A/D Conversions

In order to convert the analog video data signal to digital data, an A/D conversion is performed on the NB-MIO-16 board. The conversions must be synchronized so as to ensure that they occur during a video Word. This is accomplished through generation of an A/D Trigger output using Counter 2 of the AM9513 chip onboard the NB-MIO-16. To initiate the data acquisition operation, an active low pulse must be sent to EXTTRIG\* (pin 38) of the NB-MIO-16 I/O connector. Once the trigger is applied, Counter 3 generates pulses initiating A/D conversions once every sample interval until the sample counter reaches zero. These settings are applied using the LabVIEW GSE software discussed in the next chapter. The timing diagram shown in Figure 5-2 also shows the A/D Trigger pulse.

BDIO3 is used to trigger all three Counter/Timers simultaneously, causing the Master Start Clock, Master Clock, and A/D Trigger to all begin in unison as shown in Figure 5-3. The pulse width of the A/D Trigger is set such that the trailing edge of the pulse falls directly on the middle of the first video Word as also seen in this figure.

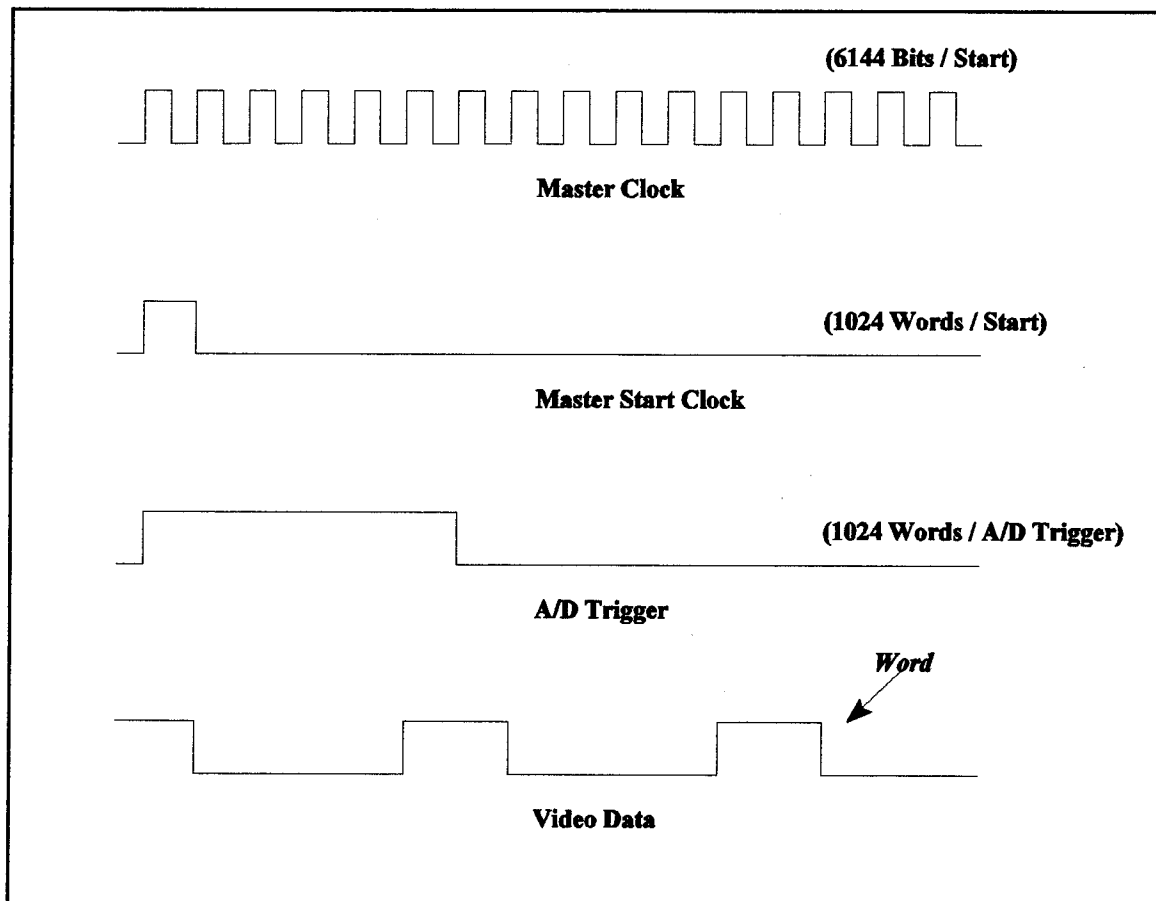


**Figure 5-3** Timing diagram for Master Clock, Master Start Clock, A/D Trigger, and Video Data. The period of the Master Clock is 10  $\mu\text{sec}$  and the period between successive video words is 60  $\mu\text{sec}$ . The Start Clock and A/D Trigger pulse every 61.44 msec (1024 x 60  $\mu\text{sec}$ ).

## 4. Digital I/O

### *a. Digital I/O Ports and Technical Specifications*

Pins 24 through 32 of the I/O connector are digital I/O signal pins and are TTL compatible. Pins 25, 27, 29, and 31 are connected to digital lines ADIO for digital I/O port A. Pins 26, 28, 30, and 32 are connected to the digital lines BDIO for digital I/O port B. Pin 24 is the digital ground pin, DIG GND, for both digital I/O ports. Technical specifications for these digital I/O lines are provided below (NB-MIO-16 User's Manual, p 2-22):

- Absolute Maximum Voltage Input Rating 5.5 V with respect to DIG GND

Digital Input Specifications (referenced to DIG GND):

- $V_{IH}$  input logic high voltage: 2 V minimum
- $V_{IL}$  input logic low voltage: 0.8 V maximum
- $I_{IH}$  input current load, logic high input voltage: 40  $\mu$ A maximum
- $I_{IL}$  input current load, logic low input voltage: -120  $\mu$ A maximum

Digital Output Specifications (referenced to DIG GND):

- $V_{OH}$  output logic high voltage: 2.4 V minimum
- $V_{OL}$  output logic low voltage: 0.5 V maximum
- $I_{OH}$  output source current, logic high: 2.6 mA maximum
- $I_{OL}$  output sink current, logic low: 24 mA maximum

With these specifications, each digital output line is capable of driving 11 standard TTL loads and 50 LS TTL loads.

### *b. Configuration of Digital I/O Ports for ISAAC GSE*

Digital ports must be specified in software as either input ports or output ports. Therefore, if port A is specified as an input port, then ADIO0, ADIO1, ADIO2, and ADIO3 must all become input lines. For the ISAAC GSE, Port A is configured as an input port and port B is an output port.

ADIO0 is an input line used to read the Fiducial Signal output (pin 8) of the Stepper Driver J1 interface. A digital high on this line indicates that the stepper driver cam is at the 'zero' position. The fiducial output continues to send a digital high for the next 29 steps of the cam beyond the 'zero' point. It then remains low until the cam has returned to the 'zero' position again.

BDIO1 is used as an output line to send pulses to the stepper driver Motor Step function (pin 6) of the Stepper Driver J1 interface. A digital high-to-low in this line causes the stepper driver to move the cam one discrete step. As discussed in the previous chapter, a complete turn of the cam is 1,998 steps. Table 4-2 in the previous chapter provides the number of steps required to reach each grating position.

BDIO3 is used to provide a trigger signal to the three Counter/Timers on the AM9513 chip. Each of these timers has a gate that allows synchronization of the timers. Each timer is initialized upon application of a digital high to its gate. Therefore, in order to start all clocks synchronized together, BDIO3 is used to simultaneously send a trigger to each of these gates (pins 42, 45, and 48).

### *c. Method to Increase Available Output Ports*

In its current configuration, the ISAAC GSE does not provide the capability to operate the dust cover door, nor does it allow direct selection of the stepper driver power source (Primary vs. Secondary, Normal vs. 3X, and Run vs. Hold). Modifications to the GSE may be desired at a future date to allow direct selection of these functions. In order to implement such options, more than the available four digital output lines would be required. In the current configuration, two of the four output lines are already in use, as can be seen in Table 5-1.

A simple method to add additional output lines is shown in Figure 5-4. This is an implementation of a demultiplexer using eight TTL AND gates and twelve TTL Inverters. In this configuration BDIO0, BDIO1, and BDIO2 would be used to select one of eight output lines as needed and BDIO3 would provide the digital high or low to that particular line. Line selection ( $G_0$  through  $G_7$ ) using BDIO0-BDIO2 is as shown in Table 5-2.

Note that this configuration is not currently implemented in the ISAAC GSE and is only presented for future modification of the GSE hardware. The preceding subsection describes the current configuration.

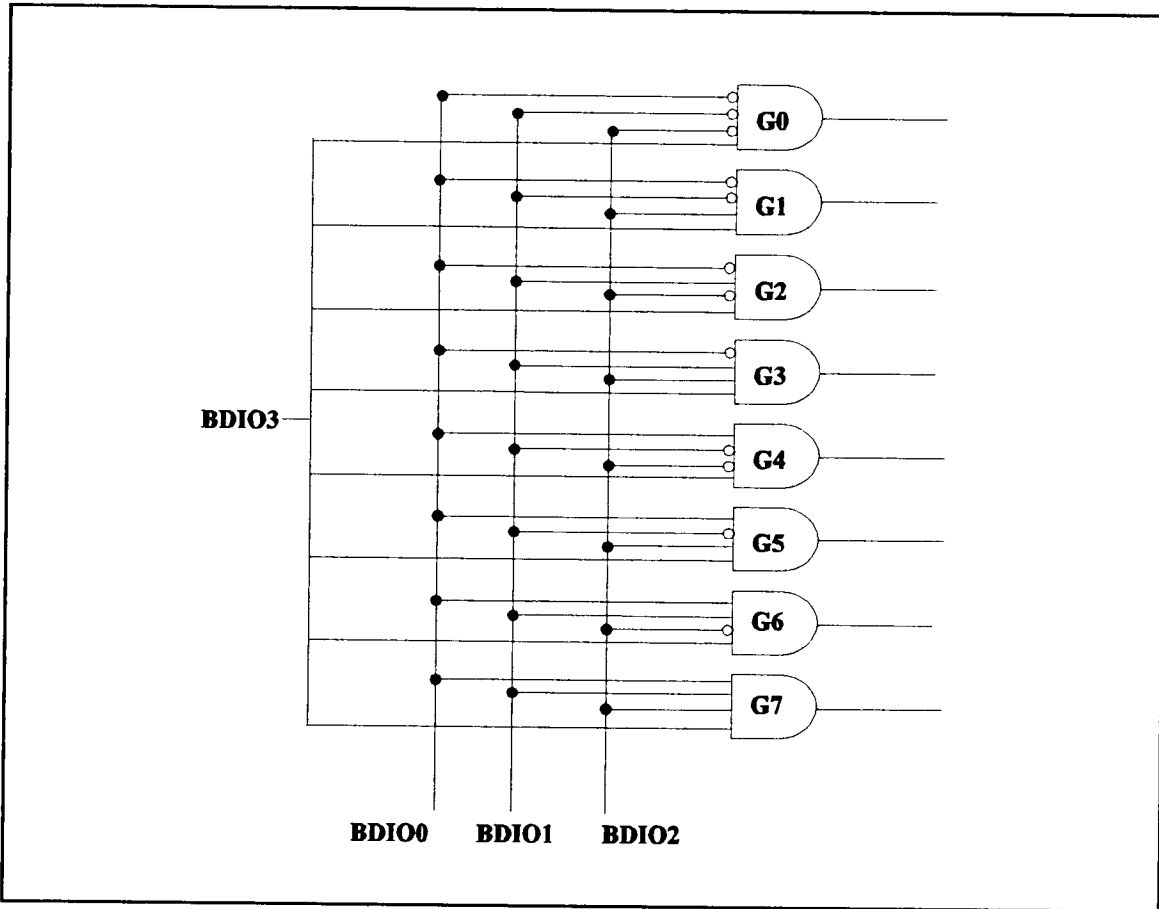


Figure 5-4 Demultiplexer that could be implemented to create additional output lines.

BDIO0	BDIO1	BDIO2	Output Line
0	0	0	G <sub>0</sub>
0	0	1	G <sub>1</sub>
0	1	0	G <sub>2</sub>
0	1	1	G <sub>3</sub>
1	0	0	G <sub>4</sub>
1	0	1	G <sub>5</sub>
1	1	0	G <sub>6</sub>
1	1	1	G <sub>7</sub>

**Table 5-2** Selections of BDIO0 through BDIO2 to create eight output lines as shown in Figure 5-4.

## B. ISAAC ELECTRONICS INTERFACE BOX

The ISAAC GSE Electronic Interface Box provides +5 V, ±15 V, variable 0 to +10 V, and +28 V to the various ISAAC components and to the stepper driver. It also provides all interfaces between the NB-MIO-16 board, the stepper-driver motor, the image intensifier, and the ISAAC detector. It allows direct monitoring of ISAAC detector video output, the stepper-driver Current Monitor and the Bit Clock and Start Clock used to initialize and drive the shift register in the detector circuit. A diagram of the interface box external connections is shown as Figure 5-5.

### 1. Power Supply

Power is generated using the circuit shown at the top of Figure 5-6. This circuit also transforms 120 V AC to ±34 V DC. Voltage regulators, shown at the bottom of Figure 5-6, are then used to provide the various required voltages. The LM340T5 is used to regulate



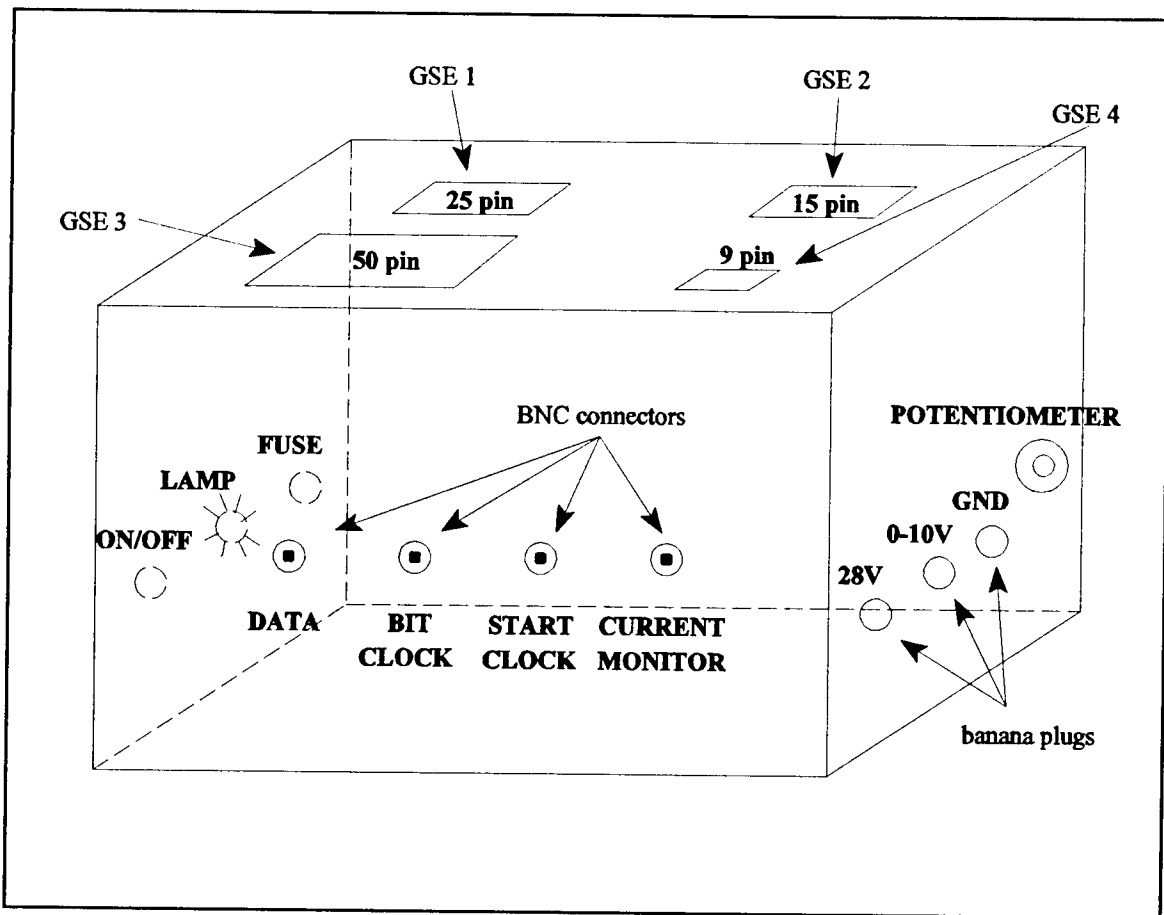


**Figure 5-5** ISAAC GSE Electronics Interface Box.

+34 V to +5 V; the 7815CT is used to regulate +34 V to +15 V; the 7915CT regulates -34 V to -15 V, and two LM317MP regulators provide +28 V and also a variable 0 to +10 V. This variable voltage, which is required for controlling the gain of the ITT image intensifier, is selectable through using a 1 k $\Omega$  potentiometer located on the right side of the interface box. As also shown in Figure 5-5, banana plugs on the right side of the interface box provide a means of monitoring the variable voltage with a voltmeter. The +28 V is also coupled to a banana plug to allow adjustment as it is regulated through use of a variable 5 k $\Omega$  resistor.

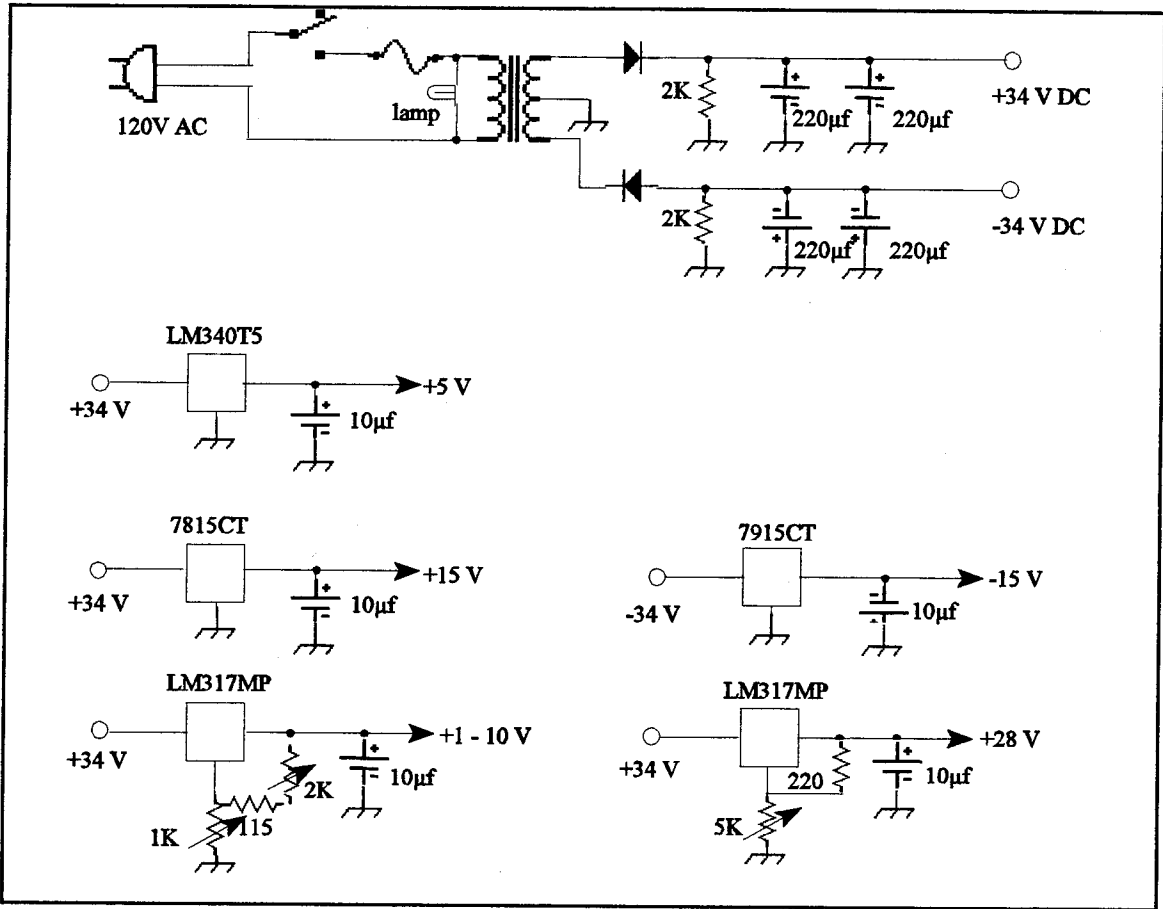


Figure 5-6 AC/DC converter and voltage regulators schematic for GSE power supply.

## **2. Front Panel Output Connections**

In addition to the banana plug connections on the side of the box to monitor voltages, there are four BNC output connectors on the front panel of the Electronic Interface Box as shown in Figure 5-5. These connectors allow direct external monitoring of the Video Data, Master Clock, Master Start Clock and the Current Monitor with a multimeter or oscilloscope.

## **3. I/O Connectors and Internal Wiring**

The I/O connectors atop the ISAAC GSE Electronic Interface Box are named for ease of reference GSE-1 through GSE-4 as indicated in Figures 5-2 and 5-5. GSE-1 is a 25-pin male I/O connector that is directly connected to the 37-pin male connector (J1) on the RSI Stepper Driver using cable A. GSE-2 is a 15-pin female connector that is connected to the ISAAC detector 15-pin connector via cable B. GSE-3 is a 50-pin male connector that provides the interface to the Macintosh computer through connection to the NB-MIO-16 I/O connector via a ribbon cable (cable D). GSE-4 is a 9-pin male I/O connector that is connected to the high-voltage power supply with cable C. The pin functions for each of these I/O connectors and also the wiring connections made from these pins inside the interface box are listed in Tables 5-3 through 5-6.

Four cables are required to interconnect all elements of the GSE. Cable A is a 25-lead cable that provides connection between a 25-pin female I/O connector and a 37-pin female connector to connect the RSI Stepper-Driver (J1) to the GSE connector (GSE-1). The connection between pins for cable A is as shown in Table 5-7. Cable B is an off-the-shelf 15-lead cable with 15-pin male and female I/O connectors to provide connection between the detector output and the GSE (GSE-2). Cable C is a three-lead cable soldered to the three leads of the GBS High-Voltage Power Supply on one end and terminating in a 9-pin female I/O connector for connection to the GSE (GSE-4). Cable D is a 50-lead ribbon cable providing direct connection between the NB-MIO-16 I/O connector in the computer and the GSE connector (GSE-3).

PIN	FUNCTION	INTERCONNECTION
1	+5 V	GSE Power Supply +5 V
2	Motor Step	GSE-3 pin 26
3	Current Monitor	GSE Front BNC
4	Fiducial Signal	GSE-3 pin 25
5	+28 V Solenoid ret	N/C
6	Micro "Y" NC	N/C
7	+28 V Solenoid	N/C
8	Micro "Y" NO	N/C
9	Micro "Y" Common	N/C
10	Micro "X" NO	N/C
11	Micro "X" Common	N/C
12	Micro "X" NC	N/C
13	Fiducial Signal	N/C
14	+5 V Return	GSE Chassis
15	+28 V Motor	GSE Power Supply +28 V
16	28 V Motor Return	GSE Chassis
17	Primary Motor Power	N/C
18	Secondary Motor Power	N/C
19	Normal Motor Power	N/C
20	3X Motor Power	N/C
21	Run Motor Power	N/C
22	Hold Motor Power	N/C
23	Not Used	N/C
24	Not Used	N/C
25	Not Used	N/C

**Table 5-3** Pin functions and internal connections for GSE-1 I/O connector.

<b>PIN</b>	<b>FUNCTION</b>	<b>INTERCONNECTION</b>
1	N/C	N/C
2	N/C	N/C
3	+15 V	GSE Power Supply (+15 V)
4	-15 V	GSE Power Supply (-15 V)
5	+5 V	GSE-3 pin 34 (+5 V)
6	Master Start Clock	GSE-3 pin 43, GSE Front BNC
7	Master Clock	GSE-3 pin 49, GSE Front BNC
8	End of Scan	N/C
9	AI Ground	GSE Chassis, GSE-3 pin 1
10	Video Data	GSE-3 pin 3, GSE Front BNC
11	Digital Ground	N/C
12	N/C	N/C
13	Digital Ground	GSE-3 pin 33
14	N/C	N/C
15	Sample and Hold	N/C

**Table 5-4** Pin functions and internal connections for GSE-2 I/O connector.

PIN	FUNCTION	INTERCONNECTION
1	AI GND	GSE-2 pin 9
2	AI GND	GSE Chassis
3	ACH0 (Video Data)	GSE-2 pin 10
4	ACH8	N/C
5	ACH1	N/C
6	ACH9	N/C
7	ACH2	N/C
8	ACH10	N/C
9	ACH3	N/C
10	ACH11	N/C
11	ACH4	N/C
12	ACH12	N/C
13	ACH5	N/C
14	ACH13	N/C
15	ACH6	N/C
16	ACH14	N/C
17	ACH7	N/C
18	ACH15	N/C
19	AI SENSE	N/C
20	DAC0 OUT	N/C
21	DAC1 OUT	N/C
22	EXTREF	N/C
23	AO GND	N/C
24	DIG GND	N/C
25	ADIO0 (Fiducial)	GSE-1 pin 4

**Table 5-5** Pin functions and internal connections for GSE-3 I/O connector.

PIN	FUNCTION	INTERCONNECTION
26	BDIO0 (Stepper Motor)	GSE-1 pin 2
27	ADIO1	N/C
28	BDIO1	N/C
28	ADIO2	N/C
30	BDIO2	N/C
31	ADIO3	N/C
32	BDIO3 (Clocks Trigger)	GSE-3 pins 42, 45, and 48
33	DIG GND	GSE-2 pin 13
34	+5 Volts	GSE-2 pin 5
35	+5 Volts	N/C
36	SCANCLK	N/C
37	EXTSTROBE*	N/C
38	EXTTRIG*	GSE-3 pin 46
39	EXTGATE	N/C
40	EXTCONV*	N/C
41	SOURCE1	N/C
42	GATE1	GSE-3 pin 32
43	OUT1 (Master Start Clock)	GSE-2 pin 6
44	SOURCE2	N/C
45	GATE2	GSE-3 pin 32
46	OUT2 (A/D Trigger)	GSE-3 pin 38
47	SOURCE 5	N/C
48	GATE5	GSE-3 pin 32
49	OUT5 (Master Clock)	GSE-2 pin 7
50	FOUT	GSE-1 pin 4

**Table 5-5 (Cont.)** Pin functions and internal connections for GSE-3 I/O connector.

PIN	FUNCTION	INTERCONNECTION
1	+5 V	GSE Power Supply (+5 V)
2	N/C	N/C
3	+0 through 10 V Variable	GSE Power Supply (0-10 V)
4	N/C	N/C
5	AI GND	GSE Chassis
6	N/C	N/C
7	N/C	N/C
8	N/C	N/C
9	N/C	N/C

**Table 5-6** Pin functions and internal connections for GSE-4 I/O connector.



LEAD	37-pin CONNECTION	25-pin CONNECTION
1	1 (+5 V)	1
2	6 (Motor Step)	2
3	7 (Current Monitor)	3
4	8 (Fiducial Signal)	4
5	11 (+28 V Solenoid Return)	5
6	12 (Micro "Y" NC)	6
7	13 (+28 V Solenoid)	7
8	14 (Micro "Y" NO)	8
9	15 (Micro "Y" Common)	9
10	16 (Micro "X" NO)	10
11	17 (Micro "X" Common)	11
12	18 (Micro "X" NC)	12
13	19 (Fiducial Signal)	13
14	20 (+5 V Return)	14
15	25 (+28 V Motor)	15
16	26 (28 V Motor Return)	16
17	29 (Primary Motor Power)	17
18	30 (Secondary Motor Power)	18
19	31 (Normal Motor Power)	19
20	32 (3X Motor Power)	20
21	33 (Run Motor Power)	21
22	34 (Hold Motor Power)	22
23	N/C	N/C
24	N/C	N/C
25	N/C	N/C

**Table 5-7** Cable A 37-pin female to 25-pin female interconnections.

## VI. GSE SOFTWARE DESIGN

The ISAAC GSE includes a user-friendly software interface that provides the ability to control the mechanical components of the ISAAC spectrograph, acquire data from the ISAAC detector and display the data in a graphic screen. This program is written using LabVIEW 2.2.1 published by National Instruments.

LabVIEW programs are called *virtual instruments (VIs)* and have three main parts: the front panel, the block diagram and the icon/connector. The block diagram is a VI's source code which is written in a programming language called G. The front panel provides a user interface to a VI, while the icon is a representation of the VI. The connector provides the ports through which data passes from diagram to VI. VIs may be used as subroutines within other VIs and are then referred to as *sub-VIs*. (LabVIEW® 2.0 User Manual, 1993).

National Instruments also provides I/O boards that can be used for data acquisition and interface with electronic components. The National Instruments NB-MIO-16 Multifunction 12-Bit A/D Board is used as part of the ISAAC GSE as discussed in the preceding chapter. This board can be directly controlled through LabVIEW software in the LabDriver VI Library also published by National Instruments. This library of VIs supports operations such as analog and digital I/O, data acquisition and counter I/O on the NB-MIO-16 board. (See *LabVIEW 2 LabDriver® VI Library Reference Manual*).

Using these software tools, a GSE software VI was developed that provides the ability to select the grating position for the ISAAC spectrograph, acquire and view spectra, and save the obtained spectra as a vector of 1024 intensities in an ASCII file. The following sections provide the details of this VI and Appendix G provides a short user's manual for the operation of the interface program. The following descriptions assume the reader has some familiarity with LabVIEW programming. Specific details for selecting options of LabDriver Library VIs may be found in the LabDriver VI Library Reference Manual.

### A. ISAAC GSE SOFTWARE USER INTERFACE

The ISAAC GSE Front Panel, represented in Figure 6-1, provides the user interface to control the spectrograph and acquire data. This front panel displays the acquired spectrum

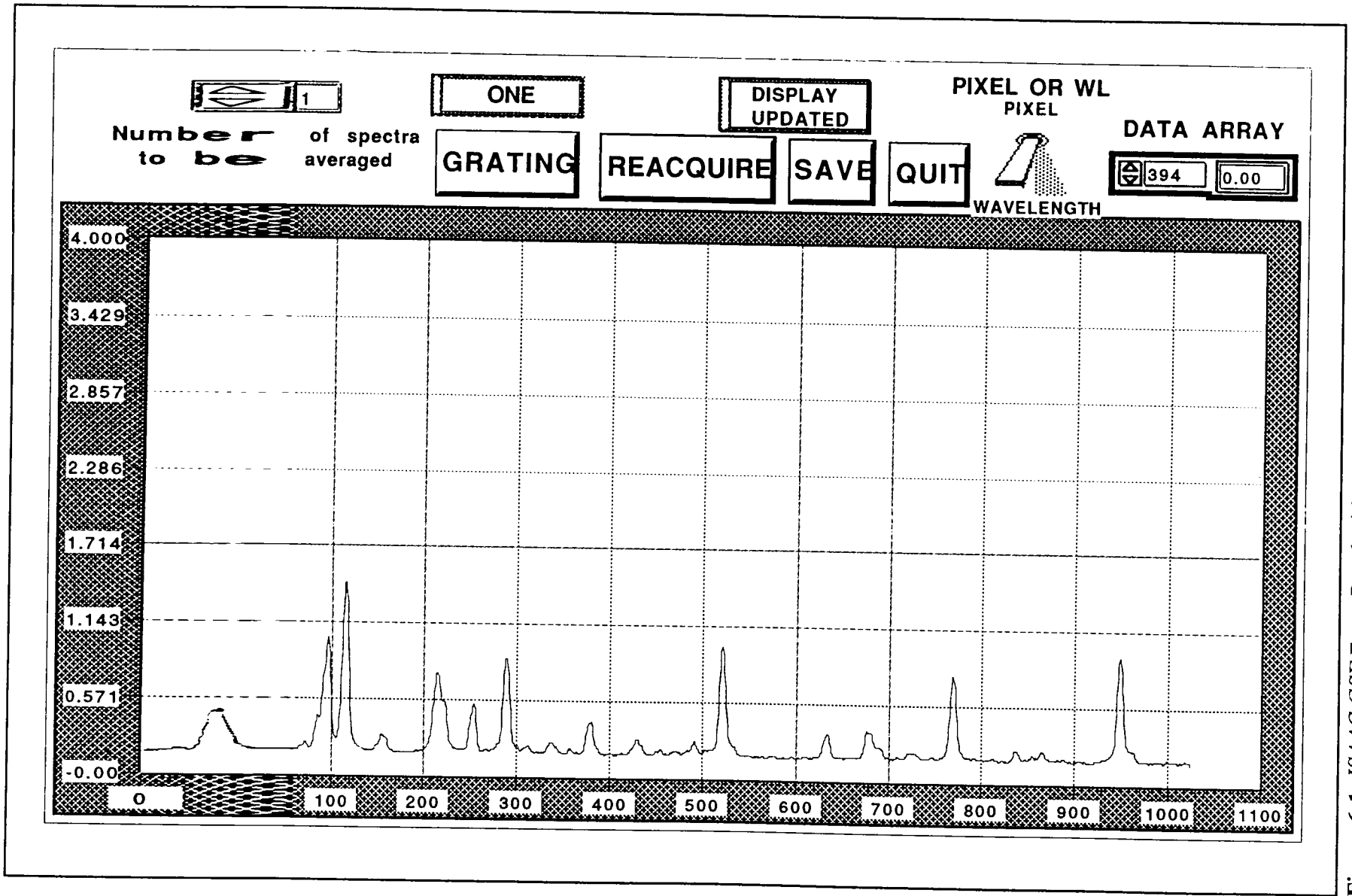


Figure 6-1 ISAAC GSE Front Panel with sample Pt-lamp spectrum.

in an *XY* plot of intensity versus wavelength or pixel number and provides user buttons that can be used to select program functions. The number of spectra to be acquired and averaged is selectable using the box in the upper left of the front panel. To the right of this function on the front panel is a button labeled **GRATING** which allows selection of the grating position of the spectrograph. Above this button is a display that shows the current grating position. The next button, **REACQUIRE**, is used to acquire a new spectrum and display it on the graph. The **SAVE** button can be selected after a spectrum has been acquired to save an array of 1024 intensities for the spectrum in an ASCII disk file. Above these last two buttons is a status display that describes the current status of the program as either: Acquiring Data, Display Updated, Adjusting Grating, or Saving Data. The **QUIT** button exits the program. A toggle switch, labeled **PIXEL or WL**, provides the ability to select the x-axis of the spectrum plot. In the up position, the spectrum intensities are plotted against the pixel number of the detector (0-1023), while the wavelength selection provides the approximate wavelengths for a given grating position along the x-axis. The **DATA ARRAY** function on the right of the screen is an array index display that allows the user to examine the intensity of the spectrum for a given pixel number. The pixel number is selected on the left of this box and the intensity is displayed immediately to its right.

## **B. THE ISAAC GSE PROGRAM**

The ISAAC GSE software interface VI consists of a hierarchy of many sub-VIs which are represented by their icons in Figure 6-2. Figure 6-3 shows the block diagram of the GSE program. This figure shows the graphical environment in which LabVIEW programs are written. Icons representing various functions are placed on the screen and connected with 'wires' to provide program steps. Sub-VIs are represented by their icons and placed within the block diagram to provide subroutine functions within the program.

Figure 6-3 shows that the GSE program begins with a sub-VI, *ISAAC INIT*, that provides routines to initialize the NB-MIO-16 board and to return the grating position to its initial position. The program then enters a *While Loop* that awaits the selection of one of the user buttons. On selection of one of these functions, a boolean TRUE value is sent to a *Build*

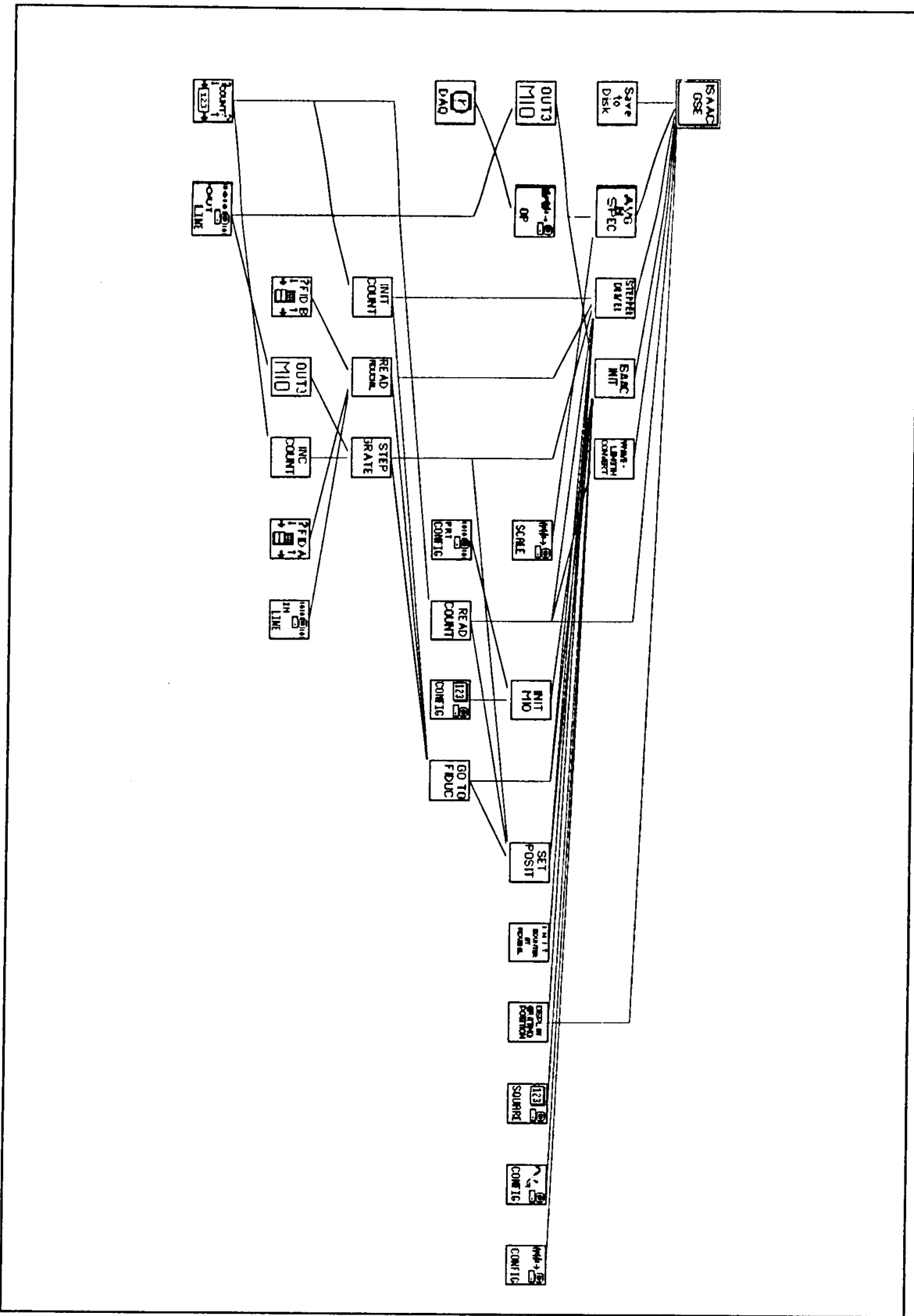


Figure 6-2 ISAAC GSE Sub-VI hierarchy.

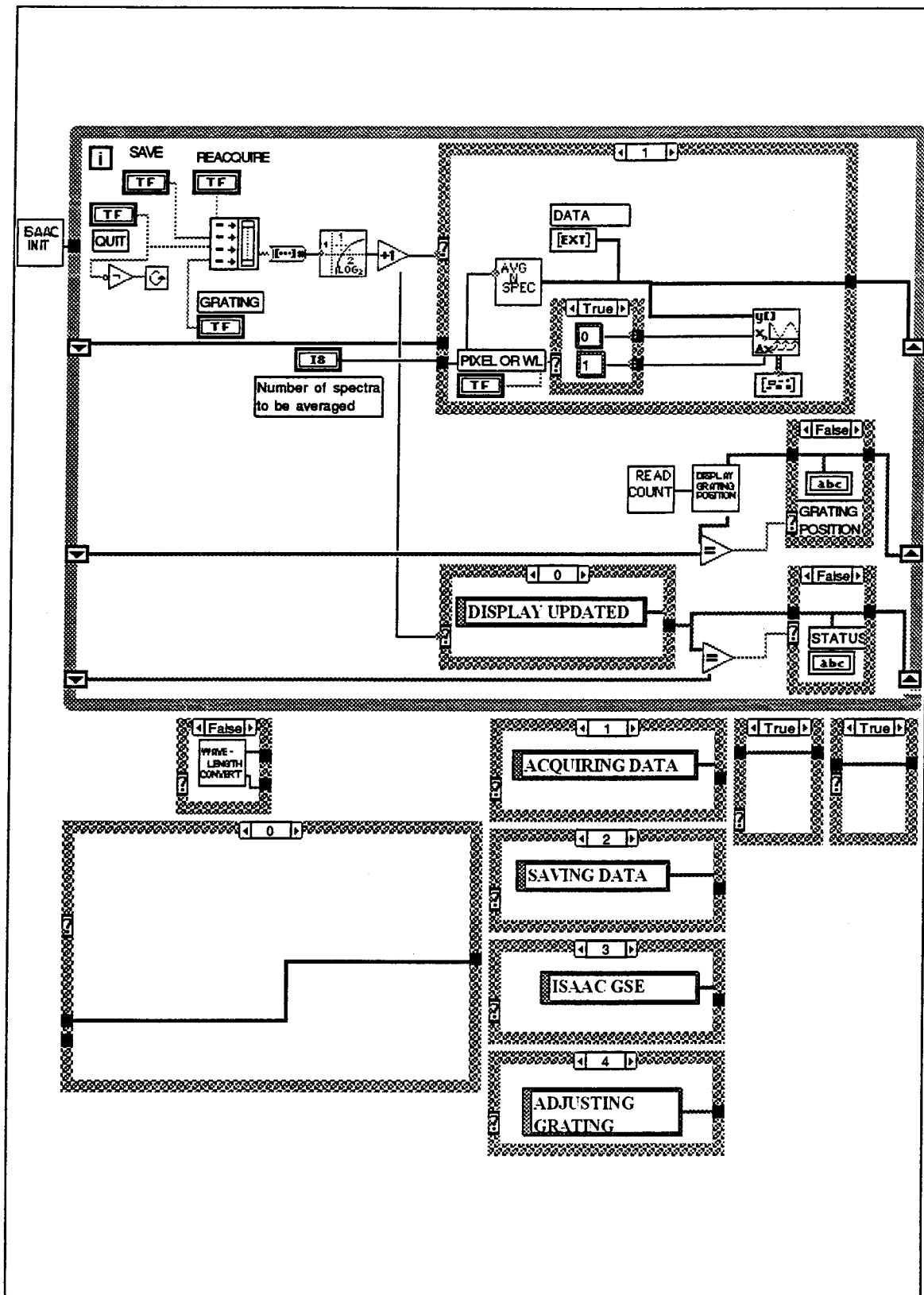


Figure 6-3 ISAAC GSE VI Block Diagram and additional cases of Case Structures.

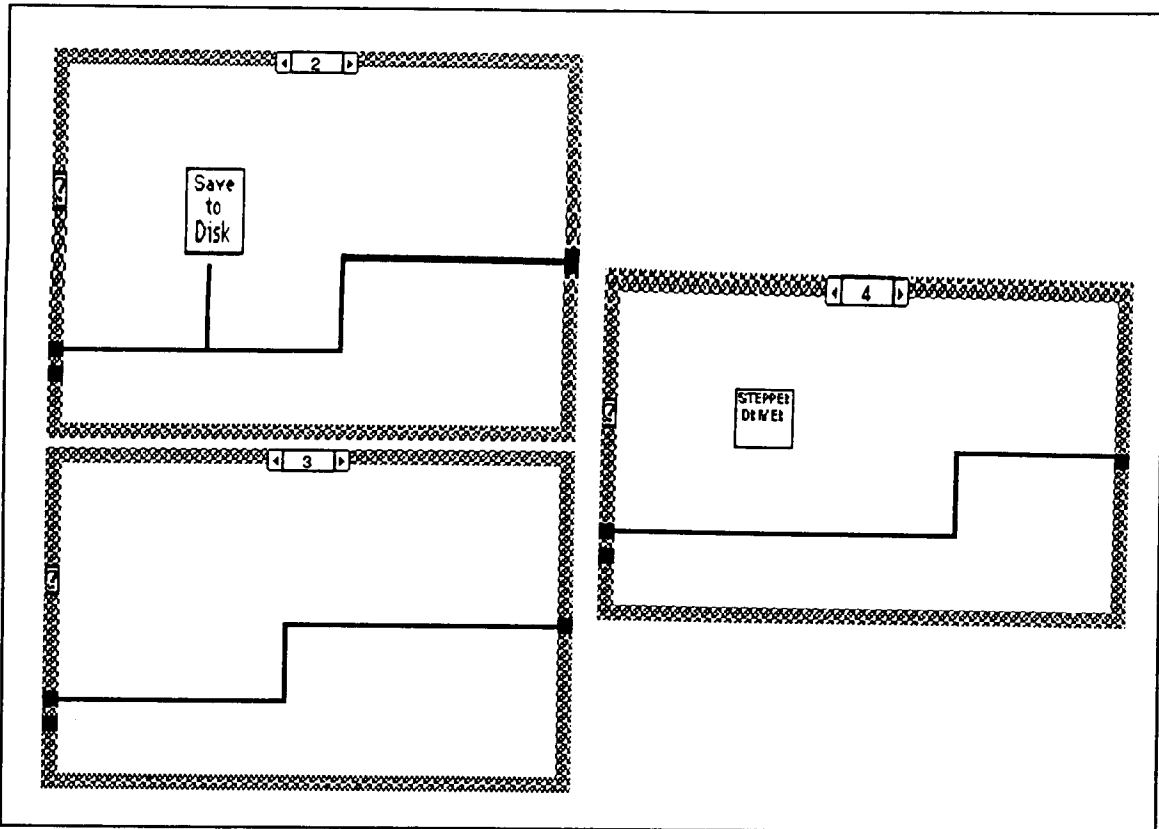


Figure 6-4 ISAAC GSE VI Block Diagram (continued).

*Array* function. This function creates an array of four boolean values. The array output is then wired to a *Boolean Array to Number* data type converter and this output is wired to a *Logarithm Base Two* function and then to an *Increment* function. These functions convert the boolean selections to sequential decimal numbers between one and four. The decimal output is then wired to the selector of the *Case Structure* shown in the upper right of Figure 6-3. This Case Structure will be referred to as the *Select-Program-Function* Case Structure. Each of the cases of this Case Structure performs the selected function.

Another Case Structure, at the bottom of the While Loop in Figure 6-3 shows the *Message-Display* Case Structure used to display the status of the program. Depending on the function the program is currently performing, this Case Structure causes one of the following messages to be displayed on the front panel: Display Updated, Acquiring Data, Saving Data, or Adjusting Grating. Above and to the right of this *Message-Display* Case Structure are two sub-VI's that in sequence first read the current position of the grating and then display the grating position. The Boolean Case Structures at the right of the While Loop

provide a means to prevent the message from flickering on the front panel. They provide that nothing is done if the message displayed would otherwise be unchanged. If the message is to change then and only then is it displayed. Figure 6-4 shows the additional Cases for the four Case Structures within the *ISAAC GSE VI*'s While Loop.

The following paragraphs address the contents of the *ISAAC INIT* sub-VI and each of the Select-Program-Function Cases of the upper Case Structure.

### 1. ISAAC Initialization Sub-VI

The *ISAAC INIT* sub-VI is used to initialize counters on the NB-MIO-16 board, to set the frequencies of these counters and to set the initial position of the spectrograph grating. The front panel for this sub-VI is shown as Figure 6-5. This front panel is not normally accessible to the user, but provides a means of changing the pulse widths of the Start Clock and the A/D Trigger and also to select the frequency of the Bit Clock. Displays on this panel include error codes for various functions of the NB-MIO-16 board. These error codes can be found in Appendix B of the *LabVIEW 2 LabDriver VI Reference Manual*. An error code of zero indicates that functions are operating normally.

The block diagram for this sub-VI is shown in Figures 6-6 through 6-11. This sub-VI consists of eleven *Sequence Structures* which are performed in numerical order (0-10). Sequence zero includes a LabDriver sub-VI, *AI\_Config*, that specifies the analog input parameters for the NB-MIO-16 board within the Macintosh computer. The sub-VI selects a unipolar input range of 0-10 V for analog input and checks for board errors.

Sequence 1 includes another sub-VI, *INIT MIO*, whose block diagram is shown in Figures 6-12 through 6-14. This sub-VI performs initialization of the three counters and configures the two ports of the NB-MIO-16. Port zero is chosen to be an input port, while port 1 is selected as an output port.

Sequence 2 clears the output of digital output line 3 (BDIO3) by setting the output to a digital logic low. This output line is later used as the trigger to start all clocks in unison.

Sequences 3 through 5 use the *CTR\_Square* LabDriver VI to set the three counters used in the GSE. The inputs to these VIs are selectable from the front panel of the *ISAAC*



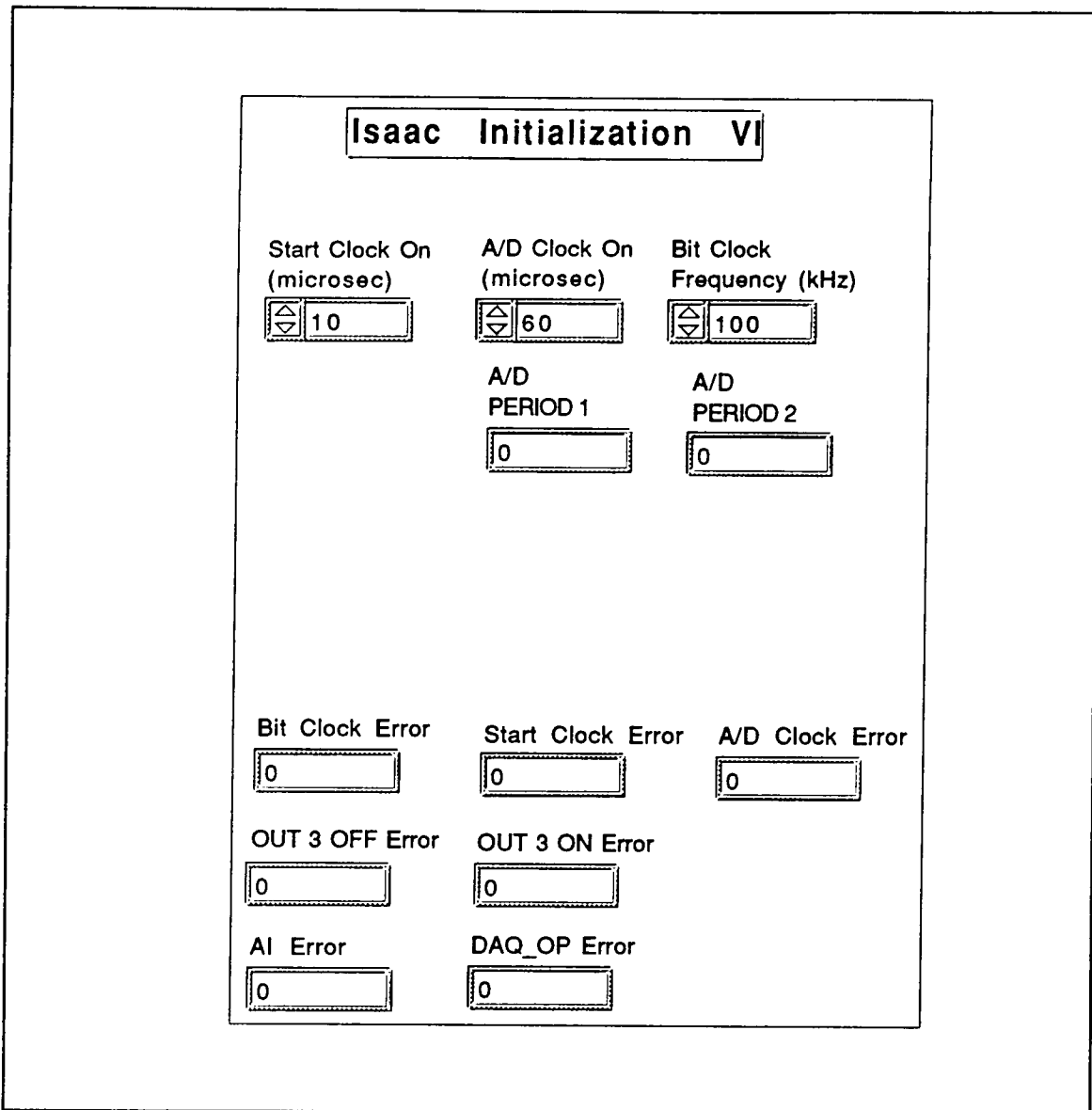


**Figure 6-5** ISAAC GSE *ISAAC INIT* sub-VI Front Panel.

*INIT* sub-VI. Counter 1 is set as the Start Clock, Counter 2 is programmed as the A/D Trigger, and Counter 5 is set as the Bit Clock. These sequences program the clocks by specifying the duration of the on-cycle and the off-cycle of the square wave. All three counters use the same timebase. The “1” selection for Timebase indicates that the internal 1-MHz clock is used as the timebase which provides a 1- $\mu$ sec resolution.

The next sequence, Sequence 6, causes the program to wait one second. Sequence 7 sends a digital logic high to BDIO3 to trigger the three clocks to begin in unison.

Sequence 8 configures the A/D Converter of the NB-MIO-16. The selected options specify that the conversion process will be controlled by an external trigger and that external gating is disabled. The last option specifies that timing is controlled by an onboard sample-interval clock to control data acquisition A/D conversions.

The next sequence, Sequence 9, causes the sub-VI, *GO TO FIDUC*, to be run. This sub-VI, shown in Figures 6-15 and 6-16, causes the grating position to be turned until the Fiducial Signal is received. It does this by reading the Fiducial Signal on ADIO0 within a While Loop. If the Fiducial Signal is a digital low (not at beginning of cam), then the sub-VI *STEP GRATE* sends a digital high and subsequent digital low to BDIO1. This causes the stepper motor to rotate the cam and thus turn the grating one step. It takes 1998 steps to turn the cam one full revolution. This While Loop continues until a digital high is first received at ADIO0 indicating that the cam and grating are at the initial position. A global counter is then set to zero to indicate the current grating position. Every future operation that causes the motor to step the grating position will also increment this counter. This provides a means of checking the current grating position at any time.

Sequence 10, the final sequence of this sub-VI, then uses a sub-VI, *SET POSIT*, to cause the stepper motor to turn the grating 55 more steps to set the grating at position ONE. The sub-VI *SET POSIT* sends an input number of paired digital high-low pulses to the stepper motor on BDIO1 and adjusts the global counter accordingly.

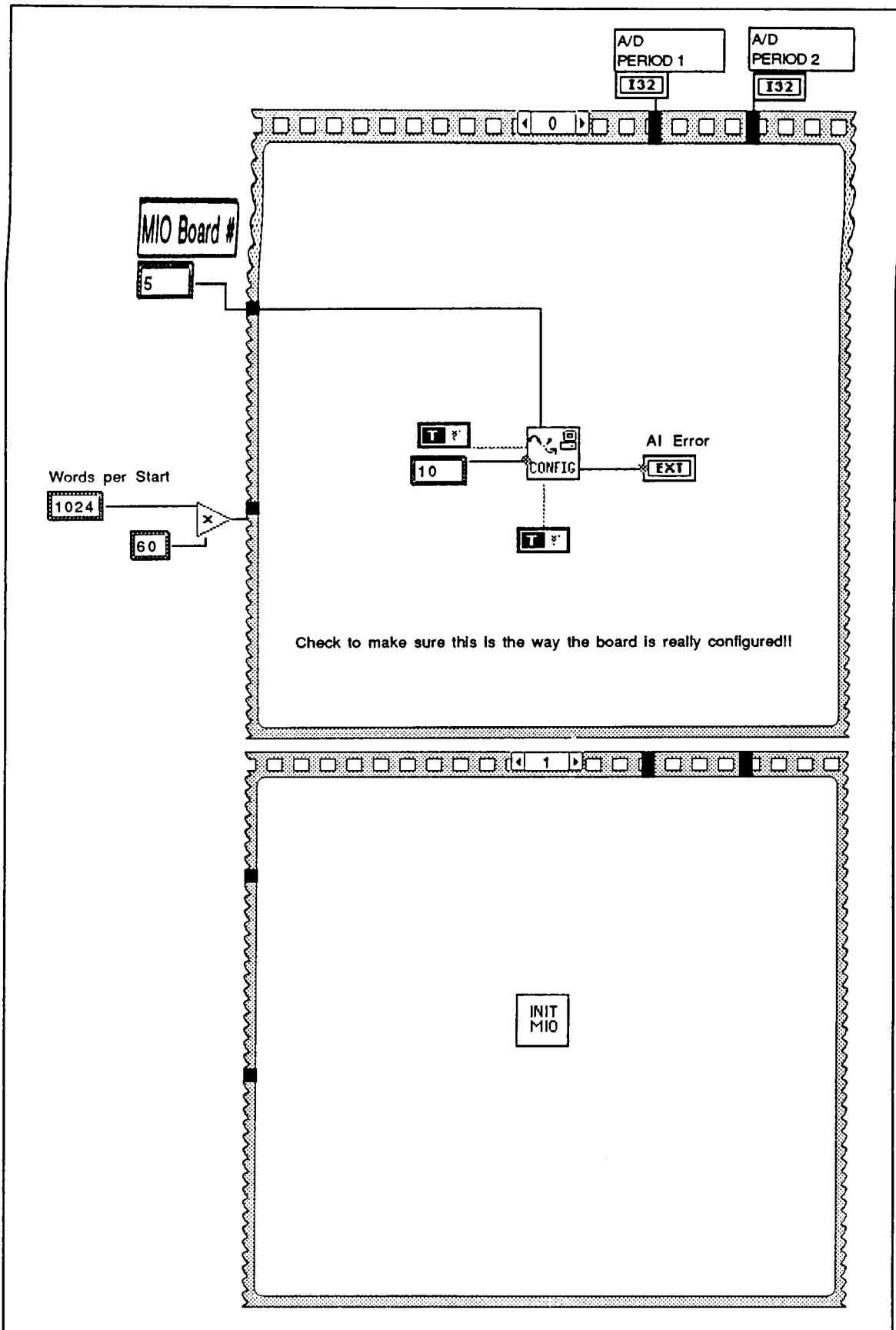


Figure 6-6 ISAAC GSE ISAAC INIT sub-VI Block Diagram.

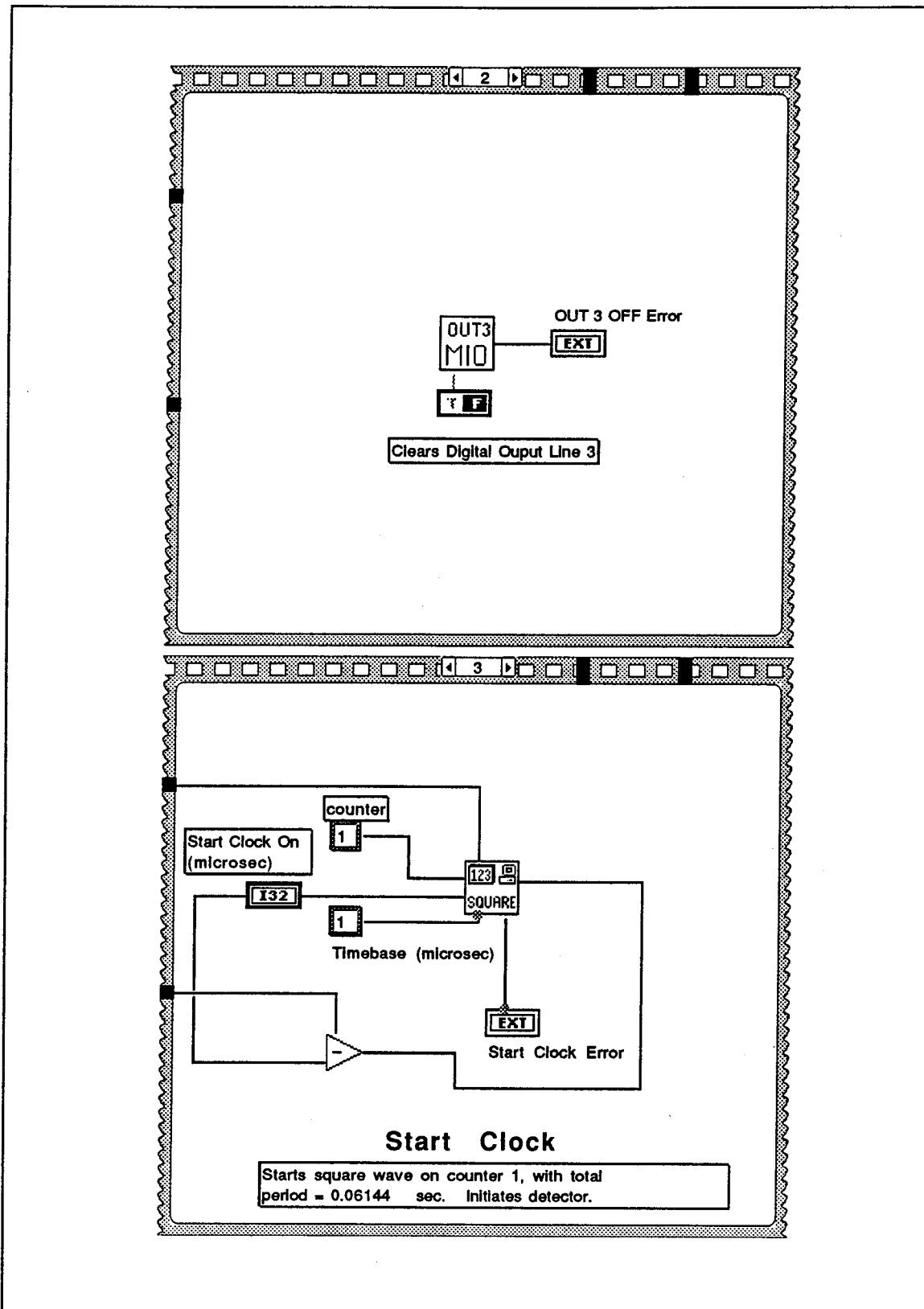


Figure 6-7 ISAAC GSE ISAAC INIT sub-VI Block Diagram (continued).

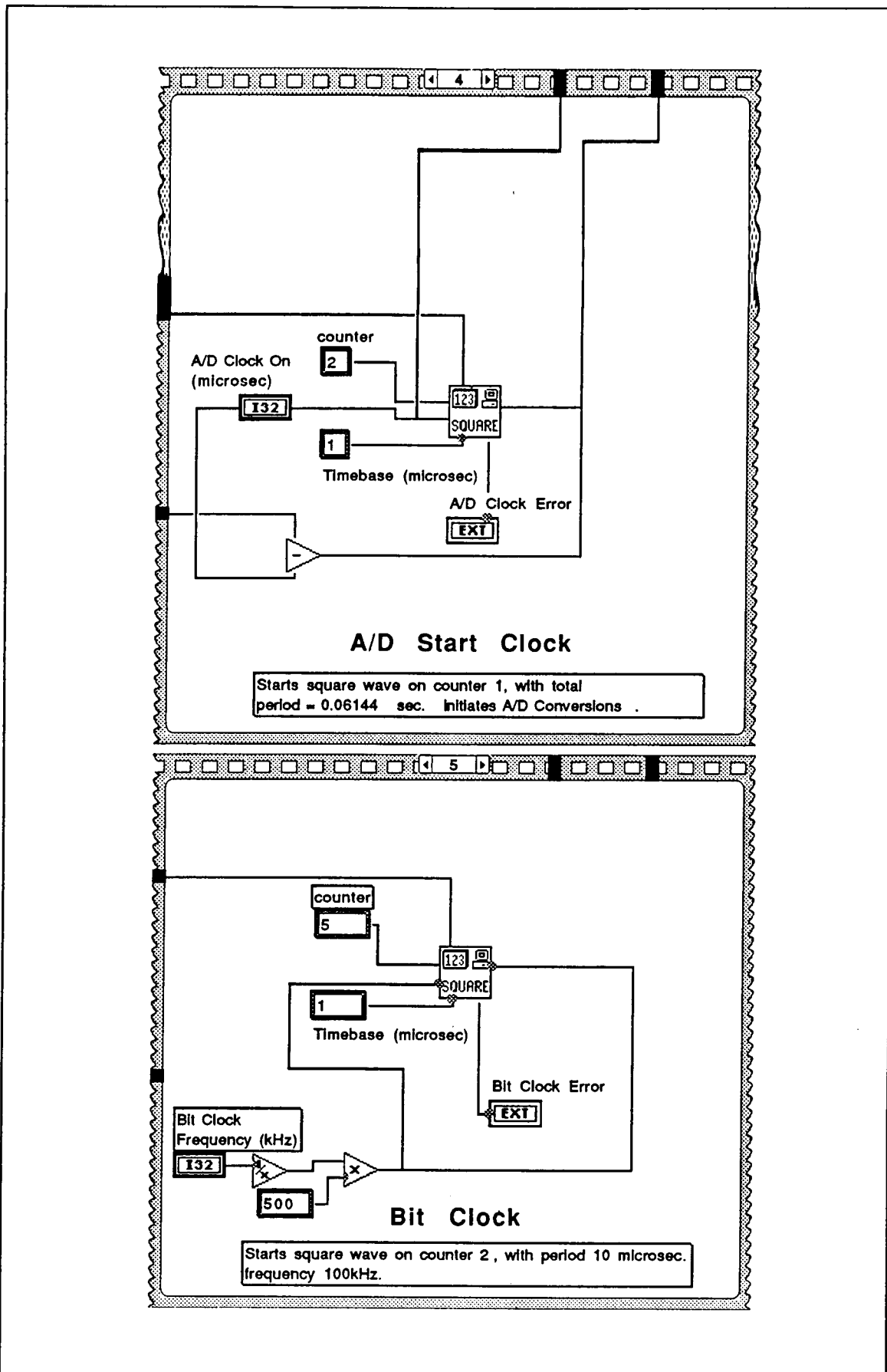


Figure 6-8 ISAAC GSE ISAAC INIT sub-VI Block Diagram (continued).

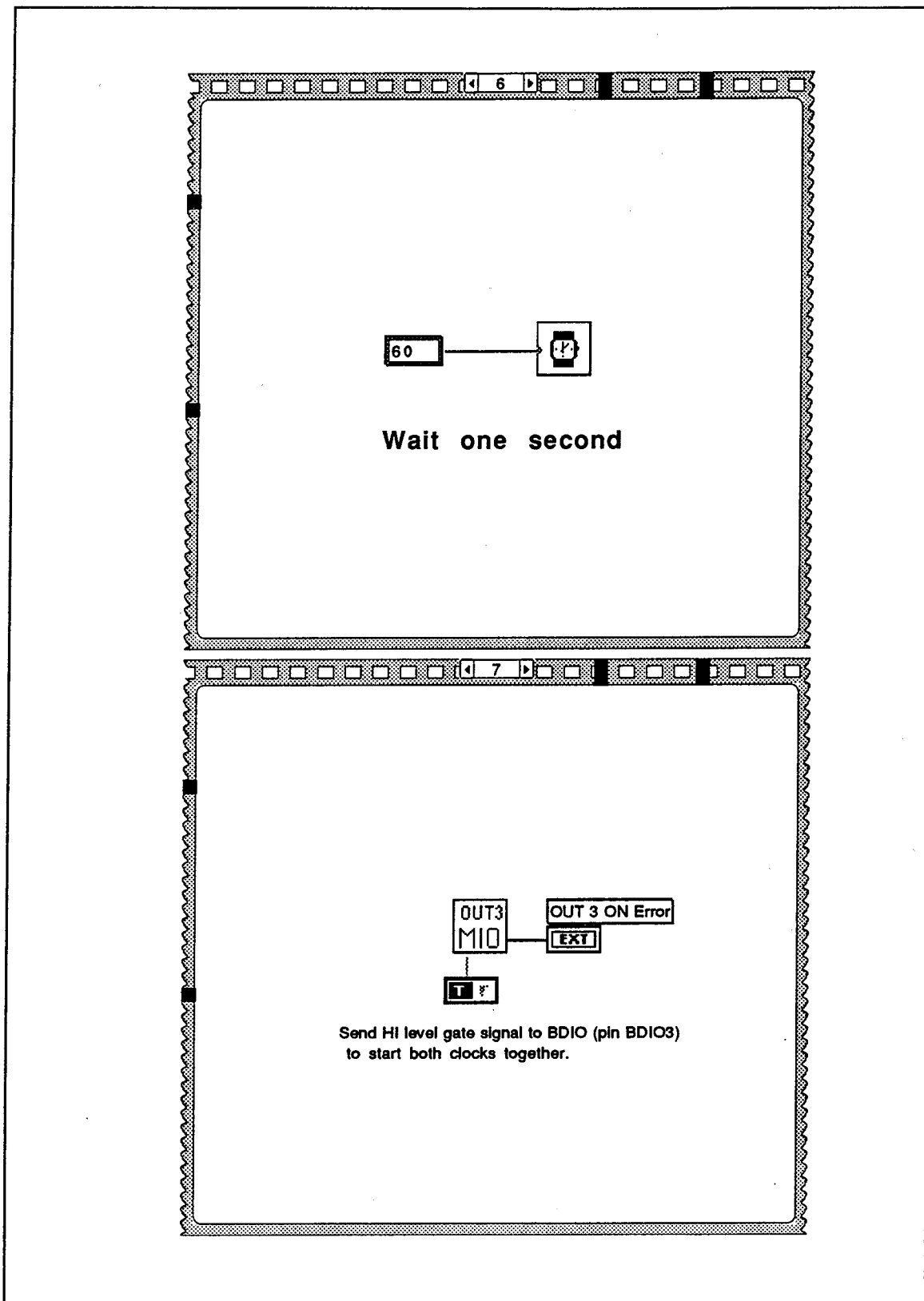


Figure 6-9 ISAAC GSE *ISAAC INIT* sub-VI Block Diagram (continued).

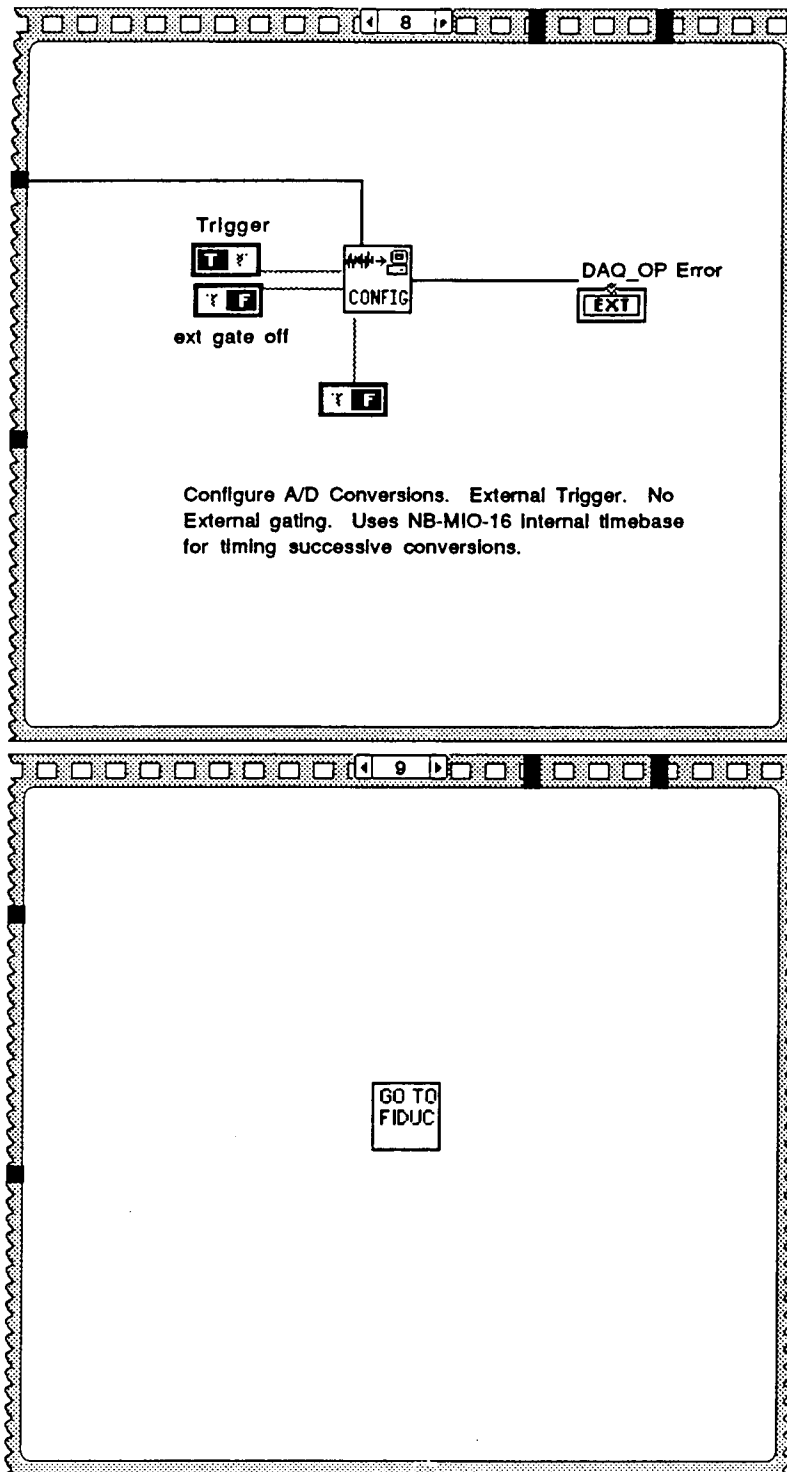


Figure 6-10 ISAAC GSE *ISAAC INIT* sub-VI Block Diagram (continued).

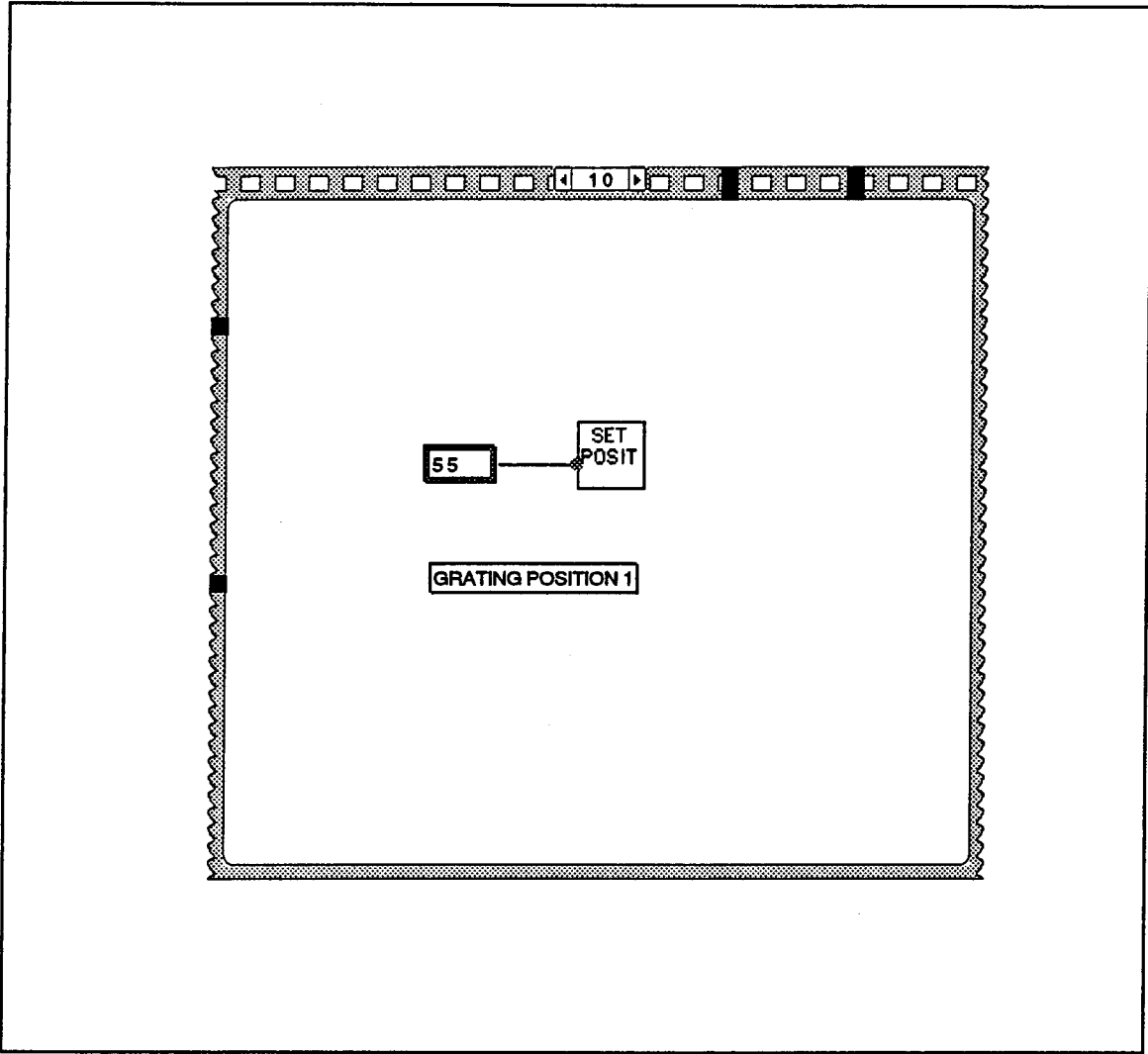


Figure 6-11 ISAAC GSE *ISAAC INIT* sub-VI Block Diagram (continued).



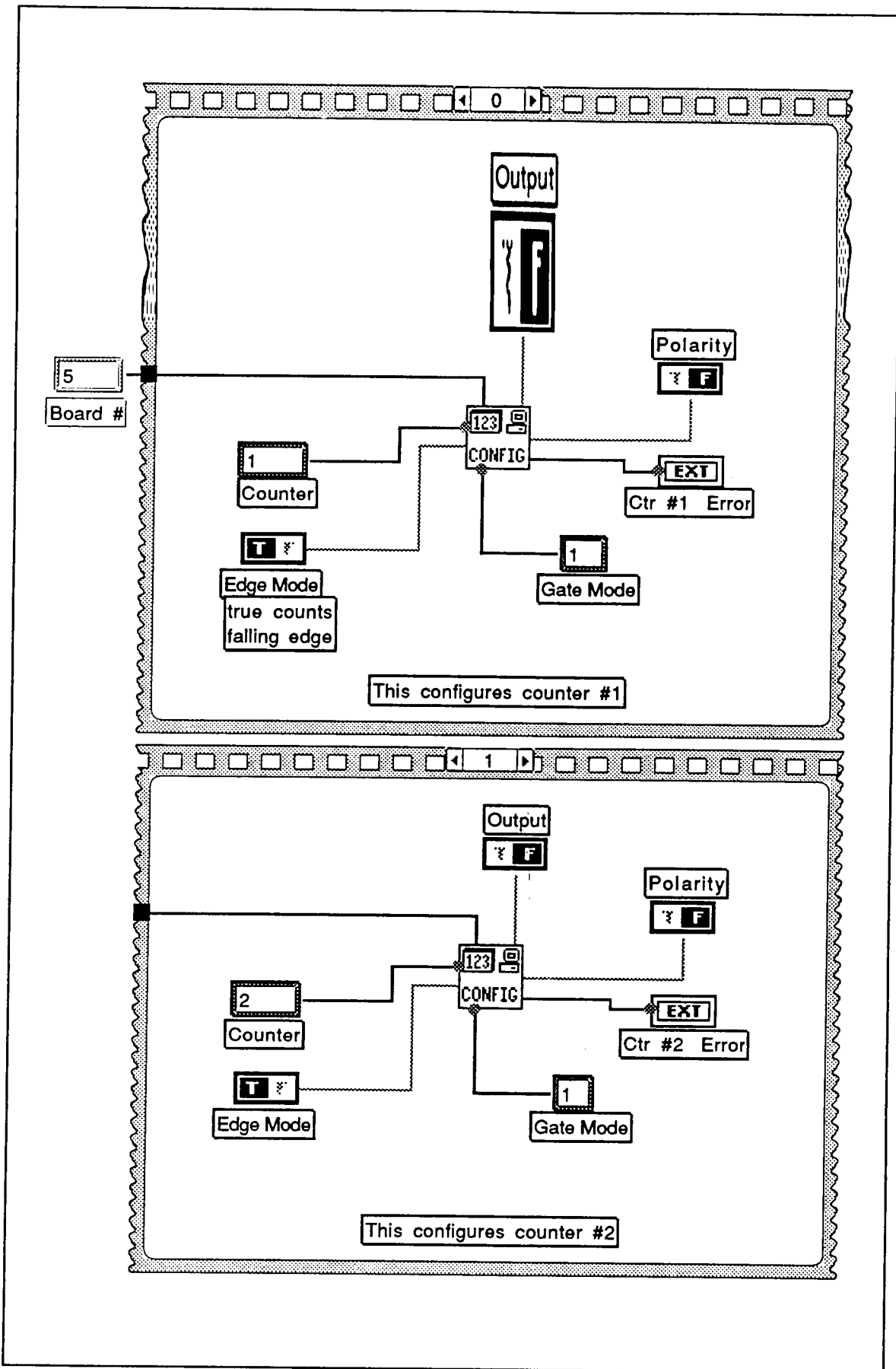


Figure 6-12 ISAAC GSE INIT ISAAC MIO sub-VI Block Diagram.

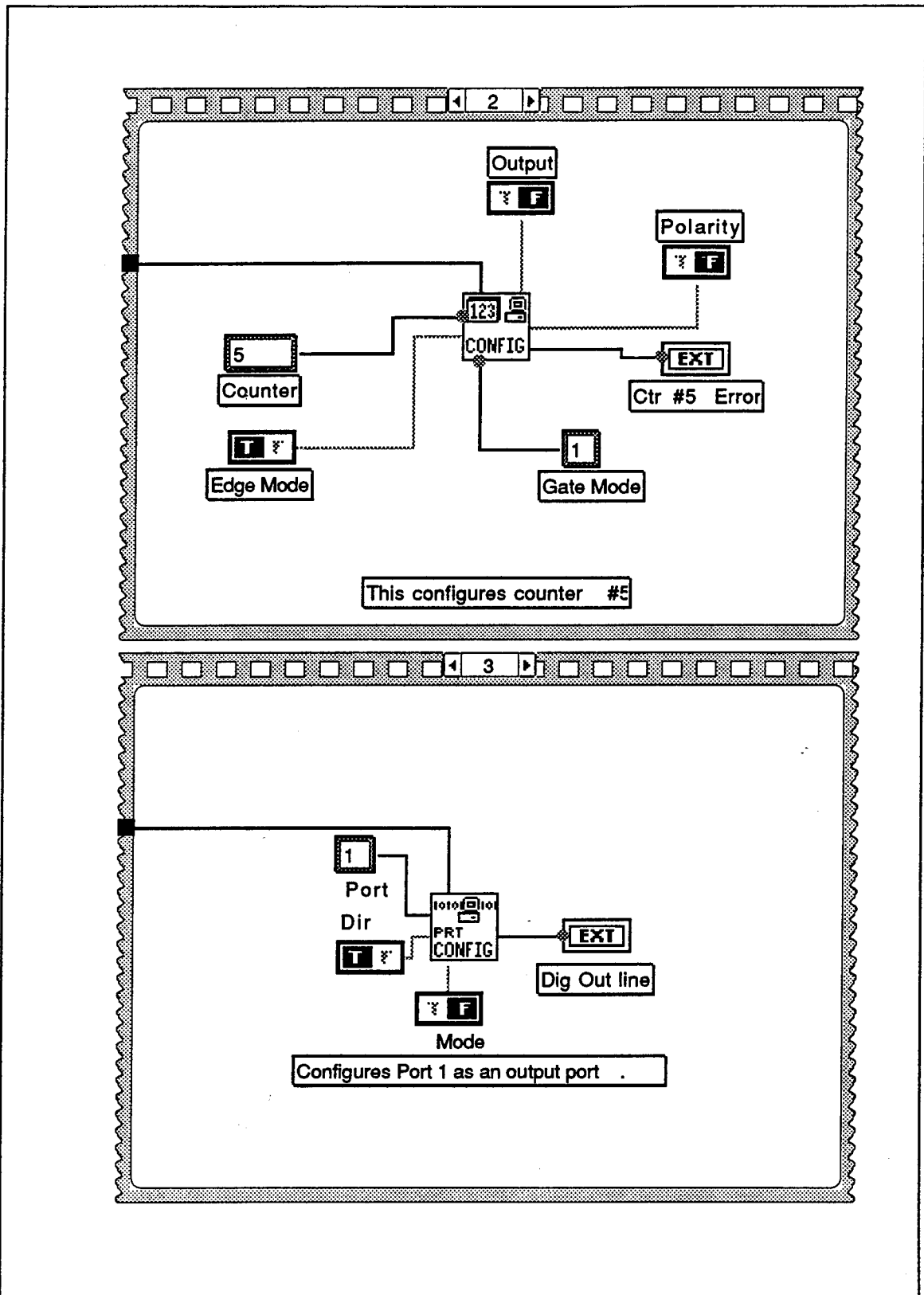


Figure 6-13 ISAAC GSE INIT ISAAC MIO sub-VI Block Diagram (continued).

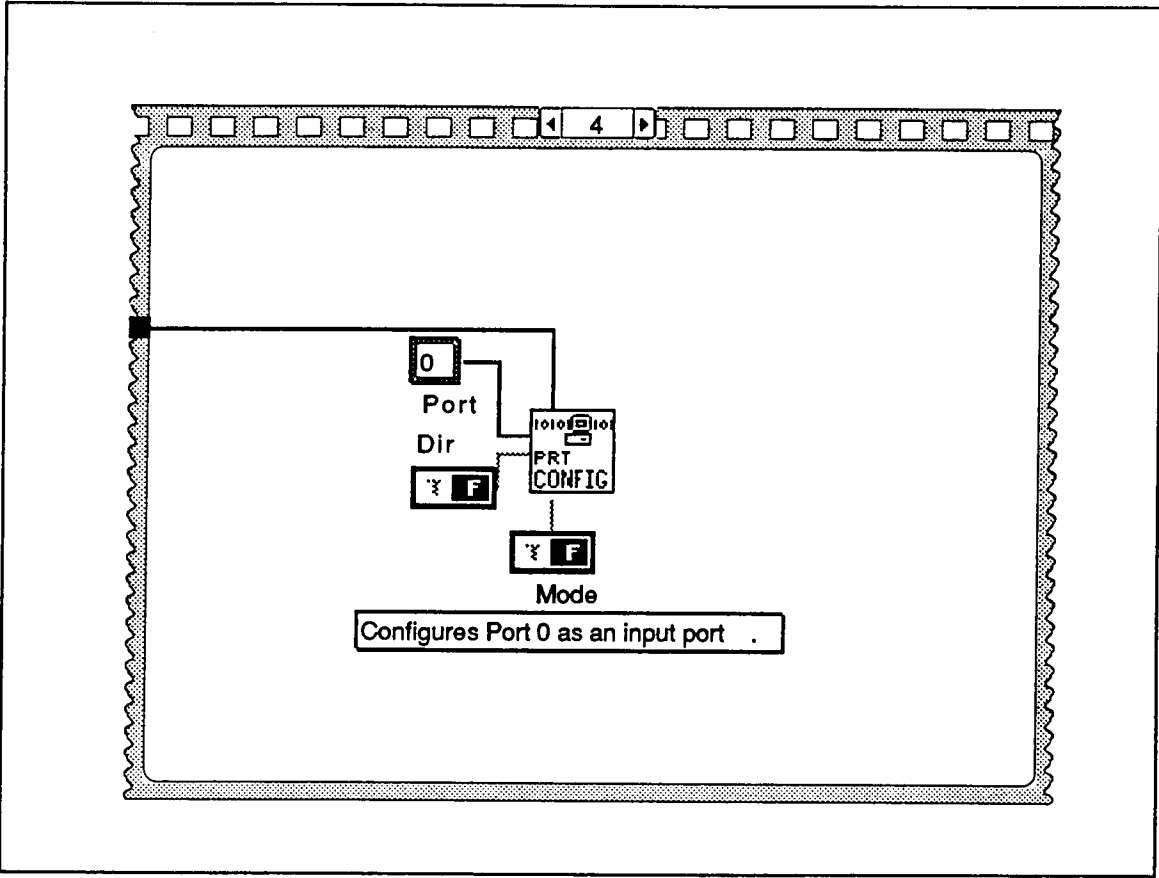


Figure 6-14 ISAAC GSE *INIT ISAAC MIO* sub-VI Block Diagram (continued).

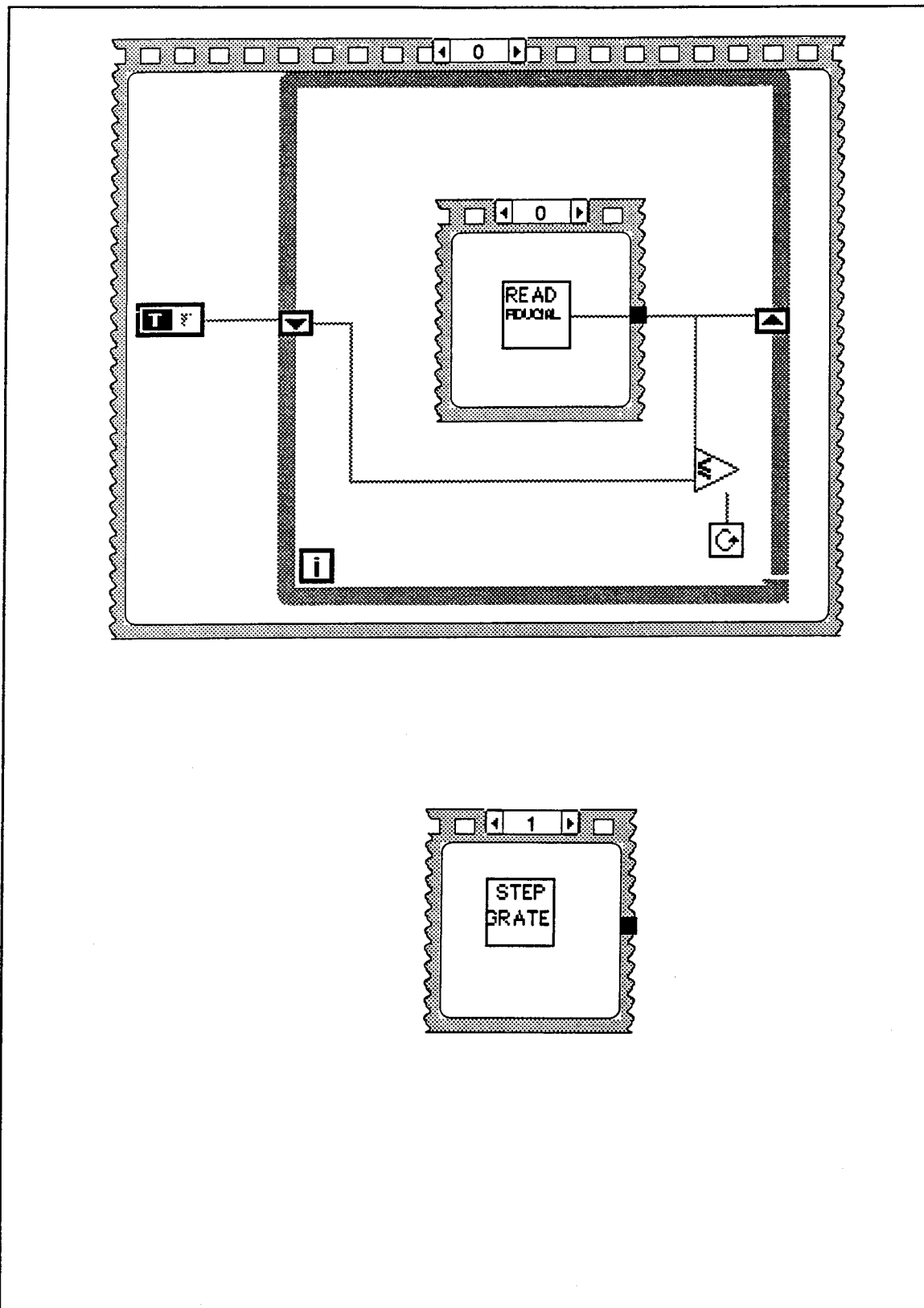
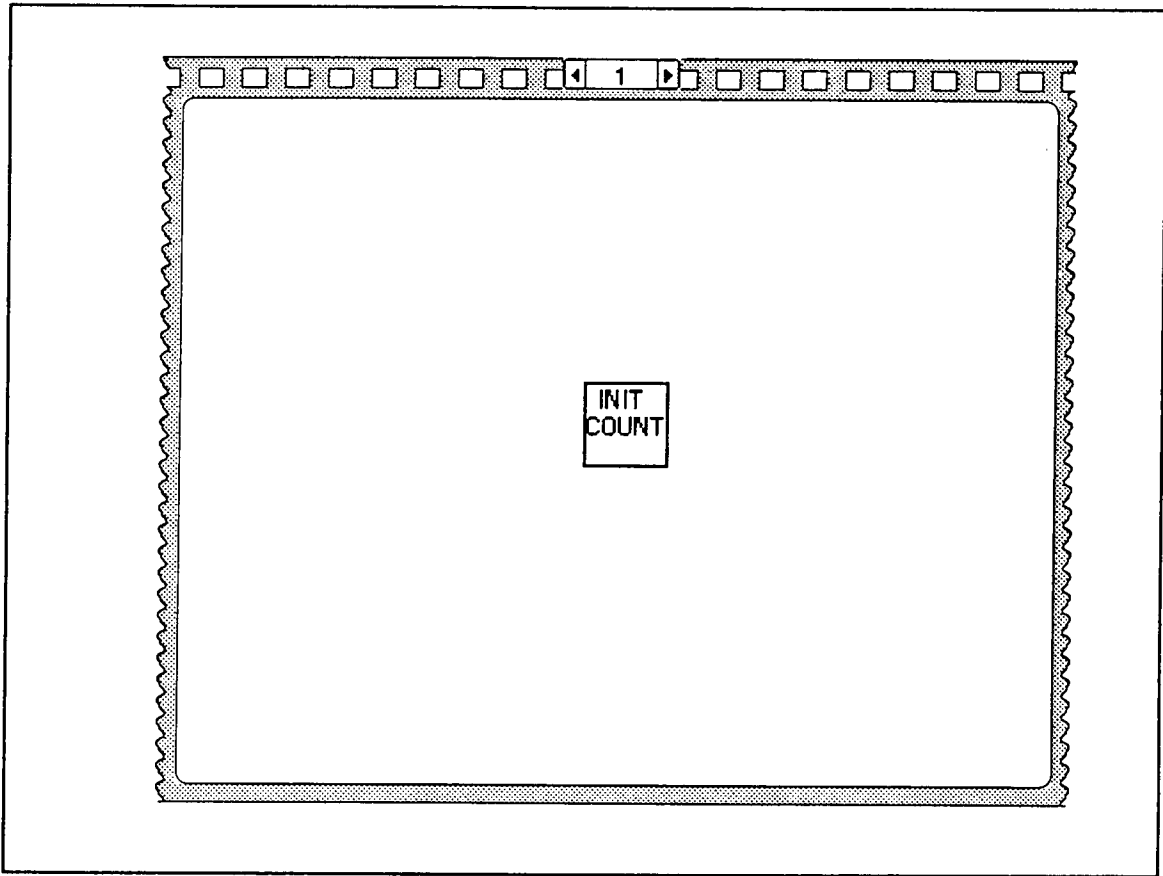


Figure 6-15 ISAAC GSE GO TO FIDUC sub-VI Block Diagram.



**Figure 6-16** ISAAC GSE *GO TO FIDUC* sub-VI Block Diagram (continued).

## 2. Acquire Data

The *Acquire Data* Case of the Case Sequence within the ISAAC GSE VI acquires analog voltages through pin 3 (ACH0) of the NB-MIO-16 board and converts these voltages to digital representations. The acquired spectrum may then be averaged with additional spectra if needed. The digital data are then converted to a floating point array representing the actual input voltages and the result is displayed graphically as a plot of intensity versus pixel number or intensity versus wavelength as selected by the user.

This case, displayed in Figure 6-3, first runs a sub-VI *AVG N SPEC*, which acquires the data, performs the A/D conversions and averages the spectra. The block diagram for this sub-VI is shown in Figures 6-17 and 6-18. Sequence zero of this sub-VI, shown in Figure 6-16, uses the LabDriver VI *DAQ\_Op* to acquire analog video words and convert them to a vector of binary data. The number of video words acquired and converted is equal to the number of spectra to be averaged (user selected) multiplied by 1024 video Words per spectrum. This sub-VI specifies that conversions are to occur every 60  $\mu$ sec as this is the period of the video Words (see Figure 5-3 for timing diagram of clocks).

The resultant array of  $N$  binary words is then sent to the next sequence which contains a For Loop that tests for the number of spectra to be averaged. For the case of only one spectrum or the first of several spectra, the FALSE case is performed in which the *Array Subset* sub-VI returns the sub-array that starts with the zero-th element and contains the first 1024 elements (0-1023). This array is then sent to Sequence 2. For the case of more than one spectrum, the first sub-array is sent back around and added to the next sub-array. Sub-arrays of 1024 elements for each spectrum to be averaged are summed and then sent to the next sequence as one array of 1024 elements.

Sequence 2 divides this array by the total number of spectra to be averaged, thus providing an array that is an average of all intensities. This array is then sent to Sequence 3, which uses the LabDriver *DAQ\_Scale* VI to convert the binary data back into a floating point array representing the input voltages for eventual plotting. Therefore, the output of this VI is an array of averaged voltages representing intensities at each of the pixels of the detector.

The output of *AVG N SPEC* is then sent both to an external indicator and to the *Array-To-Graph* function. The external indicator is present on the front panel as a digital indicator that allows the user to inspect any voltage element of the array by selecting the index for the desired array element. This indicator is seen in the upper right corner of Figure 6-2 and is labeled DATA ARRAY.

The array is also sent into the  $Y$  value of the *Array-To-Graph* representing the  $Y$ -values for an  $XY$  plot on the front panel. The  $X$ -values against which these intensities are plotted are chosen by the user through the toggle switch on the front panel. The *Array-To-Graph* function takes as its input an initial  $X_0$  value and a value for  $\Delta X$ , thus producing an array of 1024  $X$  values. If the user selects to plot intensities versus pixel number, the toggle switch is read as a boolean TRUE and the TRUE Case of the Case Sequence in Figure 6-3 sends a "0" to  $X$  and a "1" to  $\Delta X$ , thereby producing an  $X$ -axis of 0 through 1023, representing each of the photodiodes in the detector.

The Wavelength choice of the toggle switch causes a boolean FALSE to be sent to the Case Sequence and this invokes the sub-VI *WAVELENGTH CONVERTER*. The block diagram for this sub-VI is shown in Figures 6-19 and 6-20. This sub-VI reads the value of the global counter to determine the current grating position step, compares this value to the acceptable tolerances for each of the four grating positions and converts the boolean comparisons to a decimal value for use in a Case Sequence. For the case in which the grating position is at the Fiducial (step 0) or at some intermediate position that is not considered one of the four grating positions, the  $X$ -axis is chosen to be the pixel number since no wavelengths can be determined.

Sequences 2 through 5 provide the wavelength  $X_0$  and  $\Delta X$  to generate the  $X$ -axis for each of the four grating positions when the grating is determined to be at one of the four acceptable positions. The initial  $X_0$  and  $\Delta X$  values were determined through an initial wavelength calibration of the spectrograph that is detailed in the following chapter.

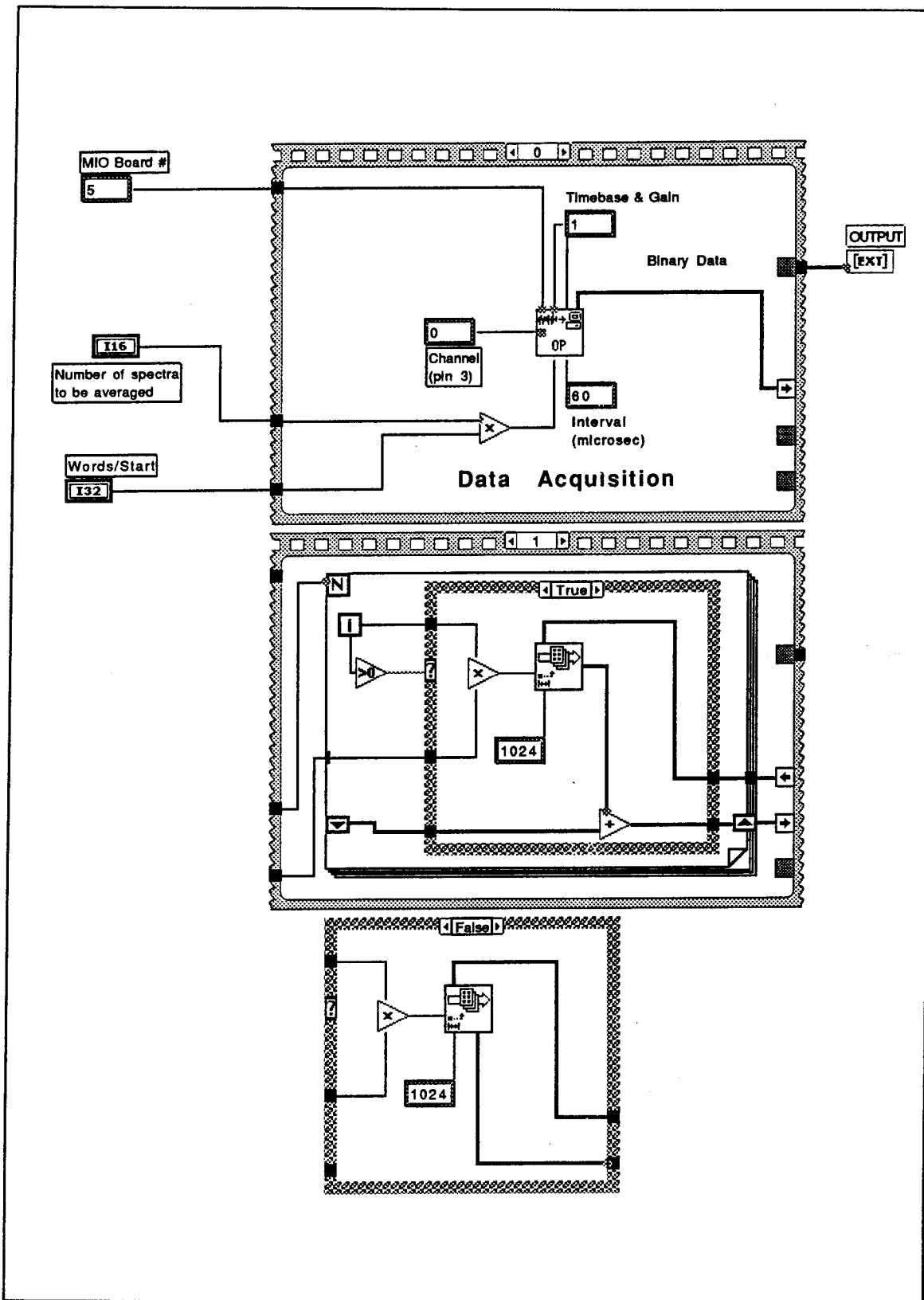


Figure 6-17 ISAAC GSE AVG N SPEC sub-VI Block Diagram.



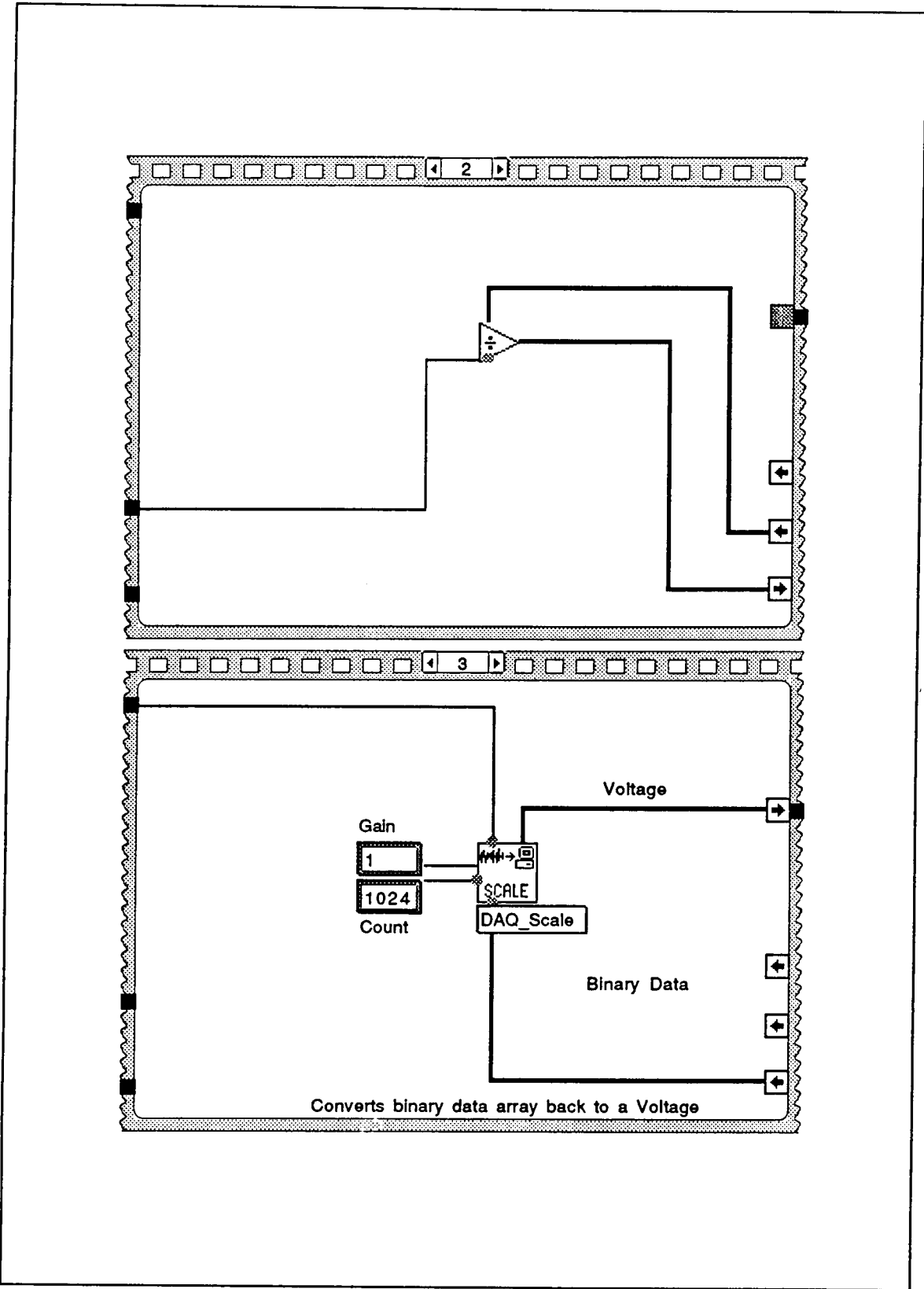


Figure 6-18 ISAAC GSE *AVG N SPEC* sub-VI Block Diagram (continued).

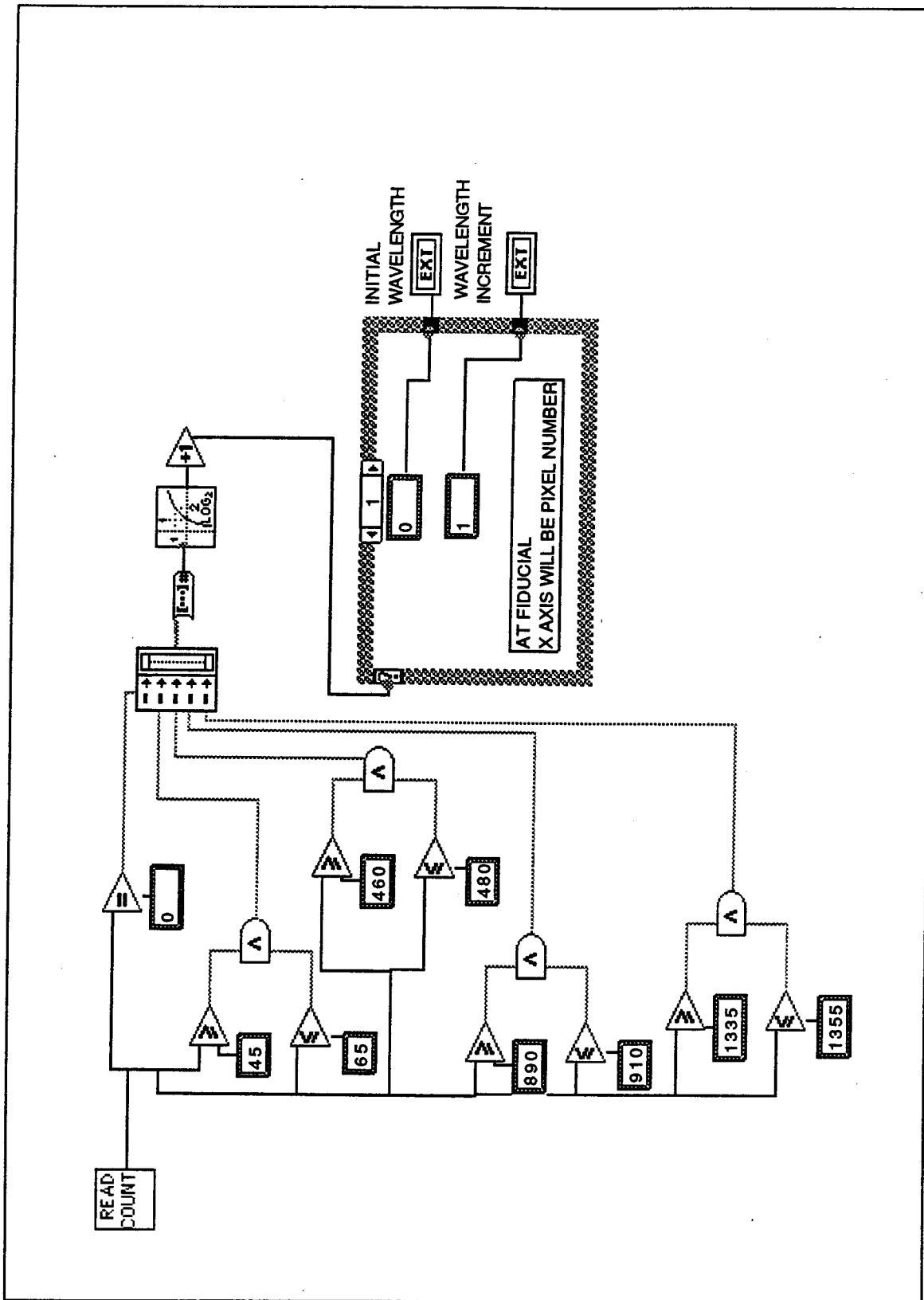
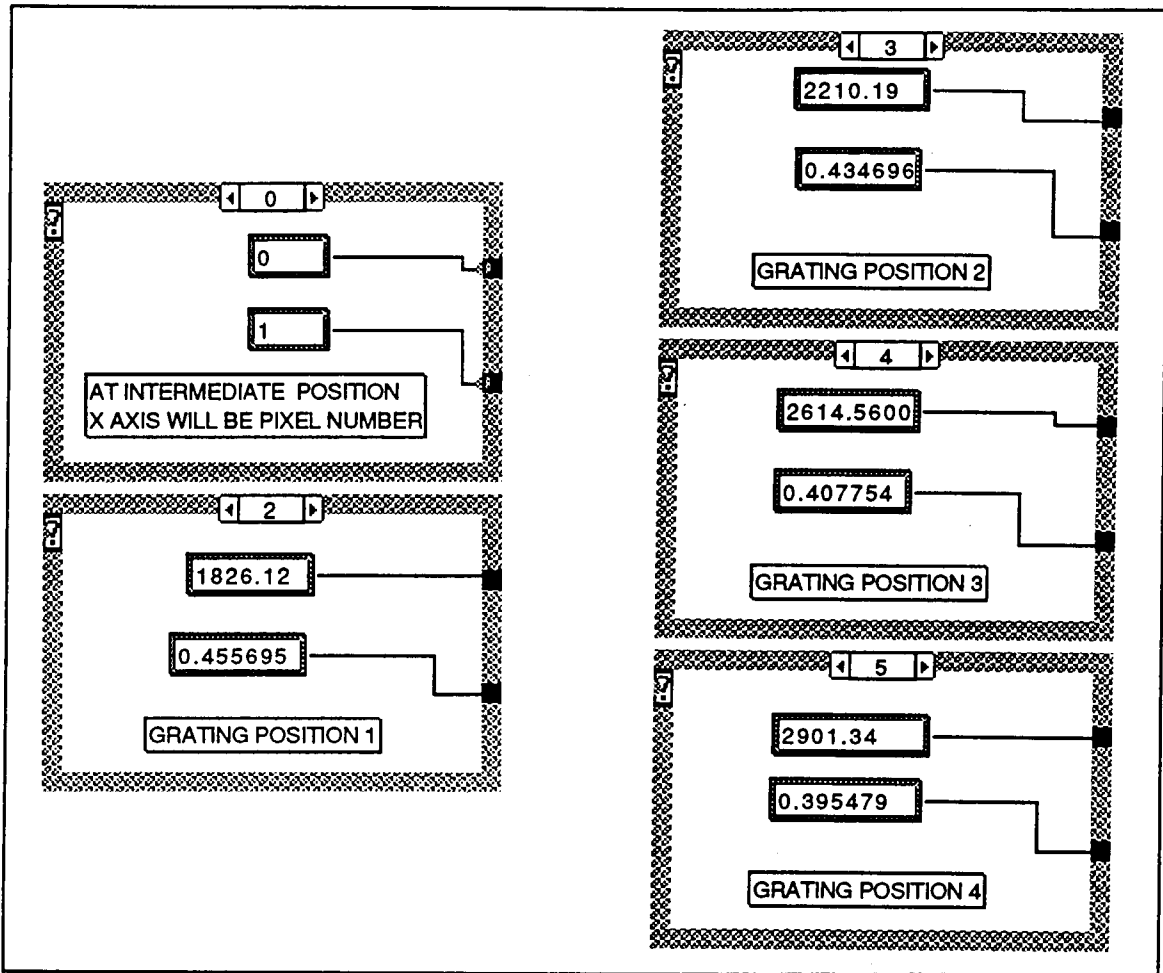


Figure 6-19 ISAAC GSE WAVELENGTH CONVERTER sub-VI Block Diagram.



**Figure 6-20** ISAAC GSE *WAVELENGTH CONVERTER* sub-VI Block Diagram (continued).

### 3. Save to Disk

The *SAVE-To-DISK* sub-VI was borrowed from a GSE written for the predecessor to ISAAC, the MUSTANG spectrograph, and its block diagram is shown as Figure 6-21 (Quint, 1991). This sub-VI reads the last plotted array and converts it to a string using the *To-Fractional-String* function. The string is specified to have a width of at least eight characters and a precision of four digits after the decimal. The sub-VI also prompts the user for a filename and writes the string array to the specified file using the *Write File* function.

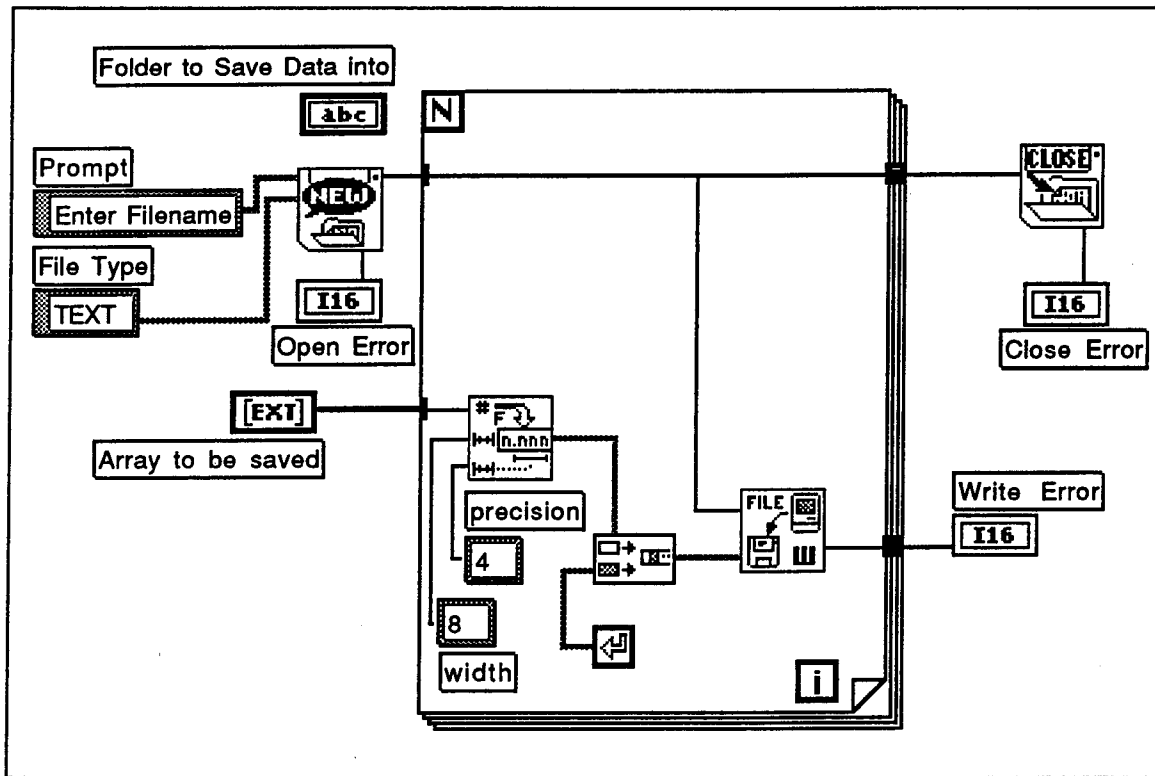


Figure 6-21 ISAAC GSE *SAVE-To-DISK* sub-VI Block Diagram.

#### 4. Select Grating Position

User selection of the **GRATING** button on the front panel causes Sequence 4 of the Case Selector to be run and this case invokes the sub-VI *STEPPER DRIVER*. Upon user selection of **GRATING**, a second smaller front panel pops up in front of the main front panel. This front panel is shown in Figure 6-22. It contains additional user selectable buttons: **STEP GRATING**, **GO TO FIDUCIAL**, **1**, **2**, **3**, **4**, and **QUIT**.

Selection of the **STEP GRATING** button causes the grating to be turned the number of steps specified in the digital control below this button. **GO TO FIDUCIAL** turns the grating until a Fiducial Signal is first received, thus placing the grating in the initial position. The artificial lamp below this button lights upon receipt of the Fiducial Signal.

The numbered buttons (**1** through **4**) turn the grating to the specified position. The displays below these buttons show the position and the grating step for the current position of the grating.

The block diagram for this sub-VI is shown as Figures 6-23 and 6-24. In these figures it can be seen that the buttons are again sent as boolean values which are converted to decimal numbers as was done for the *ISAAC GSE VI*. Sequence 1, corresponding to the **STEP GRATING** selection, invokes the *STEP GRATE* sub-VI to turn the grating the number of steps selected by the user.

Sequence 2 invokes the *GO-To-FIDUCIAL* sub-VI to turn the grating to the initial position. Sequences 3 through 6 use the *SET POSIT* sub-VI to turn the grating to the desired position. The block diagram for this sub-VI is shown as Figures 6-25 and 6-26. This sub-VI reads the current position of the grating and compares it to the desired position. If the desired position is less than the current position, the grating is first turned to the initial (Fiducial) position. Then a loop is entered in which the grating is turned one step and again compared. This continues until the desired grating position is achieved.

The following chapter details the use of this GSE to conduct an initial wavelength calibration for each grating position. This wavelength calibration was used to provide the ability in this software to plot intensities versus wavelength as discussed above.

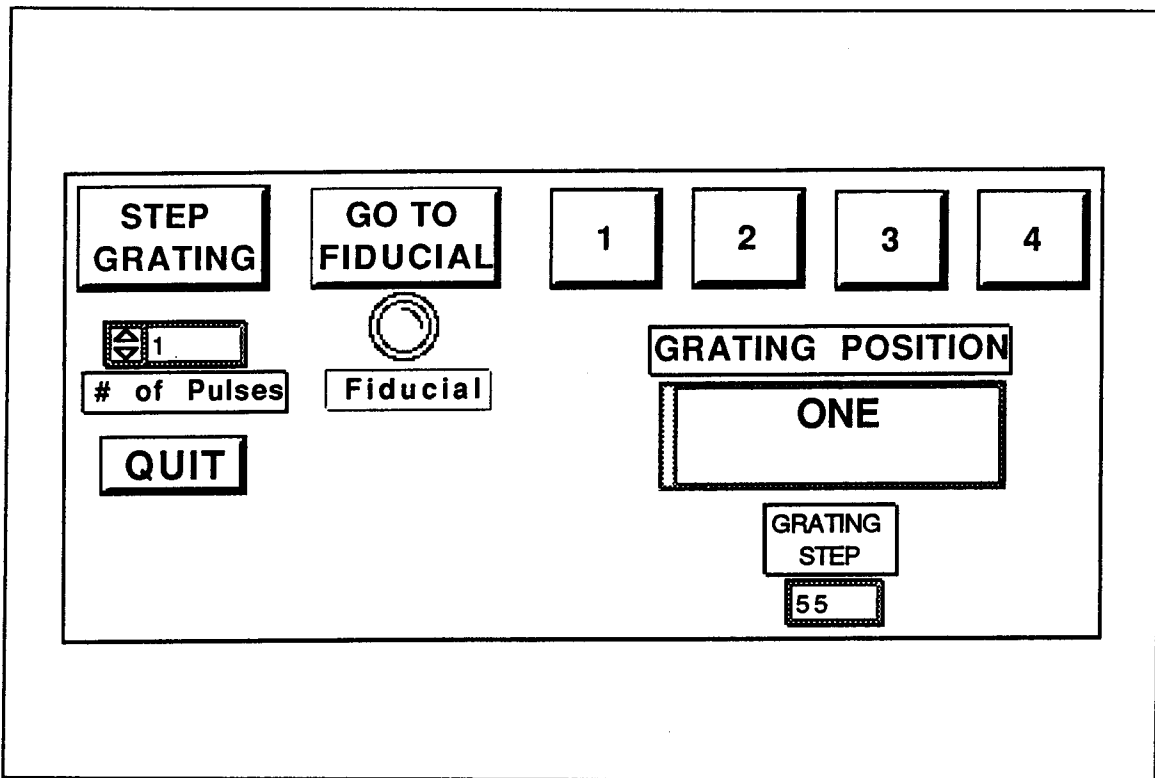


Figure 6-22 ISAAC GSE STEPPER DRIVER sub-VI Front Panel.

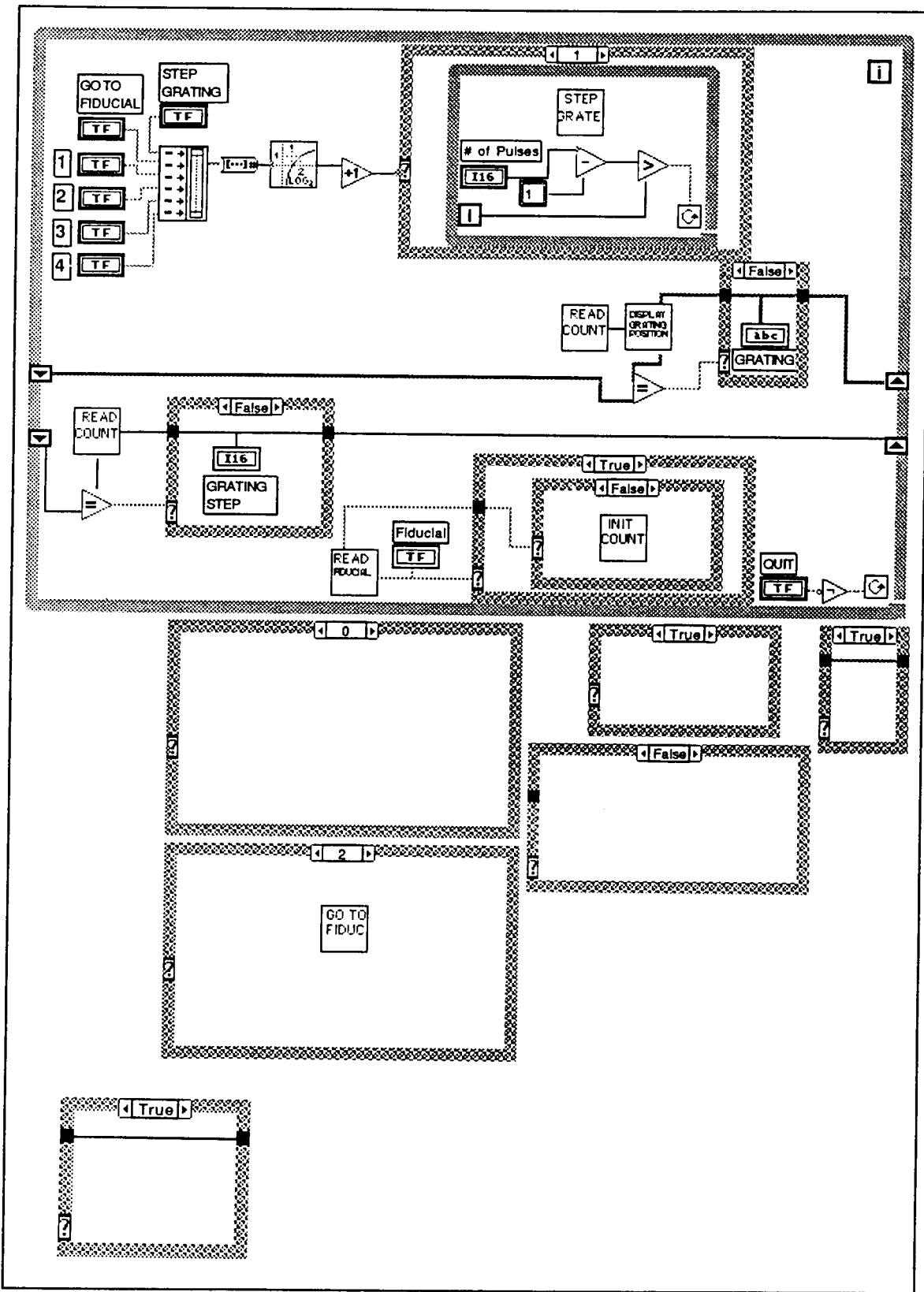


Figure 6-23 ISAAC GSE STEPPER DRIVER sub-VI Block Diagram.

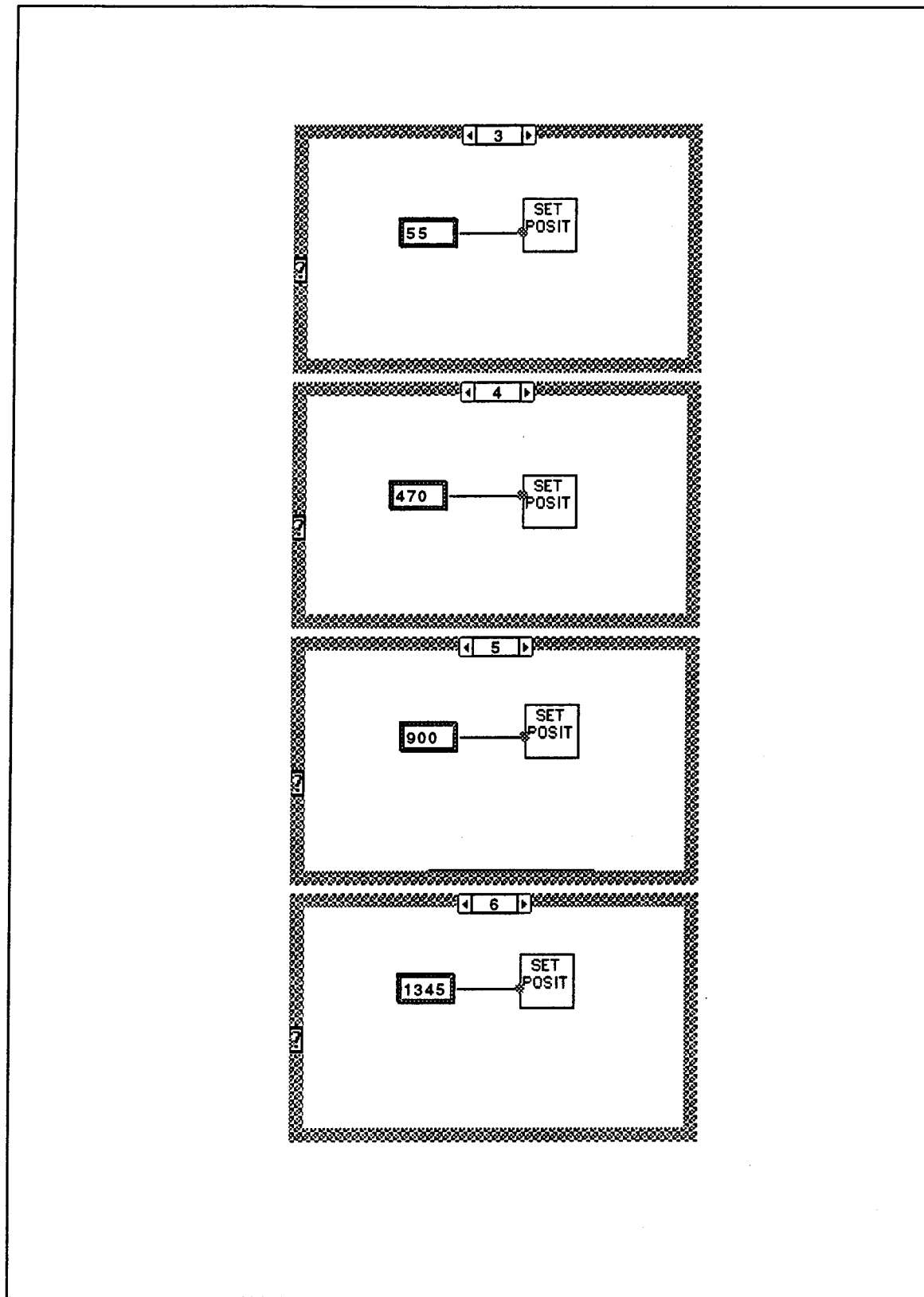


Figure 6-24 ISAAC GSE STEPPER DRIVER sub-VI Block Diagram (continued).



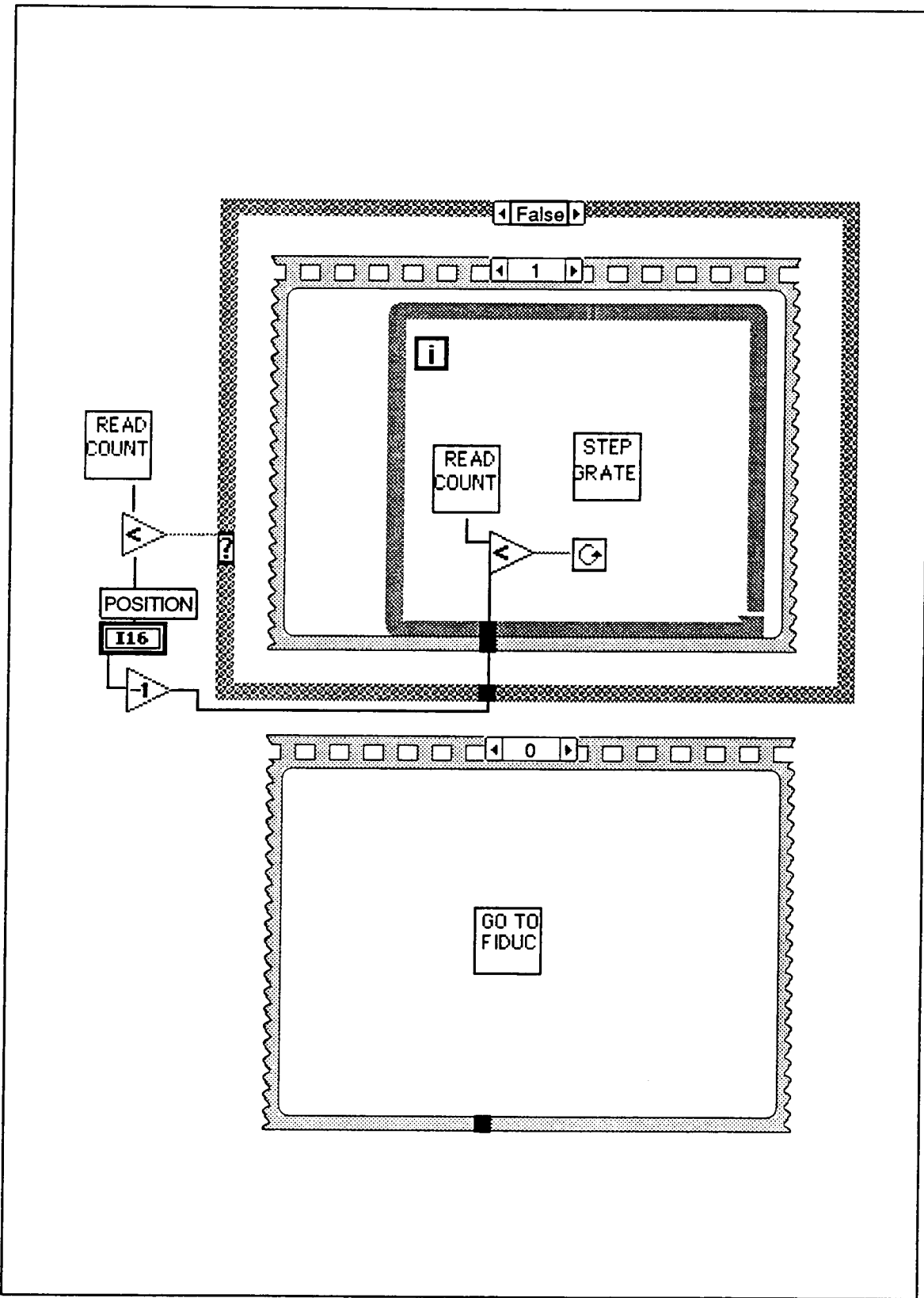


Figure 6-25 ISAAC GSE SET POSIT sub-VI Block Diagram.

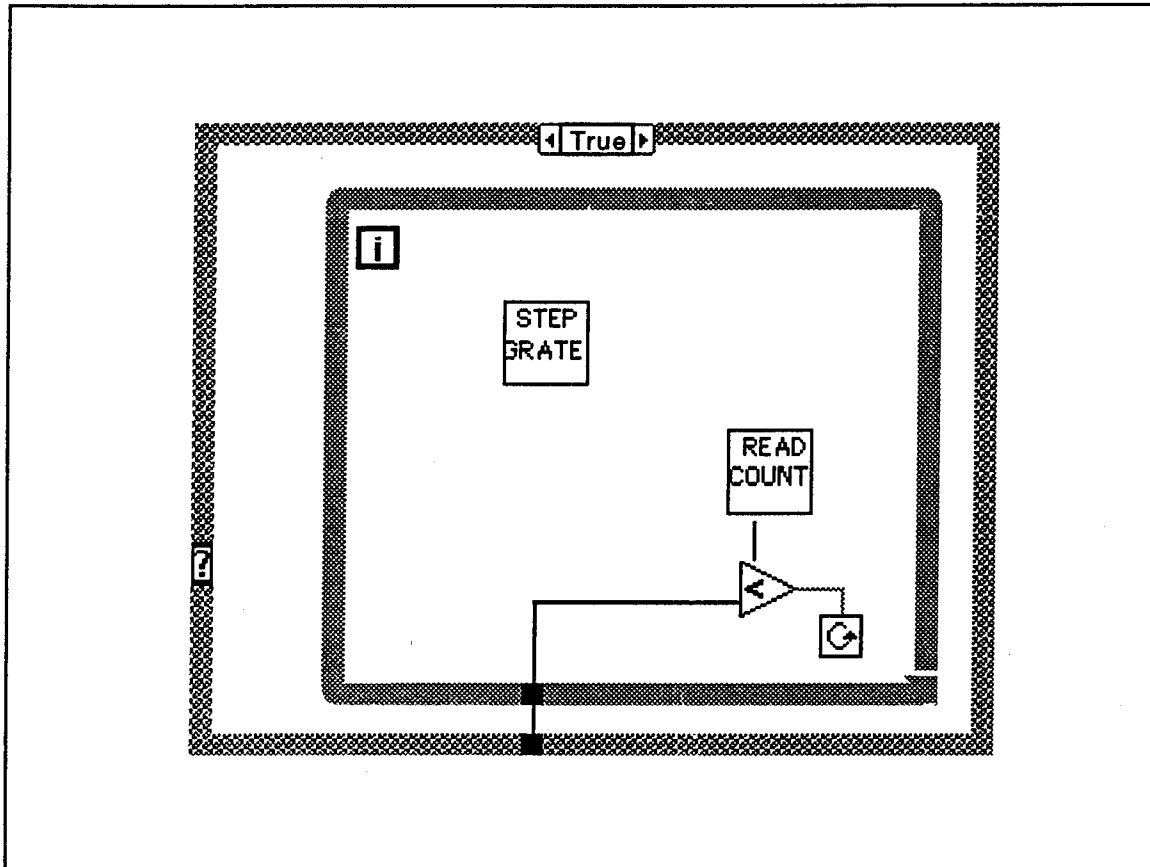


Figure 6-26 ISAAC GSE *SET POSIT* sub-VI Block Diagram (continued).



## VII. WAVELENGTH CALIBRATION

An initial wavelength calibration of the ISAAC spectrograph was performed using the ISAAC GSE. Wavelength calibration is necessary to precisely determine the UV wavelength sensed at each individual pixel in the CCD detector array. This was accomplished using known spectral emissions of a platinum hollow cathode lamp and a mercury lamp. These two sources provide many UV spectral lines in the 1800Å to 3300Å wavelength range.

Spectra of both the mercury and platinum lamps were recorded using the SAVE feature of the ISAAC GSE program at each of the four grating positions. The spectra were then evaluated using the IDL® programming language (published by Research Systems, Inc.). Thirty-six spectral emissions were identified using *Wavelengths and Transition Probabilities for Atoms and Atomic Ions* (Reader and Corliss, 1980) and are identified in Table 7-1. These emissions were individually isolated and the pixel number of each emission was estimated. Figures 7-1 through 7-8 are IDL plots of the recorded spectra. The numbers in these figures refer to the emissions in Table 7-1.

A linear regression of wavelength versus pixel number was performed for each of the four ISAAC wavelength bands using these known 36 wavelengths. Equations (7-1) through (7-4) are the resultant linear fits for each of the four grating positions, respectively.

$$\lambda_1 = 0.455695 X + 1826 .12 \text{ \AA} \quad (7-1)$$

$$\lambda_2 = 0.434696 X + 2210 .19 \text{ \AA} \quad (7-2)$$

$$\lambda_3 = 0.407754 X + 2614 .56 \text{ \AA} \quad (7-3)$$

$$\lambda_4 = 0.395479 X + 2901 .34 \text{ \AA} \quad (7-4)$$

where  $\lambda_i$  is the wavelength at the  $i$ -th grating position and  $X$  is pixel number.

The differences between the calculated linear-fit wavelengths and the actual wavelengths were then determined and are plotted in Figures 7-9 through 7-12. The errors were as much as four angstroms in some cases. These plots suggest that the relationship between pixel number and incident wavelength is not linear. One reason for this is that the detector array is planar while the focal surface of the ISAAC mirror is curved. Therefore, a second-order polynomial fit was performed for each grating position. Equations (7-5) through (7-9) are the polynomial fits for grating positions ONE through FOUR, respectively.

$$\lambda_1 = -2.53271 \times 10^{-5} X^2 + 0.487625 X + 1817.67 \text{ \AA} \quad (7-5)$$

$$\lambda_2 = -2.28669 \times 10^{-5} X^2 + 0.465610 X + 2203.80 \text{ \AA} \quad (7-6)$$

$$\lambda_3 = -3.52904 \times 10^{-5} X^2 + 0.443387 X + 2609.33 \text{ \AA} \quad (7-7)$$

$$\lambda_4 = -3.70081 \times 10^{-5} X^2 + 0.421117 X + 2897.96 \text{ \AA} \quad (7-8)$$

Figures 7-13 through 7-16 plot the actual wavelengths against pixel number and also show the resultant polynomial fits. Figures 7-17 through 7-20 plot the difference between calculated and actual wavelengths for each of the four grating positions, respectively. These plots show that the quadratic fit provides considerable improvement over the linear fit as the greatest quadratic-fit error is approximately 0.6-Å. Higher-order polynomial fits were also examined, though no significant improvement was found over the quadratic fits.

Tables 7-2 through 7-5 summarize the findings for each grating position. These tables list the 36 spectral emissions, their source, known wavelengths (Reader and Corliss, 1980), the linear and polynomial calculated wavelengths and the differences between actual and calculated wavelengths for both fits.

#	SOURCE	$\lambda$ (Å)	GRATING- PIXEL	#	SOURCE	$\lambda$ (Å)	GRATING- PIXEL
1	Ne II	1916.08	1 - 204.0	19	Pt I	2628.03	2 - 969.0
2	Pt I	2084.59	1 - 564.5	20	Pt I	2628.03	3 - 42.0
3	Pt I	2103.33	1 - 604.0	21	Pt I	2659.45	3 - 114.0
4	Pt I	2128.61	1 - 660.5	22	Pt I	2702.40	3 - 214.0
5	Pt I	2174.67	1 - 762.0	23	Pt I	2719.04	3 - 253.0
6	Pt II	2190.32	1 - 797.0	24	Pt I	2733.96	3 - 287.5
7	Pt I	2202.22	1 - 823.7	25	Pt I	2830.30	3 - 519.5
8	Pt II	2245.52	1 - 922.8	26	Pt I	2929.79	3 - 769.5
9	Pt I	2274.38	1 - 988.0	27	Hg I	2967.28	3 - 867.7
10	Pt I	2289.27	1 - 1020.0	28	Pt I	2997.97	3 - 948.0
11	Pt I	2289.27	2 - 185.0	29	Pt I	2929.79	4 - 76.0
12	Pt I	2292.40	2 - 192.5	30	Hg I	2967.28	4 - 167.3
13	Pt I	2318.29	2 - 250.5	31	Pt I	2997.97	4 - 242.3
14	Pt I	2357.10	2 - 336.5	32	Hg I	3021.50	4 - 302.0
15	Pt I	2440.06	2 - 524.5	33	Pt I	3042.64	4 - 354.3
16	Pt I	2467.44	2 - 587.0	34	Pt I	3064.71	4 - 410.7
17	Pt I	2487.17	2 - 633.0	35	Hg I	3125.67	4 - 569.0
18	Hg I	2536.51	2 - 749.3	36	Hg I	3131.55	4 - 585.0

**Table 7-1** Spectral emissions used for wavelength calibration. Numbered labels correspond to identification labels in Figures 7-1 through 7-8.

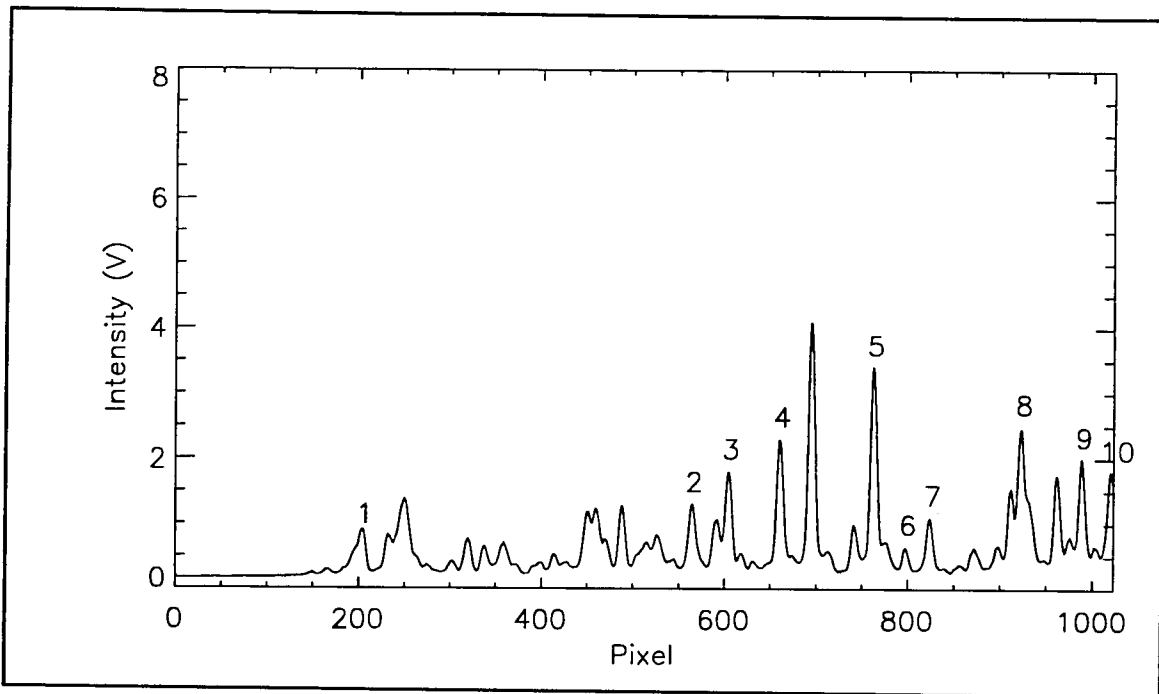


**Figure 7-1** Platinum spectrum at ISAAC grating position ONE.

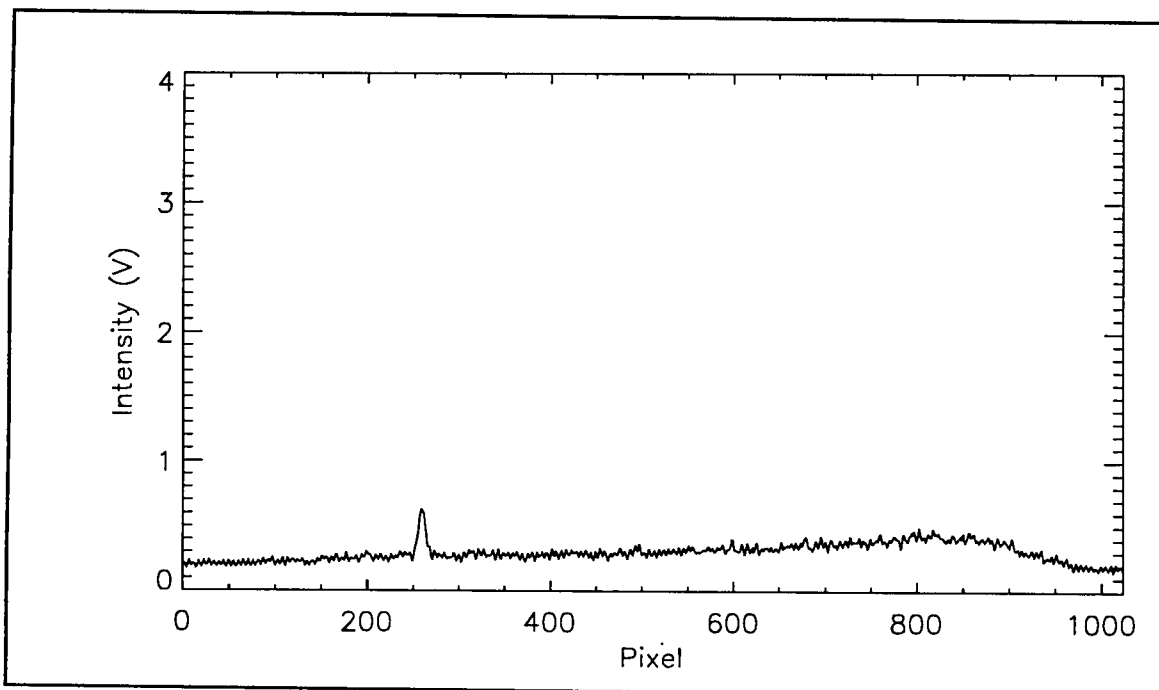


**Figure 7-2** Mercury spectrum at ISAAC grating position ONE.

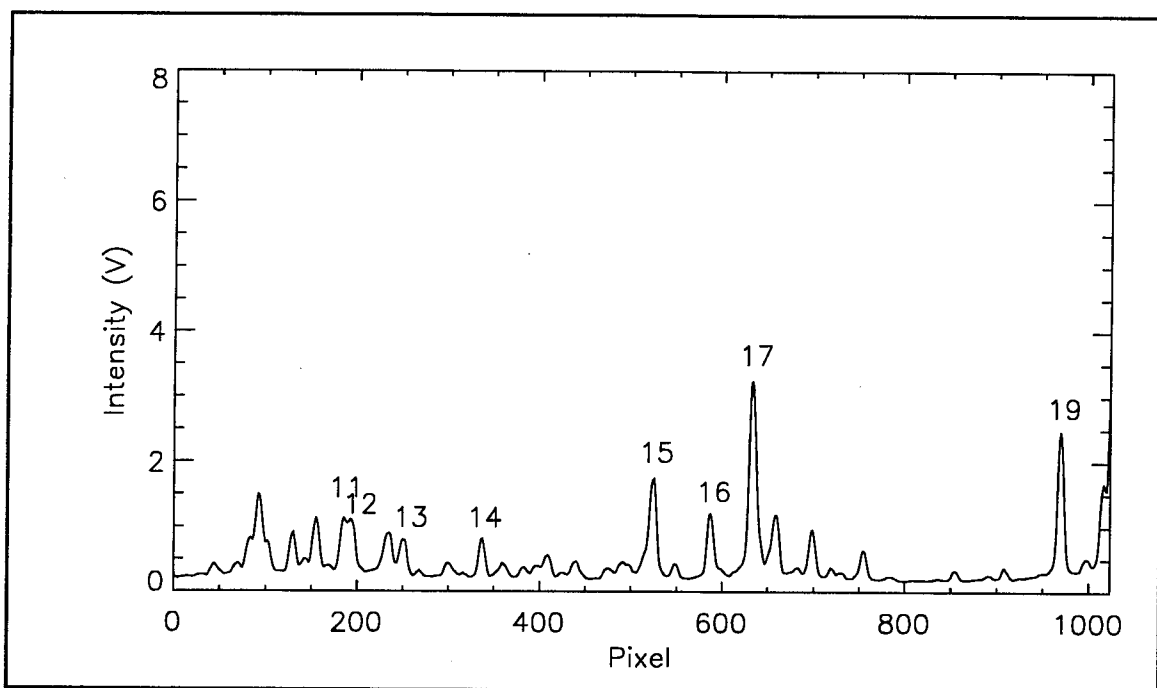


**Figure 7-3** Platinum spectrum at ISAAC grating position TWO.

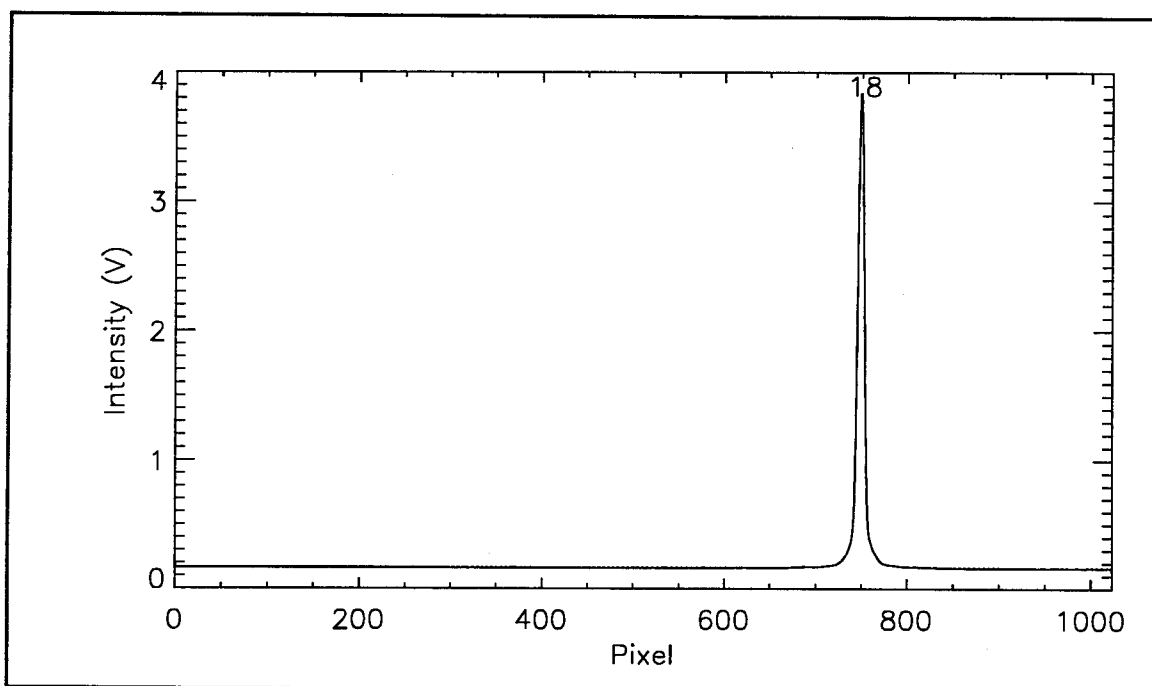


**Figure 7-4** Mercury spectrum at ISAAC grating position TWO.



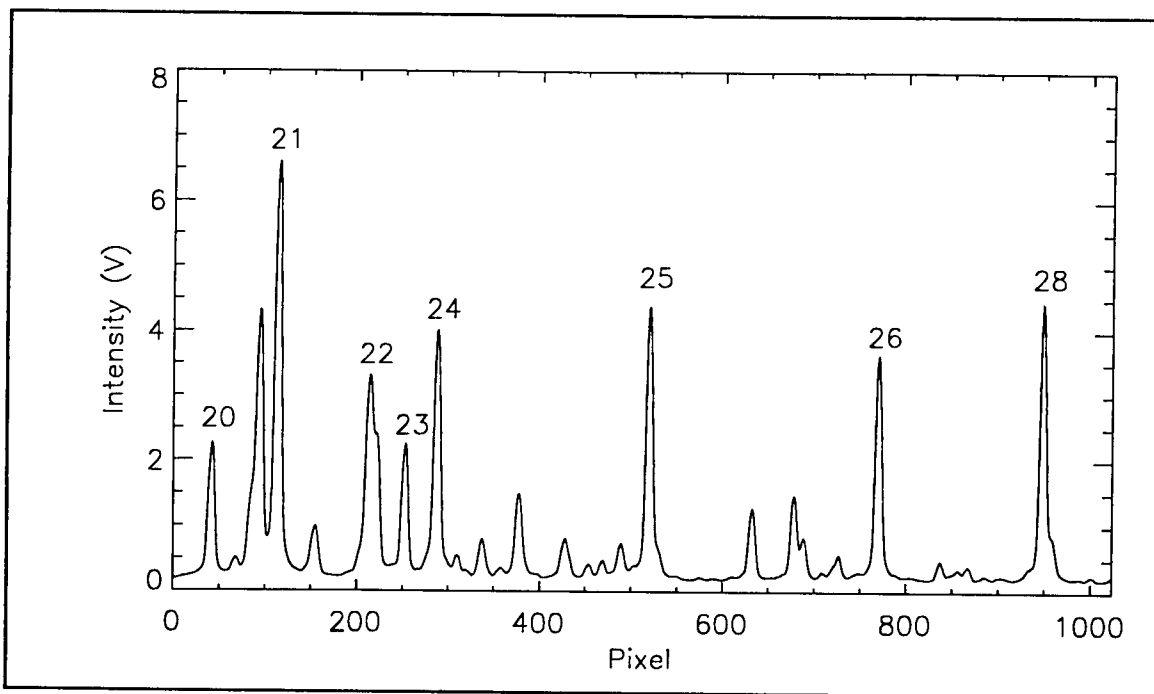


**Figure 7-5** Platinum spectrum at ISAAC grating position THREE.

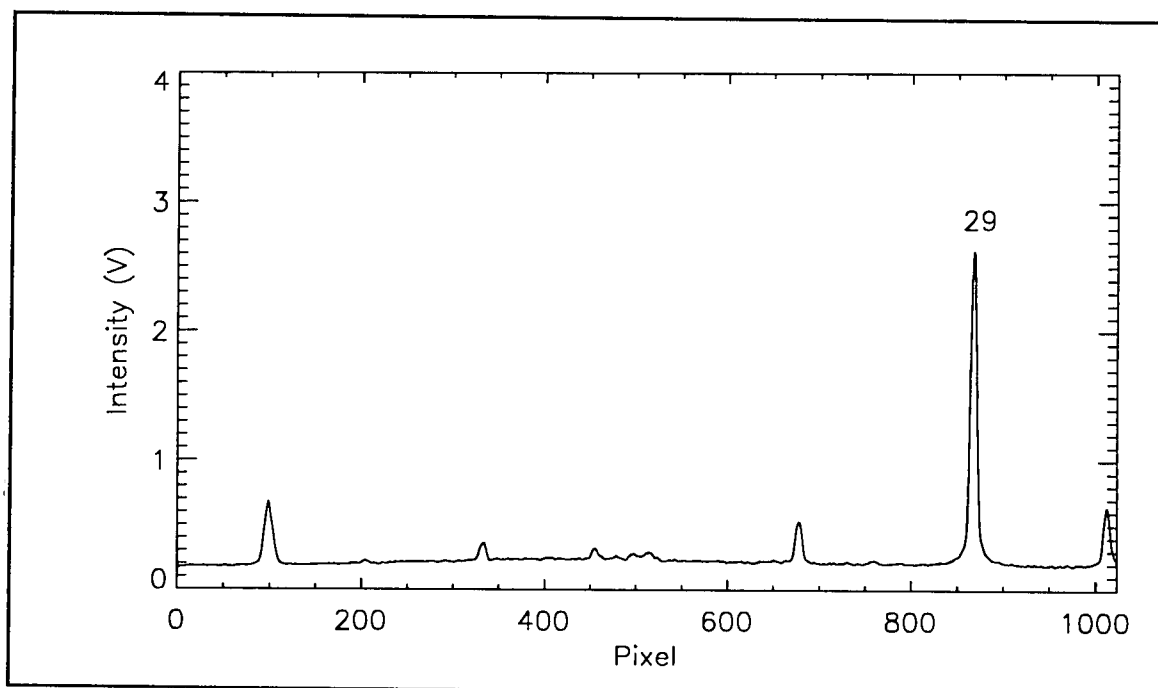


**Figure 7-6** Mercury spectrum at ISAAC grating position THREE.

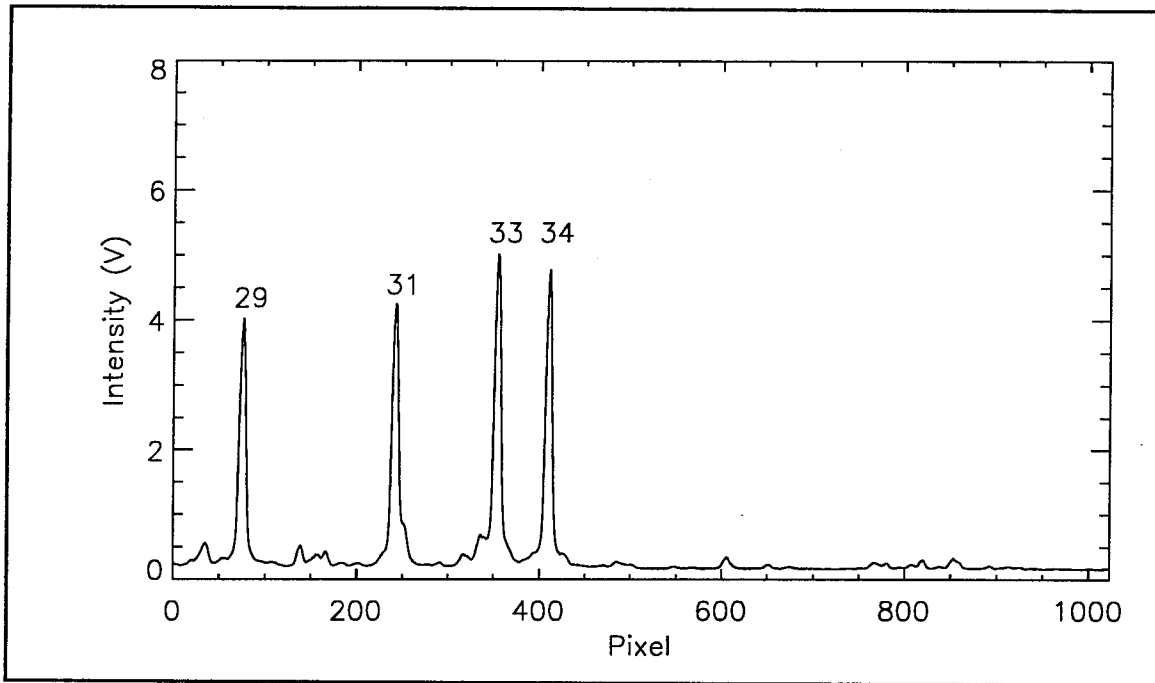


**Figure 7-7** Platinum spectrum at ISAAC grating position FOUR.

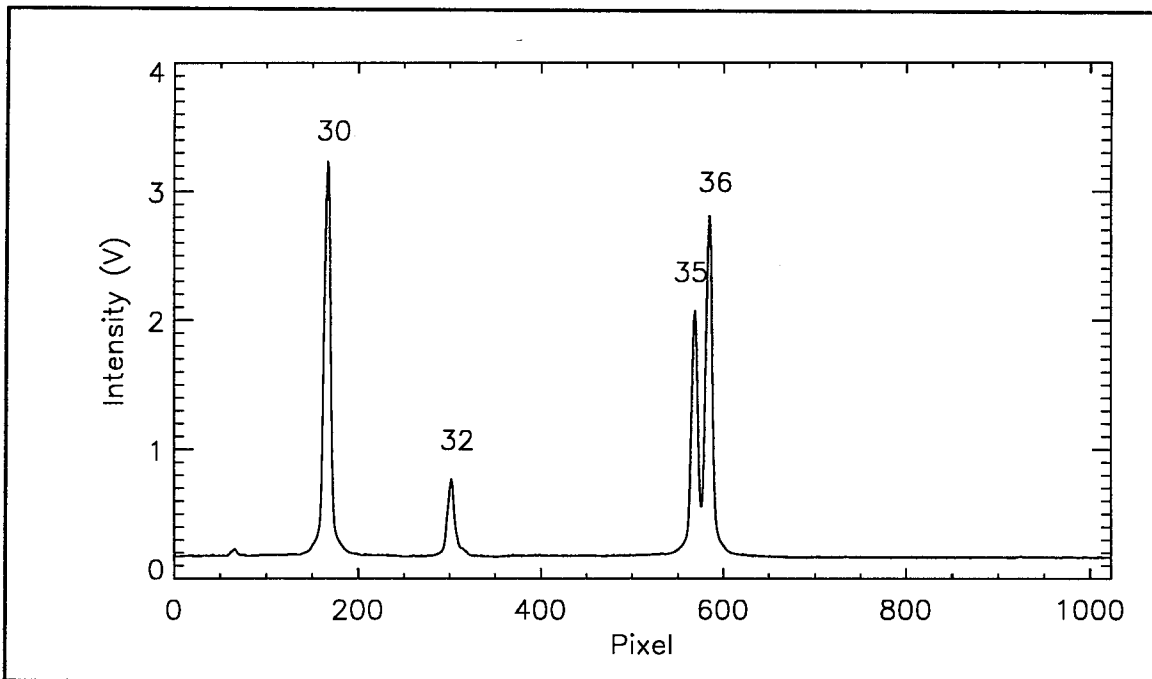


**Figure 7-8** Mercury spectrum at ISAAC grating position FOUR.

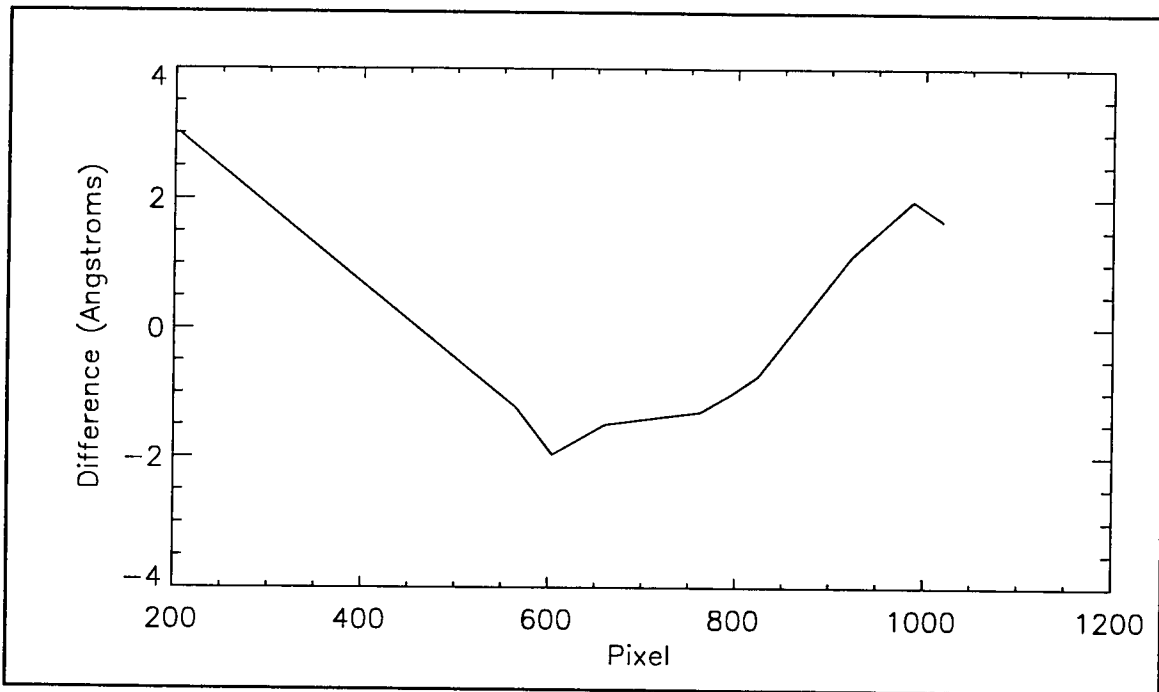


**Figure 7-9** Difference between linear fit and actual wavelengths at grating position ONE.

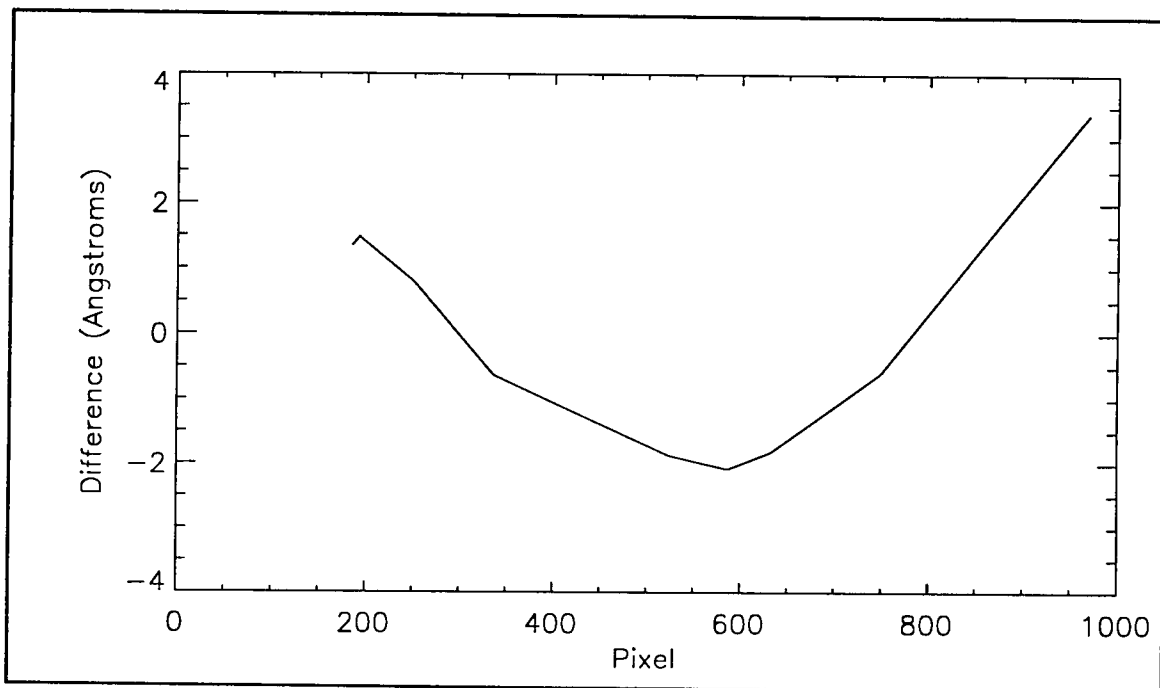


**Figure 7-10** Difference between linear fit and actual wavelengths at grating position TWO.

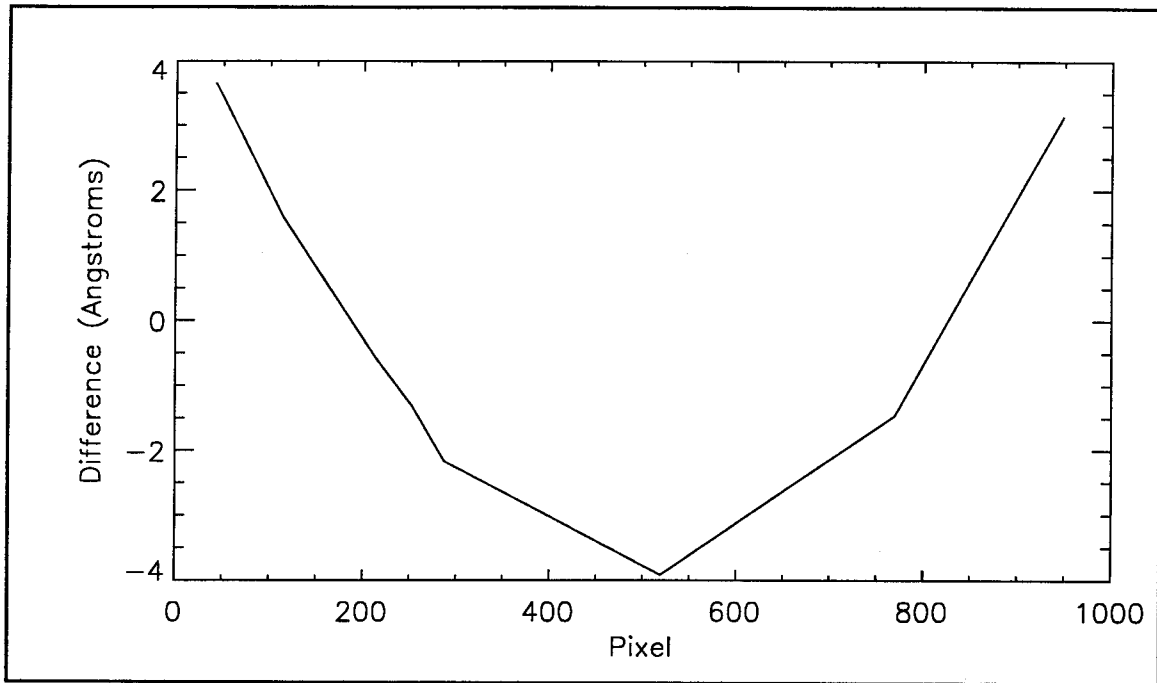


**Figure 7-11** Difference between linear fit and actual wavelengths at grating position THREE.

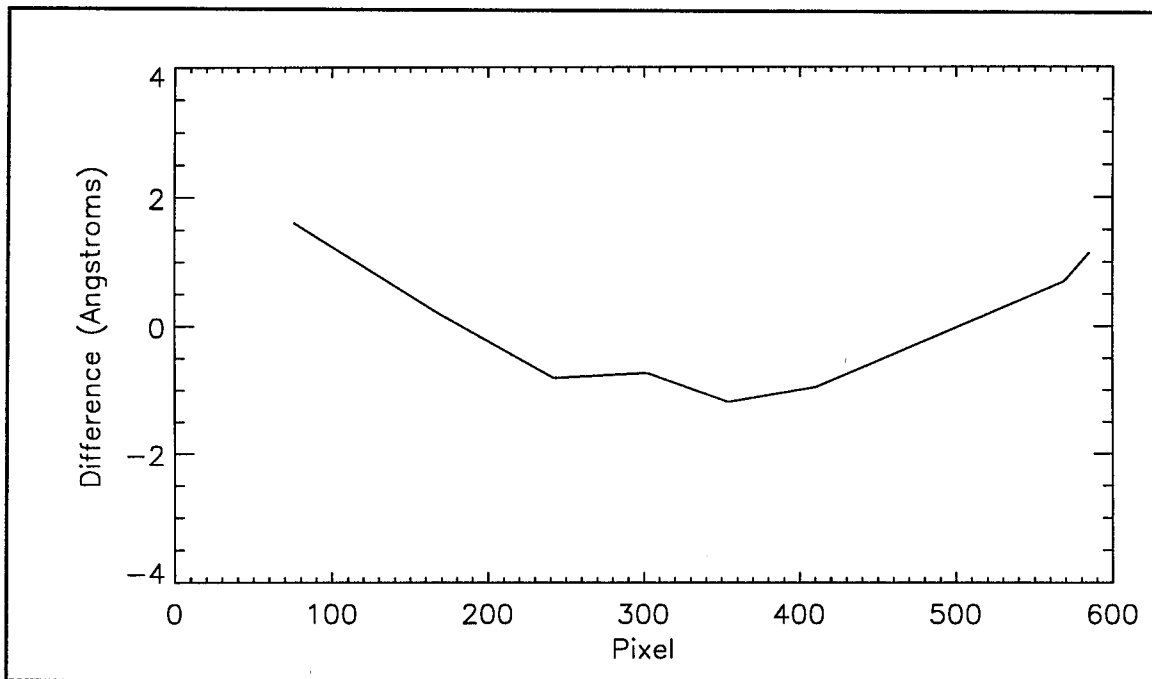


**Figure 7-12** Difference between linear fit and actual wavelengths at grating position FOUR.

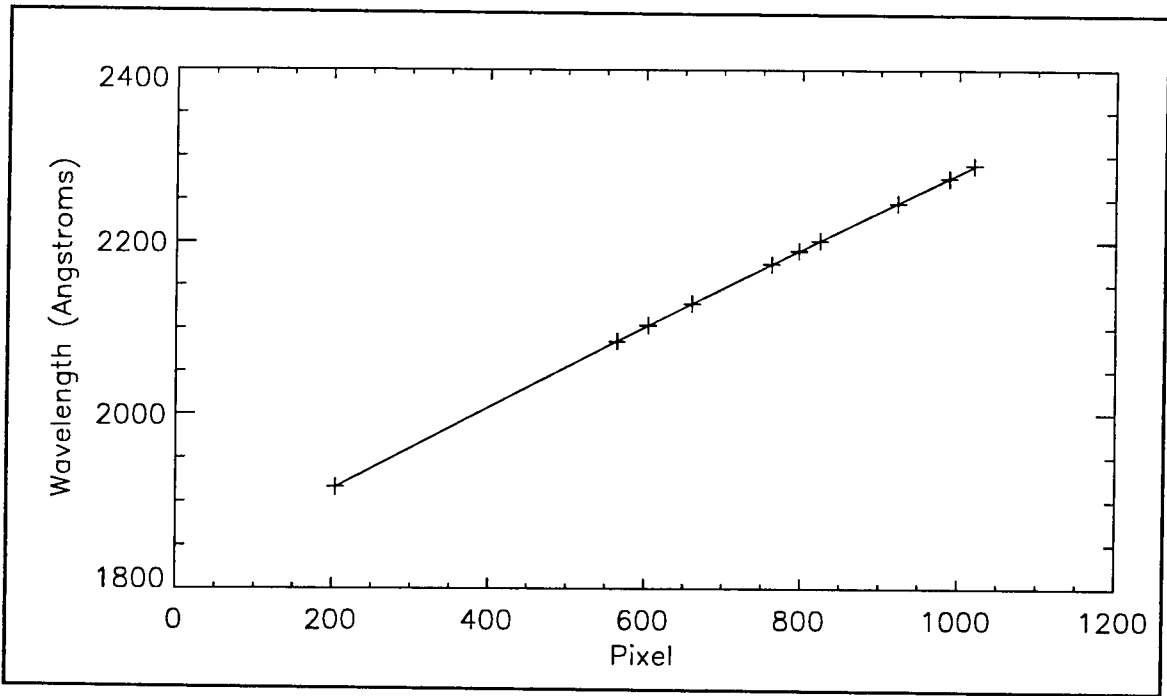


**Figure 7-13** Quadratic fit to identified platinum spectral lines at grating position ONE.

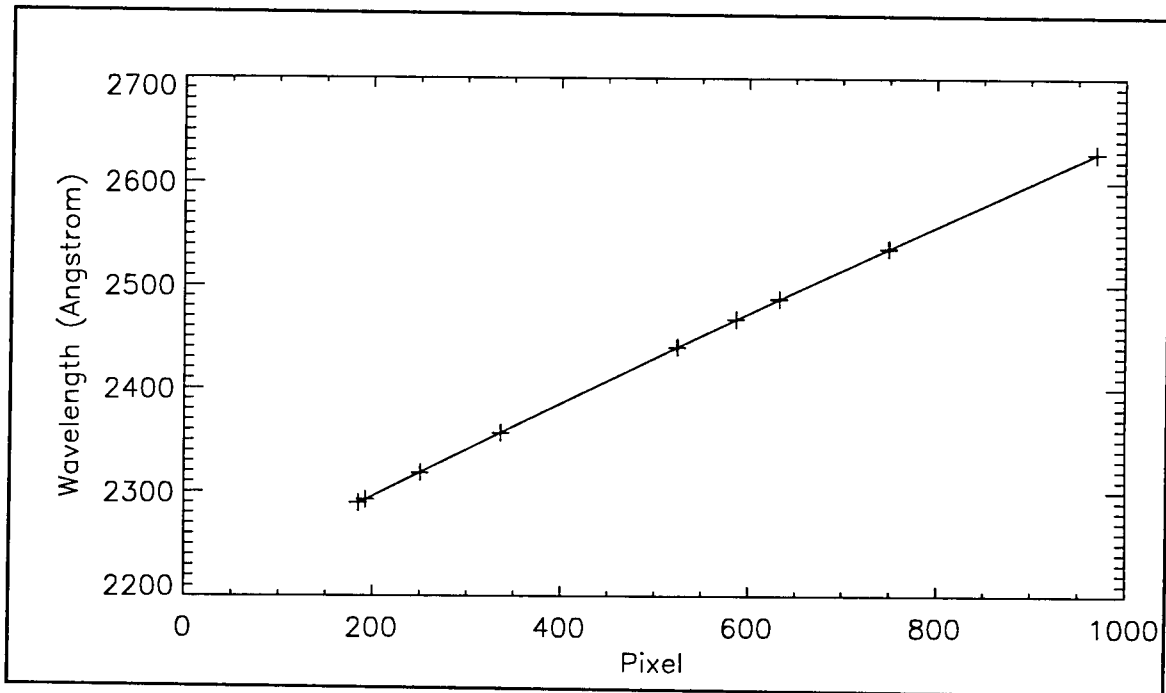


**Figure 7-14** Quadratic fit to identified platinum and mercury spectral lines at grating position TWO.

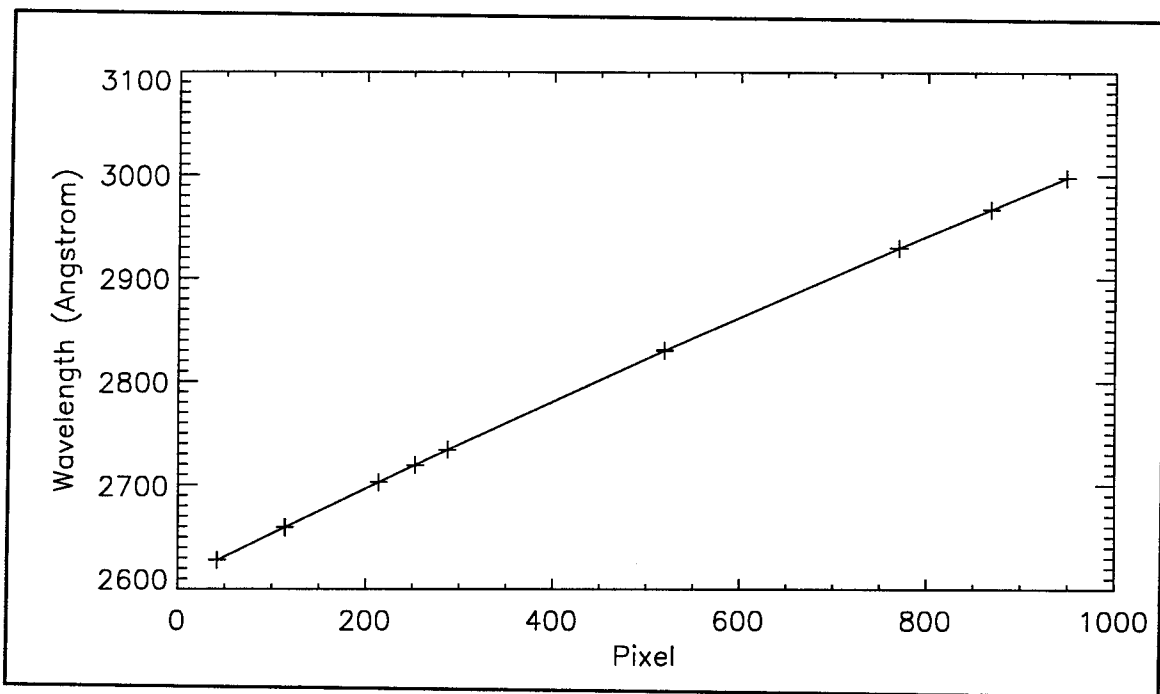


**Figure 7-15** Quadratic fit to identified platinum and mercury spectral lines at grating position THREE.

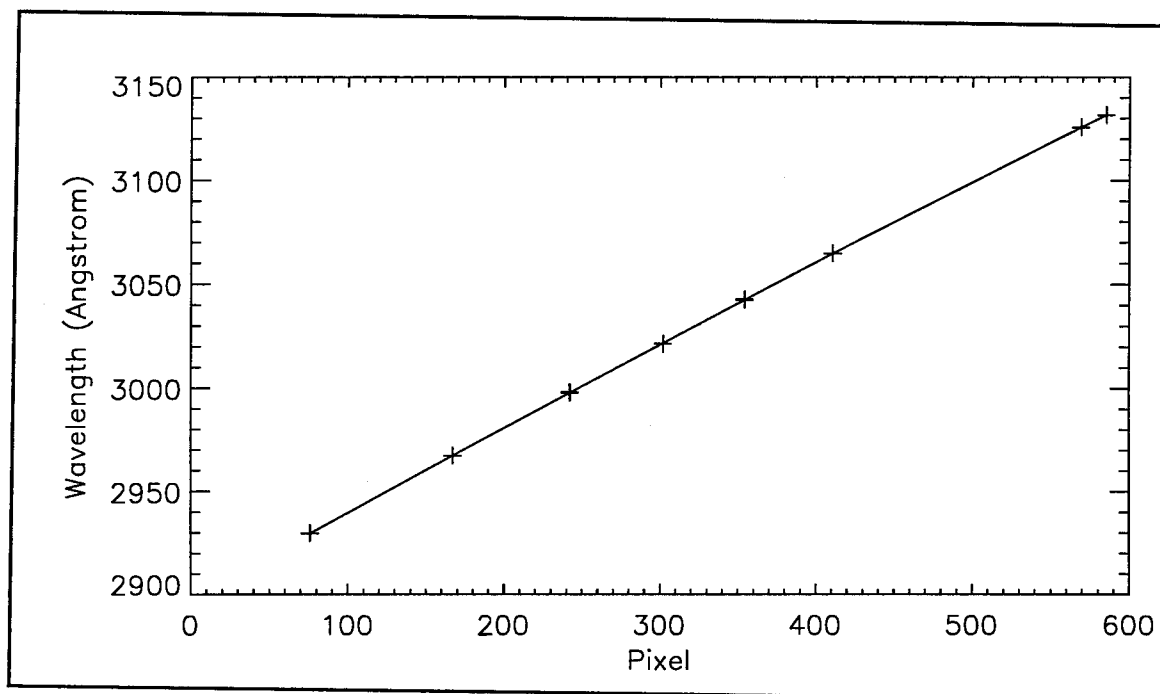


**Figure 7-16** Quadratic fit to identified platinum and mercury spectral lines at grating position FOUR.

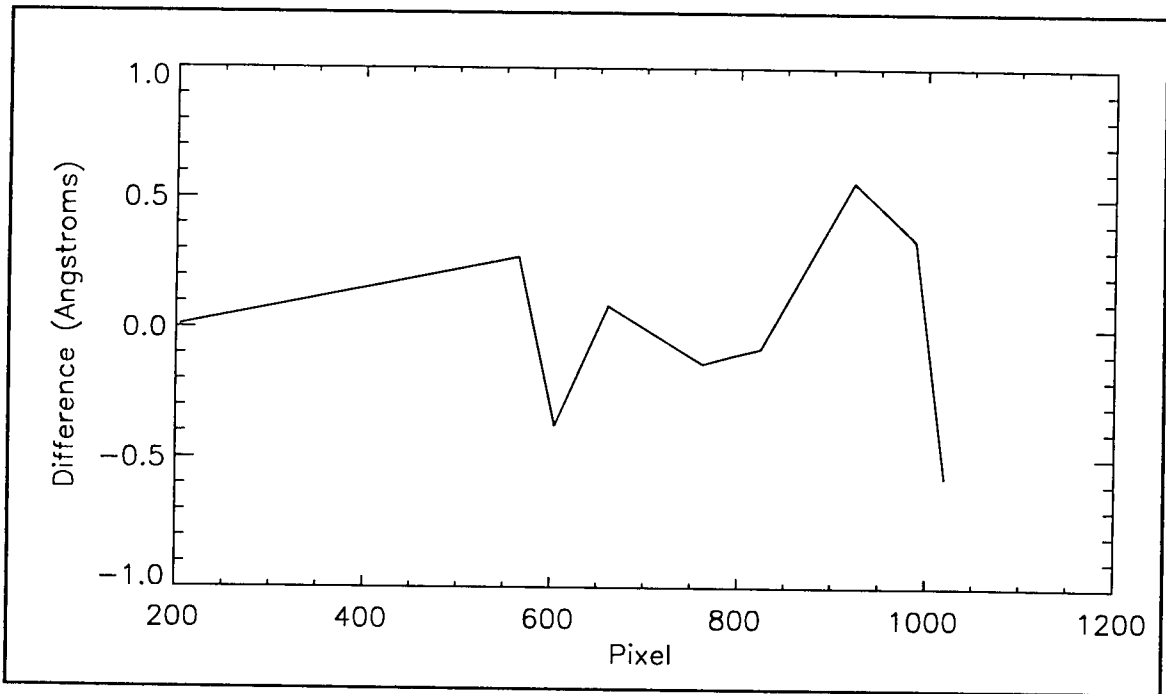


**Figure 7-17** Difference between quadratic fit and actual wavelengths at grating position ONE.

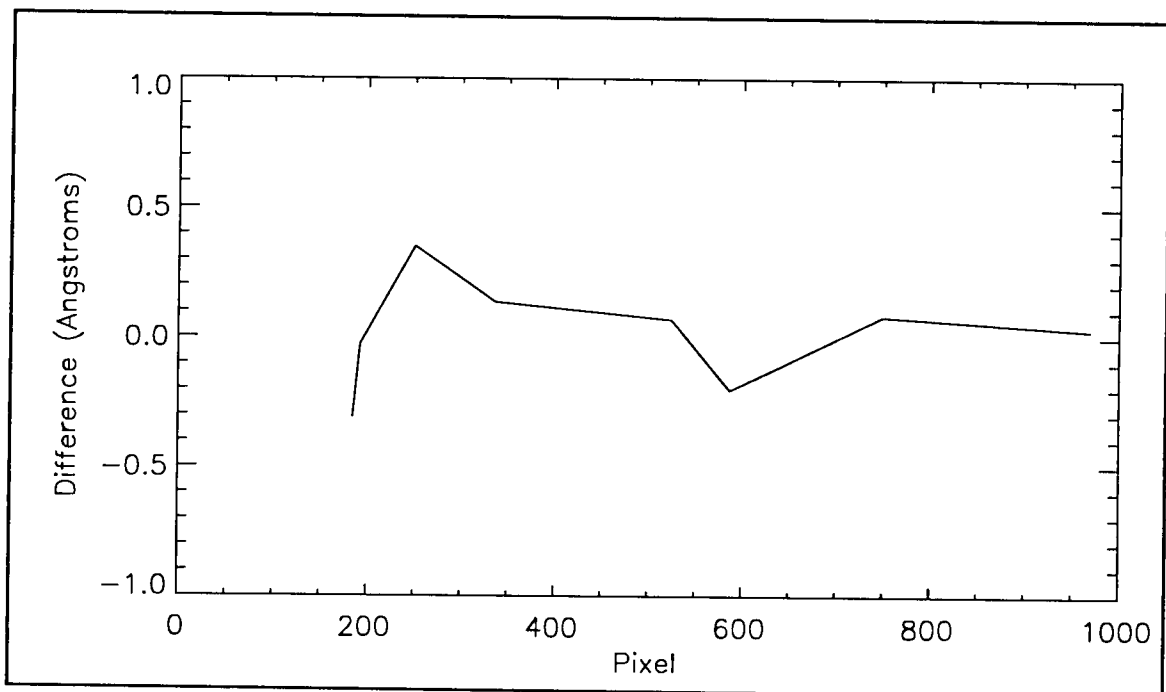


**Figure 7-18** Difference between quadratic fit and actual wavelengths at grating position TWO.

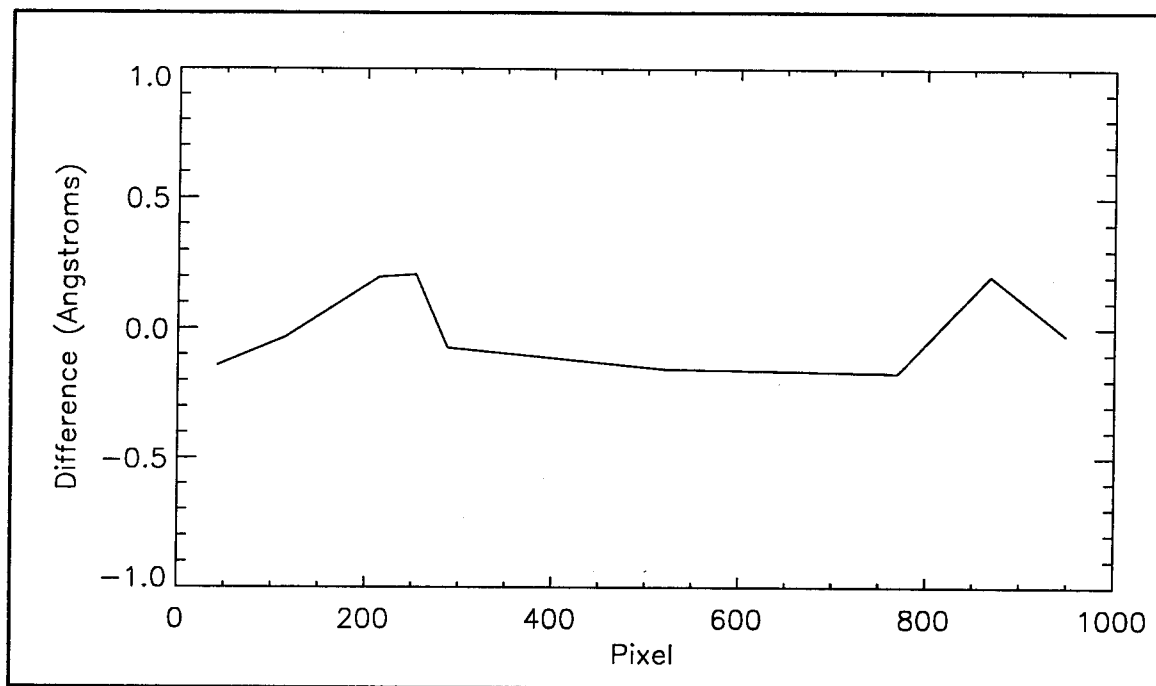


**Figure 7-19** Difference between quadratic fit and actual wavelengths at grating position THREE.

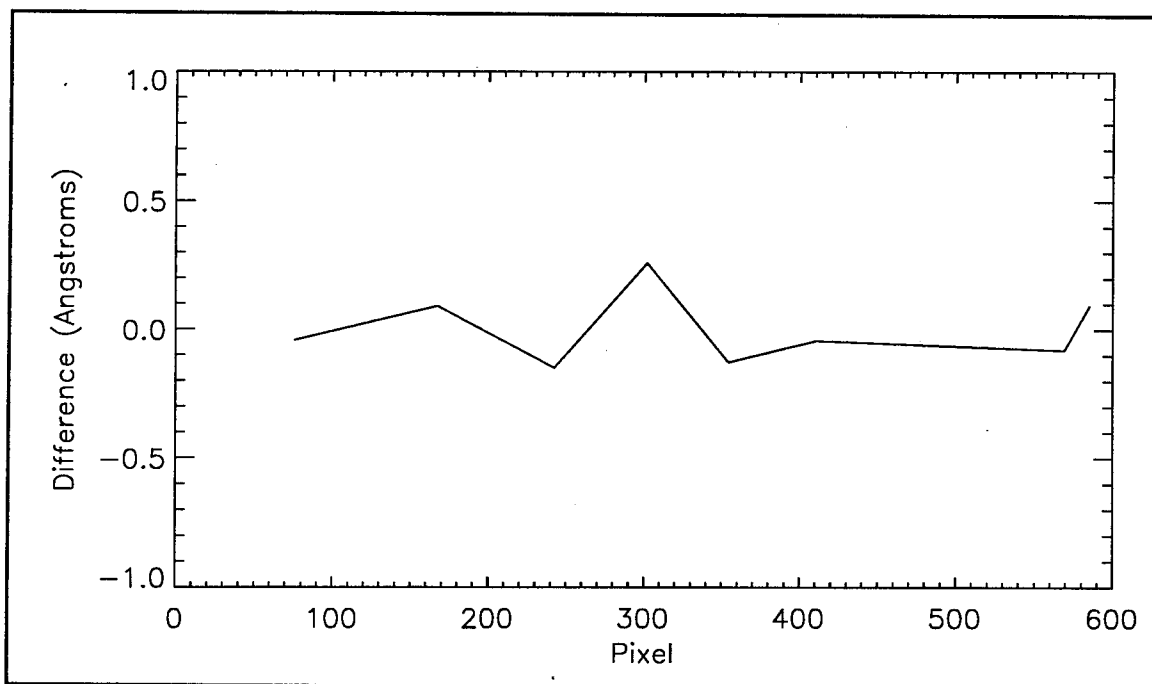


**Figure 7-20** Difference between quadratic fit and actual wavelengths at grating position FOUR.



#	SOURCE	WAVELENGTH (Å)				
		ACTUAL	LINEAR FIT	LINEAR ERROR	QUADRATIC FIT	QUADRATIC ERROR
1	Ne II	1916.08	1919.08	3.00	1916.09	0.01
2	Pt I	2084.59	2083.36	-1.23	2084.86	0.27
3	Pt I	2103.33	2101.36	-1.97	2102.95	-0.38
4	Pt I	2128.61	2127.11	-1.50	2128.70	0.09
5	Pt I	2174.67	2173.36	-1.31	2174.53	-0.14
6	Pt II	2190.32	2189.31	-1.01	2190.22	-0.10
7	Pt I	2202.22	2201.48	-0.74	2202.14	-0.08
8	Pt II	2245.52	2246.64	1.12	2246.08	0.56
9	Pt I	2274.38	2276.35	1.97	2274.72	0.34
10	Pt I	2289.27	2290.93	1.66	2288.70	-0.57

**Table 7-2** Identified spectral emissions, actual and calculated linear and polynomial wavelengths and corresponding errors in fit for grating position ONE.

#	SOURCE	WAVELENGTH (Å)				
		ACTUAL	LINEAR FIT	LINEAR ERROR	QUADRATIC FIT	QUADRATIC ERROR
11	Pt I	2289.27	2290.61	1.34	2288.96	-0.31
12	Pt I	2292.4	2293.87	1.47	2292.37	-0.03
13	Pt I	2318.29	2319.08	0.79	2318.64	0.35
14	Pt I	2357.1	2356.47	-0.63	2357.23	0.13
15	Pt I	2440.06	2438.19	-1.87	2440.13	0.07
16	Pt I	2467.44	2465.36	-2.08	2467.24	-0.2
17	Pt I	2487.17	2485.36	-1.81	2487.05	-0.12
18	Hg I	2536.51	2535.91	-0.6	2536.59	0.08
19	Pt I	2628.03	2631.41	3.38	2628.06	0.03

**Table 7-3** Identified spectral emissions, actual and calculated linear and polynomial wavelengths and corresponding errors in fit for grating position TWO.

#	SOURCE	WAVELENGTH (Å)				
		ACTUAL	LINEAR FIT	LINEAR ERROR	QUADRATIC FIT	QUADRATIC ERROR
20	Pt I	2628.03	2631.68	3.65	2627.89	-0.14
21	Pt I	2659.45	2661.04	1.59	2659.42	-0.03
22	Pt I	2702.4	2701.82	-0.58	2702.6	0.2
23	Pt I	2719.04	2717.72	-1.32	2719.25	0.21
24	Pt I	2733.96	2731.79	-2.17	2733.89	-0.07
25	Pt I	2830.3	2826.38	-3.92	2830.14	-0.16
26	Pt I	2929.79	2928.32	-1.47	2929.62	-0.17
27	Hg I	2967.28	2968.36	1.08	2967.49	0.21
28	Pt I	2997.97	3001.11	3.14	2997.94	-0.03

**Table 7-4** Identified spectral emissions, actual and calculated linear and polynomial wavelengths and corresponding errors in fit for grating position THREE.

#	SOURCE	WAVELENGTH (Å)				
		ACTUAL	LINEAR FIT	LINEAR ERROR	QUADRATIC FIT	QUADRATIC ERROR
29	Pt I	2929.79	2931.4	1.61	2929.75	-0.04
30	Hg I	2967.28	2967.5	0.22	2967.37	0.09
31	Pt I	2997.97	2997.16	-0.81	2997.82	-0.15
32	Hg I	3021.5	3020.77	-0.73	3021.76	0.26
33	Pt I	3042.64	3041.46	-1.18	3042.51	-0.13
34	Pt I	3064.71	3063.76	-0.95	3064.67	-0.04
35	Hg I	3125.67	3126.37	0.7	3125.59	-0.08
36	Hg I	3131.55	3132.69	1.14	3131.64	0.09

**Table 7-5** Identified spectral emissions, actual and calculated linear and polynomial wavelengths and corresponding errors in fit for grating position FOUR.



## VIII. CONCLUSIONS

### A. SUMMARY OF ISAAC DEVELOPMENT

This thesis presents the design and development of an electronic GSE interface for the ISAAC spectrograph. The important scientific and military contributions that this spectrograph is expected to provide were discussed and the background needed to explain these topics was reviewed. The details of the design and development of the hardware and software portions of the GSE were discussed. The hardware GSE was designed and produced to provide an electronic interface between the spectrograph and a Macintosh computer and also to provide power to the detector, stepper motor and the image intensifier. The software portion of the GSE was written using LabView 2.2 and it provides the ability to select the position of the movable grating and to obtain and record spectra. Finally, an initial wavelength calibration of the spectrograph was conducted using the completed GSE. Quadratic equations were obtained that enable correlation between detector pixel number and spectral wavelength accurate to within 0.5 Å.

The ISAAC GSE will be used to allow additional testing and calibration of the spectrograph prior to launch. Further calibration of the instrument will be required prior to integration with the HIRAAS experiment and the spacecraft bus and additional testing will be required during the integration process. Should problems arise during the integration process, this GSE will allow the instrument to be tested independent of the spacecraft bus and thus confirm that the spectrograph is responding properly to direction.

### B. POTENTIAL FOLLOW-ON WORK

The ISAAC spectrograph presents a wide array of future thesis opportunities to interested students. The GSE presented in this thesis can be further improved to test additional mechanical functions of the spectrograph as discussed in Chapter V. Modifications to the existing GSE will also be required upon completion of the spaceflight-qualified replacement driver/amplifier circuitry currently being designed and fabricated at NRL. This replacement for the C4350 Driver/Amplifier will also provide clocks to the detector shift

register. The NRL circuitry will also perform the A/D conversion, and so this function of the GSE will have to be modified.

Following launch a plethora of data will be available for analysis. Interested Computer Science or Space Systems Engineering students could develop a program to permit rapid analysis of these data. Interested Space Systems Operations students could follow the program management and integration of the spectrograph onto the HIRAAS experiment at NRL and eventually integration with the satellite bus. The ISAAC spectrograph will provide a wealth of research opportunities to interested students for many years into the future as the launch is conducted in 1996 and the satellite collects data for an estimated one-year life.

# APPENDIX A

## ITT F4145 INTENSIFIER TUBE TECHNICAL DATA



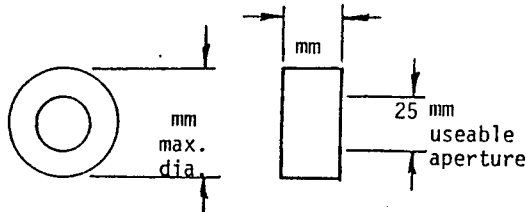
**ELECTRO-OPTICAL  
PRODUCTS DIVISION**

3700 East Pontiac Street  
P.O. Box 3700  
Fort Wayne, Indiana 46801

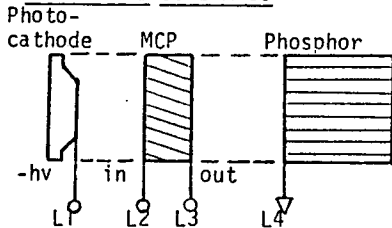
-DATA SHEET 1-

-PROXIMITY FOCUSED CHANNEL INTENSIFIER TUBE-

1.0 OUTLINE DRAWINGS



2.0 ELECTRICAL SCHEMATIC



3.0 LEAD CONNECTIONS

LEAD	COLOR	ELEMENT
1	Blue	Photocathode (neg.)
2	Red	MCP Input (neg.)
3	Orange	MCP Output (neg.)
4	Yellow	Phosphor (ground)

4.0 MAXIMUM OPERATING VOLTAGES \*

Cathode to MCP input	180	volts
MCP input to MCP output	1820	volts
MCP output to Phosphor	6000	volts
* voltages for	50,000 e	gain

4.1 USE WITH POWER SUPPLY

Model # 200057 S/N 0105

TUBE S/N XXH0967

TUBE TYPE F4145

CsTe/F.S.; P20/F0

DATE 06/91

5.0 CATHODE SENSITIVITY

- ua/lumen

6.0 RESOLUTION

- lp/mm  
@ - MCP volts

7.0 LUMINOUS GAIN

-

8.0 GAIN UNIFORMITY

13 %  
@ 50 K e gain

9.0 EQUIVALENT BACKGROUND INPUT

- lumens/cm<sup>2</sup>  
@ - gain

10.0 MCP VOLTAGE

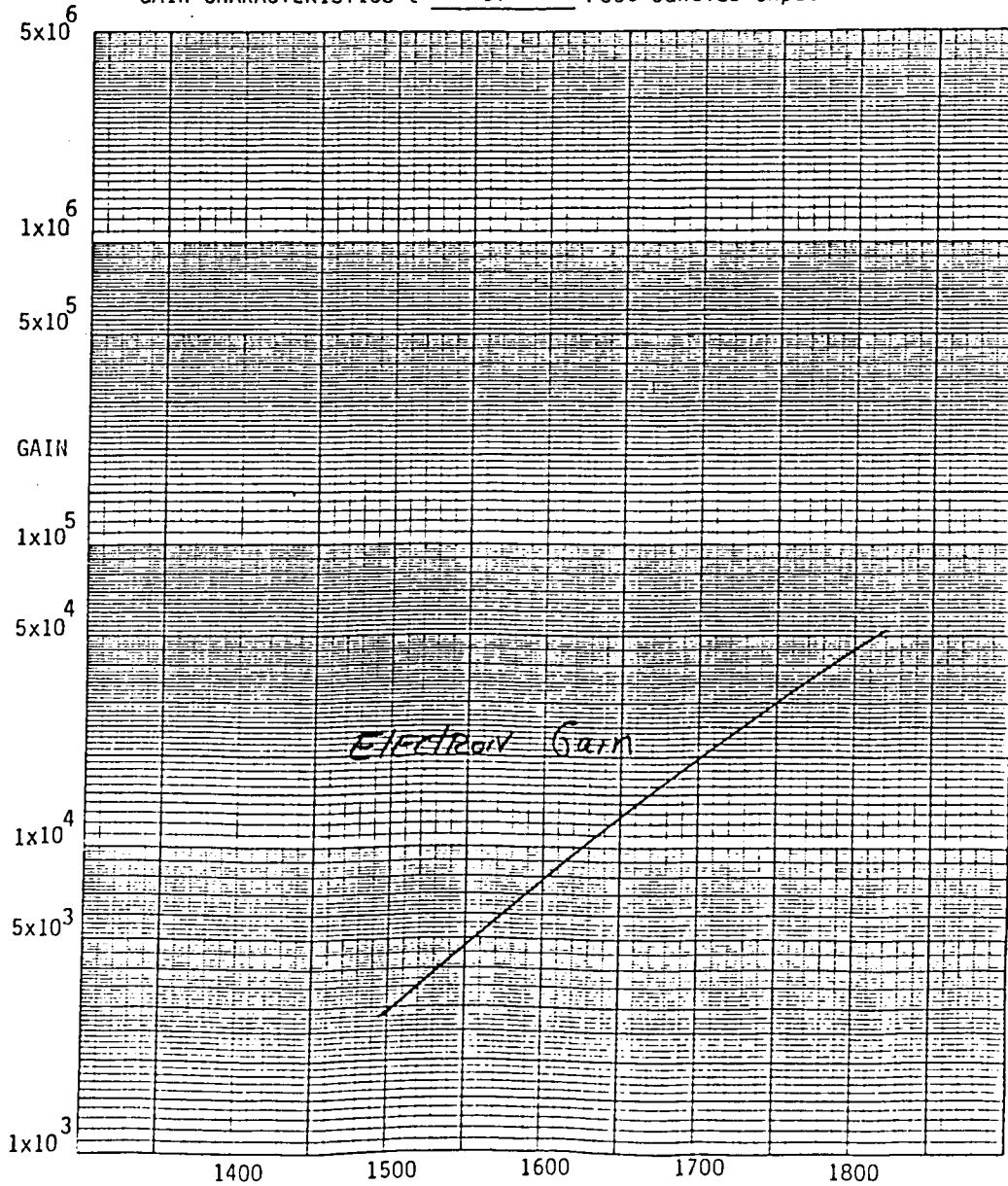
Set for 1820V at 10V Control



-PROXIMITY FOCUSED CHANNEL INTENSIFIER TUBE-

Tube S/N	<u>XXH0967</u>	Tube Type	<u>F4145</u>	Date	<u>02/90</u>
MCP Conductivity	<u><math>1.1 \times 10^{-5}</math></u>	amps @	<u>1000</u>	volts	
Photocathode Sensitivity	<u>—</u>	ua/L @	<u>—</u>	Lumens	
Photocathode Type/Window	<u>CsTe/F.S.</u>	Phosphor Type	<u>P20</u>		
Photocathode Voltage	<u>180</u>	Phosphor Voltage	<u>6000</u>		

GAIN CHARACTERISTICS @ UV Foot-Candles Input



TYPE F4145 Ser. No. XXH0967

SENSITIVITY

LUMINOUS N-A           $\mu\text{a/lumens}$

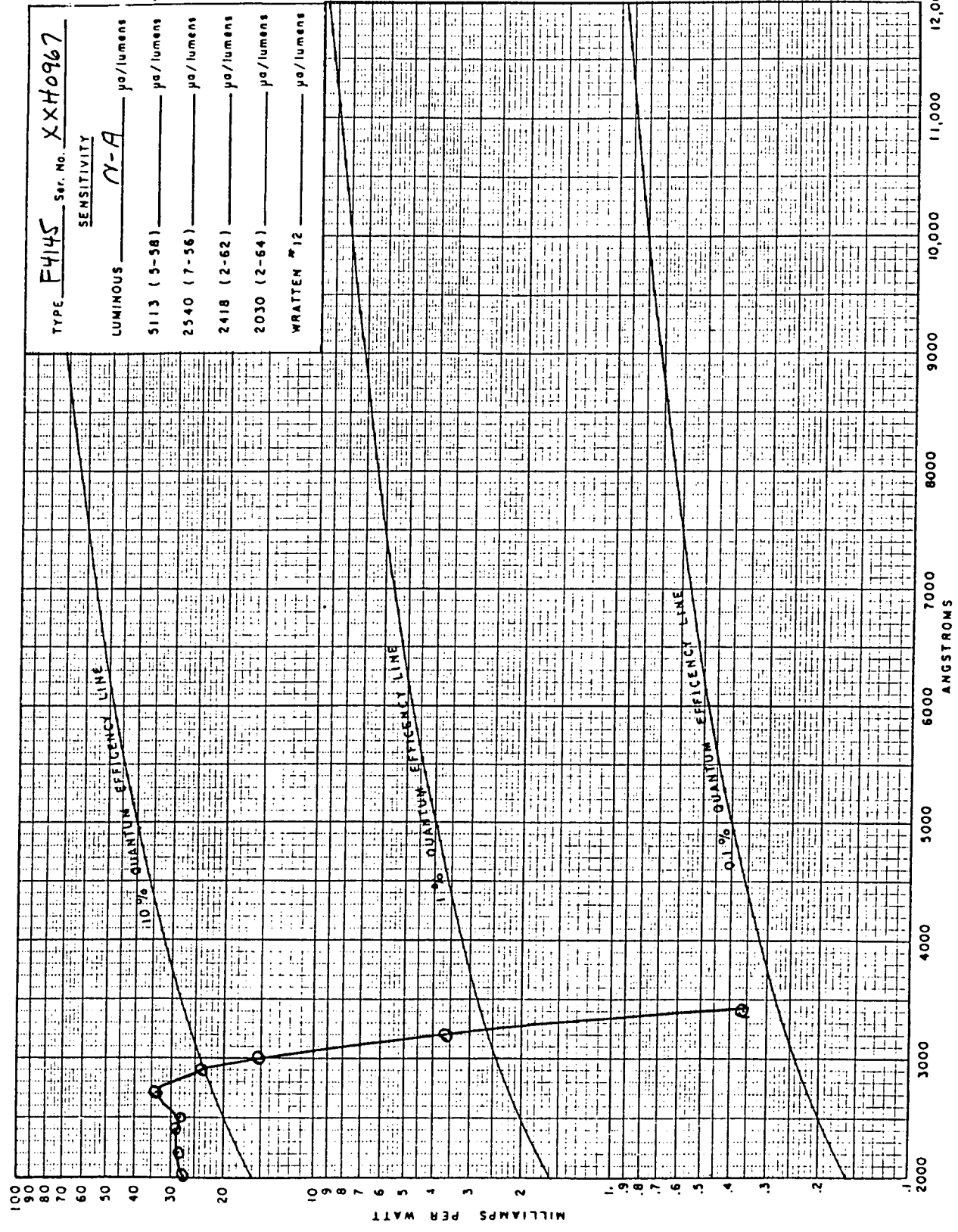
5113 (3-58)           $\mu\text{a/lumens}$

2540 (7-56)           $\mu\text{a/lumens}$

2418 (2-62)           $\mu\text{a/lumens}$

2030 (2-64)           $\mu\text{a/lumens}$

WRATTEN #12           $\mu\text{a/lumens}$





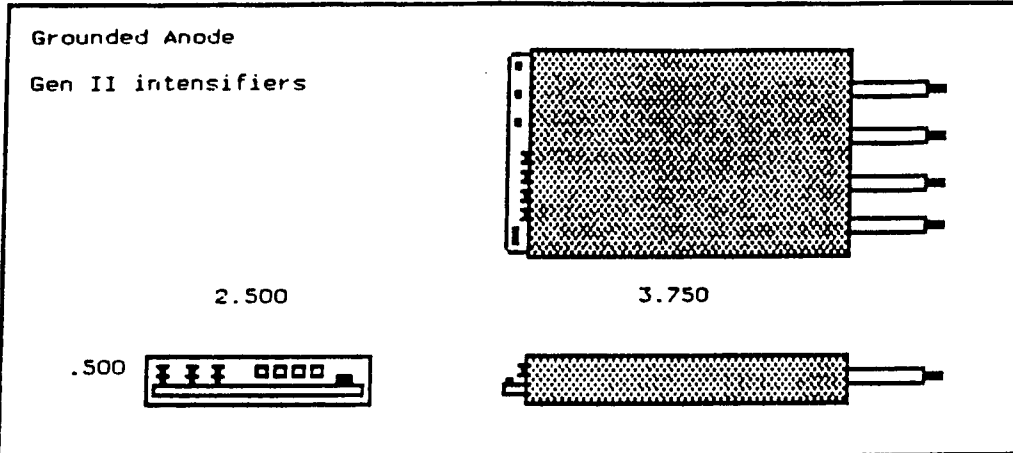
APPENDIX B

GBS HIGH-VOLTAGE MICRO POWER SUPPLY TECHNICAL DATA

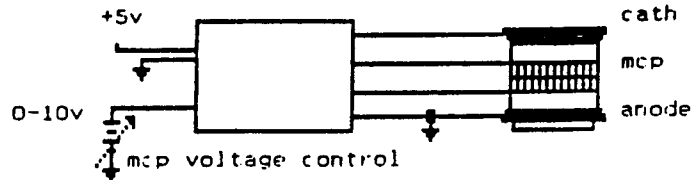
HV POWER SUPPLY

GEN II

REVITE



Model: 200057



- o Grounded Anode Gen II outputs
- o Adjustable cathode, mcp-in, mcp-out, and ABC level
- o Ext MCP voltage control
- o Ext resistor select - ABC max limit for desired tube dia

cathode voltage	min adjustable range	100 to 240	vdc
	cathode series resistance	1	Gohm
mcp-in voltage	voltage controllable	to 2kv max	vdc
	max load current	20	uA
mcp-out voltage	adjustable	3000 to 6500	vdc
	brightness current limit	.05 to 5	uA
anode output	ground return potential	0	vdc
temperature	operational	- 55 to + 70	C
mechanical	4-40 inserts bottom surface corners		

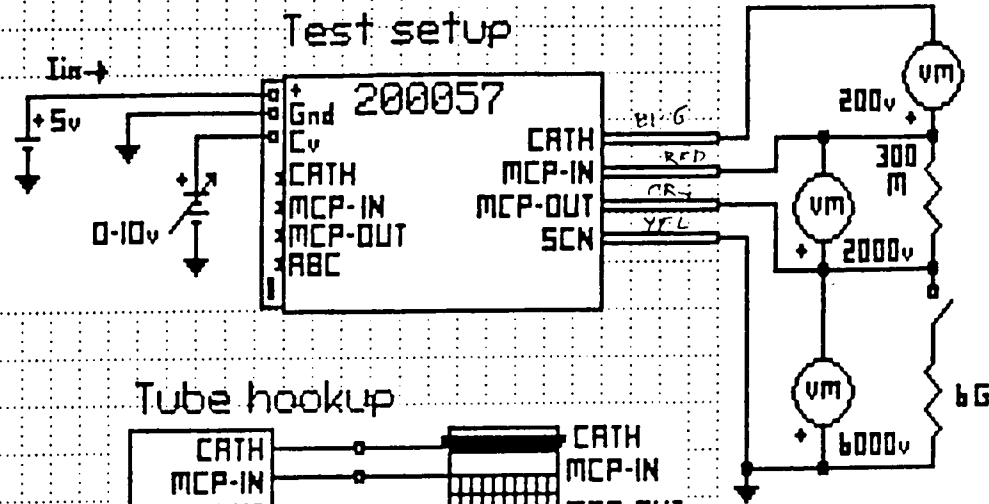
190079

GBS	NAME		Grounded Anode Gen II		DWG NUM		200057	
	SIZE	A	BY	GBS	DATE	07-27-86	SCALE	N/A
					REV	B	SHT	1 OF 1

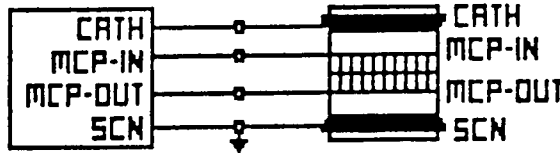
PS 200057 Test Data Sheet

180119

Test setup



Tube hookup



Test Data at Delivery S/N : CUD Date : 7-13-87 By : P.S.

Parameter	Data	Units
1. Cathode voltage @ no load	<u>2.00</u>	- VDC
Cathode voltage @ 1M	<u>4.5</u>	- VDC
2. Mcp-in voltage @ 300M @ Cv=10v	<u>1.700</u>	- VDC
8v	<u>1.700</u>	- VDC
6v	<u>1.600</u>	- VDC
4v	<u>2.00</u>	- VDC
2v	<u>2.70</u>	- VDC
3. Mcp-out voltage @ no load	<u>5.500</u>	- VDC
@ 1 uA load	<u>5.450</u>	- VDC
4. Rabc set value	<u>1.0</u>	megohm
ABC adj pot set for I-limit of	<u>1.0</u>	uA
5. Input current @ +5vdc @ ss	<u>8.1</u>	mADC
6. Burn-in	<u>4.8</u>	hrs
7. Mechanical and visual	<u>✓</u>	check

90126

**GBS**

NAME	PS 200057 Test Data Sheet			DWG NUM	200123						
SIZE	A	BY	GBS	DATE	02-16-87	SCALE	N/A	REV	A	SHT	1 OF 1

Operation and Instructions  
PS 200057 grounded anode standard GEN II

1.0 General

The model 200057 power supply is a small DC to DC converter which converts +5 vdc to multiple HV dc outputs for use by a Gen II image intensifier tube. The outputs are line regulated, and each is independently adjustable. The power supply circuitry is fully potted in an RTV encapsulant due to the high internal voltages generated, and due to the small size of the power supply.

Manufacturer : GBS Micro Power Supply  
6155 Calle Del Conejo  
San Jose, California 95120  
408-997-6720

2.0 Power Supply Inputs

The following inputs are available and marked on the power supply.

- |  |               |
|--|---------------|
| 1. Input voltage terminal                | +5 +/- .5 vdc |
| 2. Input voltage return terminal (gnd)   |               |
| 3. Voltage control terminal              | 0 to +10 vdc  |
| 4. Cathode output adj pot                |               |
| 5. MCP-IN output adj pot                 |               |
| 6. MCP-OUT output adj pot                |               |
| 7. ABC limit fine adjust pot             |               |
| 8. Rsel resistor for gross ABC limit adj |               |

3.0 Output Connections

There are 4 output leads for connection to the image intensifier.

- |                   |  |
|-------------------|--|
| 1. Cathode output | typically -175 vdc with respect to the MCP-IN output lead      |
| 2. MCP-IN output  | typically -1500 vdc with respect to the MCP-OUT output lead    |
| 3. MCP-OUT output | typically -2000 vdc with respect to the screen output lead     |
| 4. Screen output  | Gnd, and tied to the +5 return internally in the power supply. |

4.0 Voltage Control

The MCP voltage applied to the intensifier, is provided by the MCP-IN and MCP-OUT outputs, which is termed the MCP voltage. This voltage can be remotely varied from approximately -400 vdc, ( the oscillator drop out level ), to -2000 vdc, by varying the voltage applied to the voltage control terminal from 0 to +10 vdc. The +10 vdc results in -2000 vdc MCP voltage. An open at the voltage control terminal results in a 0 vdc MCP voltage.

90123

**GBS**

NAME PS 200057 operation & instructions					DWG NUM 200122	
SIZE A	BY DH	DATE 4-17-88	SCALE N/A	REV A	SHT 1	OF 3

FORM F15001

The -2000 vdc MCP voltage when the control voltage is at +10 vdc, can be lowered to near -400 vdc by adjusting the MCP-IN adjust pot counter clockwise. CW increases MCP voltage toward -2000. CCW reduces MCP voltage toward 0 vdc.

#### 5.0 Cathode Output

The cathode output is adjustable via a trim pot. CW increases the output to -250 vdc. CCW reduces the output to -100 vdc. A cathode current limiting resistor ( 1 Gigohm ) is internal in the power supply, and will drop the cathode voltage as excess tube cathode current is developed in high illumination conditions. When the cathode current, under these high current conditions, falls to approximately -3 vdc with respect to the MCP voltage, a diode in the power supply, shunts the 1 Gigohm limit resistor, with a 22 Megohm resistor, thereby extending the cathode current available, before eventual tube cutoff.

The cathode output is typically -175 vdc with respect to the MCP-IN output, but it is stacked on the other power supply outputs, so that with respect to ground, the potential on the cathode lead is approximately -9000 vdc. This high voltage is usually a source of trouble when operating the power supply, as leakage to gnd may often readily develop. This leakage will be treated by the power supply as ABC current, which is an instruction to the power supply to lower, or shut off the MCP-IN voltage. Caution is recommended in the testing of the power supply, and in the tube connections.

#### 6.0 MCP-out Voltage

The MCP-out is the voltage provided for the intensifier screen, and is -6000 vdc typically. This output is connected to the MCP-OUT intensifier lead. CW adjustment of the trim pot increases this voltage to -6500 vdc. CCW decreases the voltage to -3000 vdc. This high voltage is developed in the power supply by a stack of voltage doubler circuits. This multiplier circuit is resistor returned to gnd, so that any tube screen current flowing at any time, must pass through the resistor. A voltage is developed across the resistor, and is proportional to the tube screen current. The voltage developed, is compared to an ABC limit setting, and will shut down the MCP voltage to the tube, if the threshold level is reached.

#### 7.0 ABC

The R-select resistor ( externally available as Rsel ), is used to sense the tube screen current as described in paragraph 6.0. The power supply comparator for ABC, has a threshold level of 1 vdc and will shut down the MCP voltage when the Rsel voltage reaches this 1 vdc threshold. The choice of resistance for Rsel, then can determine at what tube current, shutdown is desired. Typically, Rsel is chosen as 1 Megohm, so that it allows ample current for normal tube use, but limits screen current to a maximum of 1 uA.

90119

<b>GBS</b>	NAME PS 20057 operation & instructions					DWO NUM 200122		
	SIZE <b>A</b>	BY DH	DATE 4-19-68	SCALE N/A	REV A	SHT 1	OF 1	

FORM F15001

The ABC trim pot allows fine resolution of the threshold voltage used by the shutdown comparator. CW increases the threshold to 1.0 vdc. CCW decreases the threshold voltage to 0 vdc. In this manner, the ABC pot can be used to fine tune the limit current circuitry for use as an automatic brightness control feature, ( ABC ).

The power supply has a 22 Megohm internal resistor in parallel with the external Rsel.  
 At delivery, Rsel is set to 1 Megohm, and the ABC pot is adjusted for so that 1 uA of screen current reduces the MCP voltage 50%.

**8.0 Mechanical, Leads**

The power supply chassis is glass epoxy with TRV potting internal. There are 4 Mounting inserts on the base of the power supply, 4-40 inserts.  
 The output leads are silicone coated teflon insulated stranded wires, rated for 15kv.

**9.0 Processing, Burn-in**

Standard processing prior to delivery includes 24 hrs of operation unpotted, at 23C, at nominal output voltage levels, followed by 48 hrs of operation at 23C, at typical output voltage levels, followed by a final electrical performance test at 23C.  
 Other tests and burn-in environments may be conducted as specified by the customer purchase order.

**10.0 Test Circuitry**

Electrostatic voltmeters or equivalent high input impedance ( > 300 Gighm ) divider probes are recommended when checking output voltage levels.  
 A dc voltage applied to Rsel can be used to simulate tube screen current for MCP shutdown verification. This voltage should not exceed 5 vdc, the input supply voltage.

20119

<b>GBS</b>	NAME PS 200057 Operation & Instructions					DWG NUM 200122		
	SIZE A	BY DH	DATE 4-17-88	SCALE N/A	REV A	SHT 5	OF 5	

FORM 15201





## APPENDIX C

# HAMAMATSU S3904 MOS LINEAR IMAGE SENSOR TECHNICAL DATA

**HAMAMATSU**  
TECHNICAL DATA

**SERIAL/CURRENT OUTPUT TYPE  
MOS LINEAR IMAGE SENSORS  
S3901, S3904 SERIES**

**Wide Sensitive Area (2.5mm Photodiode Height), High UV Sensitivity,  
Excellent Photometric Capabilities, Low Power Consumption**

### FEATURES

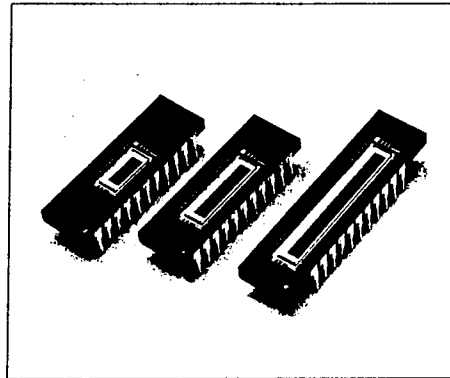
- Wide photosensitive area  
Photodiode pitch : 50 $\mu$ m (S3901), 25 $\mu$ m (S3904)  
Photodiode height : 2.5mm
- High UV sensitivity with good stability
- Excellent photometric capabilities  
Low dark current and high saturation charge  
Good linearity  
Wide dynamic range
- Low power consumption : less than 1mW
- Start pulse and clock pulses are CMOS logic compatible

### APPLICATIONS

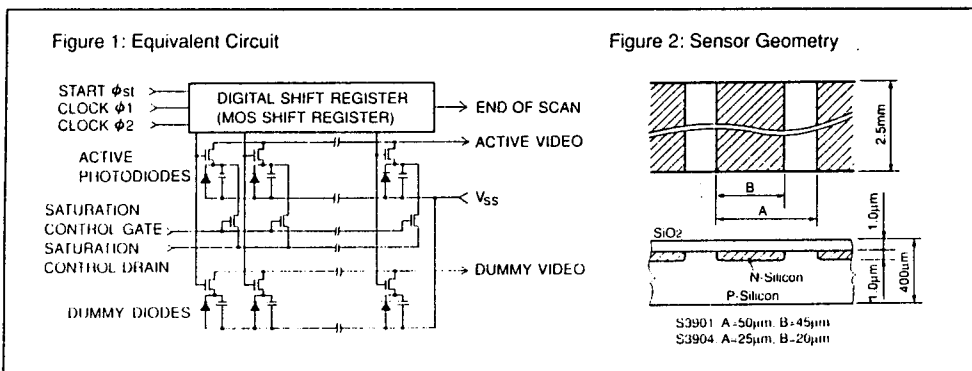
- Multichannel spectrophotometry
- Image readout systems

### DESCRIPTION

By applying NMOS technology to the manufacture of self-scanning linear photodiode arrays, Hamamatsu can offer higher performance and increased flexibility to photometric instrument manufacturers. The new design achieves high UV sensitivity without deterioration even with extended UV exposure. Application is simplified because of low power consumption and a single video output line. All members of the series are pin compatible.



The S3901 and S3904 series MOS linear image sensors feature a good output linearity over a wide dynamic range and have low power consumption. They have a wide photosensitive area with a photodiode height of 2.5mm and a photodiode pitch of 50 $\mu$ m (S3901) or 25 $\mu$ m (S3904). Each series is available with three different number of photodiodes; 128, 256 and 512 for the S3901 series, 256, 512 and 1024 for the S3904 series.



Information furnished by HAMAMATSU is believed to be reliable. However, no responsibility is assumed for possible inaccuracies or omission. Specifications are subject to change without notice. No patent rights are granted to any of the circuits described herein.

## MOS LINEAR IMAGE SENSORS S3901, S3904 SERIES

### MAXIMUM RATINGS

Parameters	Symbols	S3901, S3904 Series	Units
Supply Clock Amplitude	$V_{\phi}$	15	V
Operating Temperature (1)	$T_{opr}$	-40 to +65	°C
Storage Temperature	$T_{stg}$	-40 to +85	°C

(1) No dew

### ELECTRICAL CHARACTERISTICS (Ta=25°C)

Parameters	Symbols	S3901 Series			S3904 Series			Units
		Min.	Typ.	Max.	Min.	Typ.	Max.	
Video Bias Voltage (1)	$V_b$	1.5	$V_{\phi}$ -3.0	$V_{\phi}$ -2.5	1.5	$V_{\phi}$ -3.0	$V_{\phi}$ -2.5	V
Saturation Control Gate Voltage	$V_{scg}$	—	0	—	—	0	—	V
Saturation Control Drain Voltage	$V_{scd}$	—	$V_b$	—	—	$V_b$	—	V
Start Pulse Voltage ( $\phi_{st}$ ) (1)	-High	4.5	$V_{\phi}$	10	4.5	$V_{\phi}$	10	V
	-Low	0	—	0.4	0	—	0.4	V
Clock Pulse Voltage ( $\phi_1, \phi_2$ )	-High	4.5	5	10	4.5	5	10	V
	-Low	0	—	0.4	0	—	0.4	V
Start Pulse Rise/Fall Times ( $\phi_{st}$ )	$t_{r\phi_s}, t_{f\phi_s}$	—	—	500	—	—	500	ns
Start Pulsewidth ( $\phi_{st}$ )	$t_{pw\phi_s}$	200	—	—	200	—	—	ns
Clock Pulse Rise/Fall Times ( $\phi_1, \phi_2$ )	$t_{r\phi_1}, t_{r\phi_2},$	—	—	500	—	—	500	ns
	$t_{f\phi_1}, t_{f\phi_2}$	—	—	—	—	—	—	—
Clock Pulsewidth ( $\phi_1, \phi_2$ )	$t_{pw\phi_1}, t_{pw\phi_2}$	200	—	—	200	—	—	ns
Start Pulse ( $\phi_{st}$ ) and Clock Pulse ( $\phi_2$ ) Overlap	$t_{\phi_{ov}}$	200	—	—	200	—	—	ns
Clock Pulse Space	$X_1, X_2$	0	—	—	0	—	—	ns
Data Rate	$f$	0.1	—	2000	0.1	—	2000	kHz
Video Delay Time (50% of saturation) (2)	$t_{vd}$	—	80 (-128Q)	—	—	100 (-256Q)	—	ns
		—	120 (-256Q)	—	—	150 (-512Q)	—	ns
		—	160 (-512Q)	—	—	200 (-1024Q)	—	ns
Clock Pulse Line Capacitance ( $\phi_1, \phi_2$ ) at 5V bias	$C_{\phi}$	—	21 (-128Q)	—	—	27 (-256Q)	—	pF
		—	36 (-256Q)	—	—	50 (-512Q)	—	pF
		—	67 (-512Q)	—	—	100 (-1024Q)	—	pF
Saturation Control Gate Line Capacitance ( $V_{scg}$ ) at 5V bias	$C_{scg}$	—	12 (-128Q)	—	—	14 (-256Q)	—	pF
		—	20 (-256Q)	—	—	24 (-512Q)	—	pF
		—	35 (-512Q)	—	—	45 (-1024Q)	—	pF
Video Line Capacitance at 2V bias	$C_v$	—	7 (-128Q)	—	—	10 (-256Q)	—	pF
		—	11 (-256Q)	—	—	16 (-512Q)	—	pF
		—	20 (-512Q)	—	—	30 (-1024Q)	—	pF
Power Consumption	$P$	—	—	1	—	—	1	mW

(1)  $V_{\phi}$  is supply clock amplitude.

(2) Measured with a C4069 driver/amplifier circuit.

## ELECTRO-OPTICAL CHARACTERISTICS (Ta=25°C)

Parameters	Symbols	S3901 Series			S3904 Series			Units
		Min.	Typ.	Max.	Min.	Typ.	Max.	
Photodiode Pitch		—	50	—	—	25	—	μm
Photodiode Height		—	2.5	—	—	2.5	—	mm
Photodiode Dark Current ①	$I_d$	—	0.2	0.6	—	0.1	0.3	pA
Photodiode Capacitance ①	$C_{ph}$	—	20	—	—	10	—	pF
Spectral Response (10% of peak)	$\lambda$	200 to 1000			200 to 1000			nm
Wavelength of Peak Response	$\lambda_p$	—	600	—	—	600	—	nm
Saturation Exposure ① ②	$E_{sat}$	—	180	—	—	180	—	mlx·s
Saturation Charge ①	$Q_{sat}$	—	40	—	—	20	—	pC
Sensitivity Uniformity (50% of saturation, excluding first and last elements)		—	—	±3	—	—	±3	%

① Video bias voltage: 2.0V, Supply clock amplitude: 5.0V

② 2856 k Tungsten lamp

Figure 3: Typical Spectral Response

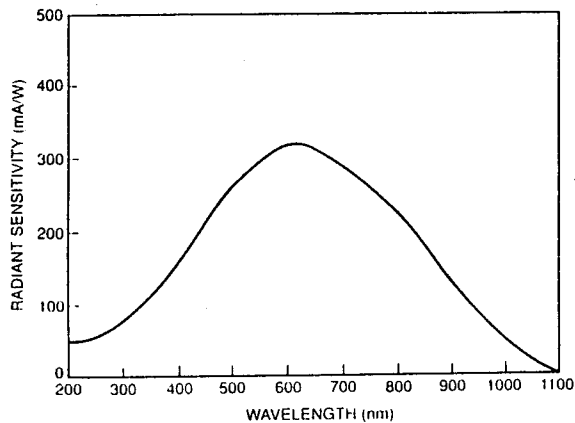
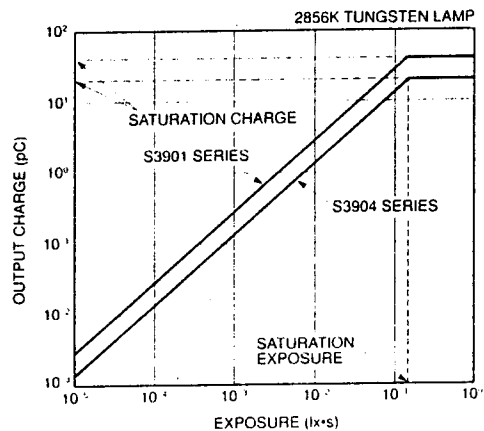


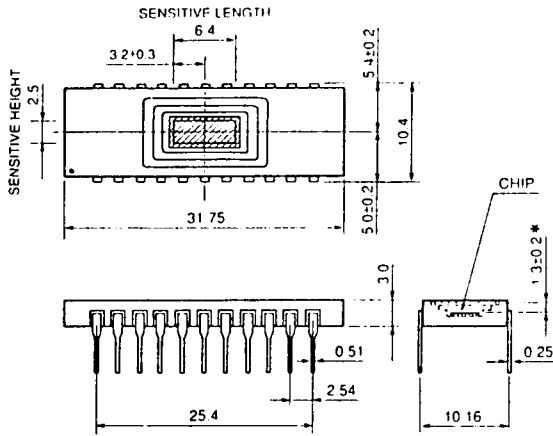
Figure 4: Output Charge vs. Exposure



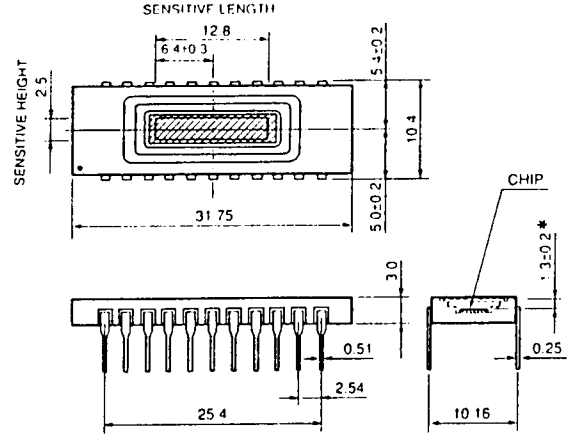
# MOS LINEAR IMAGE SENSORS S3901, S3904 SERIES

## DIMENSIONAL OUTLINES (Unit: mm)

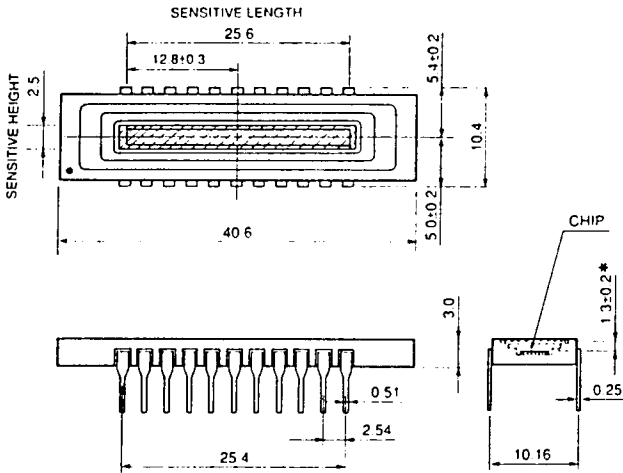
S3901-128Q  
S3904-256Q



S3901-256Q  
S3904-512Q



S3901-512Q  
S3904-1024Q



\* Optical distance from the outer surface of the quartz window to the chip surface.

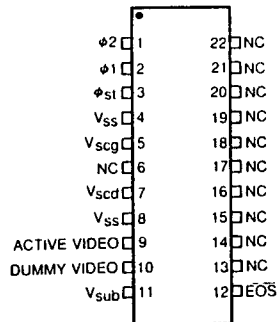
### • Mechanical Specifications

Parameters	S3901-128Q	S3901-256Q	S3901-512Q	S3904-256Q	S3904-512Q	S3904-1024Q	Units
Number of Photodiodes	128	256	512	256	512	1024	—
Ceramic Length	31.75		40.6	31.75		40.6	mm
Number of Pins	22			22			—
Window Material ①	Quartz			Quartz			—
Net Weight	3.0		3.5	3.0		3.5	g

① Fiber optic window is available

# HAMAMATSU

## PINOUT AND RECOMMENDED OPERATING CONDITIONS



$V_{ss}$ ,  $V_{sub}$  and NC should be grounded.

Terminals	Input or Output	Description
$\phi 1, \phi 2$	Input (CMOS logic compatible)	Pulses for operating the MOS shift register. As the video output signal is obtained synchronized with the rise of $\phi 2$ , the video data rate is equal to the clock pulse frequency.
$\phi_{st}$	Input (CMOS logic compatible)	Pulse to start operation of the MOS shift register. The time interval between start pulses is equal to the signal accumulation time.
$V_{ss}$	Passive node	Connected to the anode of each photodiode. This should be grounded.
$V_{scg}$	Input	Used for restricting blooming. This should be set at the base line of each input pulse and is normally the ground level.
$V_{scd}$	Input	Used for restricting blooming. This should be biased at a voltage equal to the video bias at all times.
ACTIVE VIDEO	Output	Video output signal. A positive voltage should be applied to the video line which connects the photodiode cathodes so that each photodiode is reverse-biased. It is recommended that the video bias be 2V when the amplitude of $\phi 1$ , $\phi 2$ and $\phi_{st}$ is at 5V.
DUMMY VIDEO	Output	This has the same structure as the active video, but is not connected to the photodiodes, so only spike noise is output. It should be biased at a voltage equal to the active video line. When in use otherwise, it should be open circuited.
$V_{sub}$	Passive node	Connected to the silicon substrate. This should be grounded.
EOS	Output (CMOS logic compatible)	This should be pulled up to 5V using a 10k $\Omega$ resistor. Negative polarity. The end of scan signal is obtained synchronized with $\phi 2$ right after the last photodiode is addressed.
NC		No connection. These should be grounded.

# MOS LINEAR IMAGE SENSORS S3901, S3904 SERIES

## DRIVER CIRCUIT

### • Driver Circuit

No DC supply voltage is required for driving the S3901 and S3904 series MOS linear image sensors. The  $V_{SS}$ ,  $V_{Sub}$  and all NC terminals should be grounded, however. Driving the MOS shift register requires a start pulse ( $\phi_{st}$ ) and two-phase clock pulses ( $\phi_1$ ,  $\phi_2$ ). The polarities of  $\phi_{st}$ ,  $\phi_1$  and  $\phi_2$  are positive and these pulses are CMOS logic compatible.

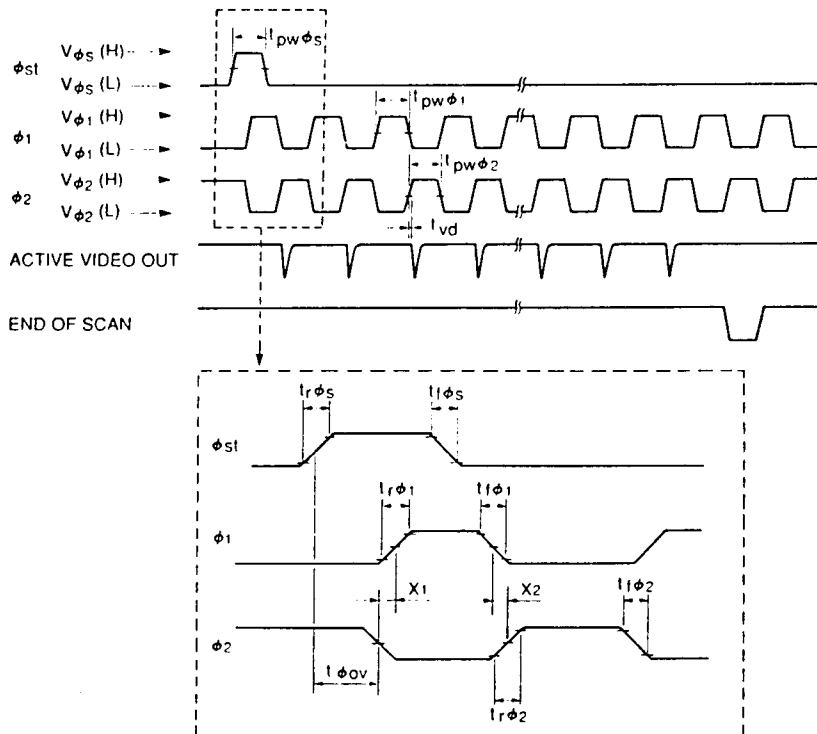
$\phi_1$  and  $\phi_2$  can be either fully separated or in the complementary relation. However, the overlap should not exist at the rise or fall edge between  $\phi_1$  and  $\phi_2$ . In other words,  $\phi_1$  and  $\phi_2$  must not be at the high level at the same time. The pulsewidth of  $\phi_1$  and  $\phi_2$  must be longer than 200 ns. Since the photodiode signal is obtained at the rise of every  $\phi_2$ , the clock pulse frequency determines the video data rate.

The amplitude of  $\phi_{st}$  should be equal to that of  $\phi_1$  and  $\phi_2$ . The shift register starts to read out the signal with the high level of  $\phi_{st}$ , so the time interval of each  $\phi_{st}$  determines the signal accumulation time. The pulsewidth of  $\phi_{st}$  must also be longer than 200ns and must be overlapped with  $\phi_2$  for at least 200ns. Moreover, in order to start the shift register normally,  $\phi_2$  must be changed only once from the high level to the low level during the high level of  $\phi_{st}$ . The timing diagram for each pulse is shown in Figure 5.

### • End of Scan ( $\overline{EOS}$ )

By wiring the  $\overline{EOS}$  terminal to 5V using a pull-up resistor of 10k $\Omega$ , the end of scan signal is obtained, synchronized with  $\phi_2$  right after the last photodiode is addressed.

Figure 5: Timing Diagram for Drive Circuit



### • Signal Readout Circuit

Signal readout methods consist of the current-detection mode (current-voltage conversion mode) using a resistive load and the current-integration mode using a charge amplifier. In either method, a positive bias must be applied to the video line because the photodiode anodes of a MOS linear image sensor are at 0V ( $V_{SS}$ ). Figure 6 shows the video bias voltage margin. Higher supply clock

amplitude allows larger video bias and saturation charge. Conversely, if the video bias is set at a low level with higher supply clock amplitude, the fall time of the video output waveform can be shortened. It is recommended that the video bias be set at 2V when the amplitude of  $\phi_1$ ,  $\phi_2$  and  $\phi_{st}$  is 5V.

To obtain a good output linearity, the current-integration mode is suggested. In this mode, immediately before each photodiode is addressed, the integration capacitance is reset at the reference voltage level, and when the address switch is turned on, the signal charge is accumulated in the integration capacitance. Figure 7 shows an example of the current-integration circuit and the pulse timing. To obtain a stable output, the rise edge

of the reset pulse should be delayed by at least 50 ns from the fall edge of  $\phi_2$ .

Hamamatsu provides driver/amplifier circuits; the C4070 for the current-integration mode and the C4069 for the current-voltage conversion mode. In addition, the C4091 pulse generator is available, which supplies these driver/amplifier circuits with a master start pulse and a master clock pulse.

Figure 6: Video Bias Voltage Margin

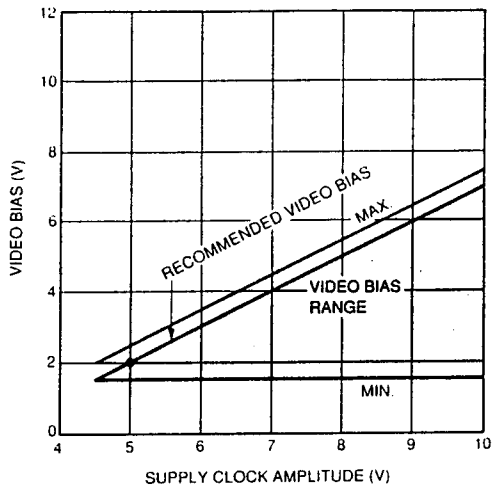
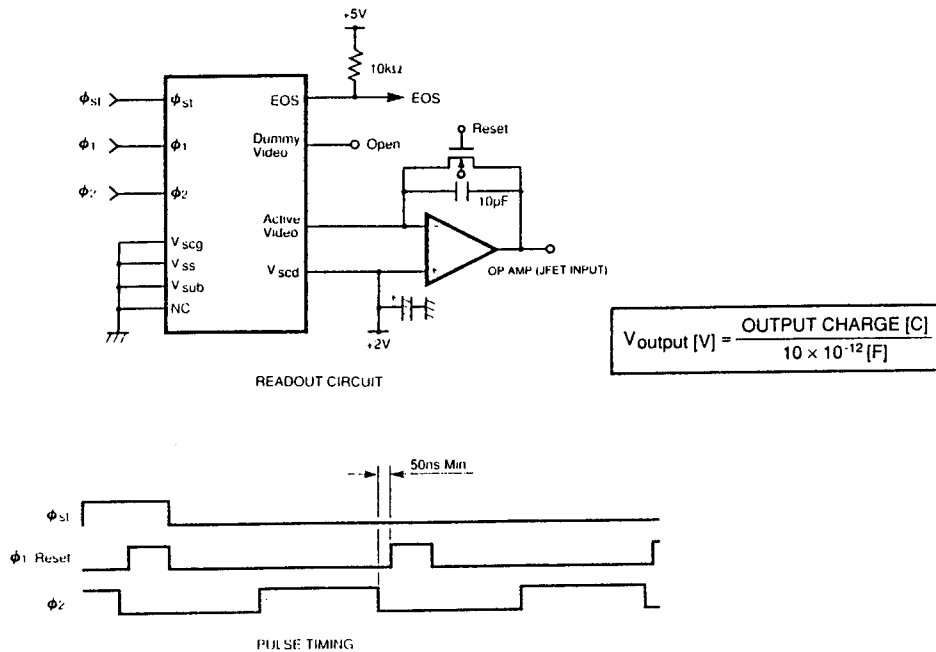


Figure 7: Recommended Readout Circuit and Timing Diagram





## MOS LINEAR IMAGE SENSORS S3901, S3904 SERIES

---

### • Operation for Anti-blooming

When light higher than the saturation exposure strikes the sensitive area, even partially, the photodiode in a MOS linear image sensor cannot accumulate a signal charge exceeding the saturation charge amount. The excess charge begins to overflow into the video line, thus causing deterioration of the signal purity. In order to eliminate this phenomenon, the saturation control drain should be set at a voltage equal to the video bias, and the gate should be grounded. Under normal operating conditions, the MOS linear image sensor will show an excellent antiblooming characteristic.

When a MOS linear image sensor is used at a light level lower than the saturation exposure, the same bias condition is applicable.

However, under extremely high contrast conditions, a voltage equal to the video bias should be applied to the saturation control drain. Also, a bias voltage (less than 1V) should be applied to the saturation control gate. The larger the bias voltage for the saturation control gate, the higher the saturation control function will be. However, a larger bias voltage also causes a decrease in the saturation charge amount.

### APPENDIX

#### 1) Operation for all photodiodes reset:

In normal operation, the charge accumulated in the photodiode is reset when the signal is read out. For the S3901 and S3904 series, the signal charge can be reset at a line other than the signal readout. This is done by adding an appropriate pulse to the saturation control gate. The amplitude of this pulse should be equal to  $\phi_1$ ,  $\phi_2$  and  $\phi_{st}$ , and the pulsewidth should be longer than  $5\mu s$ .

When the saturation control gate is set at the high level, all photodiodes are reset simultaneously at the potential of the saturation control drain. (Therefore, the saturation control drain should be set at the same potential as the video bias, and is typically 2V.) On the contrary, when the saturation control gate is set at the low level, the signal charge accumulates in the photodiode without a reset being carried out.

#### 2) Dummy video:

The S3901 and S3904 series have a dummy video line to eliminate the spike noise in the video output waveform. A video signal with lower spike noise can be obtained by the differential amplification of the active video line and the dummy video line outputs. But, in a normal operation, the dummy video line needs not to be used. Leave it unconnected.

## APPENDIX D

### HAMAMATSU C4070 DRIVER/AMPLIFIER TECHNICAL DATA

# HAMAMATSU

TECHNICAL DATA

## DRIVER/AMPLIFIER CIRCUIT C4070

#### For Serial/Current Output Type MOS Linear Image Sensors

The C4070 is a low-noise driver/amplifier circuit designed specifically for use with Hamamatsu serial/current output type MOS linear image sensors (S3901, S3904, S3902, S3903). The C4070 driver/amplifier circuit includes a generator for a start pulse and two-phase clock pulses used to drive a MOS linear image sensor and the charge amplifier used to read out the video signal in the integration mode. The signal inputs required are only a master start pulse, a master clock pulse, +5V and  $\pm 15V$ .

In addition, the C4091 pulse generator is available, which supplies the C4070 with a master start pulse and a master clock pulse.

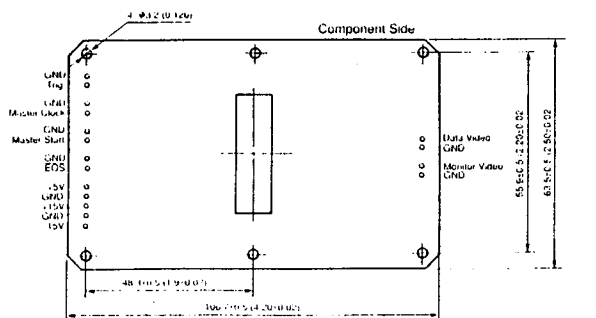
#### FEATURES

- Structure allows easy cooling and optical alignment of MOS image sensor
- Simple operation: only a master start pulse, a master clock pulse, +5V and  $\pm 15V$  required
- Low noise
- Wide dynamic range
- Simple adjustment

#### DESCRIPTIONS OF TERMINALS

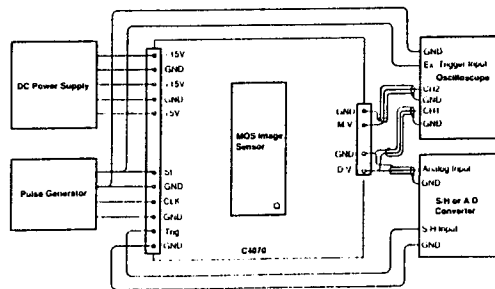
	Terminals	Symbols	Descriptions
Input	Supply Voltage	$V_d (+5)$ $V_a (+15)$ $(-15)$	+5 Vdc, 70 mA +15 Vdc, 30 mA -15 Vdc, 30 mA
	Master Start $\phi$ ms	St.	CMOS logic compatible. Positive logic. For initializing the circuit and the MOS shift register.
	Master Clock $\phi$ mc	CLK	CMOS logic compatible. The maximum frequency is 375 kHz. For synchronizing the circuit and the MOS shift register.
Output	Monitor Video	M.V.	Positive output. This is the integrated video signal from the MOS image sensor, and it is used for monitoring when cancelling the switching noises. Obtained synchronized with $\phi 2$ .
	Data Video	D.V.	Positive output. This is the integrated, low-noise video signal of the MOS image sensor.
	Sample-and-hold	Trig.	CMOS logic compatible. Positive logic. This output can be used as the trigger signal for the sample-and-hold or A/D conversion.
	End of Scan	EOS	CMOS logic compatible. Negative logic. This is the end-of-scan signal of the MOS shift register and it is obtained synchronized with $\phi 2$ right after the last element is scanned.

Figure 1: Dimensional Outline and Terminals



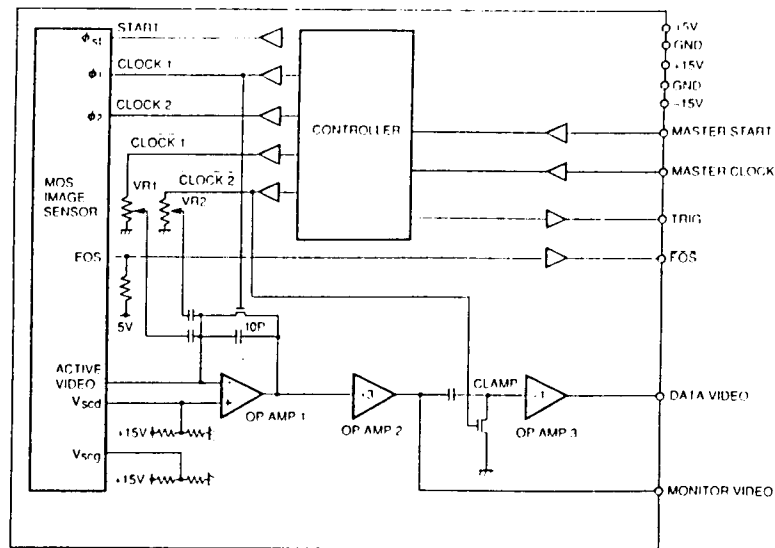
Dimensions in mm (inches)

Figure 2: Wiring Example



## DRIVER/AMPLIFIER CIRCUITS C4070

Figure 3: Block Diagram

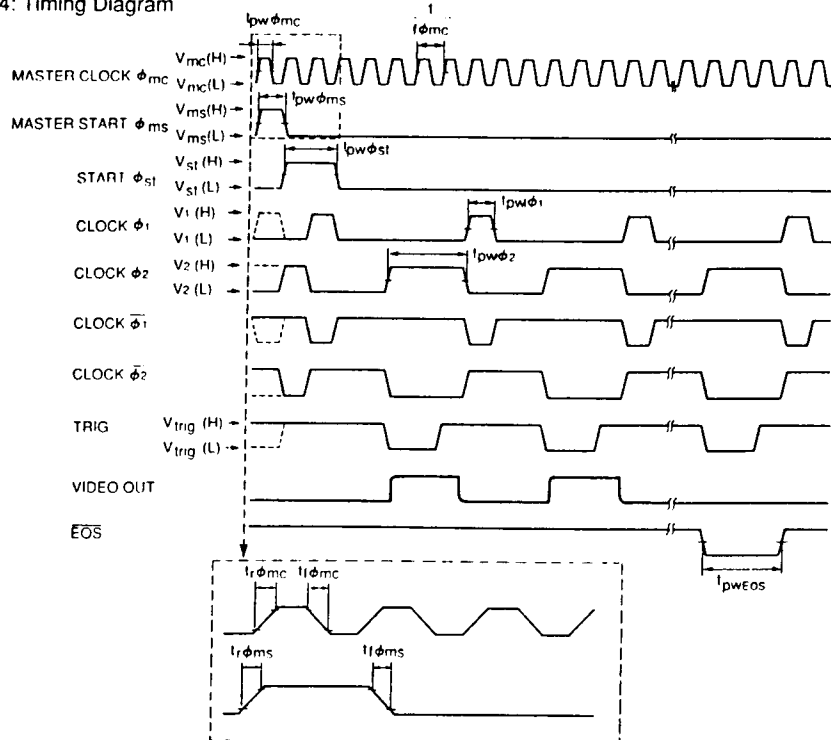


Caution)

The relation between the output charge from the MOS image sensor and the output voltage of the data video in the C4070 is represented by next equation.

$$V_{out} \text{ (DATA VIDEO) (V)} = 3 \times \frac{\text{OUTPUT CHARGE (C)}}{10 \times 10^{-12} \text{ (F)}}$$

Figure 4: Timing Diagram



## APPENDIX E

### HAMAMATSU C4070 DRIVER/AMPLIFIER OPERATION INSTRUCTION

# HAMAMATSU

OPERATION INSTRUCTION  
September, 1990

## DRIVER/AMPLIFIER CIRCUIT C4070

### For Serial/Current Output Type MOS Linear Image Sensors

The C4070 is a low-noise driver/amplifier circuit designed specifically for use with Hamamatsu serial/current output type MOS linear image sensors (S3901, S3904, S3902, S3903). The C4070 driver/amplifier circuit includes a generator for a start pulse and two-phase clock pulses used to drive the MOS linear image sensor and the charge amplifier used to read out the video signal in the integration mode. The signal inputs required are only a master start pulse, a master clock pulse, +5V and  $\pm 15V$ .

In addition, the C4091 pulse generator is available, which supplies the C4070 with a master start pulse and a master clock pulse.

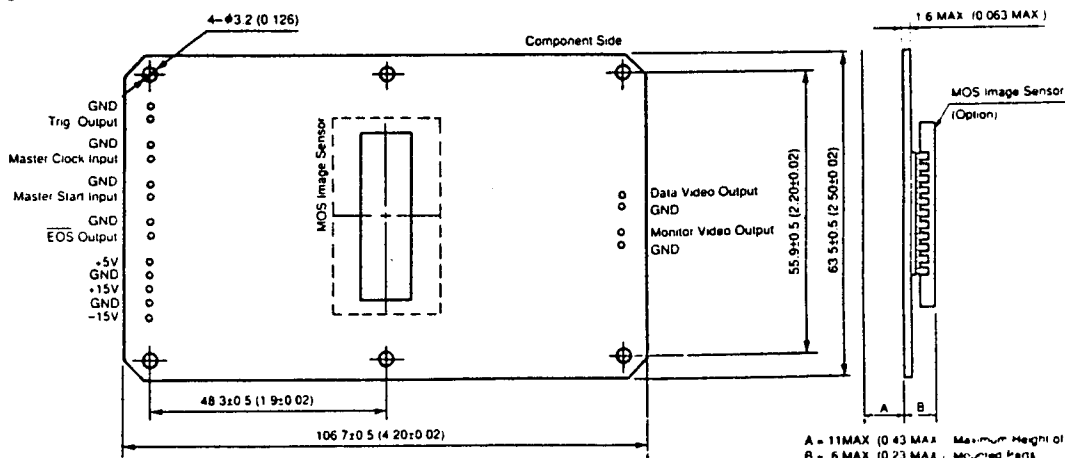
#### FEATURES

- Structure allows easy cooling and optical alignment of MOS image sensor
- Simple operation: only a master start pulse, a master clock pulse, +5V and  $\pm 15V$  required
- Low noise
- Wide dynamic range
- Simple adjustment

#### APPLICABLE MOS LINEAR IMAGE SENSORS

MOS Linear Image Sensor Type No.	Number of Photodiodes	Sensitive Area Per Element (Photodiode Pitch $\times$ Height)
S3901 - 128Q 256Q 512Q	128 256 512	50 $\mu$ m $\times$ 2.5mm
S3904 - 256Q 512Q 1024Q	256 512 1024	25 $\mu$ m $\times$ 2.5mm
S3902 - 128Q 256Q 512Q	128 256 512	50 $\mu$ m $\times$ 0.5mm
S3903 - 256Q 512Q 1024Q	256 512 1024	25 $\mu$ m $\times$ 0.5mm

Figure 1: Dimensional Outline and Terminals: mm (inches)



## DRIVER/AMPLIFIER CIRCUIT C4070

### MAXIMUM RATINGS

Parameters	Symbols	Ratings	Units
Line Source (Digital)	$V_d$	7	V
Line Source (Analog)	$V_a$	$\pm 18$	V
Operating Temperature	$T_{opr}$	50	$^{\circ}C$
Storage Temperature	$T_{stg}$	85	$^{\circ}C$

### ELECTRICAL CHARACTERISTICS ( $T_a=25^{\circ}C$ )

Parameters		Symbols	Min.	Typ.	Max.	Units
Input	Line Source (Digital)	$V_d$	4.85	5	5.5	V
	Line Source (Analog)	$V_a$	$\pm 14.5$	$\pm 15$	$\pm 15.5$	V
	Master Start Pulse ( $\phi_{ms}$ ) Voltage	$V_{ms}(H)$	2.0	5	—	V
		$V_{ms}(L)$	0	—	0.8	V
	Master Start Pulse ( $\phi_{ms}$ ) width $\text{\textcircled{1}}$	$t_{pw\phi_{ms}}$	$1/f_{\phi_{mc}}$	—	—	s
	Master Start Pulse ( $\phi_{ms}$ ) Rise/Fall Time	$t_{r\phi_{ms}}, t_{f\phi_{ms}}$	—	—	500	ns
	Master Clock Pulse ( $\phi_{mc}$ ) Voltage	$V_{mc}(H)$	2.0	5	—	V
		$V_{mc}(L)$	0	—	0.8	V
	Master Clock Pulse ( $\phi_{mc}$ ) Frequency	$f_{\phi_{mc}}$	—	—	375	kHz
Master Clock Pulse ( $\phi_{mc}$ ) width	$t_{pw\phi_{mc}}$	30	—	—	ns	
Master Clock Pulse ( $\phi_{mc}$ ) Rise/Fall Time	$t_{r\phi_{mc}}, t_{f\phi_{mc}}$	—	—	500	ns	
Output	Start Pulse ( $\phi_{st}$ ) Voltage	$V_{st}(H)$	4.75	—	5.4	V
		$V_{st}(L)$	—	—	0.4	V
	Start Pulse ( $\phi_{st}$ ) Rise/Fall Time	$t_{r\phi_{st}}, t_{f\phi_{st}}$	—	—	100	ns
	Start Pulse ( $\phi_{st}$ ) width	$t_{pw\phi_{st}}$	—	$2/f_{\phi_{mc}}$	—	s
	Clock Pulse ( $\phi_1, \phi_2$ )	$V_1, V_2(H)$	4.75	—	5.4	V
		$V_1, V_2(L)$	—	—	0.4	V
	Clock Pulse ( $\phi_1, \phi_2$ ) Rise/Fall Time	$t_{r\phi_1}, t_{r\phi_2}$	—	—	100	ns
		$t_{f\phi_1}, t_{f\phi_2}$	—	—	—	—
	Clock Pulse ( $\phi_1$ ) width	$t_{pw\phi_1}$	—	$1/f_{\phi_{mc}}$	—	s
	Clock Pulse ( $\phi_2$ ) width	$t_{pw\phi_2}$	—	$3/f_{\phi_{mc}}$	—	s
	End Of Scan Voltage	$V_{eos}(H)$	4.75	—	5.4	V
		$V_{eos}(L)$	—	—	0.4	V
	End Of Scan Rise/Fall Time	$t_{reos}, t_{feos}$	—	—	100	ns
End Of Scan Pulsewidth	$t_{pweos}$	—	$3/f_{\phi_{mc}}$	—	s	
Trigger Pulse Voltage	$V_{trig}(H)$	4.75	—	5.4	V	
	$V_{trig}(L)$	—	—	0.4	V	
Trigger Pulse Rise/Fall Time	$t_{rtrig}, t_{ftrig}$	—	—	100	ns	

$f_{\phi_{mc}}$  is Master Clock Frequency.

## DESCRIPTIONS OF TERMINALS

Terminals		Symbols	Descriptions
Input	Supply Voltage	$V_d (+5)$ $V_a (+15)$ $(-15)$	+5 Vdc, 70 mA +15 Vdc, 30 mA -15 Vdc, 30 mA
	Master Start $\phi_{ms}$	St.	CMOS logic compatible. Positive logic. For initializing the circuit and the MOS shift register.
	Master Clock $\phi_{mc}$	CLK	CMOS logic compatible. The maximum frequency is 375 kHz. For synchronizing the circuit and the MOS shift register.
Output	Monitor Video	M.V.	Positive output. This is the integrated video signal from the MOS image sensor, and is used as a monitor when cancelling the switching noise. Obtained synchronized with the $\phi_2$ .
	Data Video	D.V.	Positive output. This is the integrated, low-noise video signal of the MOS image sensor.
	Sample-and-hold	Trig.	CMOS logic compatible. Positive logic. This output is used for the timing signal for the sample-and-hold or A/D conversion.
	End of Scan	EOS	CMOS logic compatible. Negative logic. This is the end-of-scan signal of the MOS shift register and it is synchronized with the $\phi_2$ right after the last element is scanned.

## CONSTRUCTION OF CIRCUIT

Fig. 2 shows the block diagram of the C4070 driver/amplifier circuit. The C4070 is comprised of the following two main sections.

- 1) Control signal generator (controller)
- 2) Video signal processor

The control signal generator is made up of a PLD (programmable logic device). The PLD generates a start pulse ( $\phi_{st}$ ) and two phase clock pulses ( $\phi_1$  and  $\phi_2$ ) to scan the MOS shift register. The PLD also provides a reset signal and a DC restoration signal (clamp) for the signal processor, and a timing signal for the sample-and-hold or A/D conversion circuit. These signals are synchronized with the external master clock pulse, and are initialized by the master start pulse.

The video signal processor can be divided into four sections: (1) The first stage is a charge amplifier to integrate the current video signals from the image sensor. This charge amplifier has a reset switch in parallel to the feedback capacitance of 10pF. The video signal processor also includes a circuit to cancel the spike noise generated synchronized with two-phase clock pulses  $\phi_1$  and  $\phi_2$ . (2) The second stage is a non-inverting amplifier with a gain of 3, which acts as a low-pass filter also. This output is available via the monitor video terminal. (3) The next stage is a clamp circuit consisting of a capacitor and a switching element used for the DC restoration of video signals and the reduction of the reset noise generated in the first stage. (4) The last stage is a non-inverting amplifier with a gain of 1, also serving as a low-pass filter. Fig. 3 shows the timing diagram of each signal used in the C4070.

Since the photodiode anode of the MOS linear image sensor is at 0V ( $V_{ss}$ ), a positive bias must be applied to the video line so that each photodiode is reverse-biased. For the C4070, the video bias voltage is preset at 2V. As the MOS linear image sensor is operated in the charge

accumulation mode, the output signal obtained is proportional to the amount of light exposure (light intensity  $\times$  accumulation time). The accumulation time of each element of the MOS linear image sensor is equal to the interval between the master start pulses, on the other hand the readout time is determined by the master clock frequency. In the C4070, six master clock pulses are needed for the output of one element. Therefore, the readout time required for one element becomes six times the period of the master clock pulse.

In order to simplify the circuit configuration, the C4070 utilizes each pulse train efficiently. For example,  $\phi_1$  is used for both the supply clock for the MOS image sensor and the reset for the integration capacitance of the charge amplifier.  $\phi_1$  is equal to the 1/6th of the readout time.  $\phi_1$  is capacitively coupled to the inverting input terminal of the charge amplifier in order to cancel the switching noise that occurs with  $\phi_1$ .  $\phi_2$  is used only for the supply clock for the MOS image sensor. As the signal output of the MOS image sensor is obtained synchronized with  $\phi_2$ , 3/6th of the readout time is allotted for  $\phi_2$  for easy signal processing.  $\phi_2$  is also capacitively coupled to the inverted input terminal of the charge amplifier to cancel the switching noise occurs with  $\phi_2$ , and  $\phi_2$  is also used for the DC restoration signal for the clamp circuit. At the first-stage which is the charge amplifier, reset noise accompanying the reset of the integration capacitance is generated. This reset noise can be reduced during the clamping period which is the overlap between  $\phi_1$  (low) and  $\phi_2$  (high), however, noise reduction may become insufficient if the clamping period is short. The C4070 needs 5 $\mu$ s or longer for the clamping period. As stated above, the C4070 makes the efficient use of pulses, thus the pulsewidths of  $\phi_1$  and  $\phi_2$  are very different from each other.

## DRIVER/AMPLIFIER CIRCUIT C4070

The photodiodes of the MOS linear image sensor are designed for accept a high saturation charge. However, when light higher than the saturation exposure strikes the sensitive area, even partially, the photodiode cannot accumulate the signal charge in excess of the saturation charge. The excess charge begins to overflow into the

video line, thus causing deterioration of the signal. In order to eliminate this phenomenon in the MOS linear image sensor, the saturation control drain is biased at a voltage equal to the video bias (typically 2V), and the saturation control gate is grounded in the C4070.

Figure 2: Block Diagram

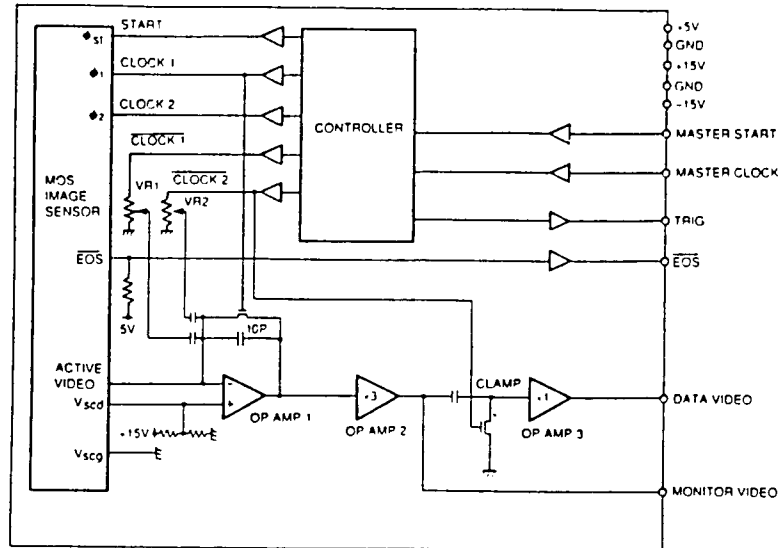
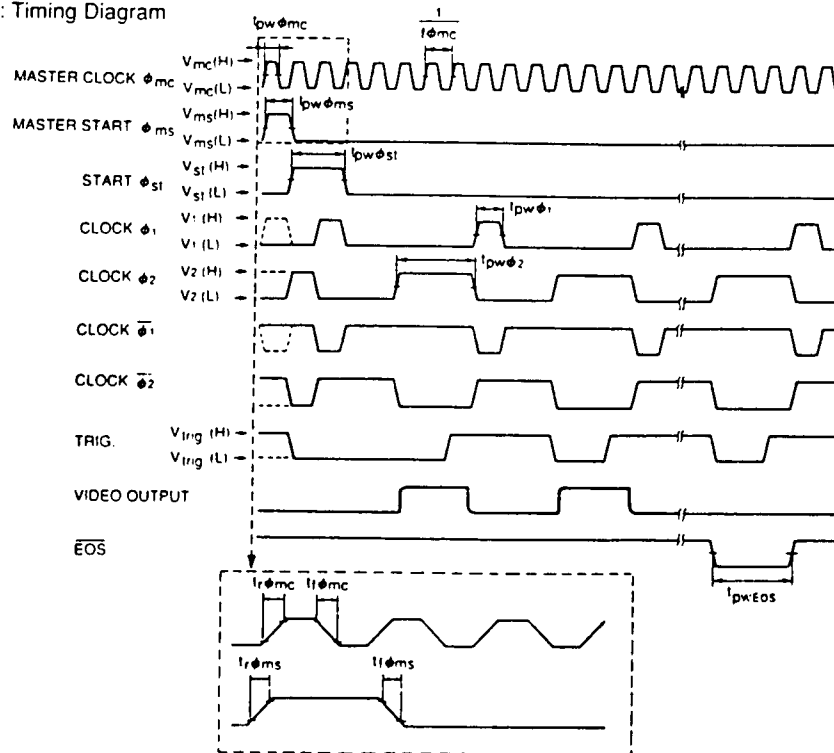


Figure 3: Timing Diagram



## CONNECTION TO PERIPHERAL DEVICES

Fig. 4 shows an example of the interconnection between the C4070 and peripheral devices. Referring to Fig. 4, follow the procedure below.

### 1) Connecting the Power Supply

Connect power sources (+5V,  $\pm 15V$ ) to the power input terminals of the C4070.

### 2) Connecting the Pulse Generator

Connect a pulse generator which generates a master start pulse and a master clock pulse to the input terminals (St. and CLK) of the C4070. Make sure to use a pulse generator that provides a master start pulse whose pulsewidth is longer than one period of the master clock pulse.

In the C4070, six master clock pulses are needed to read out one element (six dividing). Accordingly, the readout time required for one element becomes 6 times the master clock period. Hamamatsu also provides the C4091 pulse generator specially designed for the C4070.

### 3) Connecting the Oscilloscope

Connect the master start pulse terminal of the pulse generator to the trigger input of the oscilloscope, and also connect both the monitor video terminal (M.V.) and the data video terminal (D.V.) of the C4070 to the signal input terminal of the oscilloscope.

### 4) Connecting the Sample-and-Hold or A/D Converter

Connect the trigger pulse (Trig.) and the data video (D.V.) terminals of the C4070 to the timing input and the analog input terminal of the sample-and-hold or A/D converter, respectively.

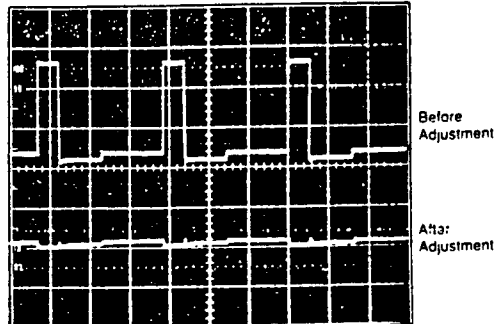
## SWITCHING NOISE CANCELLATION

There are two sources of switching noises generated in the C4070. One occurs synchronized with  $\phi 1$  and the other with  $\phi 2$ . These switching noises are canceled by taking  $\phi 1$  and  $\phi 2$ , which have an inverse phase relation.

into the inverting input terminals of the operational amplifier through a CR coupling circuit. The operational amplifier configures a charge amplifier.

When canceling the switching noises, the MOS linear image sensor should be light shielded, and while observing the monitor output on the oscilloscope, adjust variable resistors VR1 and VR2 until switching noise is minimized, as shown in the photographs below. VR1 is for noise cancellation of  $\phi 1$ , and VR2 is for  $\phi 2$ .

Adjustment of VR1



Adjustment of VR2

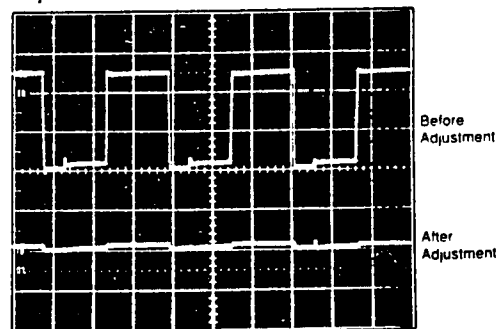
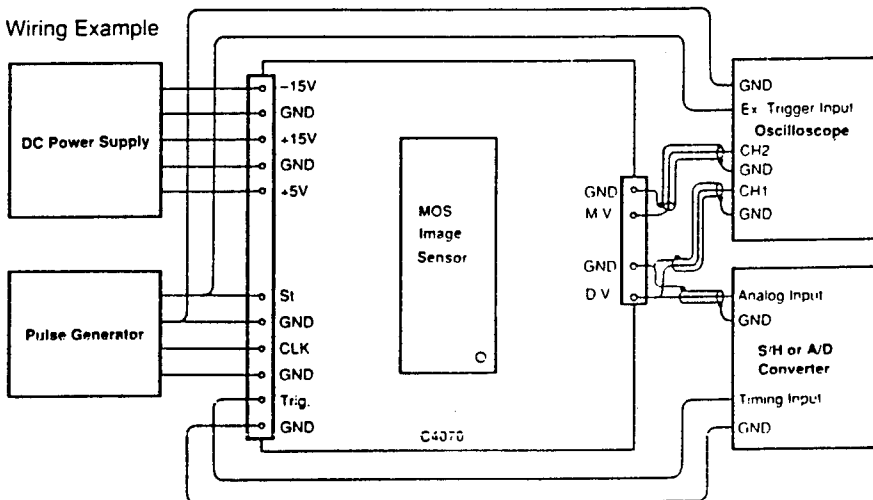


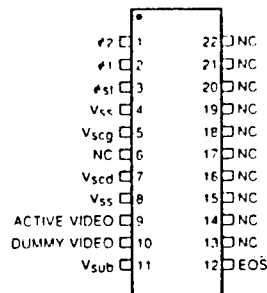
Figure 4: Wiring Example





## DRIVER/AMPLIFIER CIRCUIT C4070

PINOUT OF THE S3901, 02, 03 AND 04 MOS LINEAR IMAGE SENSOR USED WITH THE C4070



Terminals	Description
$\phi 1, \phi 2$	Pulses for operating the MOS shift register. As the video output signal is obtained synchronized with the rise of $\phi 2$ , the video data rate is equal to the clock pulse frequency.
$\phi_{st}$	Pulse to start operation of the MOS shift register. The time interval between start pulses is equal to the signal accumulation time.
$V_{ss}$	Connected to the anode of each photodiode. This terminal is grounded.
$V_{scg}$	Used for restricting blooming. This terminal is grounded.
$V_{scd}$	Used for restricting blooming. This terminal is biased at a voltage equal to the video bias.
ACTIVE VIDEO	Video output signal. A positive voltage is applied to the video line connecting the photodiode cathodes so that each photodiode is reverse-biased. The video bias is set at 2V.
DUMMY VIDEO	This is not used.
$V_{sub}$	Connected to the silicon substrate. This terminal is grounded.
EOS	The end of scan pulse is obtained synchronized with $\phi 2$ right after the last photodiode is addressed.
NC	No connection. These are grounded.

### IF NOT OPERATED NORMALLY

When the MOS linear image sensor does not operate normally, check the following.

- 1) Are the master start pulse and the master clock pulse properly supplied to the C4070?
- 2) Are the appropriate pulses, as shown in Fig. 3, supplied to pin 3 ( $\phi_{st}$ ), pin 2 ( $\phi 1$ ) and pin 1 ( $\phi 2$ ) of the MOS linear image sensor?
- 3) Are the end-of-scan pulse available from pin 12 (EOS) of the MOS linear image sensor?

## HAMAMATSU

HAMAMATSU PHOTONICS K.K., Solid State Division  
1126-1, Ichino-cho, Hamamatsu City, 435 Japan. Telephone 0534/34-3311. Fax: 0534-35-1037. Telex: 4225-185

U.S.A. Hamamatsu Corporation, 360 Foothill Road, P.O. Box 6910, Bridgewater, N.J. 08807. Telephone: 201-731-0300. Fax: 201-731-1522

W. Germany: Hamamatsu Photonics Deutschland GmbH, Arzbergerstr. 10, D-8034 Herrsching am Ammersee. Telephone: 49 8152 375 0. Fax: 49 8152 2658

France: Hamamatsu Photonics France, Z.A. Olympe, BP 5273, 3, Allée du Cdt Mourhon, Paray-Vieille-Poste 91781 Wilkoux Cedex.

Telephone: 331149 75 56 80. Fax: 331149 75 56 87

United Kingdom: Hamamatsu Photonics UK Limited, Loud Point, 2 Gladbeck Way, Windmill Hill, Entfield, Middlesex EN2 7JA, England. Telephone: 44 81 367 3560. Fax: 44 81 367 6394

North Europe: Hamamatsu Photonics Norden AB, Kanalgränd 20, S-141 81 Upplanda Väsby, Sweden. Telephone: 46 760 32190. Fax: 46 760 84567

SEP 90  
CA 100, P. 118G (1/90)

## APPENDIX F

### RSI MODEL 480-229 STEPPER MOTOR DRIVER TECHNICAL SPECIFICATIONS

The following tables provide technical specifications for the connector pinouts of the RSI Model 480-229 Stepper Motor Driver. Tables F-1 through F-3 give the description and function of each pin of the J1 through J3 connectors, respectively. Data is adapted from an RSI specification sheet.

Current requirements for this driver are as follows:

- +5 V Control power 125 mA
- +28 V Motor, Hold 100 mA
- +28 V Motor, Normal 150 mA
- +28 V Motor, 3X 220 mA

Specifications for the dust cover door solenoid are as follows:

- Voltage 22 - 34 VDC
- Coil resistance @ 20 °C 4.85 Ohms
- Test current 4.10 A @ +45 °C

<b>PIN</b>	<b>DESCRIPTION</b>	<b>FUNCTION</b>
1	+5 V Input	Control power input
2	+5 V Input	Control power input
3	+5 V Input	Control power input
4	+5 V Input	Control power input
5	Motor Step Repeat	Buffered TTL image of the Motor Step input signal referenced to control return.
6	Motor Step Input	Active Low TTL input. Motor steps on each negative edge.
7	Motor Current Monitor	TTL Square wave output.
8	Fiducial Output	TTL buffered output from J2-6.
9	Not Used	Not used.
10	Not Used	Not used.
11	+28 V Solenoid Return	Solenoid power return.
12	Micro "Y" Normally Closed (Cover Closed)	Microswitch status. Continuity between this pin and pin 15 indicates dust cover door closed.
13	+28 V Solenoid	Solenoid power.
14	Micro "Y" Normally Open (Cover Closed)	Microswitch status. Continuity between this pin and pin 15 indicates dust cover door open.
15	Micro "Y" Common (Cover Closed)	Cover closed common.
16	Micro "X" Normally Open (Cover Open)	Microswitch status. Continuity between this pin and pin 17 indicates dust cover door closed.
17	Micro "X" Common (Cover Open)	Cover open common.
18	Micro "X" Normally Closed (Cover Open)	Microswitch status. Continuity between this pin and pin 17 indicates dust cover door open.

**Table F-1** J1 Connector pinouts / function.

PIN	DESCRIPTION	FUNCTION
19	Fiducial Out	Redundant with pin 8.
20	5 V Return	Control power return.
21	5 V Return	Control power return.
22	5 V Return	Control power return.
23	5 V Return	Control power return.
24	Chassis Common	Chassis common.
25	+ 28 V Stepper Motor	Stepper motor power. 1 A maximum.
26	28 V Motor Return	Stepper motor return.
27	Not Used	Not used.
28	Not Used	Not used.
29	Primary Motor Power	Activates primary motor drive circuits. Referenced to control return. Active low enable.
30	Secondary Motor Power	Activates secondary motor drive circuits. Referenced to control return. Active low enable.
31	Normal Motor Power	Activates normal motor power. Referenced to control return. Active low enable.
32	3X Motor Power	Activates three times normal motor power. Short duration only. Referenced to control return. Active low enable.
33	Run Motor Power	Activates motor run circuit. Referenced to control return. Active low enable.
34	Hold Motor Power	Activates motor hold circuit. Minimal motor holding power referenced to control return. Active low enable.
35	Not Used	Not used.
36	Not Used	Not used.
37	Not Used	Not used.

**Table F-1** J1 Connector pinouts / function (continued).

PIN	DESCRIPTION	FUNCTION
1	Motor $\phi 1$	Motor phase 1. Referenced to +28 V motor ret.
2	Motor $\phi 2$	Motor phase 2. Referenced to +28 V motor ret.
3	Motor $\phi 4$	Motor phase 4. Referenced to +28 V motor ret.
4	+5 V Fiducial Return	Fiducial diode return output. Connected to control return output.
5	+5 V Fiducial Power	Fiducial Diode power output. 15 mA maximum. Referenced to control return.
6	Fiducial Signal	Fiducial input. TTL, active low.
7	Not Used	Not used.
8	Not Used	Not used.
9	Motor CT	Motor centertap. Referenced to +28 V motor return.
10	Motor $\phi 3$	Motor phase 3. Referenced to +28 V motor ret.
11	Chassis Common	Motor shield.
12	+5 V Fiducial Phototran. Return	Fiducial input return. Referenced to control return.
13	Not Used	Not used.
14	Not Used	Not used.
15	Not Used	Not used.

**Table F-2** J2 Connector pinouts / function.

PIN	DESCRIPTION	FUNCTION
1	Not Used	Not Used.
2	28 V Solenoid Return	Solenoid return.
3	+28 V Solenoid	Solenoid power.
4	Micro "X" NO (Cover Open)	Microswitch status. Continuity between this pin and pin 6 indicates dust cover door closed.
5	Micro "X" NC (Cover Open)	Microswitch status. Continuity between this pin and pin 6 indicates dust cover door open.
6	Micro "X" Common	Cover open common.
7	Micro "Y" NO (Cover Closed)	Microswitch status. Continuity between this pin and pin 9 indicates dust cover door open.
8	Micro "Y" NC (Cover Closed)	Microswitch status. Continuity between this pin and pin 9 indicates dust cover door closed.
9	Micro "Y" Common	Cover closed common.

**Table F-3** J3 Connector pinouts / function.

# RESEARCH SUPPORT INSTRUMENTS

## TEST REPORT

### STEPPER MOTOR DRIVER

MODEL NUMBER: 480-229  
SERIAL NUMBER: 305601

#### A: MOTOR TEST

<u>+28V</u> CURRENT ( mA )	CURRENT MONITOR ( Hz )	MOTOR CENTER TAP ( V )	TP1 ( V )	CONDITION
170.1	13.1K	13.60	1.49	MOTOR NORMAL
169.7	13.1K	13.62	1.49	MOTOR RUN
168.9	13.1K	13.71	1.49	MOTOR PRIMARY

#### B: STEP TEST

DIRECTION OF MOTOR WHEN MOTOR STEPS PULSED ? CLOCKWISE .

STEP FREQUENCY 196 Hz

#### C: PRIMARY/SECONDARY MOTOR DRIVE TEST

##### PRIMARY:

Q1 .46 Ohms    Q2 .34 Ohms    Q3 .33 Ohms    Q4 .33 Ohms  
Q5 193.7KOhms    Q6 193.7KOhms    Q7 193.7KOhms    Q8 193.7KOhms

##### SECONDARY:

Q1 193.7KOhms    Q2 193.7KOhms    Q3 193.7KOhms    Q4 193.7KOhms  
Q5 .35 Ohms    Q6 .33 Ohms    Q7 .35 Ohms    Q8 .33 Ohms

# RESEARCH SUPPORT INSTRUMENTS

## TEST REPORT

### STEPPER MOTOR DRIVER

MODEL NUMBER: 480-229  
SERIAL NUMBER: 305601

#### D: MOTOR POWER TEST

<u>+5V</u> CURRENT ( mA )	<u>+28VMOT</u> CURRENT ( mA )	<u>+28VDET</u> CURRENT ( mA )	CURRENT MONITOR ( Hz )	MOTOR CENTER TAP ( V )	CONDITION
126.9	82.5	11.1	4.25K	5.75	MOTOR HOLD
127.4	149.7	11.1	11.40K	14.87	MOTOR NORMAL
127.8	212.0	11.1	17.70K	22.90	MOTOR 3 TIMES

#### E: FIDUCIAL TEST

FIDUCIAL OUTPUT .14 V ( OPEN )

FIDUCIAL OUTPUT 4.16 V ( BLOCKED )

#### F: DETECTOR POWER TEST

DETECTOR ON: 28.0 V

DETECTOR OFF: 00.0 V

#### NOTE:

TEST BOARD REQUIRES +5V AT 25mA, +28V MOTOR AT 12mA, +28V  
DETECTOR AT 11mA.

SIGNATURE



DATE

09/01/93





## APPENDIX G

### ISAAC GSE USER'S MANUAL

This appendix serves as a guide to operation of the GSE hardware and software. It discusses how the components of the GSE hardware are connected and monitored during operation and also detail the operation of the ISAAC GSE software. It is intended that this guide will provide a simple guide for the user that does not require the detail presented in the thesis to which this manual appends.

#### A. ISAAC GSE HARDWARE SETUP AND OPERATION

The ISAAC GSE consists of the ISAAC GSE Electronics Interface Box, four cables labeled A through D, and a Macintosh computer with an installed NB-MIO-16 board and running the ISAAC GSE software. This GSE is connected to the ISAAC spectrograph and its stepper driver and high voltage power supply. The ISAAC GSE Electronics Interface Box is the hardware interface that couples all components of the GSE. This box, shown in Figure G-1, has four I/O connectors labeled GSE-1 through GSE-4 that provide interconnection to the various components. The overall GSE connected to the spectrograph is represented in Figure G-2.

Cable A is the cable with a 37-pin and a 25-pin I/O connector on each end. Connect this cable to GSE-1 on the electronic interface box and connect the 37-pin I/O connector to the 37-pin I/O connector on the RSI Stepper Driver. Two other I/O connectors (15-pin and 9-pin) on this stepper driver are for connection to the cables that extend from the ISAAC Stepper Motor and the Dust Cover Solenoid. Cable B is a 15-pin to 15-pin serial cable that is connected between the ISAAC detector output I/O connector and the GSE-2 I/O connector on the electronics interface box. Cable C is a cable extending from the GBS High-Voltage Power Supply terminating in a 9-pin I/O connector. This cable is connected to the electronic interface box I/O connector labeled GSE-4. Cable D is a 50-lead ribbon cable that connects between the GSE interface box and the NB-MIO-16 I/O connector at the back of the Macintosh computer.

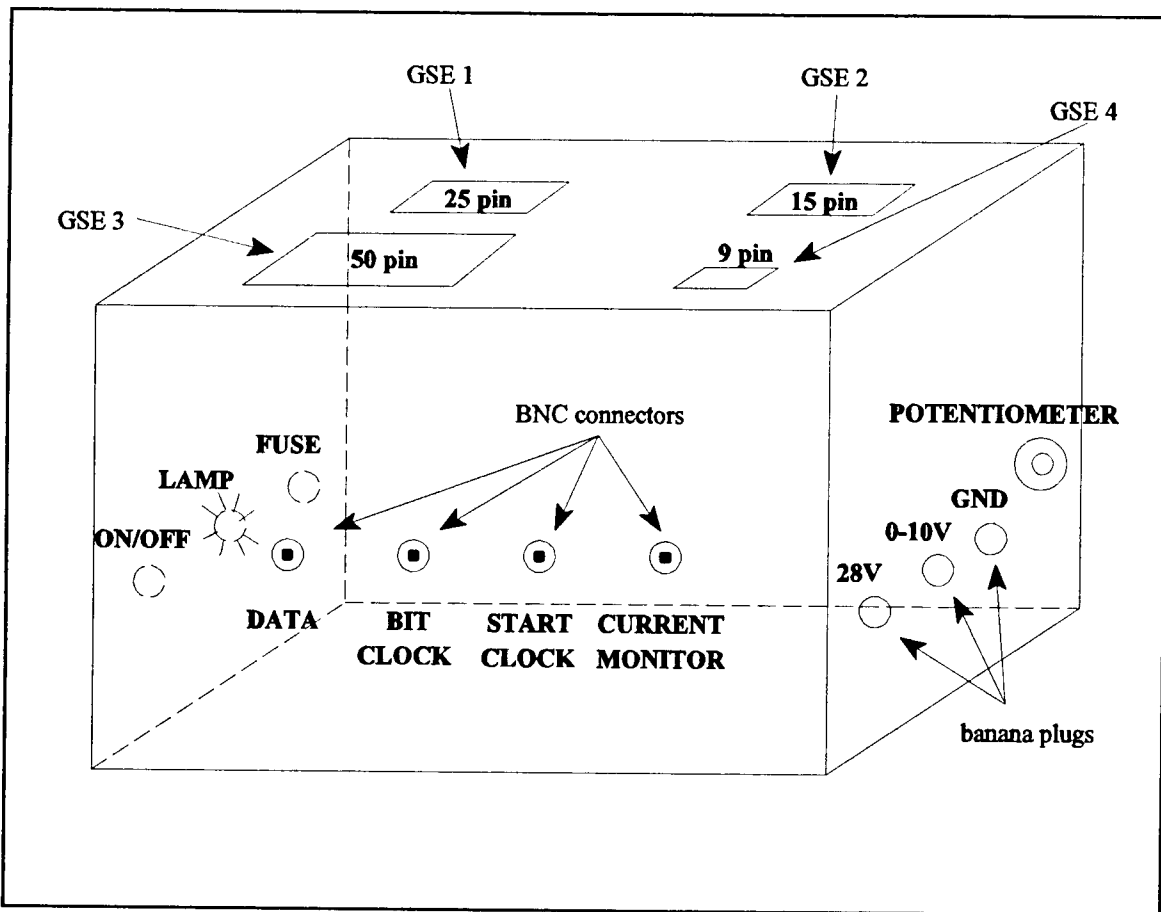


**Figure G-1** ISAAC GSE Electronics Interface Box.

After all of these connections have been made or checked, the next step is to connect a multimeter to the ground and variable voltage banana plugs on the right side of the interface box. These plugs are labeled accordingly. The dial on the right side of the box allows variation of this voltage which provides power to the high-voltage power supply. The high-voltage power supply in turn creates an electric field within the image intensifier of the spectrograph to accelerate photoelectrons into a phosphor-coated aluminum screen. Variation of this voltage on the interface box directly affects the image intensity received at the detector.

Next assure that the GSE Electronics Interface Box is connected to a 120V AC power supply. Turn on the box with the toggle switch on the left side of the box and a lamp should illuminate if power is present. Adjust the variable voltage as desired; normally this voltage

is set to 9.7 V. Finally, turn on the Macintosh computer and double click on the ISAAC GSE icon to start the software component of the GSE. The next section will detail the operation of this software.

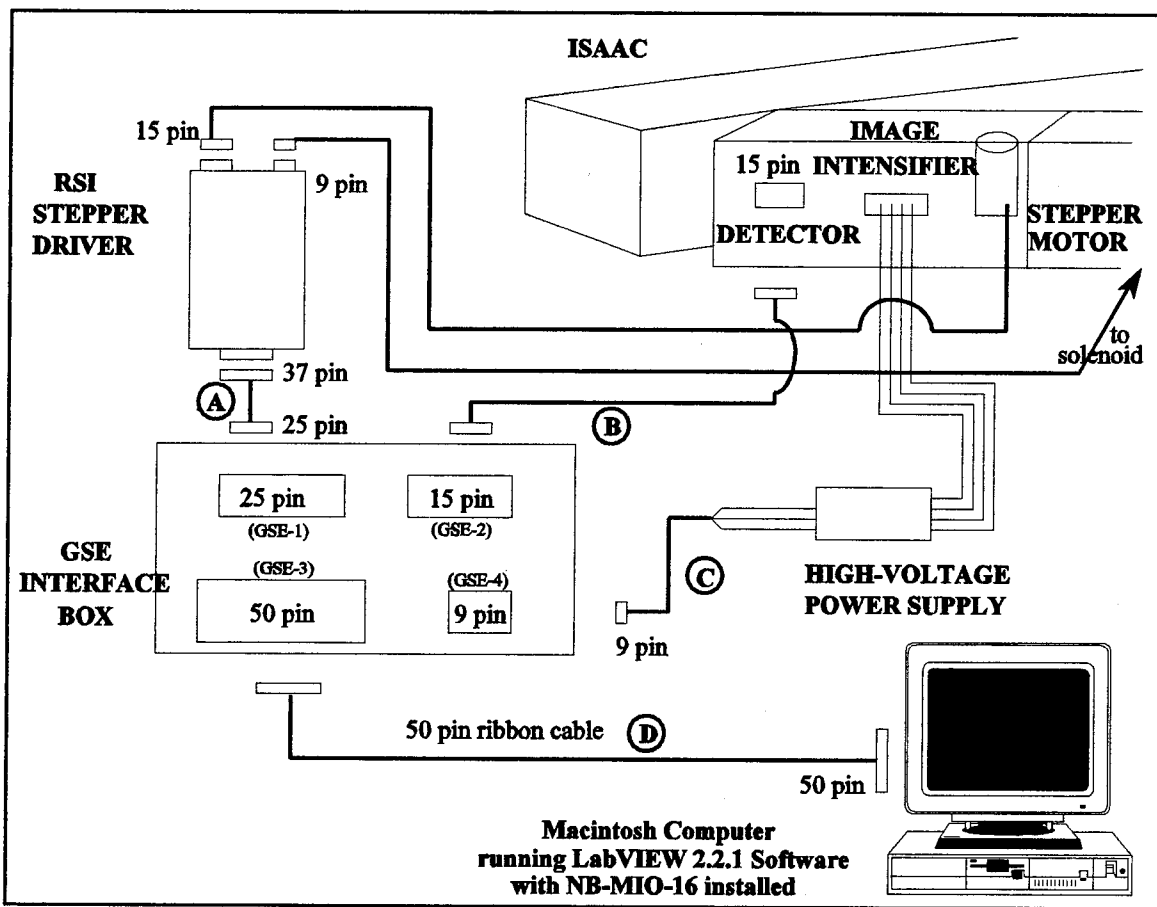


Figure G-2 ISAAC GSE hardware interface.

## B. ISAAC GSE LABVIEW 2.2.1 SOFTWARE OPERATION

The LabVIEW 2.2.1 software component of the ISAAC GSE is a user-friendly interface that allows simple point-and-click operation of the spectrograph and its stepper motor which controls the position of the spectrograph's grating. After connecting and powering all hardware components of the GSE and opening the ISAAC GSE program, you should be presented with a program front panel on the Macintosh screen. This front panel

is shown in Figure G-3. A sample spectrum is displayed upon startup. Start the program by clicking on start icon at the upper-left of the window. This function is represented by a right-pointing arrow. On start, the grating will turn automatically to grating position ONE. This is necessary so the program will know the current grating position throughout the remainder of operation.

The bottom portion of this front panel is an XY plot of obtained spectra. Along the top of the panel are indicators, controls and buttons that provide the ability to control the spectrograph. Each of these buttons and indicators are discussed in the following sections.

### **1. Number of Spectra to be Averaged**

The control at the top left of the front panel allows you to select the number of spectra that are desired to be averaged. You may click on the up and down arrows to increment or decrement the number displayed in the box to the right of the arrows or you may click once on the number and then type a new number at the keyboard.

### **2. GRATING Button**

User selection of the **GRATING** button causes a second smaller front panel to pop up in front of the main front panel. This panel is shown in Figure G-4. This panel contains additional user selectable buttons: **STEP GRATING**, **GO TO FIDUCIAL**, **1**, **2**, **3**, **4**, and **QUIT**.

#### ***a. STEP GRATING Button***

Selection of the **STEP GRATING** button causes the grating to be turned the number of steps specified in the digital control below this button. Use this button if you need to place the grating at some intermediate position for testing purposes. Normally, this function will not be required as spectra should only be obtained from one of the four primary grating position.

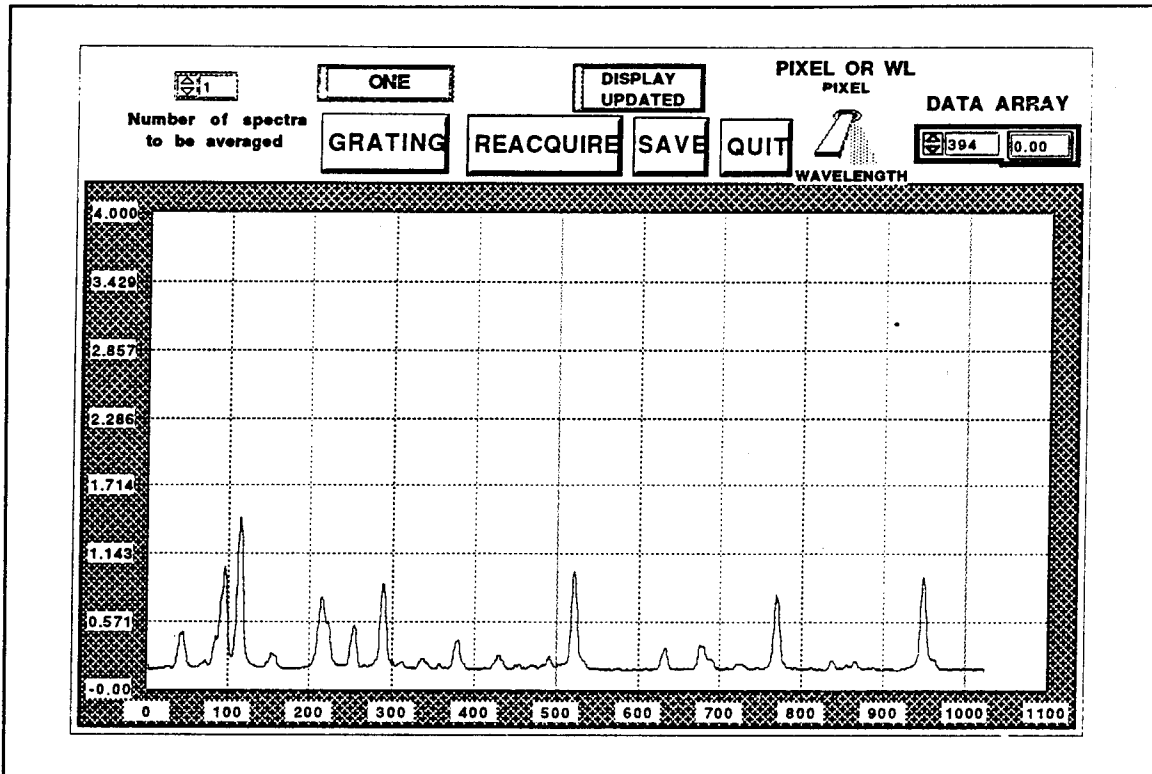


Figure G-3 ISAAC GSE front panel display.

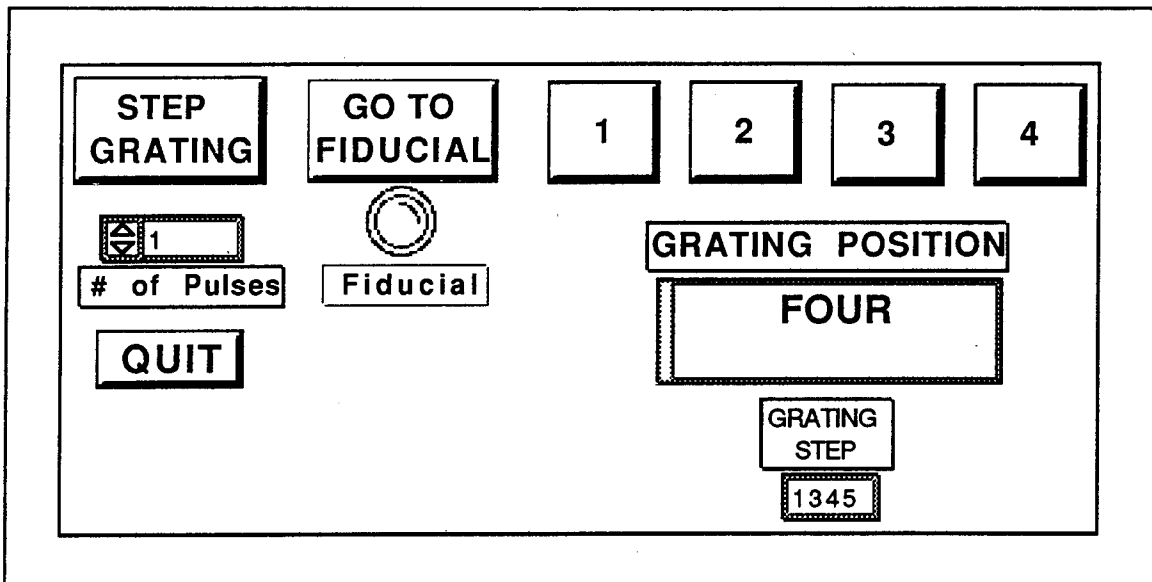


Figure G-4 Front panel of the ISAAC GSE Grating Selector.

*b. GO TO FIDUCIAL Button*

**GO TO FIDUCIAL** turns the grating until a Fiducial Signal is first received, thus placing the grating in the initial position. The artificial lamp below this button lights upon receipt of the Fiducial Signal.

*c. Buttons 1, 2, 3, and 4*

The numbered buttons (**1** through **4**) turn the grating to the specified position. The displays below these buttons show the position and the grating step for the current position of the grating. This display will also show if the grating is at some intermediate position or is at the fiducial.

*d. QUIT Button*

After selection of a grating position, click on the **QUIT** button to exit this front panel and return to the main ISAAC GSE front panel.

**3. REACQUIRE Button**

Selecting the **REACQUIRE** button acquires a new spectrum or spectra as desired. The single or averaged spectrum is displayed on the front panel XY plot. The Y-axis is intensity measured in volts, while the X-axis is either the pixel numbers of the detector (0-1023) or an approximate wavelength. The choice for this axis is determined by your selection using the toggle switch to the right of the **QUIT** button. The X-axis will be pixel number if this toggle switch is in the up position or if the grating is not at one of the four primary positions. If the grating is at position **ONE** through **FOUR**, and the toggle switch is in the down position, the X-axis will display the wavelengths associated with the current grating position.

#### **4. SAVE Button**

The **SAVE** button is used to save the spectrum currently displayed to an ASCII file for later analysis. The ASCII file will consist of 1024 lines of single numbers representing the intensities in volts at each of the 1024 detector pixels. This file can be read into other software such as IDL<sup>®</sup> published by Research Systems, Inc. for processing and display.

#### **5. QUIT Button**

The **QUIT** button, as expected, ends the program.

#### **6. DATA ARRAY Indicator**

The **DATA ARRAY** indicator at the upper right of the front panel allows you to manually inspect the intensity voltage for any selected pixel number for the currently-displayed spectrum. Click on the increment or decrement buttons or type in a number for the pixel desired in the left part of this indicator. Press Enter on the keyboard and the intensity is displayed at the right of the indicator.

#### **7. Message Displays**

Two message windows are above the selection buttons. These displays signal the current grating position and also the status of the program.

### **C. VIDEO DATA, CURRENT MONITOR, MASTER CLOCK AND START CLOCK**

BNC connectors provide a means to examine the output of the video data and clocks directly. The left-most BNC on the front of the ISAAC GSE Electronic Interface Box may be connected to an oscilloscope to examine the video output of the detector. The next two BNCs provide a means of examining the Master (Bit) Clock and the Start Clock that drives the shift register for the detector. The Bit Clock is set as a periodic square wave at 100 KHZ frequency. The Start Clock sends a 10  $\mu$ sec pulse every 61.44 msec to cause the detector to send a spectrum. There should be 1024 Video Words (pulses) per Start Pulse. A timing diagram for these clocks and data is shown in Figure G-5. The right-most BNC provides



connection to the RSI Stepper Motor Current Monitor. This monitor outputs a frequency that corresponds to a current.

#### D. FURTHER DETAIL

Detailed descriptions of the hardware design of the ISAAC GSE Electronics Interface Box and the GSE software program are available in the thesis that this manual appends. Included are pinouts for all the I/O connectors and suggestions for further modifications of the GSE hardware and software.

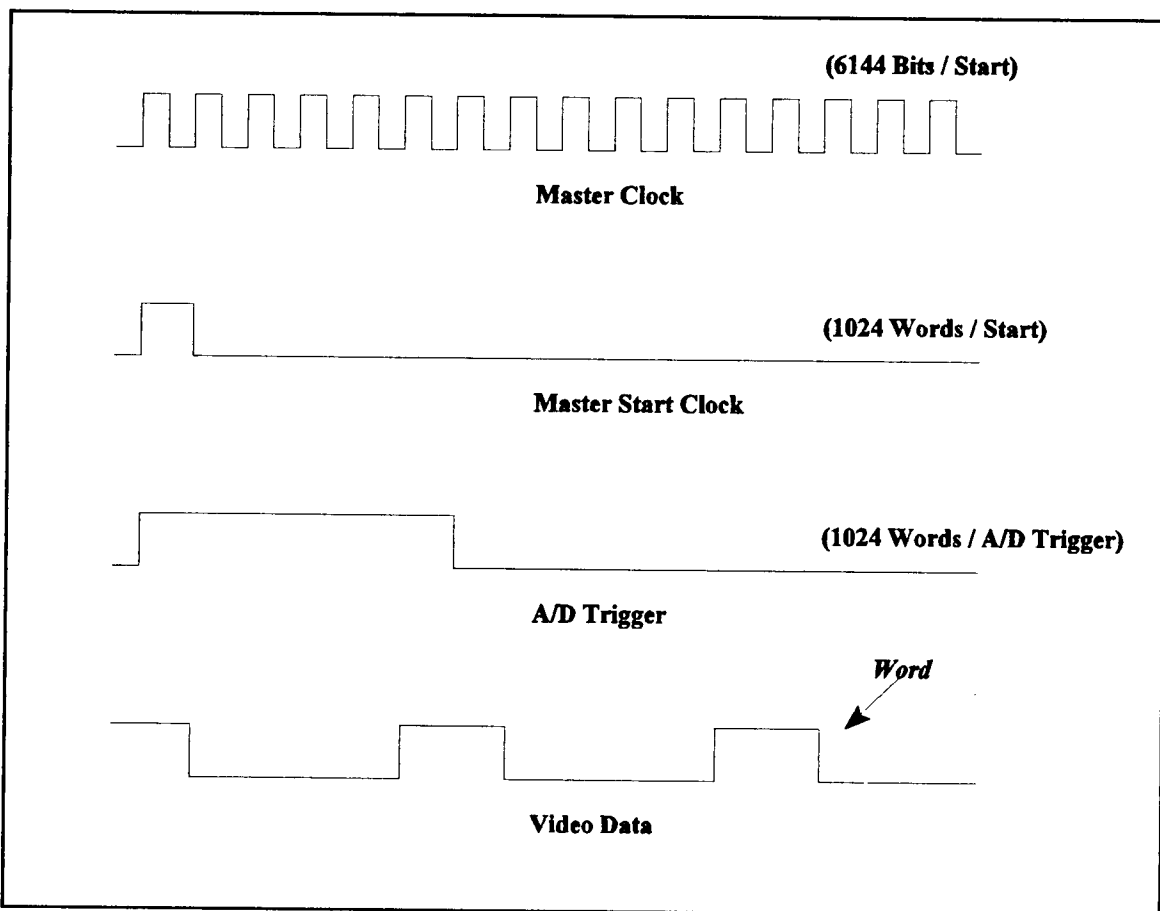


**Figure G-5** Timing diagram for Master Clock, Master Start Clock, A/D Trigger, and Video Data. The period of the Master Clock is 10 μsec and the period between successive video words is 60 μsec. The Start Clock and A/D Trigger pulse every 61.44 msec (1024 x 60 μsec).

## LIST OF REFERENCES

Agardy, F.J., and R.R. Cleave, *A Strategy for Maximizing the Scientific Return Using a Multi-phased Mission Design for ARGOS*, American Astronautical Society paper 93-594, AAS/AIAA Astrodynamics Specialist Conference, 1993.

*ARGOS Comprehensive Design Review*, Rockwell International and Naval Research Laboratory, 17 November 1993.

Barth, C.A. and F.G. Eparvier, "A Method of Measuring the Temperature of the Lower Thermosphere," *J. Geophys. Res.*, 98, 9437-9441, 1993.

Berends, John, Research Support Instruments, Inc., private communication, 12 April 1994.

Brasseur, Guy, and Susan Solomon, *Aeronomy of the Middle Atmosphere*, D. Reidel Publishing Company, 1984.

Carruthers, George R., and Timothy D. Seeley, "Global Imaging Monitor of the Ionosphere (GIMI): an ultraviolet ionospheric imaging experiment for the ARGOS satellite," *Instrumentation for Planetary and Terrestrial Atmospheric Remote Sensing*, SPIE Proceedings, vol. 1745, pp. 321-332, 1992.

Chandra, S., E.I. Reed, R.R. Meier, C.B. Opal, and G.T. Hicks, "Remote Sensing of the Ionospheric F Layer by Use of O I 6300-Å and O I 1356-Å Observations," *J. Geophys. Res.*, 80, 2327-2332, 1975.

Cleary, David D., *Analysis of Nitric Oxide Fluorescence Bands from High Latitude Rocket Observations of the Thermospheric Dayglow*, Ph.D. Dissertation, University of Colorado, 1985.

Cleary, David D., "Daytime High-Latitude Rocket Observations of the NO  $\gamma$ ,  $\delta$ , and  $\epsilon$  Bands," *J. Geophys. Res.*, 94, 11337-11344, 1986.

Cleary, David D., R.R. Meier, E.P. Gentieu, P.D. Feldman, and A.B. Christensen, "An Analysis of the Effects of N<sub>2</sub> Absorption on the O<sup>+</sup> 834-Å Emission From Rocket Observations," *J. Geophys. Res.*, 94, 17,281-17,285, 1989.

Cleary, David D., S. Gnanalingam, Robert P. McCoy, Ken F. Dymond, and F.G. Eparvier, "The Middle Ultraviolet Dayglow Spectrum," submitted *J. Geophys. Res.*, 1994.

Crowley, G., Applied Physics Laboratory, private communication, 13 Sep 1994.

Danczyk, Gary Michael, *Identification of Thermospheric Dayglow Emissions for the MUSTANG Experiment*, Master's Thesis, Naval Postgraduate School, Monterey, CA, 1989.

Eisberg, Robert, and Robert Resnick, *Quantum Physics of Atoms, Molecules, Solids, Nuclei, and Particles*, Second Edition, John Wiley & Sons, 1985.

Encyclopedia of Physics, Second Edition, VCH Publishers, Inc., 1991.

Hedin, Alan E., "MSIS-86 Thermospheric Model," *J. Geophys. Res.*, 92, 4649-4662, 1987.

Herzberg, Gerhard, *Molecular Spectra and Molecular Structure: I Spectra of Diatomic Molecules*, Second Edition, D. Van Nostrand Company, 1950.

Herzberg, Gerhard, *Atomic Spectra and Atomic Structure*, Dover Publications, 1944.

Huber, K.P., and Gerhard Herzberg, *Molecular Spectra and Molecular Structure: IV Constants of Diatomic Molecules*, Van Nostrand Reinhold Company, 1979.

Johnson, Charles Y., "Ionospheric Composition and Density from 90 to 1200 Kilometers at Solar Minimum," *J. Geophys. Res.*, 71, 330-331, 1966.

Labview 2 LabDriver VI Library Reference Manual, Version 4.2, February 1991 Edition, Part Number 320249-01, National Instruments Corporation, 1991.

McCoy, R.P., D.E. Anderson, Jr., and S. Chakrabarti, " $F_2$  Region Ion Densities From Analysis of  $O^+ 834\text{-\AA}$  Airglow: A Parametric Study and Comparisons With Satellite Data," *J. Geophys. Res.*, 90, 12,257-12,264, 1985.

McCoy, R.P., Naval Research Laboratory, private communication, 1993.

Meier, R.R., "Ultraviolet Spectroscopy and Remote Sensing of the Upper Atmosphere," *Space Science Reviews*, vol. 58, nos. 1 and 2, 1991.

NB-MIO-16 User Manual, April 1989 Edition, Part Number 320096-01, National Instruments Corporation, 1989.

*Penguin Dictionary of Astronomy*, Jacqueline Mitton, 1993.

Quint, John H., *Development of an NPS Middle Ultraviolet Spectrograph (MUSTANG) Electronic Interface Package*, Master's Thesis, Naval Postgraduate School, Monterey, CA, 1991.

Reader, J., and C.H. Corliss, *Wavelengths and Transition Probabilities for Atoms and Atomic Ions, Part I. Wavelengths*, U.S. National Bureau of Standards, 1980.

Serway, Raymond A., *Physics for Scientists and Engineers*, Third Edition, Saunders College Publishing, 1990.

Tascione, Thomas F., *Introduction to the Space Environment*, Orbit Book Company, 1988.

The Joint Chiefs of Staff Memorandum MJCS 154-86 to Under Secretary of Defense (Research and Engineering), Subject: *Military Requirements for Defense Environmental Satellites*, 1 Aug. 1986.

Tinsley, Brian A., and José A. Bittencourt, "Determination of *F* Region Height and Peak Electron Density at Night Using Airglow Emissions from Atomic Oxygen," *J. Geophys. Res.*, 80, 2333-2337, 1975.

Turner, Capt J. Brian, and F.J. Agardy, "The Advanced Research and Global Observation Satellite (ARGOS) Program," AIAA paper 94-4580, AIAA Space Programs and Technologies Conference, 1994.



## INITIAL DISTRIBUTION LIST

1. Defense Technical Information Center 2  
Cameron Station  
Alexandria, Virginia 22304-6145
2. Library, Code 52 2  
Naval Postgraduate School  
Monterey, California 93943-5101
3. Dr. William B. Colson 1  
Physics Department, Chairman PH  
Naval Postgraduate School  
Monterey, California 93943-5000
4. Dr. Daniel J. Collins 1  
Department of Aeronautics and Astronautics, Chairman AA  
Naval Postgraduate School  
Monterey, California 93943-5106
5. Dr. D.D. Cleary 3  
Physics Department, PH/CI  
Naval Postgraduate School  
Monterey, California 93943-5000
6. Dr. O. Biblarz 1  
Department of Aeronautics and Astronautics, AA/BI  
Naval Postgraduate School  
Monterey, California 93943-5106
7. Officer in Charge 1  
Naval Security Group Detachment  
Brunswick NAS  
Brunswick, Maine 04011
8. LT Jeffrey A. MacQuarrie 2  
3310 Harrison St.  
Evanston, Illinois 60201